DGK Ausschuss Geodäsie (DGK)
der Bayerischen Akademie der Wissenschaften

Reihe C Dissertationen Heft Nr. 967

Fabian Ruwisch

GNSS Feature Maps – Robust Lane-level Accurate GNSS Navigation in Urban Trenches

München 2025

Verlag der Bayerischen Akademie der Wissenschaften, München

ISSN 0065-5325 ISBN 978 3 7696 5379 3

DGK Ausschuss Geodäsie (DGK)
der Bayerischen Akademie der Wissenschaften

Reihe C Dissertationen Heft Nr. 967

GNSS Feature Maps – Robust Lane-level Accurate GNSS Navigation in Urban Trenches

Von der Fakultät für Bauingenieurwesen und Geodäsie
der Gottfried Wilhelm Leibniz Universität Hannover
zur Erlangung des akademischen Grades
Doktor-Ingenieur (Dr.-Ing.)
genehmigte Dissertation

von

Fabian Ruwisch, M. Sc.

München 2025

Verlag der Bayerischen Akademie der Wissenschaften, München

ISSN 0065-5325 ISBN 978 3 7696 5379 3

Adresse des Ausschusses Geodäsie (DGK)
der Bayerischen Akademie der Wissenschaften:

Ausschuss Geodäsie (DGK) der Bayerischen Akademie der Wissenschaften
Alfons-Goppel-Straße 11 ● D – 80 539 München
Telefon +49 – 89 – 23 031 1113 ● Telefax +49 – 89 – 23 031 - 1283 / - 1100
e-mail post@dgk.badw.de ● http://www.dgk.badw.de

Prüfungskommission:

Vorsitzender:	Prof. Dr.-Ing. habil. Christian Heipke
Referent:	Prof. Dr.-Ing. Steffen Schön
Korreferenten:	Associate Prof. Dr. Li-Ta Hsu (The Hong Kong Polytechnic University) apl. Prof. Dr.-Ing. Claus Brenner

Tag der mündlichen Prüfung: 25.03.2025

:

Diese Dissertation ist auf dem Server des Ausschusses Geodäsie (DGK)
der Bayerischen Akademie der Wissenschaften, München unter <http://dgk.badw.de/>
sowie unter Wissenschaftliche Arbeiten der Fachrichtung Geodäsie und Geoinformatik
der Leibniz Universität Hannover (ISSN 0174-1454), Nr. 415,
<https://repo.uni-hannover.de/items/a02de733-f4df-49b7-809d-b55643667551>, Hannover 2025, elektronisch publiziert

---

© 2025 Ausschuss Geodäsie (DGK) der Bayerischen Akademie der Wissenschaften, München

Alle Rechte vorbehalten. Ohne Genehmigung der Herausgeber ist es auch nicht gestattet,
die Veröffentlichung oder Teile daraus zu vervielfältigen.

ISSN 0065-5325
ISBN 978 3 7696 5379 3

Abstract

The demand for high accuracy and high integrity positioning using the Global Navigation Satellite System (GNSS) sensor is on the rise, as GNSS is the only observation system capable of providing absolute positioning information. However, all GNSS positioning strategies are sensitive to the operating environment, posing a substantial challenge in fulfilling the localization requirements of autonomous vehicles, particularly in dense urban areas. The primary error source for GNSS-based vehicle positioning in these areas is the reception of multipath signals – combinations of direct and reflected signals – and NLOS (Non-Line-of-Sight) signals, which are only reflected signals that reach the antenna. These signals can cause significant inaccuracies in vehicle position estimation regardless of the GNSS positioning technique used. To address multipath and NLOS errors, two primary strategies have been developed. One is 3DMA (3D-Mapping-Aided) GNSS, which improves urban GNSS navigation by utilizing 3D city models. Another involves using robust estimation strategies that include all observations but reduce the impact of erroneous observations on the positioning solution through various robust loss functions. However, these techniques have limitations, such as an overly conservative down-weighting of observations, lack of robustness for highly contaminated data, the need of additional 3D city model information or computationally intensive algorithms.

In this thesis, two innovative strategies are proposed to improve GNSS-based navigation in urban trenches, building upon existing multipath mitigation strategies for single, static stations (i.e., utilizing the ground-track repeatability of ranging errors) with the objective of generating a GNSS Feature Map tailored for automotive applications. The thesis discusses all critical aspects of the map generation process in detail, including the coordinate information serving as foundation of the map, its resolution in longitudinal, lateral and vertical direction, and an in-depth evaluation of the GNSS ranging error similarity. The final product is a GNSS Feature Map consisting of satellite visibility information or pseudorange residual information for all satellite positions in a regular grid along a selected trajectory. The performance of employing various robust loss functions for computing the observation weights based on map information is theoretically evaluated through a Monte-Carlo simulation. In this context, the HG-estimator, an adapted robust estimator, is introduced. Simulation results for multi-GNSS SPP (Single Point Positioning) demonstrate that when prior knowledge of ranging errors is applied to compute observation weights, a 3D position error of around 2 m is achieved even if 70 % of the observations have a standard deviation of 100 m. The map information is further incorporated into an extended Kalman filter (EKF) framework for GNSS RTK (Real-time Kinematic) positioning, allowing either the exclusion of potential NLOS satellites or the adaption of robust estimation techniques. The evaluation and validation of these strategies are carried out based on two kinematic automotive experiments, located in a medium and deep urban trench, respectively. The impact of GNSS Feature Map information is assessed by means of typical GNSS performance parameters, such as accuracy, integrity and ambiguity resolution. Improvements of 54 % and 79 %, and 60 % and 64 % in horizontal and vertical accuracy for the medium and deep urban trenches, respectively, are achieved when applying the HG-estimator with map information. Consequently, lane keeping and lane determination accuracy requirements are met. The integrity and reliable ambiguity resolution are significantly enhanced, which leads to an overall more robust state estimation. By combining the map information with raw data from different receiver grades, the hardware independence is successfully proven. Finally, the results are compared to receiver-internal RTK solutions, yielding a significant improvement in the deep urban trench.

Keywords: Urban GNSS navigation, GNSS Feature Map, multipath mitigation, robust estimation, autonomous vehicles

Zusammenfassung

Die Nachfrage nach einer hochgenauen und zuverlässigen Positionsbestimmung mittels des Global Navigation Satellite System (GNSS)-Sensors steigt, da GNSS das einzige Beobachtungssystem ist, das absolute Positionsdaten liefern kann. Allerdings sind alle GNSS-Positionierungsstrategien sensitiv gegenüber der Umgebung, was eine Herausforderung bei der Erfüllung der Lokalisierungsanforderungen autonomer Fahrzeuge darstellt, insbesondere in dichten Stadtgebieten. Die Hauptfehlerquelle für die GNSS-basierte Fahrzeugortung in diesen Gebieten ist der Empfang von Mehrwegesignalen – Kombinationen aus direkten und reflektierten Signalen – und NLOS-Signalen (Non-Line-of-Sight), bei denen es sich nur um reflektierte Signale handelt, die die Antenne erreichen. Zur Behebung dieser Fehler wurden zwei Hauptstrategien entwickelt. Die eine ist *3D-Mapping-Aided* (3DMA) GNSS, das die GNSS-Navigation in Städten durch die Verwendung von 3D-Stadtmodellen verbessert. Zum anderen werden robuste Schätzstrategien verwendet, die alle Beobachtungen einbeziehen, aber die Auswirkungen fehlerhafter Beobachtungen auf die Positionierungslösung durch verschiedene robuste Verlustfunktionen reduzieren. Diese Verfahren weisen jedoch Einschränkungen auf, wie z. B. eine zu konservative Herabgewichtung, mangelnde Robustheit bei stark kontaminierten Daten, die Notwendigkeit zusätzlicher Gebäudemodellinformationen oder rechenintensive Algorithmen.

In dieser Arbeit werden zwei innovative Strategien zur Verbesserung der GNSS-Navigation in städtischen Gräben vorgeschlagen, die auf bestehenden Strategien zur Verringerung von Mehrwegeffekten für statische Stationen aufbauen, mit dem Ziel, eine Karte zu erstellen, die im Automobilbereich anwendbar ist. In dieser Arbeit werden alle kritischen Aspekte des Kartenerstellungsprozesses erörtert, einschließlich der Koordinaten, ihrer Auflösung in Längs-, Quer- und Vertikalrichtung, sowie einer Bewertung der Ähnlichkeit der GNSS-Entfernungsfehler. Das Endprodukt ist eine GNSS-Merkmalskarte, die aus Sichtbarkeitsinformationen oder Entfernungsfehlern für alle Satellitenpositionen in einem regelmäßigen Gitter entlang einer ausgewählten Trajektorie besteht. Die Leistung der verschiedenen robusten Verlustfunktionen zur Berechnung der Beobachtungsgewichte aus Karteninformationen wird durch eine Monte-Carlo-Simulation bewertet. In diesem Kontext wird der HG-Schätzer eingeführt, ein angepasster robuster Schätzer. Simulationsergebnisse für Multi-GNSS SPP (*Single Point Positioning*) zeigen, dass ein 3D-Positionsfehler von etwa 2 m erreicht wird, selbst wenn 70 % der Beobachtungen eine Standardabweichung von 100 m aufweisen, wenn Vorwissen über Entfernungsfehler verwendet wird. Diese Karteninformationen werden in einen *extended Kalman-Filter* (EKF) für die RTK-Positionierung (*Real-Time Kinematic*) integriert, was entweder den Ausschluss von NLOS-Satelliten oder die Anpassung robuster Schätzverfahren ermöglicht. Die Bewertung und Validierung dieser Strategien erfolgt anhand von zwei kinematischen Experimenten in einem mittleren bzw. tiefen städtischen Graben. Die Auswirkungen der GNSS-Merkmalskarte werden anhand typischer Parameter wie Genauigkeit, Integrität und Mehrdeutigkeitsauflösung bewertet. Verbesserungen von 54 % und 79 % sowie 60 % und 64 % bei der horizontalen und vertikalen Genauigkeit für den mittleren bzw. tiefen städtischen Graben werden durch die Anwendung des HG-Schätzers mit Karteninformationen erreicht. Folglich werden die Anforderungen an Fahrspurhaltungs- und Fahrspurbestimmungs-Anwendungen erfüllt. Die Integrität und die zuverlässige Auflösung von Mehrdeutigkeiten werden erheblich verbessert, was zu einer insgesamt robusteren Zustandsschätzung führt. Durch die Anwendung der Karteninformationen auf Rohdaten von verschiedenen Empfängertypen wird die Hardwareunabhängigkeit erfolgreich nachgewiesen. Schließlich werden die Ergebnisse mit empfängerinternen RTK-Lösungen verglichen, was zu einer signifikanten Verbesserung in tiefen städtischen Gräben führt.

Schlagwörter: Städtische GNSS-Navigation, GNSS-Merkmalskarte, Mehrwegeabschwächung, Robuste Schätzung, Autonome Fahrzeuge

Contents

Acronyms **ix**

List of Figures **xiii**

List of Tables **xv**

1 Introduction **1**
- 1.1 Motivation . . . 1
- 1.2 Objective and Outline . . . 2

2 Basics **5**
- 2.1 Fundamentals of Global Navigation Satellite Systems . . . 5
  - 2.1.1 Observables . . . 5
  - 2.1.2 Combination of Observations . . . 8
  - 2.1.3 Weighting of Observations . . . 10
- 2.2 Kalman Filtering . . . 14
- 2.3 GNSS Precise Positioning . . . 15
- 2.4 Integer Ambiguity Resolution . . . 18
- 2.5 Robust Statistics . . . 23
- 2.6 GNSS Positioning in Urban Environments . . . 28
  - 2.6.1 3D Mapping Aided GNSS . . . 29
  - 2.6.2 Consistency Checking . . . 34
  - 2.6.3 Multi-Sensor Combination . . . 35
  - 2.6.4 Machine Learning-based Approaches . . . 35
  - 2.6.5 Robust Estimation . . . 36
- 2.7 Performance Parameters . . . 38
  - 2.7.1 Accuracy . . . 38
  - 2.7.2 Integrity . . . 39
  - 2.7.3 Availability and Continuity . . . 40
  - 2.7.4 Performance Specifications for Intelligent Transportation Systems . . . 41

3 An Extended Kalman Filter Framework for Urban Navigation **45**
- 3.1 State Estimation . . . 45
- 3.2 Outlier Detection . . . 48
- 3.3 3D-Mapping-Aided Fault Detection and Exclusion . . . 49
- 3.4 Computation Procedure . . . 50

4 GNSS Feature Map-Aided Robust EKF **53**
- 4.1 Motivation . . . 53
- 4.2 Adapted Robust Estimation . . . 55
  - 4.2.1 GNSS Feature Map-Aided NLOS Exclusion . . . 58
  - 4.2.2 GNSS Feature Map-Aided Robust Weighting . . . 58
  - 4.2.3 The HG-estimator – An Adapted Robust Weight Model . . . 59
  - 4.2.4 Performance Simulation of Robust Estimators . . . 61
- 4.3 GNSS Feature Map . . . 63
  - 4.3.1 Concept . . . 63
  - 4.3.2 Map Generation . . . 64
  - 4.3.3 Waypoint Resolution . . . 70
  - 4.3.4 On the Similarity of GNSS Ranging Errors . . . 73

4.3.5 Fully Populated Map Provision . . . 76

5 Application Examples and Case Studies 83
5.1 Kalman Filter Settings . . . 83
5.2 Automotive Experiment in Medium Urban Trench . . . 84
5.2.1 Setup . . . 84
5.2.2 Accuracy Performance . . . 85
5.2.3 Attainable Integrity . . . 88
5.2.4 Ambiguity Resolution . . . 90
5.3 Automotive Experiment in Deep Urban Trench . . . 92
5.3.1 Setup . . . 92
5.3.2 Accuracy Performance . . . 94
5.3.3 Attainable Integrity . . . 101
5.3.4 Ambiguity Resolution . . . 103
5.3.5 Evaluation of Hardware-dependency . . . 105
5.3.6 Comparison with Receiver-internal RTK Solution . . . 112

6 Conclusions 117
6.1 Summary . . . 117
6.2 Outlook . . . 120

Bibliography 123

Acknowledgments 135

Curriculum vitae 135

Acronyms

3DMA	3D-Mapping-Aided.
3DMA-FDE	3D-Mapping-Aided Fault Detection and Exclusion.
3DMA-NE	3DMA NLOS exclusion.
ADAS	Advanced Driver Assistance Systems.
AI	Artificial Intelligence.
AL	Alert Limit.
BDS	BeiDou Navigation Satellite System.
BIE	Best Integer Equivariant.
C/N_0	Carrier-to-Noise-Power-Density Ratio.
CDF	Cumulative Distribution Function.
CIR	Cascade Integer Resolution.
CityGML	City Geography Markup Language.
CMC	Code-Minus-Carrier.
CODE	Center for Orbit Determination in Europe.
CORS	Continuously Operating Reference Station.
COST	Cooperation in Science and Technology.
CP	Carrier Phase.
DD	Double Difference.
DGNSS	Differential GNSS.
DLL	Delay-Locked-Loop.
DOY	Day of Year.
ECEF	Earth-centered, Earth-fixed.
EKF	Extended Kalman Filter.
GLONASS	Globalnaja Nawigazionnaja Sputnikowaja Sistema.
GM	Generalized M.
GM-KF	Generalized M-estimator Kalman Filter.
GMM	Gaussian Mixture Model.
GNSS	Global Navigation Satellite System.
GNSS FMA-NE	GNSS Feature Map-Aided NLOS Exclusion.
GNSS FMA-W	GNSS Feature Map-Aided Weighting.
GPS	Global Positioning System.
GS	Greedy Search.
HMI	Hazardous Misleading Information.
HPL	Horizontal Protection Level.
I-VKF	Independent indicator Variational Bayesian Kalman Filter.
IAR	Integer Ambiguity Resolution.
IB	Integer Bootstrapping.
ICAO	International Civil Aviation Organization.
IGS	International GNSS Service.
ILS	Integer Least-squares.
IMU	Inertial Measurement Unit.
INS	Inertial Navigation System.
IONEX TEC	Ionosphere Exchange Total Electron Content.
IR	Integer Rounding.
IRLS	Iteratively Reweighted Least-squares.
ITCAR	Integrated Three Carrier Ambiguity Resolution.

ITS	Intelligent Transportation System.
LAD	Least Absolute Deviation.
LAMBDA	Least-squares AMBiguity Decorrelation Adjustment.
LC	Linear Combination.
LEO	Low Earth Orbit.
LiDAR	Light Detection and Ranging.
LKF	Linearized Kalman Filter.
LMS	Least Median of Squares.
LoD	Level of Detail.
LOS	Line-Of-Sight.
LSA	Least-squares Adjustment.
LTS	Least Trimmed Squares.
MAD	Median Absolute Deviation.
MEMS	Micro-electromechanical System.
ML	Machine Learning.
MLE	Maximum Likelihood Estimator.
MLTS	Modified Least Trimmed Squares.
MP	multipath.
NCO	Numerically Controlled Oscillator.
NLOS	Non-Line-Of-Sight.
NO	Nominal Operation.
NTRIP	Network Transportation of RTCM Internet Protocol.
OMC	Observed-Minus-Computed.
OSM	Open Street Map.
OSR	Observation Space Representation.
PAR	Partial Ambiguity Resolution.
pdf	Probability Distribution Function.
PE	Position Error.
PF	Particle Filter.
PL	Protection Level.
PLL	Phase-Locked-Loop.
PPP	Precise Point Positioning.
PR	Pseudorange.
PTV	Position and Time Variation.
RAIM	Receiver Autonomous Integrity Monitoring.
RIF	Robust Information Filter.
RINEX	Receiver Indeptendent Exchange Format.
RMS	Root Mean Square.
RTCM	Radio Technical Commission for Maritime Services.
RTK	Real-Time Kinematic.
S-VKF	Scalar Variational Bayesian Kalman Filter.
SaPPART	Satellite Positioning Performance Assessment for Road Transport.
SD	Single Difference.
SDR	Software-defined Radio.
SPP	Single Point Positioning.
SSR	State Space Representation.
STD	Standard Deviation.
TCAR	Three Carrier Ambiguity Resolution.
TTA	Time to Alert.

UKF	Unscented Kalman Filter.
VB-KF	Variational Bayesian Kalman Filter.
VMF3	Vienna Mapping Functions 3.
VPL	Vertical Protection Level.
WGS84	World Geodetic System 84.
XML	Extensible Markup Language.

List of Figures

2.1 Double difference combination of GNSS observations 9
2.2 Principle of the PPP method 17
2.3 Principle of the RTK positioning method. 17
2.4 Three-step GNSS integer ambiguity resolution process 18
2.5 Pull-in regions of different integer estimators for a two dimensional example . . 20
2.6 Bias and breakdown point of three traditional estimators for a one-dimensional estimation and different number of outliers 24
2.7 Overview of loss functions, score functions, and weighting functions 27
2.8 Main GNSS error sources in urban environments 29
2.9 Exemplary situation of ray tracing for a given situation in San Francisco, USA 31
2.10 LOS/NLOS determination algorithm 32
2.11 Satellite ray reflection on a building surface 33
2.12 Principle of shadow matching 34
2.13 Hierarchy of GNSS performance parameters 38
2.14 Protection level scaling factors for different probabilities and the Rayleigh and normal distribution 40
2.15 Relation between position error, protection level and alert limit 40
2.16 Comparison of bounding box geometry for different levels of autonomy: lane keeping, lane determination and road determination 42

3.1 Erroneous signal reception in urban areas and its mitigation in positioning algorithms 50
3.2 Flowchart of the developed EKF framework for GNSS RTK positioning 51

4.1 Multi-GNSS satellite availability for a kinematic trajectory in a typical urban area in the city of Hannover 54
4.2 Multi-GNSS satellite constellation of the simulation configuration 55
4.3 Loss functions of the MLE at the normal model, Huber and Geman-McClure estimators for the SPP formulation 56
4.4 Conceptual application of GNSS Feature Maps for localization of autonomous vehicles 57
4.5 EKF framework integration of adapted robust estimation approaches 57
4.6 Loss function, score function and weighting function of the proposed adapted robust HG-estimator 60
4.7 Loss functions of the HG estimator for the SPP formulation 61
4.8 RMS errors of the 3D position obtained by different estimators for 30 %, 50 % and 70 % contamination proportion 62
4.9 GNSS Feature Map design 64
4.10 GNSS Feature Maps based on real data from a kinematic experiment in the city of Hannover 65
4.11 Exemplary way element in an OSM file 66
4.12 OSM lane model and its interpolation 66
4.13 Skyplots for ten exemplary map waypoints of a satellite visibility classification map 68
4.14 Training data experiment setup 69
4.15 General concept of the data aggregation and GNSS Feature Map generation . . 69
4.16 GNSS Feature Map box polygon assignment 70
4.17 Waypoint resolution simulation setup 71
4.18 Changes in ray classification conditions with longitudinally distant waypoints . 71

4.19 Changes in ray classification conditions with laterally distant waypoints 72
4.20 Changes in ray classification conditions with varying height of the waypoints . 73
4.21 Fitted GMM curves in conjunction with the histogram of the respective data . 74
4.22 GPS L1 pseudorange error map for two exemplary locations 77
4.23 Multi-GNSS L1 pseudorange error map for two exemplary locations 78
4.24 Skyplots for ten exemplary map waypoints of a pseudorange residuals map generated by aggregating multi-GNSS L1 pseudorange 79
4.25 Skyplots for ten exemplary map waypoints of a pseudorange residuals map generated by aggregating multi-GNSS L1 pseudorange 80

5.1 Kinematic experiment setup of the automotive experiment in a medium urban trench 85
5.2 Horizontal and vertical position errors of the different approaches versus time and as cumulative frequency diagrams 86
5.3 Integrity evaluation of the horizontal component 88
5.4 Integrity evaluation of the vertical component 89
5.5 3D position error of the float and fixed solution along with the ambiguity success rate 90
5.6 Percentage of fixed ambiguities versus time, as cumulative distribution, and versus the 3D position error 91
5.7 Kinematic experiment setup of the automotive experiment in a deep urban trench 93
5.8 Horizontal and vertical position errors of the different approaches versus time and as cumulative distribution diagram 95
5.9 Longitudinal and lateral position errors of the different approaches as cumulative distribution diagram 97
5.10 Horizontal and vertical position error with respect to the LOS ratio 97
5.11 Analysis of the location-dependency of errors 99
5.12 Comparison of DD pre-fit residuals and GNSS Feature Map residuals 100
5.13 Integrity evaluation of the horizontal component for the different methods . . . 101
5.14 Integrity evaluation of the vertical component for the different methods 102
5.15 3D position error of the float and fixed solution along with the ambiguity success rate 103
5.16 Percentage of fixed ambiguities versus time, as cumulative distribution and versus the 3D position error 104
5.17 Number of carrier phase observations available for the Septentrio PolaRx5e, Septentrio mosaicX5 and u-blox F9P (L1/L5) receivers 105
5.18 Septentrio mosaicX5 receiver: Horizontal and vertical position errors of the different approaches versus time and as cumulative distribution diagram 107
5.19 Septentrio mosaicX5 receiver: Comparison of DD pre-fit residuals and GNSS Feature Map residuals 108
5.20 u-blox F9P (L1/L5) receiver: Horizontal and vertical position errors of the different approaches versus time and as cumulative distribution diagram 109
5.21 u-blox F9P (L1/L5) receiver: Comparison of DD pre-fit residuals and GNSS Feature Map residuals 111
5.22 Septentrio PolaRx5e receiver: Positioning accuracy of the 3DMA-NE and GNSS FMA-W HG methods compared to the receiver-internal RTK solution 113
5.23 Septentrio mosaicX5 receiver: Positioning accuracy of the 3DMA-NE and GNSS FMA-W HG methods compared to the receiver-internal RTK solution 114
5.24 u-blox F9P (L1/L5) receiver: Positioning accuracy of the 3DMA-NE and GNSS FMA-W HG methods compared to the receiver-internal RTK solution 115

List of Tables

2.1 Overview on the different positioning methods 16
2.2 Overview of ambiguity resolution methods 23
2.3 Overview of loss functions, score functions, and weighting functions 26
2.4 State of the art literature summary for GNSS positioning algorithms including NLOS exclusion or observation rectification strategies 30
2.5 Literature review for robust GNSS positioning 37
2.6 Protection level scaling factors for different probabilities and the Rayleigh and normal distribution 40
2.7 Stanford diagram conditions 41
2.8 Quantitative evaluation of performance requirements for road applications . . . 41
2.9 Accuracy classification boundaries from the application perspective 42
2.10 Combined localization and map error budget for U.S. local roads 42
2.11 Localization requirements for U.S. local roads for different vehicle sizes and lane keeping application 43

4.1 Simulation configuration 54
4.2 Loss function, score function and weighting function of the proposed adapted robust HG-estimator 60
4.3 Parameters configuration for the Monte-Carlo simulation. 61
4.4 GMM parameters for the four component estimation 75
4.5 GMM parameters for the components 1 to 3 of the four component estimation using DD residual differences between right and left antenna 76

5.1 GNSS RTK EKF Settings 83
5.2 Observation data recorded by the Septentrio PolaRx5e receiver 85
5.3 Horizontal and vertical position accuracy of the different approaches given in percentiles 87
5.4 Observation data recorded by the three receivers 94
5.5 Horizontal and vertical position accuracy of the different approaches given in percentiles 96
5.6 Septentrio mosaicX5 receiver: Horizontal and vertical position accuracy of the different approaches given in percentiles 106
5.7 u-blox F9P (L1/L5) receiver: RMS of the horizontal and vertical position error for the different approaches 110
5.8 Proportion of DGNSS modes, number of carrier phase observations, and number of carrier phase interruptions for the different receiver types 111

1

Introduction

1.1 Motivation

Global Navigation Satellite System (GNSS) is a geospatial infrastructure that allows users with compatible devices to determine their position, velocity and time by processing signals from satellites. The use of the GNSS sensor for position, navigation and timing is a significant enabler of functionality across a number of markets, including agriculture and precision farming, aviation and drones, insurance and finance, maritime and inland waterways, rail, and road and automotive. The focus of this thesis is on navigation in the automotive sector.

Accurate localization in urban environments plays a crucial role in many Intelligent Transportation System (ITS) applications, such as autonomous driving. The demand for high accuracy and high integrity positioning using the GNSS sensor is on the rise, as GNSS is the only observation system capable of providing absolute positioning information. To fulfill the stringent localization requirements for autonomous vehicles, such as for lane determination or lane keeping applications, carrier phase-based positioning techniques must be utilized. The employment of high-precision GNSS positioning strategies, such as Precise Point Positioning (PPP), Real-Time Kinematic (RTK) or PPP-RTK, enables the achievement of centimeter-level accuracy in the determination of the users' location. However, all GNSS positioning strategies are sensitive to the operating environment, which presents a significant challenge in meeting the localization requirements for autonomous vehicles in dense urban environments.

The GNSS signal is subject to a number of different error sources along its path from the satellite to the user antenna. The satellite clock error is addressed by the broadcast navigation message, which is transmitted concurrently with the pseudoranges or by orbit and clock products of the International GNSS Service (IGS). Furthermore, atmospheric effects, such as ionospheric and tropospheric delays, are either physically modeled, estimated within the positioning model, or corresponding corrections are transmitted by GNSS correction service providers. The primary source of error in GNSS-based vehicle positioning in urban environments is the reception of multipath signals – combinations of direct and reflected signals – and Non-Line-Of-Sight (NLOS) signals, which are only reflected signals that reach the antenna. Regardless of the high-precision GNSS positioning strategy employed, these signals can introduce significant errors in the vehicle's position estimation.

The characteristics of GNSS signals are dependent upon both the location of the user antenna and the positions of the satellites. In static multipath environments, a common method is to consider the ground-track repeatability of reflection-based errors in order to map errors induced by the local environment. In dynamic urban scenarios, the signal propagation-related characteristics exhibit a complex spatiotemporal behavior, whereby they are dependent on the moving user antenna location, the changing satellite positions, and the buildings in the surrounding area. However, the ground-track repeatability of reflection-based errors still shows potential for generating such a map for automotive applications, yet there is a lack of research contributions in this field. Consequently, numerous other multipath and NLOS error mitigation strategies have been investigated with the objective of enhancing GNSS-based navigation. However, all of these strategies exhibit constraints with respect to their applicability to autonomous vehicles in urban environments. The performance of a GNSS-based navigation system can be significantly enhanced when information regarding the propagation characteristics of the signal is accessible, which is achieved through the utilization of 3D city models and ray tracing computation. However, an accurate initial user position is necessary, and the performance is limited due to inaccuracies of the 3D city models and the computational complexity that depends on the environmental situation. While the effectiveness of satellite exclusion strategies is dependent on the number of available Line-Of-Sight (LOS) signals, error rectification strategies have only been studied for pseudorange-based positioning.

Another method of mitigating multipath and NLOS signal reception errors is the utilization of robust estimation strategies. They substantially improve the accuracy of the resulting GNSS positioning solution, provided that the number of faulty satellites is moderate. Robust estimation techniques retain all observations, but significantly dampen the impact of erroneous observations on the positioning solution through the implementation of diverse designs of robust loss functions. However, in the event that the number of measurement errors exceeds the number of available nominal observations, it becomes impossible to compute an optimal solution.

The aforementioned limitations of existing methods to enhance GNSS-based navigation in urban environments and the lack of research contributions in the field of mapping GNSS signal propagation conditions and ranging errors for automotive applications present a substantial opportunity for a comprehensive scientific investigation into the generation of such a map. This encompasses not only the generation of the map but also the combination with and adaptation of robust estimation techniques, with the objective of leveraging the advantages of existing methods while mitigating their inherent limitations.

1.2 Objective and Outline

The main focus of this thesis is the generation of a GNSS Feature Map tailored for automotive applications, aimed at improving GNSS navigation in urban trenches. A comprehensive review of the map generation process is provided, addressing all critical aspects, including the coordinate information that serves as the foundation of the map, its resolution in the longitudinal, lateral, and vertical directions, and an in-depth evaluation of the GNSS ranging error similarity. The potential of combining these map information with existing robust estimation techniques is theoretically assessed through Monte-Carlo simulation for pseudorange-based Single Point Positioning (SPP). As the localization requirements for automotive applications are very stringent, carrier phase-based positioning has to be implemented. To this end, the map information is further incorporated into an Extended Kalman Filter (EKF) framework for GNSS RTK positioning, allowing either the exclusion of potential NLOS satellites or the adaption of robust estimation techniques. The evaluation and validation of these strategies are carried out based on two kinematic automotive experiments, located in a medium and deep urban trench, respectively. The impact of GNSS Feature Map information is assessed by means of typical GNSS performance parameters, such as accuracy, integrity and ambiguity resolution. Additionally, the thesis investigates the hardware dependency and performance with respect to the receiver-internal RTK solution. In alignment with the aforementioned objectives, this thesis is organized as follows.

Chapter 2 provides an overview of the methodologies and models employed in this thesis, as well as an examination of the most advanced techniques from the literature. First, the fundamentals of GNSS are presented, including an overview of the various observation types and the combination of observations. Additionally, the discussion addresses the variance models assigned to GNSS measurements. Secondly, Kalman filtering is examined as a foundation for subsequent filter implementation with respect to the GNSS positioning formulation. Thirdly, the discussion turns to the precise GNSS positioning techniques, with an examination of their respective advantages and disadvantages. Subsequently, this section will review integer ambiguity resolution techniques, which are necessary when utilizing carrier phase-based positioning. Furthermore, an extensive review of the mathematical foundation for robust estimation techniques is presented, along with a discussion of the robust loss functions that are applied in this thesis. Next, current state of the art strategies for GNSS positioning in urban environments are reviewed with respect to their applicability and limitations. Finally, the most important GNSS performance parameters are introduced, together with the performance specifications for ITS.

Chapter 3 is devoted to the EKF framework for urban navigation. It includes a detailed overview of the state estimation formulation, an in-depth presentation of the outlier detection methodology, an illustration of the incorporation of 3D-Mapping-Aided (3DMA) fault detection and exclusion strategy, and a thorough explanation of the computation procedure involving all essential components of the positioning algorithm.

Chapter 4 introduces the GNSS Feature Map-aided robust EKF by providing initial motivation and a detailed description of the adapted robust estimation. This is followed by a performance analysis of existing and newly introduced robust estimators through a Monte-Carlo simulation study. The second part of this chapter provides extensive information on the GNSS Feature Map generation, including the concept, map generation, waypoint resolution study, observation error similarity analyses and, finally, the provision of fully populated map information.

After introducing the theoretical framework and methodology employed in this work, chapter 5 extensively evaluates the proposed methods and models using data from two automotive experiments, classified as medium urban trench and deep urban trench. The achieved improvement of the GNSS Feature Map-aided robust EKF is quantified in terms of various performance parameters, including accuracy, integrity, and ambiguity resolution. Additionally, the applicability of these approaches when utilizing different hardware is assessed, along with a performance comparison with the receiver-internal RTK solution.

The thesis concludes with a summary of the most significant results and findings in chapter 6. Additionally, it provides an outlook that addresses open questions and defines topics for future investigations.

2

Basics

2.1 Fundamentals of Global Navigation Satellite Systems

2.1.1 Observables

One of the prevailing technologies to globally determine the absolute position, velocity or time are GNSS with billions of users and a vast number of applications (Betz, 2021). The market for GNSS applications is growing in recent years (EUSPA, 2024), especially due to the increasing availability of various GNSS, i.e. the American Global Positioning System (GPS), the Russian Globalnaja Nawigazionnaja Sputnikowaja Sistema (GLONASS), the European Galileo and the Chinese BeiDou Navigation Satellite System (BDS). The transmitted GNSS signals are electromagnetic waves that, in theory, propagate at the speed of light. The signals frequencies are part of the L-band between 1.2 GHz and 1.6 GHz or equivalently at signal wavelengths between 19 cm and 25 cm, enabling measurements of high precision. In addition, these signals are not attenuated in the atmosphere under common weather conditions and thus, reasonably simple user equipment is sufficient in order to receive the transmitted signals (Langley et al., 2017).

For the computation of position, velocity and time, three basic GNSS observation types are used, namely the pseudorange, carrier phase and Doppler observations. A fourth observable, the signal strength, which is often represented as Carrier-to-Noise-Power-Density Ratio (C/N_0), provides information about the signal quality. Further, it is adequate for developing C/N_0-based weighting models (Brunner et al., 1999; Luo et al., 2009) or for detecting and mitigating multipath effects (Larson et al., 2007; Rost and Wanninger, 2009; Smyrnaios, 2016).

Pseudorange

The basic measurement of every GNSS is the observed difference between the time of transmission with respect to the satellite timescale and the time of reception with respect to the receiver time scale (Hauschild, 2017a). By multiplying this measured time difference with the speed of light, the signal travel time is converted to a range measurement which can be expressed as the geometric range between user A and satellite i and is written as

$$\varrho_A^i = \sqrt{\left(X^i - X_A\right)^2 + \left(Y^i - Y_A\right)^2 + \left(Z^i - Z_A\right)^2} \tag{2.1}$$

with the respective Earth-centered, Earth-fixed (ECEF) Cartesian coordinates X, Y, Z of the user and satellite, respectively. Since the receiver and satellite timescales are asynchronous, biases for the receiver and satellite clock need to be introduced and thus, the measurements become the so-called pseudorange measurement. Due to other error sources along the signal path, the basic observation equation for pseudoranges yields

$$\rho^i_A = \varrho^i_A + c\left(\delta t_A - \delta t^i\right) + \delta t^i_{A,rel} + \delta T^i_A + \delta I^i_A + \delta_{A,\rho} - \delta^i_\rho + \epsilon^i_{A,\rho} \tag{2.2}$$

with

ρ^i_A	the pseudorange observation in meters,
ϱ^i_A	the Euclidean distance in meters,
c	the speed of light in meters per second,
δt_A	the receiver clock bias in seconds,
δt^i	the satellite clock bias in seconds,
$\delta t^i_{A,rel}$	the relativistic correction term in meters,
δT^i_A	the tropospheric correction in meters,
δI^i_A	the ionospheric correction in meters,
$\delta_{A,\rho} - \delta^i_\rho$	the hardware delays of the receiver and satellite in meters,
$\epsilon^i_{A,\rho}$	the pseudorange measurement noise in meters.

Depending on the application, the parameters in Eq. 2.2 may either be estimated, corrected by using models, eliminated by combining observations, or even neglected in accordance with application and accuracy requirements.

Carrier Phase

An additional observation type of the signal travel time measurement is the so-called carrier phase, which is 100 - 1000 times more precise than the pseudorange measurement thanks to its short wavelengths of approximately 19 to 25 cm. The receiver does not observe the absolute distance but continuously measures the fractional phase shift between a generated replica of the carrier signal and the incoming carrier signal from the satellite. Contrary to the pseudorange measurement, the carrier phase produces ambiguous measurements, since the integer number of full cycles between the satellite and user is randomly initialized and remains unknown (Hauschild, 2017a). In case the signal tracking is interrupted, e.g. due to obstructions, multipath effects or ionospheric scintillation, the integer number of full cycles is re-initialized which yields a so-called cycle slip. The observation equation for the carrier phase measurement is

$$\Phi^i_A = \varrho^i_A + c\left(\delta t_A - \delta t^i\right) + \delta t^i_{A,rel} + \delta T^i_A - \delta I^i_A + \delta_{A,\Phi} - \delta^i_\Phi + \lambda N^i_A + \epsilon^i_{A,\Phi} \tag{2.3}$$

with

Φ^i_A	the carrier phase observation in meters,
ϱ^i_A	the Euclidean distance in meters,
c	the speed of light in meters per second,
δt_A	the receiver clock bias in seconds,
δt^i	the satellite clock bias in seconds,
$\delta t^i_{A,rel}$	the relativistic correction term in meters,
δT^i_A	the tropospheric correction in meters,
δI^i_A	the ionospheric correction in meters,
$\delta_{A,\Phi}$, δ^i_Φ	the hardware delays of the receiver and satellite in meters,
λ	the wavelength of the carrier signal in meters,
N^i_A	the integer number of full cycles,
$\epsilon^i_{A,\Phi}$	the carrier phase measurement noise in meters.

Differences to the pseudorange equation (Eq. 2.2) are the negative sign of the ionospheric correction, the additional term of the carrier phase ambiguity and the smaller observation noise.

Doppler

A relative motion between a transmitter – the satellite – and a receiver – the user – results in a frequency shift called the Doppler shift. The receiver measures the shift between the nominal frequency and the observed frequency of the satellite signal, which differs from its nominal frequency due to the relative motion. According to Hofmann-Wellenhof et al. (2008), the equation of the frequency shift reads

$$\Delta f = f_A - f^i = -\frac{1}{c}\nu_\varrho f^i \tag{2.4}$$

where f_A is the received frequency at receiver A, f^i the emitted frequency from satellite i and ν_ϱ is the line-of-sight velocity between satellite and receiver:

$$\nu_\varrho = \frac{\partial \varrho}{\partial t} = \dot{\varrho}. \tag{2.5}$$

Since the Doppler shift is linearly dependent on the relative velocity, it allows for instantaneous velocity determination of the receiver.

Including the most relevant error sources, the basic Doppler observation equation is denoted as

$$\dot{\rho}^i_A = -\lambda D^i_A = \dot{\varrho}^i_A + \delta f_A + \delta f^i + \delta f^i_{A,rel} + \delta \dot{T}^i_A + \delta \dot{I}^i_A + \epsilon^i_{A,D} \tag{2.6}$$

with

λ	the wavelength of the carrier signal in meters,
D^i_A	the Doppler shift in Hertz,
$\dot{\varrho}^i_A$	the relative velocity between satellite and receiver in meters per second,
δf_A	the receiver clock frequency bias in meters per second,
δf^i	the satellite clock frequency bias in meters per second,
$\delta f^i_{A,rel}$	the relativistic frequency correction term in meters per second,
δT^i_A	the tropospheric rate correction in meters per second,
δI^i_A	the ionospheric rate correction in meters per second,
$\epsilon^i_{A,P}$	the Doppler shift measurement noise in meters.

Denoting the relative velocity between satellite and receiver by its velocities and ranges, the geometric change reads

$$\dot{\varrho}^i_A = \begin{pmatrix} V^i_X - V_{X,A} \\ V^i_Y - V_{Y,A} \\ V^i_Z - V_{Z,A} \end{pmatrix}^T \frac{\begin{pmatrix} X^i - X_A \\ Y^i - Y_A \\ Z^i - Z_A \end{pmatrix}}{\left\| \begin{pmatrix} X^i - X_A \\ Y^i - Y_A \\ Z^i - Z_A \end{pmatrix} \right\|} \tag{2.7}$$

with the respective ECEF Cartesian coordinates and velocities X, Y, Z and V_X, V_Y, V_Z. In Eq. 2.6, the Doppler shift measurement is transformed into a metric value, also referred to as pseudorange rate measurement $\dot{\rho}$, by multiplying with the negative of the carrier wavelength.

In addition to the main error sources listed in Eq. 2.2, Eq. 2.3 and Eq. 2.6, further GNSS errors are present in undifferenced measurements, such as phase windup effects or site displacements. However, these signal delays are eliminated through a process referred to as *double differencing* (Kouba and Héroux, 2001; Bisnath, 2021), which will be described in the next section. As this thesis mainly focuses on double difference observations and the accuracy requirements are rather at the centimeter to decimeter level than in the millimeter range, these effects will be neglected.

Signal Power

The fourth observable generated by the receiver for each tracked signal is the estimated received signal power. Unlike the GNSS observables described above, the signal power is independent from the Numerically Controlled Oscillator (NCO). It is derived from averaging over all prompt I/Q correlator values that are available during a measurement interval:

$$\widehat{C/N_0} = \frac{I^2 + Q^2 - 2}{2T}, \tag{2.8}$$

where T is the integration time of the receiver. For more details on the internal receiver signal processing steps, it is referred to textbook literature (Won and Pany, 2017). The estimate of the $\mathrm{C/N_0}$ is affected by thermal noise but is otherwise an unbiased estimate. In general, the $\mathrm{C/N_0}$ is a good indicator for the GNSS signal quality, because the signal power and the standard deviations of the receiver's Delay-Locked-Loop (DLL) and Phase-Locked-Loop (PLL) are directly correlated with each other (Hauschild, 2017a):

$$\sigma_{DLL} \approx \sqrt{\frac{dB_L}{2C/N_0}}\lambda_C, \tag{2.9}$$

$$\sigma_{PLL} \approx \sqrt{\frac{B_P}{C/N_0}}\frac{\lambda_L}{2\pi}, \tag{2.10}$$

where d is the correlator spacing in units of code chips, B_L is the equivalent code loop noise bandwidth in Hz, λ_C is the wavelength of the code in meters, B_P is the carrier loop noise bandwidth in Hz and λ_L is the carrier-phase wavelength in meters. From Eq. 2.9 and Eq. 2.10 it is obvious that the $\mathrm{C/N_0}$ directly affects the measurement noise of the receiver's DLL and PLL. Typically, current receivers achieve a standard deviation of the code measurement noise of a decimeter or less while a typical carrier-phase noise standard deviation is less than a millimeter for high $\mathrm{C/N_0}$ values.

2.1.2 Combination of Observations

Multiple observations – either from the same type (e.g., pseudorange observations) or different types (e.g., pseudorange and carrier phase observations or from various frequencies) – can be combined for GNSS data processing or analysis applications. The advantage of combining observations is that, depending on the type of application, various nuisance parameters can either be eliminated, reduced or separated (Hauschild, 2017b). Two major strategies of combining observations exist.

The utilization of a *Linear Combination (LC)* typically includes different types of observations, such as different frequencies or pseudorange and carrier phase observations. These are linked in a way that different error sources of the signals are eliminated or separated. Examples for LCs are the ionosphere-free LC, which almost completely eliminates the frequency-dependent ionospheric refraction of GNSS signals and the multipath LC, which separates the pseudorange multipath error from other signal components. Other LCs (wide-lane LC, Melbourne-Wübbena LC, geometry-free LC) can be applied in ambiguity resolution studies and to cycle slip fixing algorithms. All of the above mentioned LCs have their own characteristics in terms of the resulting wavelength and noise amplification. As none of the aforementioned LCs are utilized in this thesis, the reader is referred to standard literature for more detailed information, e.g. Hauschild (2017b).

Differencing of observations, which will be utilized in this thesis, is the second major strategy of combining observations. Assuming time-synchronized carrier phase measurements from two satellites i and j to two receivers A and B

$$\Phi^i_A = \varrho^i_A + c\left(\delta t_A - \delta t^i\right) + \delta t^i_{A,rel} + \delta T^i_A - \delta I^i_A + \delta_{A,\Phi} - \delta^i_\Phi + \lambda N^i_A + \epsilon^i_{A,\Phi} \tag{2.11}$$

$$\Phi^j_A = \varrho^j_A + c\left(\delta t_A - \delta t^j\right) + \delta t^j_{A,rel} + \delta T^j_A - \delta I^j_A + \delta_{A,\Phi} - \delta^j_\Phi + \lambda N^j_A + \epsilon^j_{A,\Phi} \tag{2.12}$$

$$\Phi^i_B = \varrho^i_B + c\left(\delta t_B - \delta t^i\right) + \delta t^i_{B,rel} + \delta T^i_B - \delta I^i_B + \delta_{B,\Phi} - \delta^i_\Phi + \lambda N^i_B + \epsilon^i_{B,\Phi} \tag{2.13}$$

$$\Phi^j_B = \varrho^j_B + c\left(\delta t_B - \delta t^j\right) + \delta t^j_{B,rel} + \delta T^j_B - \delta I^j_B + \delta_{B,\Phi} - \delta^j_\Phi + \lambda N^j_B + \epsilon^j_{B,\Phi} \tag{2.14}$$

there are two possible options of linking observations in order to form a Single Difference (SD): i) between-receiver SD, further denoted as Δ and between-satellite SD, further denoted as ∇. Both combinations are shown in Fig. 2.1(a) and Fig. 2.1(b), respectively. The two receivers A and B thereby form a so-called *baseline*.

Combining the observations from one satellite to two receivers eliminates the receiver clock error and the receiver hardware delay and the SD observation equation reads as

$$\begin{aligned}&\Delta\Phi^i_{A,B} = \\ &\Delta\varrho^i_{A,B} + c\left(\delta t^i - \delta t^j\right) + \Delta\delta t^i_{A,B,rel} + \Delta\delta T^i_{A,B} - \Delta\delta I^i_{A,B} - \delta^i_\Phi + \delta^j_\Phi + \lambda\Delta N^i_{A,B} + \Delta\epsilon^i_{A,B,\Phi}.\end{aligned} \tag{2.15}$$

When forming the difference of the observations from two satellites to one receiver, the satellite clock bias and the satellite hardware delay are eliminated and the SD observation equation yields

$$\begin{aligned}&\nabla\Phi^{i,j}_A = \\ &\nabla\varrho^{i,j}_A + c\left(\delta t_A - \delta t_B\right) + \nabla\delta t^{i,j}_{A,rel} + \nabla\delta T^{i,j}_A - \nabla\delta I^{i,j}_A + \delta_{A,\Phi} - \delta_{B,\Phi} + \lambda\nabla N^{i,j}_A + \nabla\epsilon^{i,j}_{A,\Phi}.\end{aligned} \tag{2.16}$$

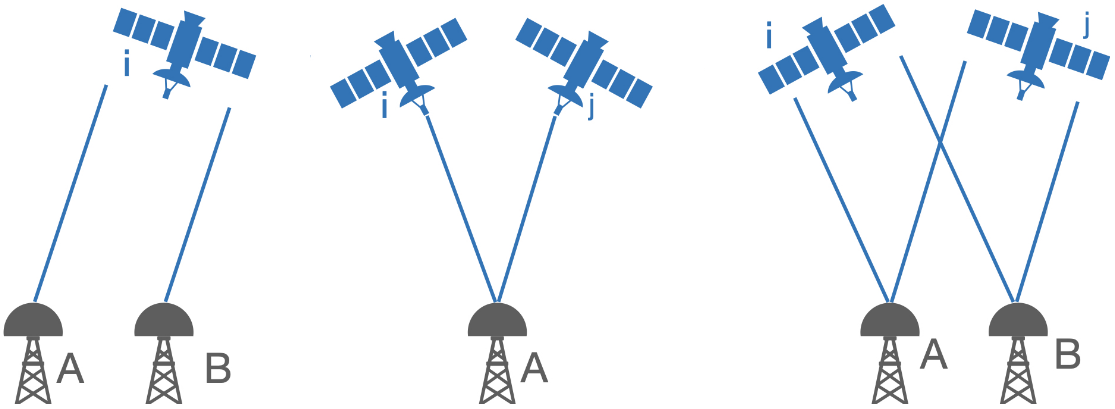

(a) (b) (c)

Figure 2.1: Double difference combination of GNSS observations derived from two single differences. (a) between-receiver single difference, (b) between-satellite single difference, (c) double difference.

Both SD combinations lead to an increased noise level of $\sqrt{2}\sigma$, assuming an identical standard deviation σ for the uncombined observations.
When forming the Double Difference (DD), i.e. the difference of the two SD combinations (see Fig. 2.1(c)), the advantages of both observation combinations are utilized, meaning that the receiver and satellite clock errors as well as the receiver and satellite hardware delays are eliminated. Therefore, the DD carrier phase observation equation reads

$$\begin{aligned}\nabla\Delta\Phi^{i,j}_{A,B} &= \Phi^{i}_{A} - \Phi^{i}_{B} - \left(\Phi^{j}_{A} - \Phi^{j}_{B}\right)\\ &= \nabla\Delta\varrho^{i,j}_{A,B} + \nabla\Delta\delta t^{i,j}_{A,B,rel} + \nabla\Delta\delta T^{i,j}_{A,B} - \nabla\Delta\delta I^{i,j}_{A,B} + \lambda\nabla\Delta N^{i,j}_{A,B} + \nabla\Delta\delta\epsilon^{i,j}_{A,B,\Phi}.\end{aligned} \tag{2.17}$$

Considering short baselines (e.g., < 1 km), the relativistic error, the tropospheric error and the ionospheric error are greatly reduced and thus, can be neglected, which yields the simplified DD carrier phase observation equation

$$\nabla\Delta\Phi^{i,j}_{A,B} = \nabla\Delta\varrho^{i,j}_{A,B} + \lambda\nabla\Delta N^{i,j}_{A,B} + \nabla\Delta\epsilon^{i,j}_{A,B,\Phi}, \tag{2.18}$$

containing the DD Euclidean distance $\nabla\Delta\varrho^{i,j}_{A,B}$, the DD integer ambiguity $\nabla\Delta N^{i,j}_{A,B}$ and the DD carrier phase measurement noise $\nabla\Delta\epsilon^{i,j}_{A,B,\Phi}$, which is amplified by a factor of 2 compared to the uncombined observations.
The same derivations and characteristics hold true for the DD pseudorange measurements, but no ambiguity is present in that observation equation.

2.1.3 Weighting of Observations

The functional model describes the mathematical relation between observations and parameters, denoted in the observation equations. Many solvers, such as Least-squares Adjustment (LSA) or Kalman filters, require unbiased and normal distributed input data in order to compute optimal state estimates (Gelb, 1974). In the case of GNSS, all remaining parts which are neither modeled nor canceled, e.g. multipath effects, have to be either eliminated or incorporated into the stochastic model. Otherwise, biased observations would deteriorate the state estimation. Hence, the distribution of the measurements and determination of its variance-covariance matrix is essential for obtaining optimal results. The stochastic model is expressed in the so-called variance-covariance matrix, containing information on the precision and mathematical correlation of observations (Tiberius and Kenselaar, 2000). An appropriate modeling of the observations uncertainty is essential, since in addition to the states themselves, the quality measures of the parameters are affected by the selection of the stochastic model. Depending on the application, e.g., the uncertainty of carrier phase ambiguities (Teunissen, 2000; Wang et al., 2002), site coordinates (Schön and Brunner, 2008) or troposphere parameters (Jin and Park, 2005) is influenced. For weighting the observations, only the relative magnitude of variances is important and impact the estimated parameters, however, the absolute values of the uncertainties play a crucial role in quality control and integrity monitoring and thus, need to be chosen adequately (Kim and Langley, 2001; Wieser and Brunner, 2002).

Equal variances for GNSS observations are unrealistic and suffer from neglected physical characteristic of the transmitted signals. Due to atmospheric effects or site-specific effects, the antenna gain of the satellites' antenna, antenna gain of the receiving antenna and the distance between receiver and satellite, the precision of GNSS measurements is varying (Butsch and Kipka, 2004). Therefore, suitable weighting schemes that assign higher weights to precise observations and lower weights to observations with higher noise have to be applied in order to improve the parameter estimation by balancing the impact of different measurements (Hartinger and Brunner, 1999; Brunner et al., 1999; Wieser and Brunner, 2000; Luo et al., 2009).

Elevation-dependent Model

One commonly applied weighting model in GNSS processing – other than the scaled identity matrix – are elevation-dependent models due to the simplicity and global efficiency. The model takes into account that satellites at low elevation suffer from larger atmospheric errors and are more likely to be prone to multipath effects. Also, GNSS antennas are designed to have the maximum antenna gain in zenith direction and minimum gain values at low elevation angles in order to directly suppress lower quality satellite signals (Maqsood et al., 2017). This is the reason why the received signal power and thus, also the received observation noise show an elevation-dependent behaviour (Wanninger et al., 2021). Therefore, the elevation-dependent weighting model is expecting higher noise at low elevation angles and thus, assigning lower weights and higher uncertainties to these satellites, respectively. Possible mathematical expressions for the weighting model are the scaling by the sine of the elevation angle (Rothacher and Beutler, 1998; Li et al., 2016)

$$\sigma^2 = \frac{c_0^2}{\sin^2 e_i} \tag{2.19}$$

or an exponential form (Euler and Goad, 1991)

$$\sigma^2 = c_0^2 + c_1^2 \cdot \exp \frac{-e_i}{e_0} \tag{2.20}$$

where e_i is the elevation angle of satellite i and c_0, c_1, e_0 are model parameters depending on the used hardware and environment.

A strong correlation between the satellites elevation angle and GNSS signal quality is assumed, which is true for scenarios under good observation conditions (e.g., open-sky GNSS data). However, the elevation-dependent model suffer from deficiencies in more complex environments, such as urban areas, where satellites at higher elevations may also be affected by multipath effects. In these cases, the elevation-dependent model cannot compensate for these errors.

C/N$_0$-dependent Models

For measurements collected under challenging conditions, the signal-to-noise-power-density ratio can be used to apply a weighting model, which is more appropriate to describe the GNSS signal quality for non-ideal observations. The relation of the received signal power and the measurement noise is defined in Eq. 2.9 and Eq. 2.10. In addition to pseudorange, carrier phase and Doppler shift observations, C/N$_0$ values are recorded, which makes a more realistic signal quality evaluation easily accessible.

In Hartinger and Brunner (1999), the SIGMA-ϵ model is developed. The SIGMA-ϵ model directly links the measured C/N$_0$ value to the signal quality of the measured range observation, which can be expressed as

$$\sigma^2 = V_a + C_a \cdot 10^{-\frac{\mathrm{C/N_0}}{10}} \tag{2.21}$$

with the model parameters V_a [m^2] and C_a [m^{2}Hz] and the receiver/antenna type and signal type index a. As soon as the model parameters for the desired receiver/antenna combination are determined, the weights can be adjusted during GNSS signal processing using the observed C/N$_0$ values.

Another C/N$_0$-dependent weighting model is the SIGMA-Δ model (Brunner et al., 1999). To apply the SIGMA-Δ model, a receiver/antenna type dependent template function has to be determined beforehand, which represents the elevation dependency of $\mathrm{C/N_0}$ values. Signal distortions lead to a change of the signal-to-noise ratio and are accounted for via the deviation of the actual received $\mathrm{C/N_0}$ from the template function:

$$\sigma^2 = V_a + C_a \cdot 10^{-\frac{\mathrm{C/N_0} - \alpha \cdot |\Delta|}{10}} \tag{2.22}$$

with the deviation from the $\mathrm{C/N_0}$ template Δ and an empirical constant factor α. Signal distortions may also increase the signal-to-noise ratio and that is why $|\Delta|$ is used instead of Δ (Wieser and Brunner, 2000).

In contrary to the existing $\mathrm{C/N_0}$-dependent weighting models which need a priori calibration of the receiver/antenna influenced model parameters, Luo et al. (2009) derived an empirically $\mathrm{C/N_0}$-dependent weighting model. The observed signal-to-noise ratios are evaluated and global minimum and maximum $\mathrm{C/N_0}$ values, which correspond to the most extreme signal strengths representative for the sites environment and receiver/antenna characteristics, are determined. All observed GNSS measurements are then weighted with respect to the observed $\mathrm{C/N_0}$ values scaled by the ratio of the minimum and maximum $\mathrm{C/N_0}$ value. The resulting mathematical expression for the weighted variance reads

$$\sigma^2 = \frac{1}{\left(a + (1+a) \cdot \frac{\mathrm{C/N}_0^i - \mathrm{C/N}_0^{\mathrm{min}}}{\mathrm{C/N}_0^{\mathrm{max}} - \mathrm{C/N}_0^{\mathrm{min}}}\right)^2}, \tag{2.23}$$

where $\mathrm{C/N}_0^i$ is the observed $\mathrm{C/N_0}$ of satellite i, $\mathrm{C/N}_0^{\mathrm{min}}$ and $\mathrm{C/N}_0^{\mathrm{max}}$ are the minimum and maximum signal strength corresponding to the data set, respectively, and a is a parameter introduced to avoid numerical issues.

Hybrid Models

Since the $\mathrm{C/N_0}$-dependent weighting models still exhibit weaknesses – especially in harsh environments and severe signal reception conditions – hybrid weighting models have been developed to further minimize these deficiencies. Hybrid models usually require additional information complementary to the received GNSS signals, e.g. 3D city model information, in order to realistically weight measurements in harsh environments.

In Zhu (2018), a hybrid model is proposed combining the information of $\mathrm{C/N_0}$, satellite elevation and the Urban Multipath Model which is based on the Urban Trench Model (Betaille et al., 2013). Since not all GNSS signals with high signal strength possess high quality and in urban areas, multipath errors can occur for satellites at high elevations, an additional indicator whether a satellite is in LOS or NLOS condition is included. The weighted hybrid model variance can be written as

$$\sigma^2 = k \cdot \frac{m \cdot 10^{-0.1 \cdot \mathrm{C/N}_0^i}}{\sin e_i} \tag{2.24}$$

with the receiver/antenna dependent model parameter m and the factor k, which differentiates between LOS and NLOS signal conditions expressed as

$$k = \begin{cases} k_1, & \text{LOS signal} \\ k_2, & \text{NLOS signal} \end{cases} \tag{2.25}$$

and $k1 < k2$. In this way, the received $\mathrm{C/N_0}$ and the satellites elevation contribute to the respective variance of the signal and additionally, the uncertainty of NLOS signals is scaled compared to LOS signals.

Another hybrid weighting model is proposed by Xin et al. (2022), where well established elevation-dependent (Rothacher and Beutler, 1998) and C/N$_0$-dependent (Realini and Reguzzoni, 2013) weighting schemes are combined with a newly developed 3DMA weighting factor. The combined weighting model reads

$$W\left(\text{3DMA}, \text{C/N}_0, \text{Elev}\right) = W_{\text{Elev}} \cdot \Big(\alpha \cdot W_{\text{C/N}_0} + \beta \cdot W_{\text{3DMA}}\Big)\,, \tag{2.26}$$

where W_{Elev}, $W_{\text{C/N}_0}$ and W_{3DMA} are the elevation-dependent, C/N$_0$-dependent and 3DMA-dependent weighting factors, respectively, and α, β are coefficients that linearly fit the measurement errors to the weighting factors in a way that $\alpha + \beta = 1$. The key parameter of the 3DMA-dependent weighting model is the difference of the elevation angles between the satellite and the building boundary ΔElev, which takes into account that LOS signals are received at elevations higher than the building boundary, reflection-caused multipath occur close to the building boundary and measurements in NLOS condition with large biases are received at elevation angles lower than the building boundary. The mathematical expression therefore reads

$$W_{\text{3DMA}} = \tag{2.27}$$

$$\begin{cases} 1, & \Delta\text{Elev} \geq T^{\circ}_{\text{3DMA}} \\ 10^{-\frac{\Delta\text{Elev} - T^{\circ}_{\text{3DMA}}}{b_{\text{3DMA}}}}, & 0^{\circ} < \Delta\text{Elev} < T^{\circ}_{\text{3DMA}} \\ 10^{-\frac{\Delta\text{Elev} - T^{\circ}_{\text{3DMA}}}{a_{\text{3DMA}}}} \cdot \left(\left(\frac{A_{\text{3DMA}}}{10^{-\frac{F^{\circ}_{\text{3DMA}} - T^{\circ}_{\text{3DMA}}}{a_{\text{3DMA}}}}} - 1\right) \cdot \frac{\Delta\text{Elev} - T^{\circ}_{\text{3DMA}}}{F^{\circ}_{\text{3DMA}} - T^{\circ}_{\text{3DMA}}} + 1\right), & \Delta\text{Elev} \leq 0^{\circ} \end{cases} \tag{2.28}$$

where a_{3DMA}, b_{3DMA}, A_{3DMA} and F°_{3DMA} are model parameters which can be tuned or estimated in a nonlinear least-squares optimization problem. The threshold parameter T°_{3DMA} is set to 30°. The C/N$_0$-dependent weighting model is formulated as

$$W_{\text{C/N}_0} = \begin{cases} 1, & \text{C/N}_0^i \geq T_{\text{C/N}_0} \\ 10^{-\frac{\text{C/N}_0^i - T_{\text{C/N}_0}}{a_{\text{C/N}_0}}} \cdot \left(\left(\frac{A_{\text{C/N}_0}}{10^{-\frac{F_{\text{C/N}_0} - T_{\text{C/N}_0}}{a_{\text{C/N}_0}}}} - 1\right) \cdot \frac{\text{C/N}_0^i - T_{\text{C/N}_0}}{F_{\text{C/N}_0} - T_{\text{C/N}_0}} + 1\right), & \text{C/N}_0^i < T_{\text{C/N}_0} \end{cases} \tag{2.29}$$

and the model parameters $a_{\text{C/N}_0}$, $A_{\text{C/N}_0}$ and $F_{\text{C/N}_0}$ and $T_{\text{C/N}_0}$ are also set by nonlinear least-squares optimization. Finally, the elevation-dependent weighting model complements the proposed hybrid model and can be written as

$$W_{\text{Elev}} = \begin{cases} 1, & e_i \geq 30^{\circ} \\ \frac{1}{2\sin e_i}, & e_i < 30^{\circ} \end{cases}. \tag{2.30}$$

The outcome of the hybrid model is a scale factor which is applied to the standard deviation of the measurements and hence, scales the uncertainties of the received GNSS signals.

An alternative hybrid weighting model, which is based on the SIGMA-ϵ model and 3D city model information, has been developed in Schaper et al. (2022). The C/N$_0$ dependent weighted variance of the SIGMA-ϵ model is scaled by a calibrated factor f, which depends on the receiver/antenna combination and the environment:

$$\sigma^2 = \sigma_{\epsilon}^2 \cdot f, \tag{2.31}$$

where σ_{ϵ}^2 is the obtained variance from the SIGMA-ϵ model (see Eq. 2.21). For each of the possible signal reception condition classes, a different scaling factor is determined, which fits the uncertainty with the measurement error distribution in the specific environment. In addition to the reflection-based error sources in urban areas, the proposed model also adds information on signal diffraction leading to eight signal reception condition classes and thus, in total eight different scaling factors applied in the hybrid weighting model.

As described above, a solver is optimal in the case of unbiased, normal distributed observations. The main objective of applying a weighting model is to adjust the stochastic information for measurements, which derogate from this restriction. Especially the described hybrid models are typically evaluated with respect to an improved accuracy of the positioning solution. However, the adequateness of the model – which is the additionally introduced stochastic information matching the observation distribution – has not been evaluated. A sound analysis of whether the weighted observations or the weighted residuals, respectively, follow the normal distribution, is essential for an unobjectionable utilization of these weighting models.

2.2 Kalman Filtering

Kalman filtering (Kalman, 1960) describes a recursive state estimation algorithm that optimally combines the time propagated state vector and its covariance matrix from a previous epoch and the measurements at the current epoch. According to standard literature, the estimation of the state of a dynamic system is described by a linear ordinary differential equation (Gelb, 1974; Simon, 2006b; Farrell, 2008). The inhomogeneous linear differential equation of a Kalman filter reads

$$\dot{\mathbf{x}}(t) = \mathbf{F}(t)\mathbf{x}(t) + \mathbf{L}(t)\mathbf{u}(t) + \mathbf{G}(t)\boldsymbol{\omega}(t), \tag{2.32}$$

with state vector $\mathbf{x}$, control-input vector $\mathbf{u}$, white process noise vector $\boldsymbol{\omega}$, dynamics matrix $\mathbf{F}$, control-input matrix $\mathbf{L}$ and noise distribution matrix $\mathbf{G}$. All parts are given at time instance t. The deterministic control-input components are usually unknown and thus will be neglected from this point on:

$$\dot{\mathbf{x}}(t) = \mathbf{F}(t)\mathbf{x}(t) + \mathbf{G}(t)\boldsymbol{\omega}(t). \tag{2.33}$$

The first homogeneous part of Eq. 2.33 can be solved by means of a Taylor series expansion up to the linear segment which yields

$$\mathbf{x}(t) = \mathbf{F}(t, t_0)\mathbf{x}(t_0), \tag{2.34}$$

where $\mathbf{F}$ is the state transition matrix propagating the state vector from time instance t_0 to t. The particular solution of the inhomogeneous part reads

$$\mathbf{x}(t) = \int_{t_0}^{t} \mathbf{F}(t, t')\mathbf{G}(t')\boldsymbol{\omega}(t')dt'. \tag{2.35}$$

Solving Eq. 2.33 therefore yields

$$\mathbf{x}(t) = \mathbf{F}(t, t_0)\mathbf{x}(t_0) + \int_{t_0}^{t} \mathbf{F}(t, t')\mathbf{G}(t')\boldsymbol{\omega}(t')dt'. \tag{2.36}$$

Input values for such a system model are available at discrete time instances in the majority of the cases. Hence, the continuous system model in Eq. 2.36 has to be transformed to the linear discrete-time system equation

$$\mathbf{x}_k = \mathbf{F}_{k-1}\mathbf{x}_{k-1} + \mathbf{w}_{k-1}, \tag{2.37}$$

where at a certain time instance k, $\mathbf{x}_k$ is the state, $\mathbf{F}_k$ is the state transition matrix. The corresponding measurement equation reads

$$\mathbf{l}_k = \mathbf{H}_k \mathbf{x}_k + \mathbf{v}_k \tag{2.38}$$

with the noisy measurement vector $\mathbf{y}_k$. The noise processes of the system ($\mathbf{w}_k$) and the measurements ($\mathbf{v}_k$) are white, zero-mean, uncorrelated and the corresponding covariance matrices are known:

$$\mathbf{w}_k = \mathbf{G}_k \boldsymbol{\omega}_k \sim \mathcal{N}\left(0, \mathbf{Q}_{w,k}\right), \tag{2.39}$$

$$\mathbf{v}_k \sim \mathcal{N}\left(0, \mathbf{Q}_{v,k}\right). \tag{2.40}$$

The above described method only applies for linear systems. For non-linear system formulations, such as those on which this thesis is based on (see GNSS measurement equations in Eq. 2.2 and Eq. 2.3), non-linear Kalman filters are introduced which approximate the solution to the above problem.

The *Linearized Kalman Filter (LKF)* is usually implemented for applications where the trajectory is predetermined or an accurate reference trajectory is available. Hence, the linearization point is known and the system is linearized at, e.g., given coordinates of a vehicle. The advantage of this non-linear Kalman filter is that online computations can be simplified, since all related data to the nominal trajectory can be computed beforehand. The resulting state estimate is the error between the nominal trajectory and the actual trajectory. Moreover, a control law can be introduced to further minimize this error.

For many applications, such as autonomous vehicles, the trajectory cannot be accurately predetermined and thus, the nominal trajectory is not known a priori. Therefore, the nominal trajectory is defined to be equal to the estimated trajectory. In this case, the system is linearized at the estimated state. If sufficiently accurate measurements are available, the estimated linearization point should be close to the actual state and the performance of the EKF similar to the performance of the LKF. However, the EKF is riskier due to the possibility of a rapid divergence in the case when the estimated state is far from the actual state.

The two non-linear Kalman filters utilize the same formulae and computation procedure to estimate the state vector, though they differ in terms of nominal trajectory and linearization point. Consequently, the selection of a particular Kalman filter is contingent upon the specific requirements of the application. Alternatives to the two introduced Kalman filters are the Unscented Kalman Filter (UKF) and Particle Filter (PF), which themselves demonstrate specific advantages and disadvantages compared to the EKF. As the objective of this thesis is not to provide a comprehensive comparison of different filtering techniques, the reader is referred to standard textbooks for more detailed information on this topic (Simon, 2006a). Within the scope of this thesis, the EKF is employed for vehicle navigation applications, which necessitate real-time capability.

2.3 GNSS Precise Positioning

GNSS have transformed the field of positioning, navigation and timing, providing ubiquitous and accurate location information for a variety of applications. The demand for high-precision positioning has grown with the increasing precision requirements of modern safety-critical applications. That is why standard pseudorange-based positioning techniques, such as SPP (Langley et al., 2017) and pseudorange Differential GNSS (DGNSS) (Odijk, 2017), are not suitable due to their precision limitations. Instead, the importance of carrier phase-based positioning methods such as PPP (Zumberge et al., 1997), RTK (Bisnath, 2021) and PPP-RTK (Wübbena et al., 2005) is becoming increasingly prominent, because of their much higher precision due to the smaller noise level of carrier phase observations compared to pseudorange observations. An overview on the different positioning methods in terms of nominal accuracy, convergence time, coverage area and the positioning type is summarized in Tab. 2.1.

Table 2.1: Overview on the different positioning methods in terms of nominal accuracy, convergence time, coverage area and the positioning type (adapted from European GNSS Agency (2020) and Medina (2021)).

Method		Accuracy	Convergence	Coverage	Type
Pseudorange-based	SPP	< 10 m	Instantaneous	Global	Absolute
	DGNSS	0.5 - 2 m	Instantaneous	Regional	Relative
Carrier phase-based	PPP	1 - 2 dm	< 20 min	Global	Absolute
	RTK	< 1 dm	Instantaneous	Local	Relative
	PPP-RTK	< 1 dm	< 5 - 100 s	Regional	Absolute[1]

[1] Positioning model is absolute but correction data from a network of reference stations is required.

Precise Point Positioning

PPP is the logical extension of a standard SPP algorithm. As described in Teunissen (2021), the pseudorange observations are complemented with their much more precise counterpart, which is the carrier phase observation. Usually observations from two or more frequencies are combined to eliminate ionospheric delays. Broadcast satellite orbit and clock information are replaced by precise estimates, which are downloaded or obtained in real-time from service providers (e.g., IGS products (Kouba and Héroux, 2001; Montenbruck et al., 2014)) using internet or satellite links. Since no measurements from nearby reference stations are required, PPP is globally available using a single GNSS receiver and thus, is operational flexible, especially in areas without a dense reference station network. This flexibility comes with the cost of carefully modelling local station and environmental effects in order to reach decimeter-level accuracy. By using the State Space Representation (SSR) method, the various error sources are estimated separately by a network of Continuously Operating Reference Station (CORS), as shown in Fig. 2.2, before being sent to the receiver. While PPP is capable of delivering highly precise positioning results worldwide, it often requires longer observation periods to achieve this accuracy. The convergence time is mainly influenced by the existing carrier phase ambiguities and its linear dependency with other parameters to be estimated, which also leads to a loss of the integer nature of the ambiguities (Du et al., 2020).

Real-Time Kinematic

DGNSS positioning describes the concept of computing a rover's position with respect to a base station. While pseudorange DGNSS reaches meter-level positioning accuracy, RTK carrier phase DGNSS is essential for precise positioning applications with centimeter-level accuracy (Odijk, 2017). The RTK positioning method combines GNSS measurements from one (or more) reference stations with the user data, as described in Sec. 2.1.2, in order to eliminate satellite and receiver clock errors and reduce satellite orbit errors and atmospheric propagation delay errors. When requiring RTK positioning in real-time, GNSS corrections from the base station are usually transmitted using a standardized format proposed by the Radio Technical Commission for Maritime Services (RTCM). The single-compound ranging corrections, as

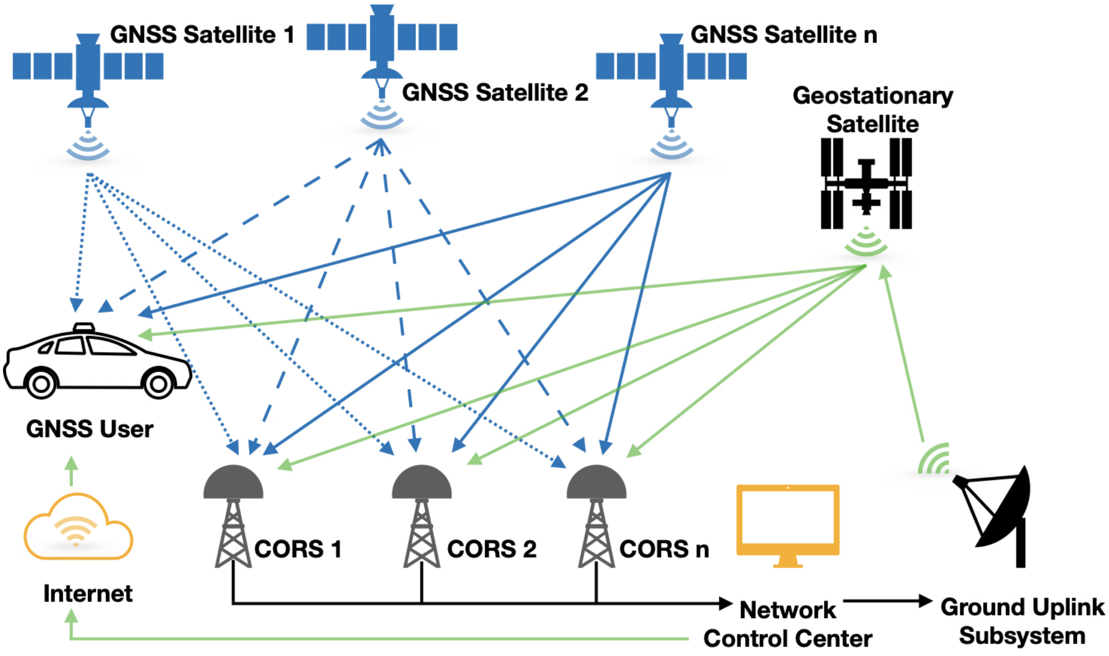
GNSS Satellite 1
GNSS Satellite 2
GNSS Satellite n
Geostationary Satellite
GNSS User
Internet
CORS 1
CORS 2
CORS n
Network Control Center
Ground Uplink Subsystem

Figure 2.2: Principle of the PPP method.

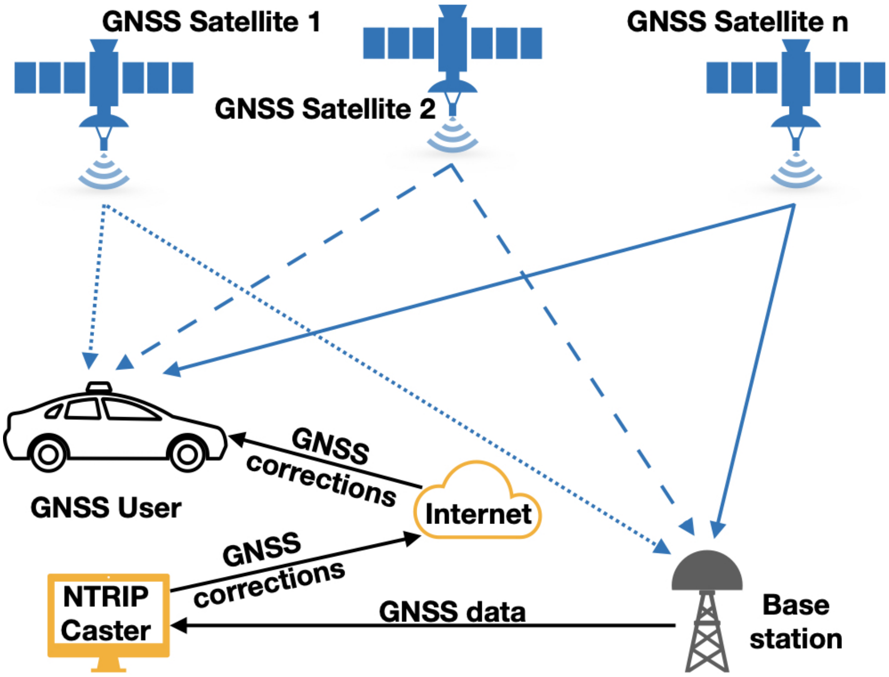
GNSS Satellite 1
GNSS Satellite 2
GNSS Satellite n
GNSS User
GNSS corrections
Internet
GNSS corrections
NTRIP Caster
GNSS data
Base station

Figure 2.3: Principle of the RTK positioning method.

observed in a nearby (real or virtual) base station and provided as Observation Space Representation (OSR), are transmitted, e.g., via the Internet using Network Transportation of RTCM Internet Protocol (NTRIP), as illustrated in Fig. 2.3.

The achievable accuracy of RTK positioning directly depends on the distance of the rover to the base station and if the real-valued carrier phase ambiguities are resolved to their integer values. For short baselines (< 10 km), instantaneous integer ambiguity resolution is feasible, leading to cm-level positioning accuracy after a single epoch. The weaker the underlying positioning model (e.g., single GNSS usage, single frequency usage or long baselines), the more time is required before the ambiguities can be reliably fixed to their integer values.

PPP-RTK

The idea of PPP-RTK is a synthesis of the positive characteristics of both, PPP and RTK positioning (Wübbena et al., 2005). All relevant GNSS error sources, such as satellite orbits, clocks, pseudorange and carrier phase biases and ionosphere and troposphere errors, derived from an reference station monitoring network, are determined and transmitted via SSR. Since the main limitation of PPP in terms of accuracy and convergence time is the estimation of integer ambiguities due to the correlation with other parameters, PPP-RTK can have significant advantages in ambiguity resolution, convergence time and accuracy. Due to the merging of PPP with state-space RTK, precise estimates of the above mentioned GNSS error sources are transmitted to the user and thus, integer ambiguity resolution within a reduced convergence time is feasible.

2.4 Integer Ambiguity Resolution

GNSS carrier phase measurements are much more precise compared to its pseudorange measurement counterpart. However, the precision gained by a factor of approximately 100 comes with the challenge of an ambiguous range, since the receiver does not measure the absolute distance but the fractional phase phase shift between a generated replica of the carrier signal and the incoming carrier signal from the satellite. Therefore, GNSS Integer Ambiguity Resolution (IAR) is essential for high-precision GNSS positioning algorithms. This includes to resolve the unknown number of cycles in the carrier phase observation data as integer values. Successful IAR enables very precise positioning and navigation, since carrier phase measurements are transformed into high-precision pseudorange data.

The GNSS IAR process is decomposed in three steps, as e.g. explained in Teunissen and Montenbruck (2017). The flowchart of the ambiguity estimation process is shown in Fig. 2.4, where $\mathbf{N}$ corresponds to the ambiguity vector and $\mathbf{x}$ corresponds to the baseline vector.

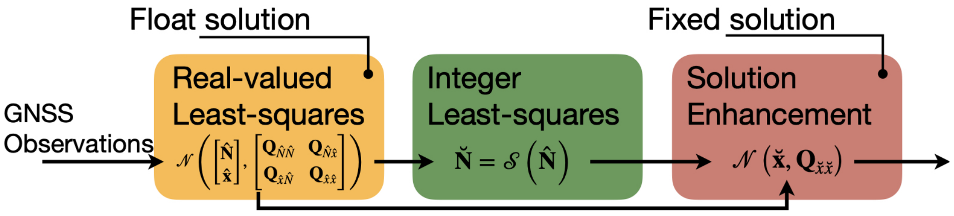
Float solution
Fixed solution
GNSS Observations
Real-valued Least-squares
$\mathcal{N}\left(\begin{bmatrix}\hat{\mathbf{N}}\\ \hat{\mathbf{x}}\end{bmatrix}, \begin{bmatrix}\mathbf{Q}_{\hat{N}\hat{N}} & \mathbf{Q}_{\hat{N}\hat{x}}\\ \mathbf{Q}_{\hat{x}\hat{N}} & \mathbf{Q}_{\hat{x}\hat{x}}\end{bmatrix}\right)$
Integer Least-squares
$\check{\mathbf{N}} = \mathcal{S}\left(\hat{\mathbf{N}}\right)$
Solution Enhancement
$\mathcal{N}\left(\check{\mathbf{x}}, \mathbf{Q}_{\check{x}\check{x}}\right)$

Figure 2.4: Three-step GNSS integer ambiguity resolution process.

1. First, a *float solution* is computed in a standard LSA which can also be referred to a Kalman filter update step. The integer nature of the ambiguities is disregarded and floating numbers are estimated with distribution

$$\begin{bmatrix}\hat{\mathbf{N}}\\ \hat{\mathbf{x}}\end{bmatrix} \sim \mathcal{N}\left(\begin{bmatrix}\hat{\mathbf{N}}\\ \hat{\mathbf{x}}\end{bmatrix}, \begin{bmatrix}\mathbf{Q}_{\hat{N}\hat{N}} & \mathbf{Q}_{\hat{N}\hat{x}}\\ \mathbf{Q}_{\hat{x}\hat{N}} & \mathbf{Q}_{\hat{x}\hat{x}}\end{bmatrix}\right), \tag{2.41}$$

where $\mathbf{Q}$ is the corresponding covariance matrix including the uncertainties of $\hat{\mathbf{N}}$ and $\hat{\mathbf{x}}$ and their cross-correlation.

2. The second step is the *integer solution*, where integer ambiguities are estimated based on the float ambiguities, their uncertainties and by taking the integer contraint $\breve{\mathbf{a}} \mapsto \mathbb{Z}^n$ into account. Thus, a mapping function $\mathcal{S} : \mathbb{R}^n \mapsto \mathbb{Z}^n$ is introduced that maps the real-valued float ambiguities to their corresponding integer values so that

$$\breve{\mathbf{N}} = \mathcal{S}\left(\hat{\mathbf{N}}\right). \tag{2.42}$$

3. The last step is the solution enhancement by computing the so-called *fixed solution*. Once the integer solution $\breve{\mathbf{N}}$ is accepted, the ambiguity residual $\hat{\mathbf{N}} - \breve{\mathbf{N}}$ is used to re-adjust the float solution:

$$\breve{\mathbf{x}} = \hat{\mathbf{x}} - \mathbf{Q}_{\hat{x}\hat{N}}\mathbf{Q}_{\hat{N}\hat{N}}^{-1}\left(\hat{\mathbf{N}} - \breve{\mathbf{N}}\right), \tag{2.43}$$

$$\mathbf{Q}_{\breve{x}\breve{x}} = \mathbf{Q}_{\hat{x}\hat{x}} - \mathbf{Q}_{\hat{x}\hat{N}}\mathbf{Q}_{\hat{N}\hat{N}}^{-1}\mathbf{Q}_{\hat{N}\hat{x}}. \tag{2.44}$$

Whenever the ambiguities are fixed to their true integer values, the maximum precision from carrier phase observations is gained. However, if the estimated integer ambiguities do not match with the true values, the solution is biased.

The *integer solution* in step 2 is a real-to-integer mapping with $\mathcal{S} : \mathbb{R}^n \mapsto \mathbb{Z}^n$ and the estimator $\mathcal{S}$ is a many-to-one map, since different real-valued vectors are mapped to one integer vector. Therefore, a subset $\mathcal{P}_{\breve{N}} \subset \mathbb{R}^n$ can be assigned to each integer vector $\breve{\mathbf{N}} \in \mathbb{Z}^n$:

$$\mathcal{P}_{\breve{N}} = \left\{\hat{\mathbf{N}} \in \mathbb{R}^n \| \breve{\mathbf{N}} = \mathcal{S}(\hat{\mathbf{N}})\right\}, \ \breve{\mathbf{N}} \in \mathbb{Z}^n. \tag{2.45}$$

The subset, which is the *pull-in region* of $\breve{\mathbf{N}}$, is the region in which all float solutions are pulled to the same integer vector via the estimator $\mathcal{S}(\cdot)$. For a subset to be a pull-in region, according to Teunissen (1999), three conditions must be met:

$$\begin{aligned} a): \ & \bigcup_{\breve{\mathbf{N}} \in \mathbb{Z}^n} \mathcal{P}_{\breve{N}} = \mathbb{R}^n, \\ b): \ & \mathcal{P}_{\breve{N}_1} \bigcap \mathcal{P}_{\breve{N}_2} = \varnothing, \ \forall \breve{\mathbf{N}}_1, \breve{\mathbf{N}}_2 \in \mathbb{Z}^n, \ \breve{\mathbf{N}}_1 \neq \breve{\mathbf{N}}_2, \\ c): \ & \mathcal{P}_{\breve{N}} = \mathcal{P}_0 + \breve{\mathbf{N}}, \ \forall \breve{\mathbf{N}} \in \mathbb{Z}^n. \end{aligned} \tag{2.46}$$

The first one states that the union of the pull-in region should cover the n-dimensional space completely to avoid gaps. The second property is that any two distinct regions should not have an overlap to ensure unique assignments of a float solution to an integer one. The third condition is that the pull-in regions are translational invariant, which allows to work with the fractional parts of the float solution instead of the full real-valued vector. Exemplary two-dimensional pull-in regions for different integer estimators – i.e., Integer Rounding (IR), Integer Bootstrapping (IB) and Integer Least-squares (ILS) – are shown in Fig. 2.5.

Integer Rounding

The simplest integer estimator is the IR method, where the float ambiguity vector is component-wise rounded to the nearest integer value to obtain the integer ambiguity vector. The IR estimator therefore reads

$$\breve{\mathbf{N}}_{\mathrm{IR}} = \left(\lceil \hat{N}_1 \rfloor, \ldots, \lceil \hat{N}_n \rfloor\right)^T, \tag{2.47}$$

where $\lceil \cdot \rfloor$ denotes the operator which rounds the real-valued float ambiguity to the nearest integer. Since each component of $\hat{\mathbf{N}}$ is rounded to its nearest integer value, the maximum

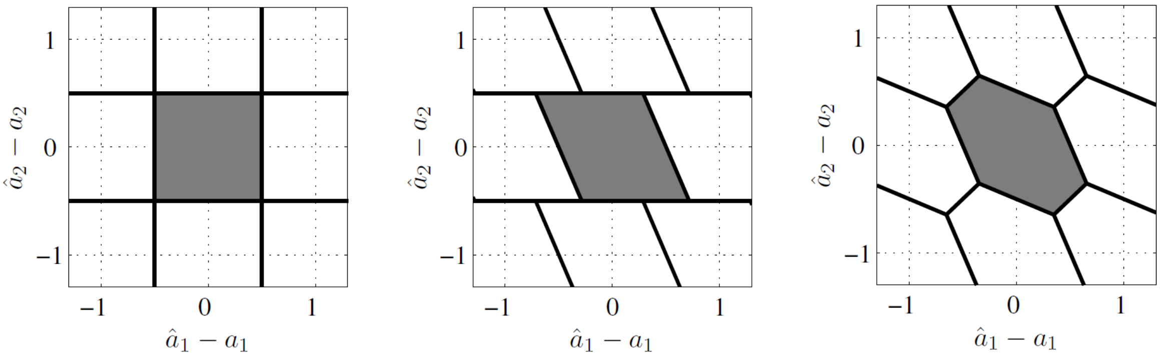

Figure 2.5: Pull-in regions $\mathcal{P}_{\breve{N}}$ of different integer estimators for a two dimensional example: (a) Integer Rounding, (b) Integer Bootstrapping, (c) Integer Least-squares. The regions that lead to correct integer estimates are marked in gray (Verhagen, 2005).

ambiguity residual is 1/2. The volume of the covariance matrix $\mathbf{P}_{\hat{N}\hat{N}}$ and cross-correlations between ambiguities are not considered using the IR estimator. The pull-in region of this estimator therefore reads

$$\mathcal{P}_{\mathrm{IR}}\left(\breve{\mathbf{N}}\right) = \left\{\hat{\mathbf{N}} \in \mathbb{R}^n \mid |\hat{N}_i - \breve{N}_i| \leq \frac{1}{2},\ i = 1, \ldots, n\right\},\ \forall \breve{\mathbf{N}} \in \mathbb{Z}^n \tag{2.48}$$

and describes n-dimensional cubes having sides of length one and centred at $\breve{\mathbf{N}} \in \mathbb{Z}^n$.

Integer Bootstrapping

The IB estimator is a generalization of the IR estimator (Blewitt, 1989; Dong and Bock, 1989). It still uses the rounding to the nearest integer technique, but additionally considers correlations between the ambiguities in a sequential conditional LSA. Usually, the real-valued ambiguity vector is sorted in descending order according to the uncertainty. The starting point is the rounding of the last element of the sorted float ambiguity vector $\hat{N}_n$ to its nearest integer value. After obtaining the first integer ambiguity, the remaining elements of the float ambiguity vector are then corrected by virtue of their correlation with the previous element. This process is continued until all elements are considered. Starting with the nth ambiguity, the IB estimator is given as

$$\begin{aligned}
\breve{N}_{\mathrm{IB},n} &= \left\lceil \hat{N}_n \right\rfloor, \\
\breve{N}_{\mathrm{IB},n-1} &= \left\lceil \hat{N}_{n-1|n} \right\rfloor = \left\lceil \hat{N}_{n-1} - \sigma_{\hat{N}_{n-1}\hat{N}_n} \sigma^{-2}_{\hat{N}_n} \left(\hat{N}_n - \breve{N}_{\mathrm{IB},n}\right) \right\rfloor, \\
&\vdots \\
\breve{N}_{\mathrm{IB},1} &= \left\lceil \hat{N}_{1|2,\ldots,n} \right\rfloor = \left\lceil \hat{N}_1 - \sum_{i=2}^{n} \sigma_{\hat{N}_1 \hat{N}_{i|I}} \sigma^{-2}_{\hat{N}_{i|I}} \left(\hat{N}_{i|I} - \breve{N}_{\mathrm{IB},i}\right) \right\rfloor,
\end{aligned} \tag{2.49}$$

where $\hat{N}_{i|I}$ is the ith estimated element of $\hat{\mathbf{N}}$, which is obtained by conditioning on the previously $I = \{i+1, \ldots, n\}$ sequentially rounded ambiguities. According to Medina (2021), the IB estimator can also be expressed in a compact vector form as

$$\breve{\mathbf{N}}_{\mathrm{IB}} = \left\lceil \hat{\mathbf{N}} + \left(\mathbf{L}^{-1} - \mathbf{I}_n\right)\left(\hat{\mathbf{N}} - \breve{\mathbf{N}}_{\mathrm{IB}}\right) \right\rfloor, \tag{2.50}$$

where $\mathbf{L}$ is the lower unit triangle matrix computed by decomposing the float ambiguity covariance to $\mathbf{P}_{\hat{N}\hat{N}} = \mathbf{L}^T \mathbf{P}'_N \mathbf{L}$ with the diagonal matrix of the conditional variances $\mathbf{P}'_N$.

Thus, the resulting pull-in region of the IB estimator is defined as

$$\mathcal{P}_{\text{IB}}\left(\check{\mathbf{N}}\right) = \left\{\hat{\mathbf{N}} \in \mathbb{R}^n \mid \left|\mathbf{c}_i^T \mathbf{L}^{-T}\left(\hat{\mathbf{N}} - \check{\mathbf{N}}\right)\right| \le \frac{1}{2},\ i = 1, \ldots, n\right\},\ \forall \check{\mathbf{N}} \in \mathbb{Z}^n \tag{2.51}$$

with $\mathbf{c}$ denoting the ith canonical unit vector having a 1 as the ith entry.

Integer Least-squares

The ILS estimator was firstly introduced in Teunissen (1993) and is defined as

$$\check{\mathbf{N}}_{\text{ILS}} = \arg \min_{\check{\mathbf{N}} \in \mathbb{Z}^n} \|\hat{\mathbf{N}} - \check{\mathbf{N}}\|^2_{\mathbf{P}_{\hat{N}\hat{N}}} \tag{2.52}$$

with its pull-in region being defined by an ellipsoidal search

$$\mathcal{P}_{\text{ILS}}\left(\check{\mathbf{N}}\right) = \left\{\hat{\mathbf{N}} \in \mathbb{R}^n \mid \|\hat{\mathbf{N}} - \check{\mathbf{N}}\|^2_{\mathbf{P}_{\hat{N}\hat{N}}} \le \|\hat{\mathbf{N}} - \check{\mathbf{N}}'\|^2_{\mathbf{P}_{\hat{N}\hat{N}}},\ \forall \check{\mathbf{N}}' \in \mathbb{Z}^n\right\},\ \forall \check{\mathbf{N}} \in \mathbb{Z}^n. \tag{2.53}$$

For the two-dimensional example, the ILS pull-in region has the shape of a hexagon while the pull-in regions of the IR and IB methods are shaped as a square and a parallelogram, respectively (see Fig. 2.5). The ILS estimator requires searching for mapping the real-valued ambiguities to the optimal integer vector. The search space is an n-dimensional hyper-ellipsoid centred in $\hat{\mathbf{a}}$ and its size is defined by the covariance matrix $\mathbf{P}_{\hat{N}\hat{N}}$.

Partial Ambiguity Resolution

The above three estimators have the property of the so-called *full ambiguity resolution*, meaning that for the full set of float ambiguities, a corresponding integer ambiguity vector is estimated. However, under challenging circumstances, e.g. poor observation quality of single satellites, the precision of the float ambiguity solution might be degraded and thus, integer ambiguity resolution is not possible. Also, the probability of correct integer ambiguity estimation is decreasing with increasing number of observations (Verhagen, 2004). To overcome this issue, Partial Ambiguity Resolution (PAR) is introduced (Teunissen et al., 1999), which is the reliable estimation of a subset of integer ambiguities instead of estimating the full set of integer ambiguities.

The mapping $\mathcal{S} : \mathbb{R}^n \mapsto \mathbb{Z}^{|\mathcal{I}|}$ from the n-dimensional space of reals to the $|\mathcal{I}|$-dimensional space of integers, i.e., mapping a subset of the float ambiguities to its corresponding integer vector, is denoted as

$$\mathcal{P}_{\check{N}} = \left\{\hat{\mathbf{N}} \in \mathbb{R}^n \| \check{\mathbf{N}} = \mathcal{S}(\hat{\mathbf{N}})\right\},\ \forall \check{\mathbf{N}} \in \mathbb{Z}^{|\mathcal{I}|}, \tag{2.54}$$

where $\mathcal{I}$ is the index set of any of the $2^n - 1$ possible non-empty realizations. The constraints of Eq. 2.46 remain the same, but with the amendment of the dimension of the index set $\mathcal{I}$:

$$\begin{aligned} a) &: \bigcup_{\check{\mathbf{N}} \in \mathbb{Z}^{|\mathcal{I}|}} \mathcal{P}_{\check{N}} = \mathbb{R}^n, \\ b) &: \mathcal{P}_{\check{N}_1} \bigcap \mathcal{P}_{\check{N}_2} = \varnothing,\ \forall \check{\mathbf{N}}_1, \check{\mathbf{N}}_2 \in \mathbb{Z}^{|\mathcal{I}|},\ \check{\mathbf{N}}_1 \neq \check{\mathbf{N}}_2, \\ c) &: \mathcal{P}_{\check{N}} = \mathcal{P}_0 + \check{\mathbf{N}},\ \forall \check{\mathbf{N}} \in \mathbb{Z}^{|\mathcal{I}|}. \end{aligned} \tag{2.55}$$

In literature, different approaches of selecting the subset of ambiguities to fix have been proposed. If full ambiguity resolution is not possible, one method is to fix only the widelane ambiguities in case of multi-frequency GNSS observations (Hatch et al., 2000; Li et al., 2010).

Another approach is to take constraints into account, e.g., a threshold for the ambiguities' variances, minimum elevation angle of the satellites or minimum C/N$_0$ (Parkins, 2011). Yet another method is to select a subset of integer ambiguities which are consistent in the best and second-best solution (Lawrence, 2009).

Most of the above mentioned approaches require a long search time due to the iterative subset evaluation procedure and are not based on the success rate or precision improvement (Teunissen and Montenbruck, 2017). Therefore, another approach is proposed by Teunissen et al. (1999) which searches for the largest possible subset of decorrelated ambiguities $\hat{\mathbf{z}} = \mathbf{Z}\hat{\mathbf{N}}$ to be fixed using the success rate criterion

$$\prod_{i=1}^{k} \left[2\Phi\left(\frac{1}{2\sigma_{\hat{z}_{i|I}}}\right) - 1 \right] \geq P_{\min}, \tag{2.56}$$

where $\mathbf{Z}$ is the so-called Z-transformation matrix for ambiguity decorrelation (Teunissen, 1995b) and $P_{\min}$ is the user-defined minimum required success rate. The number of ambiguities k which determines the size of the subset to be fixed, is chosen such that the inequality in Eq. 2.56 holds true.

LAMBDA Method

The Least-squares AMBiguity Decorrelation Adjustment (LAMBDA) method is a well-established method for solving the integer ambiguity problem in GNSS, based on the ILS procedure (Teunissen, 1993, 1995a; De Jonge and Tiberius, 1996; Verhagen, 2005). The search space is defined as

$$\mathcal{P}_{\check{N}} = \left\{ \check{\mathbf{N}} \in \mathbb{Z}^n \mid (\hat{\mathbf{N}} - \check{\mathbf{N}})^T \mathbf{Q}_{\hat{N}\hat{N}}^{-1} (\hat{\mathbf{N}} - \check{\mathbf{N}}) \leq \chi^2 \right\}, \tag{2.57}$$

where χ^2 is a positive constant to be chosen. The search space is an n-dimensional ellipsoid centered at $\hat{\mathbf{N}}$. Its shape is determined by the covariance matrix $\mathbf{Q}_{\hat{N}\hat{N}}$ and its size by χ^2. Due to the high correlation between the individual ambiguities, the search space in the case of GNSS is extremely expanded, so that the search for the integer solution can take very long. Therefore, the search space is first transformed into a more spherical shape by decorrelating the original float ambiguities. This decorrelation is achieved by a transformation:

$$\hat{\mathbf{z}} = \mathbf{Z}^T \hat{\mathbf{N}}, \quad \mathbf{Q}_{\hat{z}} = \mathbf{Z}^T \mathbf{Q}_{\hat{N}\hat{N}} \mathbf{Z}, \quad \check{\mathbf{N}} = \mathbf{Z}^{-1} \check{\mathbf{z}}. \tag{2.58}$$

The transformation requires $\mathbf{Z}$ and $\mathbf{Z}^{-1}$ to contain integer values, so that the integer nature of ambiguities is preserved. Further, the transformation is volume-preserving with respect to the search space, since the determinant of $\mathbf{Z}$ is equal to 1. The transformed search space is then defined as

$$\mathcal{P}_{\check{z}} = \left\{ \check{\mathbf{z}} \in \mathbb{Z}^n \mid (\hat{\mathbf{z}} - \check{\mathbf{z}})^T \mathbf{Q}_{\hat{z}\hat{z}}^{-1} (\hat{\mathbf{z}} - \check{\mathbf{z}}) \leq \chi^2 \right\}. \tag{2.59}$$

Once the integer ambiguities are identified in the transformed space, a back transformation into the original space is computed.

Other Integer Ambiguity Resolution Methods

There are a number of other well-known IAR methods in the literature, which differ mainly in the definition of the ambiguity search space. A summary of other IAR methods, including references, is given in Tab. 2.2. Only Three Carrier Ambiguity Resolution (TCAR) and

Table 2.2: Overview of ambiguity resolution methods (modified from Verhagen (2005)).

Method	Name	References
Least-Squares Ambiguity Search Technique	LSAST	Hatch (1991)
Fast Ambiguity Resolution Approach	FARA	Frei and Beutler (1990)
SIGMA-Method	SIGMA	Dach et al. (2015)
Quasi Ionosphere-Free algorithm	QIF	Dach et al. (2015)
Modified Cholesky decomposition		Euler and Landau (1992)
Least-squares AMBiguity Decorrelation Adjustment	LAMBDA	Teunissen (1993)
Null method		Martin-Neira et al. (1995) Fernàndez-Plazaola et al. (2004)
Fast Ambiguity Search Filter	FASF	Chen and Lachapelle (1995)
Three Carrier Ambiguity Resolution	TCAR	Harris (1997)
Integrated TCAR	ITCAR	Vollath et al. (1998)
Optimal Method for Estimating GPS Ambiguities	OMEGA	Kim and Langley (1999)
Cascade Integer Resolution	CIR	Jung et al. (2000)
Best Integer Equivariant Estimator	BIE	Teunissen (2003)

Cascade Integer Resolution (CIR) are based on the bootstrapping estimator, all other methods are based on the ILS principle of minimizing the squared norm of the residuals (Verhagen, 2005). In Kim and Langley (2000) a conceptual comparison of some of the methods presented is made, while in Joosten and Tiberius (2002) and Verhagen (2004) a comparison of LAMBDA with CIR, TCAR, Integrated Three Carrier Ambiguity Resolution (ITCAR) and the null method is made. Another method of determining a set of integer ambiguities is the Best Integer Equivariant (BIE) estimator proposed by Teunissen (2003), where no separate ambiguity validation step is needed.

2.5 Robust Statistics

Whenever the distribution of measurements exactly fulfill the Gaussianity requirements with perfectly known covariance matrix, a Maximum Likelihood Estimator (MLE) for the normal model provides an optimal solution (Kim and Shevlyakov, 2008). In reality, the underlying assumptions on the probability distribution of observations are not perfectly met and thus, even for minor deviations from the assumed model (e.g., due to outliers or contaminated observations), optimality is not guaranteed. Many areas of engineering show that measurements contain outliers, resulting in heavy-tailed distributions, e.g. presented in Blankenship et al. (1997), Abramovich and Turcaj (1999), Middleton (1999) and Etter (2003), causing the estimator to be biased or even break down (Zoubir et al., 2012). The same applies for GNSS-based applications, where exact Gaussianity cannot be guaranteed and the assumption of the normal model is violated – especially in multipath and NLOS contaminated situations (Medina, 2021). Contrary to the MLE, Robust Statistics addresses the development of estimators that are able to provide nearly optimal solutions for Gaussian data distributions as well as for deviations from the model (Huber and Ronchetti, 2009). Its theory was derived in the work of Tukey (1960), Huber (1964) and Hampel (1971), which established the framework for the application of robust statistics to various applications in the field of technology and engineering.

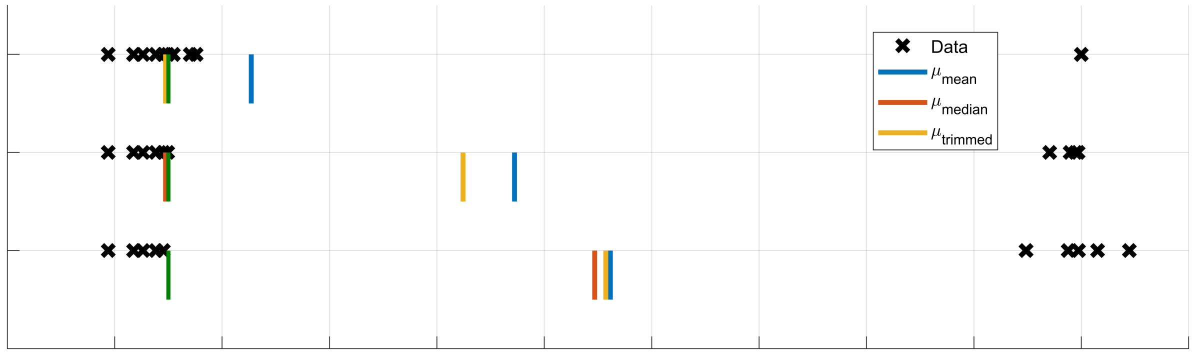

Figure 2.6: Bias and breakdown point of three traditional estimators for a one-dimensional estimation and different number of outliers. The true value is given in green, sample mean estimator is shown in blue, sample median is shown in red and the α-trimmed mean ($\alpha = 0.25$) is shown in yellow.

The simplified example for a one-dimensional location estimation in Fig. 2.6 is emphasizing the need of robust statistics. The solution of three traditional estimators are compared, namely the sample mean estimator (corresponds to minimizing the l_2-norm), the sample median estimator (corresponds to minimizing the l_1-norm) and the α-trimmed mean estimator (the largest and smallest 25 % of the measurements are trimmed from the estimation for $\alpha = 0.25$). Due to the influence of an outlier, the MLE at the normal distribution (sample mean estimator) results in a significant impact on the estimation of location. This bias can be characterized as a systematic deviation from the true value of the location parameter. In the scenario involving a single outlier, the sample median estimator and the α-trimmed mean estimator exhibit a high degree of proximity to the true value, effectively nullifying the influence of the outlier. Conversely, when confronted with six inliers and four outlying measurements, the α-trimmed mean estimation solution demonstrates a bias, while the sample median estimator continues to attain a solution that is nearly optimal. However, when the number of outliers exceeds half of the total measurements, the sample median estimator breaks down, resulting in a biased location estimation.

Breakdown Point

The breakdown point is a metric used to quantify the robustness of an estimator. As illustrated in Fig. 2.6, the performance of different estimators varies with increasing proportions of outliers. The breakdown point indicates the maximum proportion of outliers that an estimator can handle without producing a biased solution. The MLE for the normal model encounters failure when one outlier is present, thereby establishing a breakdown point of zero for the estimator. In contrast, the sample median estimator demonstrates a breakdown point of 50 %. When the fraction of outliers exceeds 50 %, the distinction between nominal and contaminated observations becomes indistinguishable. Consequently, the maximum attainable breakdown point for an estimator founded on robust statistics is also 50 %.

Maximum Likelihood Estimation for One-dimensional Data

Recalling the one-dimensional location estimation, we have a vector of measurements available, which are distributed around the location μ with noise v_i:

$$y_i = \mu + v_i, \tag{2.60}$$

with the vector of n measurements $\mathbf{y}^T = \left[y_1, \dots, y_n\right]$ and independent and identical distributed noise v_i following a distribution F_0. The likelihood function of the observations is defined as

$$L(\mathbf{y}|\mu) = \prod_{i=1}^{n} f(y_i - \mu), \tag{2.61}$$

where $f(\cdot)$ is the Probability Distribution Function (pdf). By maximization of the likelihood, the MLE yields an estimate $\hat{\mu}$ for the location μ:

$$\hat{\mu}(\mathbf{y}) = \arg\max_{\mu} L(y_1, \dots, y_n|\mu). \tag{2.62}$$

In the case the distribution of the measurements is $F_0 = \mathcal{N}(\mu, \sigma^2)$, i.e. the Gaussian model, the pdf for the measurements is given by

$$f(y_i|\mu, \sigma^2) = \frac{1}{\sqrt{2\pi\sigma^2}} \exp\left(-\frac{(y_i - \mu)^2}{2\sigma^2}\right). \tag{2.63}$$

Since $L(\mathbf{y}|\mu)$ is positive in all cases, the maximization problem outlined in Eq. 2.61 for the Gaussian model can be expressed equivalently as the following minimization

$$\hat{\mu}_{\text{mean}} = \arg\min_{\mu} \sum_{i=1}^{n} (r_i)^2, \tag{2.64}$$

where the ith residual $r_i = y_i - \mu$ is the difference between the ith observation and the estimate. Equation 2.64 describes the minimization of the l_2 norm corresponding to a LSA and it is obvious that the sample mean aligns with the MLE for the normal model.

Alternatively, if the measurements follow the Laplace distribution, the pdf for the measurements is given by

$$f(y_i|\mu, \sigma^2) = \frac{1}{\sqrt{2}\sigma} \exp\left(-\frac{\sqrt{2}|y_i - \mu|}{\sigma^2}\right) \tag{2.65}$$

and the corresponding MLE solves the following minimization

$$\hat{\mu}_{\text{median}} = \arg\min_{\mu} \sum_{i=1}^{n} |r_i|. \tag{2.66}$$

Equation. 2.66 describes the minimization of the l_1 norm or the Least Absolute Deviation (LAD) adjustment and it is obvious that the sample median aligns with the MLE for the Laplace distribution.

M-estimator

M-estimators are a generalization of MLE introduced by Huber (1964) and can resist outliers by solving following minimization:

$$\hat{\mu}_{\text{M}} = \min_{\mu} \sum_{i=1}^{n} \rho\left(\frac{r_i}{\sigma}\right), \tag{2.67}$$

where $\rho(\cdot)$ denotes the loss function. For symmetric and differentiable loss functions, its score function is defined as the loss functions derivative

$$\psi(x) = \frac{d\rho(x)}{dx}, \tag{2.68}$$

which can be solved as

$$\sum_{i=1}^{n} \psi\left(\frac{y_i-\mu}{\sigma}\right) = 0. \tag{2.69}$$

Intuitively, M-estimators for one-dimensional location estimation can also be interpreted as a weighted average with weights given by the weighting function

$$w(x) = \begin{cases} \frac{\psi(x)}{x}, & \text{if} \ \ x \neq 0 \\ 1, & \text{if} \ \ x = 0 \end{cases}. \tag{2.70}$$

Typically, for robust M-estimators, the weights are one (or close to one) for the inliers, while the outliers are down-weighted according to the score function. Many score functions $\psi(x)$ exist in order to penalize outliers in the measurements, achieving high efficiency under the nominal model as well as robustness against outlying observations and a high breakdown point. It is typically distinguished between monotone and redescending M-estimators, where the latter are useful especially for data with extreme outliers.

The loss functions $\rho(x)$, score functions $\psi(x)$ and weighting functions $w(x)$ of one typical monotone M-estimator based on the Huber's family of functions (Huber, 1964) and of one common redescending M-estimator based on the Tukey's bisquare family of functions (Tukey, 1960) are displayed together with the functions of the MLE in Tab. 2.3. The parameters c_H and c_T are set to control the robustness and efficiency of the M-estimators. If they are set to $c_H, c_T \to \infty$ or $c_H, c_T \to 0$, the M-estimator corresponds to the sample mean or sample median, respectively. Typically, the parameters are chosen to meet 95 % relative efficiency at the normal model, which yield the values $c_H = 1.345$ and $c_T = 4.685$. Another robust family of functions – originally defined for image analysis – is based on the Geman-McClure loss (Geman and McClure, 1985; Barron, 2019), which is also a redescending type of estimator but is damping large values even more using continuous functions without residual-based decisions. The tuning parameter of the Geman-McClure function is typically set to 1. Close to zero, it behaves similar to the MLE loss and outside it is significantly bounded being robust to large outliers.

It is evident that monotone and redescending M-estimators possess distinct traits: the former results in convex optimization problems for Eq. 2.67, ensuring solution uniqueness, whereas the latter are entirely bounded, providing enhanced quantitative robustness albeit with a non-convex optimization for Eq. 2.67 and reduced efficiency within the nominal model. The Huber, Tukey and Geman-McClure functions, as well as the MLE at the normal model, are

Table 2.3: Loss functions $\rho(x)$, score functions $\psi(x)$ and weighting functions $w(x)$ of the MLE at the normal model, the Huber-based monotone M-estimator and the redescending Tukey bisquare M-estimator.

Estimator	$\rho(x)$	$\psi(x)$	$w(x)$
MLE	$\frac{x^2}{2}$	x	1
Huber $\begin{cases} \lvert x\rvert \le c_H \\ \lvert x\rvert > c_H \end{cases}$	$\begin{cases} \frac{x^2}{2} \\ c_H\lvert x\rvert - \frac{c_H^2}{2} \end{cases}$	$\begin{cases} x \\ c_H \operatorname{sign}(x) \end{cases}$	$\begin{cases} 1 \\ \frac{c_H}{\lvert x\rvert} \end{cases}$
Tukey $\begin{cases} \lvert x\rvert \le c_T \\ \lvert x\rvert > c_T \end{cases}$	$\begin{cases} \frac{c_T^2}{6}\left(1-\left(1-\frac{x^2}{c_T^2}\right)^3\right) \\ \frac{c_T^2}{6} \end{cases}$	$\begin{cases} x\left(1-\frac{x^2}{c_T^2}\right)^2 \\ 0 \end{cases}$	$\begin{cases} \left(1-\frac{x^2}{c_T^2}\right)^2 \\ 0 \end{cases}$
Geman-McClure	$\frac{2\frac{x^2}{c_G^2}}{\frac{x^2}{c_G^2}+4}$	$\frac{16c_G^2 x}{(4c_G^2+x^2)^2}$	$\frac{16c_G^2}{(4c_G^2+x^2)^2}$

visualized in Fig. 2.7. In terms of inliers, the Huber-based M-estimator is anticipated to exhibit greater efficiency in the normal model compared to the redescending counterparts due to the alignment of their loss, score, and weighting functions with the MLE for nominal measurements. The example in Fig. 2.6 shows that the presence of one single sufficiently large outlier can lead to a breakdown of the MLE at the normal model. The impact of large residuals is demonstrated in the score and weighting functions, where the monotone Huber-based M-estimator would mitigate the influence of such outliers, while the redescending Tukey-based M-estimator would nullify their effect on the solution and the Geman-McClure-based M-estimator is largely reducing the impact by weights close to zero.

The computation of robust M-estimators is typically performed in an Iteratively Reweighted Least-squares (IRLS) adjustment with an initially computed robust scale estimate using the Median Absolute Deviation (MAD):

$$\hat{\sigma}(\mathbf{x}) = 1.4826 \cdot \text{median}\left(|\mathbf{x} - \text{median}(\mathbf{x})|\right). \tag{2.71}$$

Thereby, the normalization factor 1.4826 corresponds to the standard deviation at the normal model. The procedure of the IRLS adjustment is displayed in Alg. 1. Given a set of measurements $\mathbf{y}$ and predictors $\mathbf{A}$, the first step is to compute an initial solution $\hat{\mu}$ and scale $\hat{\sigma}$ using a LSA. In the initialization step, the weighting matrix $\mathbf{W}$ is typically configured to assign unit weights to the measurements. Subsequently, the weighting matrix is adapted through the use of robust weighting functions until the convergence criterion is met. Robust weighting functions are utilized, such as those based on the Huber family of functions, as outlined in Tab. 2.3. Concurrently, the location parameter $\hat{\mu}$ is estimated iteratively.

If M-estimation is extended from the one-dimensional location estimation to, e.g. linear regression (i.e., Generalized M (GM)-estimation), the limitation of the generalized M-estimators is that they typically show a low breakdown point of at most $1/(p+1)$ (p is the number of parameters to be estimated) and - depending on the particular situation - do not necessarily reach this upper bound (Maronna et al., 1979).

S-estimator

The class of S-estimators is designed to have a high breakdown point and is based on the Least Median of Squares (LMS)

$$\hat{\mu}_{\text{LMS}} = \arg\min_{\mu} \text{median}(\mathbf{r}) \tag{2.72}$$

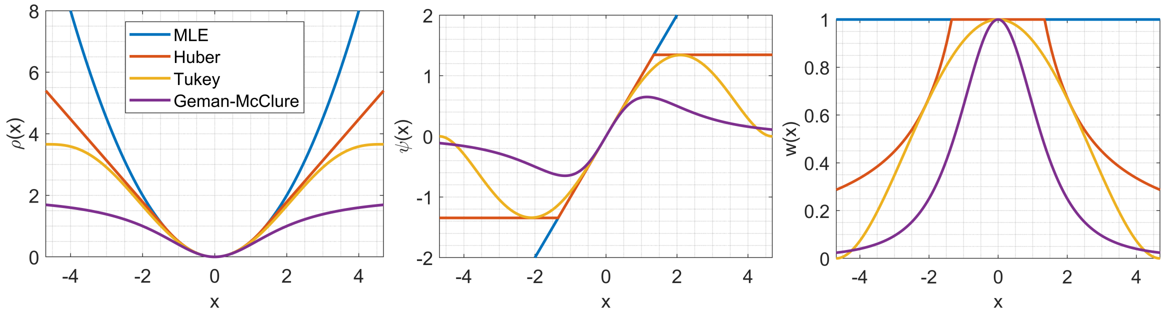

(a) (b) (c)

Figure 2.7: Loss functions $\rho(x)$ (a), score functions $\psi(x)$ (b), and weighting functions $w(x)$ (c) of the MLE at the normal model and M-estimators based on the Huber's, Tukey's and Geman-McClure's family of functions. The control parameters are set to $c_H = 1.345$, $c_T = 4.685$ for 95 % relative efficiency at the normal model and to $c_G = 1$.

Algorithm 1 IRLS adjustment using M-estimators.

```
Estimate initial $\hat{\sigma}$ and $\hat{\mu}$
while $\frac{\hat{\mu}^{(t+1)}-\hat{\mu}^{(t)}}{\hat{\sigma}} \geq \epsilon$ do
    Compute weighting matrix according to the weighting function:
        $\mathbf{W} = \mathrm{diag}(w_1, \ldots, w_n)$ with $w_i = w\left(\frac{r_i^{(t)}}{\hat{\sigma}}\right)$
    Perform weighted LSA:
        $\hat{\mu}^{(t+1)} = (\mathbf{A}^T\mathbf{W}\mathbf{A})^{-1}\mathbf{A}^T\mathbf{W}\mathbf{y}$
end while
```

and the Least Trimmed Squares (LTS)

$$\hat{\mu}_{\text{LTS}} = \arg\min_{\mu} \sum_{i=1}^{h} (r_i)^2, \tag{2.73}$$

where the residuals in LTS are sorted in ascending order such that $r_1^2 \leq \ldots r_n^2$ and h is chosen to attain a high breakdown point, e.g., $h = n/2$ yields a breakdown point of 50 % (Rousseeuw, 1984). The S-estimator, i.e. the minimization of a robust scale estimate for the residuals, is then defined as

$$\hat{\mu}_S = \arg\min_{\mu} \hat{\sigma}(\mathbf{r}) \tag{2.74}$$

and the scale estimate is the solution of

$$\frac{1}{n}\sum_{i=1}^{n} \rho\left(\frac{r_i}{\hat{\sigma}}\right) = \delta, \tag{2.75}$$

where δ balances the consistency at a particular distribution and the breakdown point, e.g., for maximum breakdown point $\delta = 0.5(1 - n/p)$. The S-estimator typically considers the use of redescending score functions. A high breakdown point of up to 50 % can be achieved while the drawback is a relatively low efficiency at the normal model.

MM-estimator

The MM-estimator proposed by Yohai (1987) is a two-step approach to achieve both a high breakdown point and high relative efficiency. First, an initial estimate $\hat{\mu} = \hat{\mu}_S$ and its scale $\hat{\sigma}_1$ is computed via S-estimation using a redescending function ρ_1 tuned for a high breakdown point. The MM-estimator is then computed using a IRLS adjustment by minimizing the following equation using a second redescending function such that $\rho_2 \leq \rho_1$:

$$\hat{\mu}_{MM} = \arg\min_{\mu} \sum_{i=1}^{n} \rho_2\left(\frac{r_i(\hat{\mu}_S)}{\hat{\sigma}_1}\right). \tag{2.76}$$

2.6 GNSS Positioning in Urban Environments

GNSS signals provide information about the absolute position of a user on a global scale with accuracy in the centimeter range, depending on the positioning method (see Sec. 2.3). In urban environments, nearby objects (e.g., buildings, trees or vehicles) block the direct LOS between the transmitting satellite and the receiving antenna and signal reflections resulting in numerous NLOS and multipath signal receptions. These effects are the dominant source of

GNSS positioning errors in dense urban environments (McGraw et al., 2021). Both types of errors are visualized in Fig. 2.8. NLOS and multipath errors – often synonymously referred to as multipath in the GNSS community – are influenced by the geometric signal path of the direct and indirect signals, which are defined by the local environment and satellite positions. Additionally, these errors are affected by the complex signal-antenna-receiver interaction. Although these two effects are often grouped, their error characteristics are different. When considering a signal reflection, the reflected signal is always longer than the direct signal. Therefore, NLOS reception always results in a positive ranging error, while the coherent nature of multipath interference produces both positive and negative ranging errors, which also vary with signal and receiver design (Groves, 2013a). NLOS delays can reach up to twice the orthogonal distance to the reflector plane (e.g., tens of meters for smaller urban trenches in European inner cities (Betaille et al., 2013; Icking et al., 2020) and up to hundreds of meters for urban canyons in metropolitan cities (Hsu, 2017a; Icking et al., 2022). The delay caused by multipath depends on the extra path delay and the receiver settings. Its assessment is typically conducted by the multipath envelope function for pseudorange observations, yielding delays ranging from 30 to 50 meters. For the carrier phase measurement, the impact ranges from millimeters to a maximum of a quarter of the wavelength (Braasch, 2017).

Several multipath and NLOS error mitigation strategies have been researched to improve GNSS-based localization in urban environments, as accurate positioning plays a crucial role in many applications and emerging technologies, such as autonomous driving or pedestrian navigation. The demand for high accuracy and high integrity positioning models is increasing and, due to the fact that the GNSS sensor is the only one that provides absolute positioning information, the advancement of research into GNSS positioning is ongoing. In order to achieve an adequate level of accuracy, it is essential to employ not only carrier phase-based positioning techniques but also to integrate multipath and NLOS error mitigation strategies. The details of application requirements are outlined in Sec. 2.7.

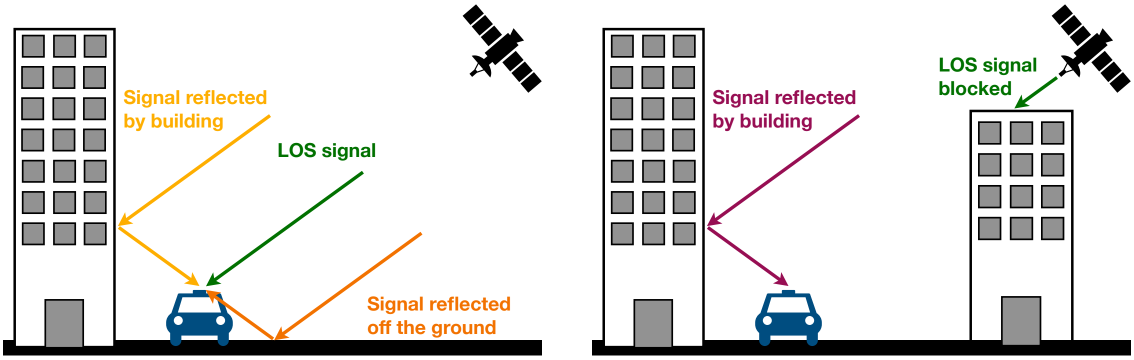
Signal reflected by building
LOS signal
Signal reflected off the ground
Signal reflected by building
LOS signal blocked

(a) (b)

Figure 2.8: Main GNSS error sources in urban environments: (a) multipath and (b) NLOS signal reception.

2.6.1 3D Mapping Aided GNSS

The availability of 3D city models in the standardized City Geography Markup Language (CityGML) format (Gröger et al., 2012), e.g. provided by the city of Hannover (Landeshauptstadt Hannover, FB Planen und Stadtentwicklung, Bereich Geoinformation, 2017) and other cities around the world (Berlin (Business Location Center, 2022), Amsterdam (van den Brink et al., 2013), New York (Department of Information Technology and Telecommunications (DoITT), 2022), Hongkong (Land Information Centre (LIC), Survey and Mapping Office

(SMO), Lands Department, 2021)) is increasing. Google has deployed 3DMA-GNSS in Android phones for almost 4,000 cities, covering major cities in North America and Europe, Japan, Taiwan, Brazil, Argentina, Australia, New Zealand, and South Africa (van Diggelen, 2021). A 3D city model, combined with knowledge of satellite positions, enables prediction of which signals will be affected and where.

Ray Tracing

Once an accurate 3D city model is at hand, the satellite positions are available and an approximate user location is known, ray tracing can be performed. When these conditions are met, ray tracing is a powerful tool for distinguishing between LOS and NLOS satellite ray conditions and for characterizing multipath error in an urban environment. The observation error is dependent on the satellite-reflector-antenna geometry and thus, ray tracing simulations were used to characterize and estimate multipath errors in different static environments, e.g. using a steel reflector in a controlled environment (Lau and Cross, 2007), ship and aircraft environments (Weiss et al., 2007), ground reflections (Smyrnaios et al., 2012) or complex urban scenarios using a virtual city model (Bradbury et al., 2007).

Besides the multipath and NLOS receptions, the diffraction effect frequently occurs in urban canyons, which will severely attenuate the signal strength when the satellite LOS transmitting path is close to the building edge. The impact of diffraction effects on the GNSS signal is studied, e.g. in Zimmermann et al. (2019), Zhang and Hsu (2021), Schaper et al. (2022) and Zhang et al. (2023).

In recent years, the significance of the GNSS sensor in the domain of automotive applications and emerging technologies has grown. Consequently, research involving ray tracing is being expanded to include the integration into positioning algorithms, with the objective of either eliminating or rectifying GNSS observations. A comprehensive review of the latest literature on GNSS positioning algorithms, with a particular focus on the incorporation of NLOS exclusion or observation rectification strategies, is given in Tab. 2.4.

In addition to the necessity for an accurate city model and the typical absence of knowledge regarding the user position, the most significant constraint of ray tracing for GNSS positioning is its high computational complexity. Figure 2.9 depicts an illustrative example in the city of San Francisco, USA. The scenario on the left appears relatively straightforward, with direct rays from the satellites to the user. However, the scenario on the right, which is a zoomed-in plot, provides a more accurate representation of the actual situation. In scenarios with multiple reflecting surfaces, scattering and diffraction situations, the number of candidate

Table 2.4: State of the art literature summary for GNSS positioning algorithms including NLOS exclusion or observation rectification strategies.

NLOS exclusion strategies	Observation rectification strategies
Obst et al. (2012)	Betaille et al. (2013)
Peyraud et al. (2013)	Suzuki and Kubo (2013)
Betaille et al. (2013)	Miura et al. (2015)
Hsu et al. (2015)	Hsu et al. (2015)
Zimmermann et al. (2019)	Hsu et al. (2016)
Icking et al. (2020)	Icking et al. (2020)
Ruwisch and Schön (2022b)	Ruwisch and Schön (2022a)
O’Connor et al. (2024)	Lyu and Gao (2023)

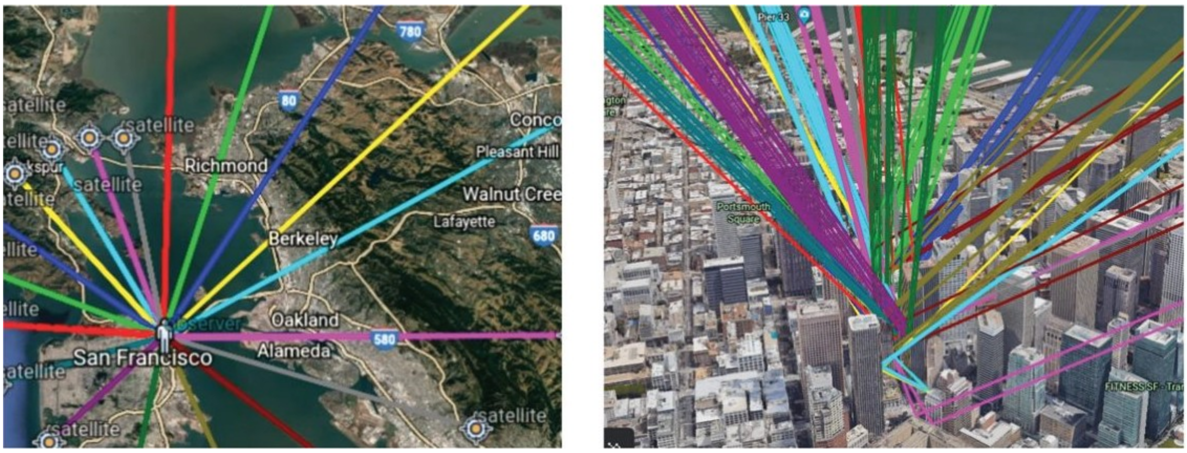

Figure 2.9: Exemplary situation of ray tracing for a given situation in San Francisco, USA. The right image is a zoom-in plot of the left image. Source: van Diggelen (2021).

rays becomes enormous, which is, e.g., more than a phone can handle (van Diggelen, 2021). Therefore, special techniques are required in order to maintain the real-time applicability (O'Connor et al., 2021).

Ray Tracing Software

The software utilized for ray tracing in the context of this thesis is developed by Icking et al. (2020) and subsequently refined by Baasch et al. (2023). In order to assess satellite visibility, a 3D CityGML model provided by the City of Hannover is employed. This model contains all buildings within the city, stored across multiple files in the CityGML, a format based on Extensible Markup Language (XML) designed for geographic data representation. The selected Level of Detail (LoD) 2 includes building models that capture roof geometries, eaves, and ridges, with a vertical accuracy of ± 1 meter.

Once a specific area within the city is selected and the user coordinates are set, the satellite visibility analysis is conducted. The two core components of the algorithm are as follows (see Fig. 2.10):

1. Dividing the building model into smaller bounding boxes.
2. Decomposing each polygon into triangles to simplify the intersection test.

It is imperative to subdivide the selected portion of the building model in order to reduce the computational run-time. Accordingly, a reasonable area of interest is identified prior to each data analysis, determining the amount of building information considered for the computation steps. Once the LOS between the antenna and the satellite has been established, a ray-box intersection test based on Williams et al. (2005) is performed to determine which boxes are intersected by the LOS ray. Subsequently, only these boxes are subjected to analysis, as the ray intersects only a minor subset of all the boxes within the area. This approach results in a notable reduction in computational run-time. Once the boxes that have been intersected have been identified, the subsequent step is to ascertain which of the building polygons that are within these boxes impede the LOS. To streamline the computation and minimize processing time, each polygon is triangulated. A triangle-ray intersection test, as outlined in Möller and Trumbore (2005), is then performed. If an intersection with any triangle is detected, the satellite is considered not visible (NLOS). If no intersection occurs, the satellite is marked as visible (LOS).

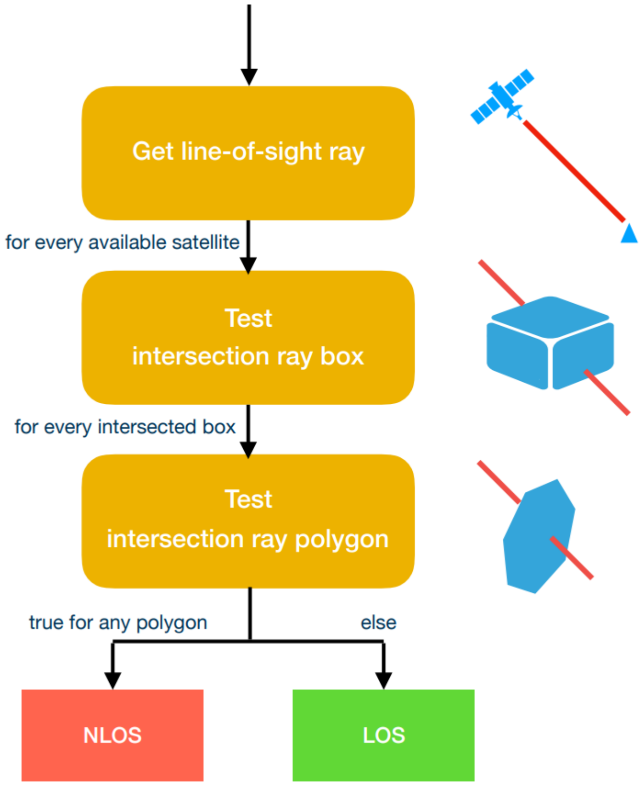

Figure 2.10: LOS/NLOS determination algorithm. Source: Icking et al. (2020).

To ascertain whether a signal is susceptible to multipath or reflections from building surfaces, i.e. two-dimensional planes, it is first necessary to identify the reflection points. This, in turn, requires that the ray vector between the antenna and the satellite, as well as the nearby building surfaces, be expressed in a common coordinate frame (Baasch et al., 2023). Figure 2.11 shows the geometry of the reflection calculation. To calculate the reflection point $\mathbf{R}$ on the reflecting surface P, the antenna position $\mathbf{A}$ is mirrored with respect to this plane:

$$\mathbf{K} = \mathbf{A} + \frac{(\mathbf{P}_0 - \mathbf{A}) \cdot \mathbf{n}'}{\mathbf{n} \cdot \mathbf{n}'}\mathbf{n}. \tag{2.77}$$

The projection of the antenna onto the reflecting surface $\mathbf{K}$ is computed using the normalized outer normal vector $\mathbf{n}$ of the reflecting plane and any point $\mathbf{P}_0$ on the plane. The point $\mathbf{P}_0$ can be any vertex and $\mathbf{n}$ can be calculated from three vertices of the surface. Next, the virtual antenna point $\mathbf{A}'$ is calculated:

$$\mathbf{A}' = \mathbf{A} + 2(\mathbf{K} - \mathbf{A}). \tag{2.78}$$

The intersection between the ray from the mirrored antenna point $\mathbf{A}'$ to the satellite $\mathbf{S}$ will give the reflection point $\mathbf{R}$:

$$\mathbf{R} = \mathbf{A}' + \frac{(\mathbf{K} - \mathbf{A}')\mathbf{n}}{(\mathbf{S} - \mathbf{A}')\mathbf{n}}(\mathbf{S} - \mathbf{A}'). \tag{2.79}$$

Finally, the satellite ray is classified into one of the four categories:

1. LOS: Satellite ray is not obstructed and no possible reflection point exists
2. Multipath: Satellite ray is not obstructed but a signal reflection with reflection point is calculated

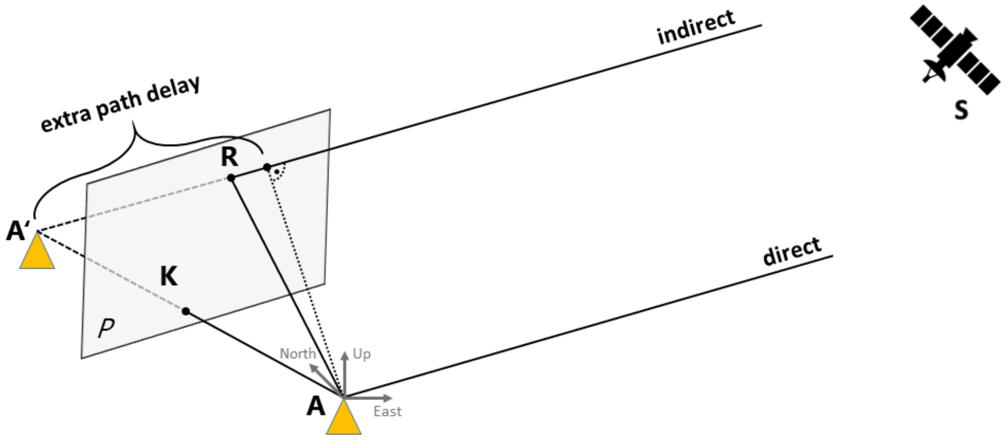

Figure 2.11: Satellite ray reflection on a building surface P at the reflection point $\mathbf{R}$. The user position is denoted by $\mathbf{A}$, its projection with respect to P as $\mathbf{A}'$. The extra path delay is represented by the difference between the satellite S and the mirrored antenna point $\mathbf{A}'$, as well as the satellite $\mathbf{S}$ and antenna $\mathbf{A}$. Source: Baasch et al. (2023).

3. NLOS: the direct LOS is obstructed by a building and the signal can be received via single reflection on a buildings surface
4. Blocked: the direct LOS is obstructed by a building and no possible reflection point exists

The integration of the ray tracing software into the developed positioning algorithm is described in Sec. 3.3.

Shadow Matching

GNSS shadow matching is a positioning technique used in urban environments to enhance accuracy by comparing predicted and observed satellite signal availability through the use of predicted and measured C/N_0. As demonstrated in Groves (2011) and Groves et al. (2015), this technique employs 3D models of the environment to predict regions of shadow, i.e., areas where satellite signals are impeded by buildings or other structures, as well as the GNSS signals that are visible with a direct LOS path. The principle of shadow matching is illustrated in Fig. 2.12. A user is assumed to be in one of the shadowed areas if the measured C/N_0 is low or the signal is not received at all. If the observed C/N_0 is high, shadow matching assumes that the user is in a region with direct LOS to the respective satellite. The basis of the LOS/NLOS decision criterion is an empirically determined function of the direct LOS probability as a function of C/N_0. As the characteristics of antenna-receiver combinations are inherently different, a function tailored to the respective equipment in use is required. This function can be derived from C/N_0 data collected at a known location under ideal conditions (Wang et al., 2015).

In order to determine an initial approximate GNSS position and a search space, it is necessary to compute match probabilities for each signal for a number of candidate positions within that search space (McGraw et al., 2021):

$$\begin{aligned} P_{ij} &= p(\mathrm{LOS}|\mathrm{C/N_0})_j p(\mathrm{LOS}|\mathrm{map})_{ij} + (1 - p(\mathrm{LOS}|\mathrm{C/N_0})_j)\,(1 - p(\mathrm{LOS}|\mathrm{map})_{ij})\,, \\ &= 1 - p(\mathrm{LOS}|\mathrm{C/N_0})_j - p(\mathrm{LOS}|\mathrm{map})_{ij} + 2p(\mathrm{LOS}|\mathrm{C/N_0})_j p(\mathrm{LOS}|\mathrm{map})_{ij}, \end{aligned} \tag{2.80}$$

where $p(\mathrm{LOS}|\mathrm{C/N_0})$ is the observed direct LOS probability, $p(\mathrm{LOS}|\mathrm{map})$ is the predicted direct LOS probability, j is the satellite and i is the candidate position. A probability score for each candidate position is computed by multiplying the match probabilities for each signal by

$$\Lambda_i = \prod_j P_{ij}. \tag{2.81}$$

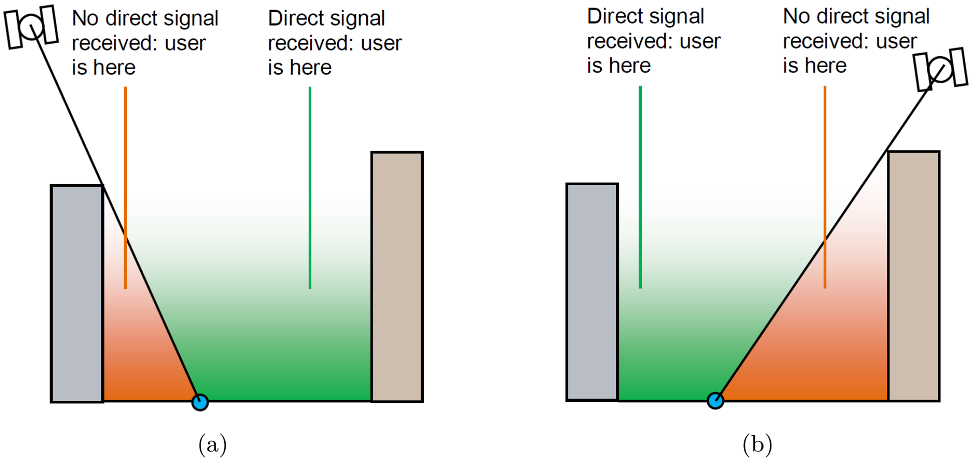
No direct signal received: user is here
Direct signal received: user is here
(a)
Direct signal received: user is here
No direct signal received: user is here
(b)

Figure 2.12: Principle of shadow matching. Source: Groves et al. (2015).

The position solution is then determined by a weighted average of the candidate positions:

$$\hat{\mathbf{x}}_{\text{pos}} = \frac{\sum_i \Lambda_i \mathbf{x}_{\text{pos},i}}{\sum_i \Lambda_i}, \tag{2.82}$$

where $\mathbf{x}_{\text{pos},i}$ is the position of the i-th candidate and Λ_i is a positive weighting factor.

It has been demonstrated by several research groups that shadow matching is an effective method for determining the user's cross-street position with greater accuracy, particularly in areas with significant signal obstructions. This approach yields positioning accuracies of better than 3 m, as evidenced by the findings of several studies, including those by Suzuki and Kubo (2012), Wang et al. (2012), Isaacs et al. (2014), Yozevitch and Moshe (2015), and Strandjord et al. (2020). Further research demonstrates that the signal strength of a diffracted GNSS signal may be attenuated depending on the percentage of blockage of the signal's Fresnel ellipsoid (Liso Nicolas et al., 2012; Zhang and Hsu, 2021; Schaper et al., 2022). Consequently, the incorporation of diffraction information into a shadow matching algorithm is advantageous (Zhang et al., 2023).

2.6.2 Consistency Checking

Consistency checking is a strategy that makes use of redundant measurement information in a navigation filter or least-squares estimation (Teunissen, 1990). The quality of an estimator directly depends on the assumptions that the measurements align with the mathematical model. Model misspecifications, such as outliers and sensor failures, can invalidate estimation results and any conclusions drawn from them. It is therefore essential to implement quality control procedures to ensure the integrity of the mathematical model. The quality of the measurements is evaluated with the prior stochastic assumptions, whereby an individual observation is assigned a specific uncertainty (for further details on GNSS variance models, please refer to Sec. 2.1.3). Consequently, an accurate stochastic model is essential for precisely determining measurements that deviate from these assumptions.

In other words, within the context of urban GNSS positioning, this implies that signals affected by multipath and NLOS are inconsistent with other nominal observations and can therefore be identified through the consistency check (Groves and Jiang, 2013). The same principle is applied in Receiver Autonomous Integrity Monitoring (RAIM), where the integrity of a GNSS receiver is monitored (Brown, 1992; Walter and Enge, 1995; Pervan et al., 1998). The effectiveness and performance of consistency checking algorithms for multipath and NLOS error detection and exclusion in vehicle applications have been investigated in various studies (Iwase et al., 2012; El-Mowafy, 2020; Elsayed et al., 2023). Further improvement potential is also explored by combining RAIM methodology with 3D city model information (El-Mowafy et al., 2020). Considering a dense urban environment, a large number of measurements are contaminated by multipath and NLOS and therefore, a consistency checking strategy for excluding multiple faults is required (Hsu et al., 2017).

The limitations of conventional consistency checking are discussed in Sec. 2.5. The consistency checking methodology, which is implemented in the scope of this thesis, is described in Sec. 3.2.

2.6.3 Multi-Sensor Combination

Since GNSS measurements tend to be biased in urban environments, another strategy to overcome the limitations of GNSS-only positioning is to incorporate other sensors, such as Inertial Navigation System (INS), odometer or Light Detection and Ranging (LiDAR), into a multi-sensor system. The integration of the GNSS sensor with an INS assists in providing continuous navigation through situations where GNSS signal outages occur, e.g. in deep urban canyons. The integration of the INS and GNSS in a tightly coupled navigation filter enhances positioning accuracy in urban environments, particularly when compared to GNSS-only positioning, as demonstrated in Groves (2013b) and Falco et al. (2017). In the event of GNSS signal failure, the INS serves to bridge the navigation output, while the GNSS sensor is able to calibrate the drifting INS error. This allows the sensor combination to have a complementary characteristic, which helps to maintain centimeter-level accuracy. The utilization of high-quality navigation-grade inertial sensors has the potential to attenuate the propagation of errors. However, their cost is not aligned with the financial constraints of automotive vehicle applications (Brown and Hwang, 2012).

The use of an Inertial Measurement Unit (IMU) based on a Micro-electromechanical System (MEMS) (lightweight, small size and low cost) allows for the implementation of an INS at a reduced cost, making it a suitable solution for navigation applications. The use of a GNSS/MEMS INS has been shown to mitigate GNSS signal disturbances, as evidenced, e.g., by the findings of Godha and Cannon (2007) and Yang et al. (2013). When carrier phase observations are utilized, for example, through PPP-RTK/INS integration, such a navigation system provides decimeter-level accuracy in GNSS-challenged environments (Li et al., 2021). Moreover, the GNSS/INS integration enhances the availability of a navigation system.

The incorporation of additional sensors, such as LiDAR sensors or wheel speed sensors, further improves the system's performance. The introduction of zero velocity updates and non-holonomic or holonomic constraints also enhances the system's capabilities, as demonstrated, e.g. in Nagai et al. (2024). The LiDAR sensor is capable of providing additional assistance to the navigation solution, e.g., through relative positioning with respect to landmarks (Nagai et al., 2024). Furthermore, a 3D map can be constructed from LiDAR point clouds, and subsequently, NLOS satellite signals can be identified and rectified within the estimation process (Wen, 2020; Wen and Hsu, 2021).

2.6.4 Machine Learning-based Approaches

In the modern digital age, data is generated at a constant and exponential rate in different field of applications. In response to this situation, technologies have been developed that take advantage of this characteristic. These technologies enable not only the measurement and understanding of their origin, but also the collection, quantification, decoding, and analysis of data to identify behaviors and trends, formulate strategies, and gain insights. Artificial Intelligence (AI) has already become a significant contributor to the fields of big data, image processing, and signal processing (França et al., 2021). Consequently, it is also playing a prominent role in the development of specific applications for ITS and autonomous driving, e.g. in scene understanding, motion planning, decision making, vehicle control, social behavior, and communication (Elallid et al., 2022).

In recent years, there has been a notable increase in the utilization of AI, particularly Machine Learning (ML) algorithms, for GNSS positioning. The capacity of these models to describe complex phenomena and relationships between parameters is a promising approach for multipath and NLOS detection, characterization, and mitigation in urban environments (Crespillo et al., 2023). ML methods for urban GNSS positioning can be distinguished by the specific purpose for which they are employed. This may be either the LOS/NLOS classification, as demonstrated by a binary decision tree (Yozevitch et al., 2016), an adaptive neuro fuzzy interference system (Sun et al., 2019), a gradient boosting decision tree (Sun et al., 2020) or a support vector machine classifier (Ozeki and Kubo, 2022). The other purpose is to use ML methods for multipath and NLOS detection for mitigation with or without a distinction between the two states of reception (Hsu, 2017b; Suzuki et al., 2017). Multipath errors were successfully mitigated at the receiver level by focusing on the auto-correlation function computed in the receiver (Orabi et al., 2020) and at the pseudorange error level by considering signal strength, satellite elevation angle and pseudorange residuals (Sun et al., 2020). A more comprehensive review of ML techniques for urban GNSS positioning is beyond the scope of this thesis. For further details, including an exploration of current challenges and limitations of these methods, the reader is directed to, e.g., Crespillo et al. (2023).

2.6.5 Robust Estimation

In general, robust estimators are capable of providing solutions that are nearly optimal in the presence of outliers. This is achieved by identifying the outliers and reducing their impact on the estimation process. The mathematical foundation of robust estimators was addressed in Sec. 2.5. In this section, recent contributions to the field of robust estimation in the context of GNSS positioning in challenging environments are discussed. The necessity for such robust estimators for GNSS positioning is becoming increasingly apparent as the probability of multiple outliers rises due to the growing number of satellites with multiple fully operational satellite systems and the GNSS sensor's role in automotive applications in challenging environments, e.g. urban areas. Robust methods retain all observations but either down-weight suspect observations or minimize alternatives to the sum of the squared residuals. The latest contributions to this field of research can be classified into two distinct categories: firstly, the pure performance simulation of various methods utilising solely simulated observations; and secondly, the evaluation based on real data measurements for inland waterborne or urban vehicular applications. A collection of the most notable research is presented in Tab. 2.5.
Simulation studies have demonstrated the ability of robust least-squares estimators, including the LMS, LTS, Modified Least Trimmed Squares (MLTS), Greedy Search (GS), Position and Time Variation (PTV), R-estimator, M-estimator, GM-estimator, S-estimator and MM-estimator to effectively detect the error-induced observations and to mitigate their impact with respect to standard weighted LSA (Knight and Wang, 2009; Medina et al., 2019; Wendel, 2022).

Further simulation studies indicate that robust estimation theory can be employed to modify the Kalman filter update step. This approach is effective for integrating the GNSS/INS coupled EKF using pseudorange observations with the M-estimator (Crespillo et al., 2018) and the variational inference method (Variational Bayesian Kalman Filter (VB-KF)) for RTK

Table 2.5: Literature review for robust GNSS positioning. Estimators: LMS, LTS, MLTS, GS, PTV, R-, M-, GM, S-, MM-estimator, EKF+M-estimator, CQKF, VB-KF, GM-KF, RIF, I-VKF, S-VKF, CAR-EKF. Observations: Pseudorange (PR), Carrier Phase (CP), INS.

Application	Estimator	Observations	Reference
Performance Simulation	LMS, LTS, R, M, GM, S, MM	Simulated PR	Knight and Wang (2009)
Inland Waterborne	LMS, M, S, Ransac, CQKF	Measured PR, INS	Medina et al. (2016)
Inland Waterborne	S	Measured PR	Pozo-Pérez et al. (2017)
Urban Vehicular	M, LTS	Measured PR	Gaglione et al. (2017)
Urban Vehicular	MM	Simulated/Measured PR	Akram et al. (2018)
Performance Simulation	EKF+M	Simulated PR, INS	Crespillo et al. (2018)
Performance Simulation	M, S, MM	Simulated PR	Medina et al. (2019)
Performance Simulation	VB-KF	Simulated PR, CP	Li et al. (2019)
Urban Vehicular	M	Measured PR	Crespillo et al. (2020)
Inland Waterborne	GM-KF, RIF, I-VKF, S-VKF	Simulated/Measured PR, CP	Medina et al. (2021)
Performance Simulation	GS, M, LTS, MLTS, PTV	Simulated PR	Wendel (2022)
Urban Vehicular	EKF+M, CAR-EKF	Measured PR	Ding et al. (2023)
Urban Vehicular	EKF+M	Simulated/Measured PR, CP	Wang et al. (2023)

positioning as described by Li et al. (2019). The influence of heavy-tailed measurement distributions on position distortion can be reduced, as demonstrated by Medina et al. (2021).

The simulation results are highly promising for robust GNSS positioning. Consequently, research is ongoing to apply robust estimation theory to real measurements in GNSS-challenged environments. Many studies have demonstrated that the application of robust estimation techniques to pseudorange-based GNSS positioning can enhance the accuracy in both inland waterborne scenarios (Medina et al., 2016; Pozo-Pérez et al., 2017) and urban vehicular applications (Gaglione et al., 2017; Akram et al., 2018; Crespillo et al., 2020; Ding et al., 2023). Conversely, there is a paucity of analyses for evaluating the performance of robust carrier phase-based GNSS positioning techniques using real measurements in challenging environments. In a recent study, Medina et al. (2021) extended the investigation of robust filtering techniques for RTK positioning. The performance of four algorithms, namely Generalized M-estimator Kalman Filter (GM-KF), Robust Information Filter (RIF), Independent indicator Variational Bayesian Kalman Filter (I-VKF), and Scalar Variational Bayesian Kalman Filter (S-VKF), has been evaluated in a challenging waterborne scenario. Robust filtering techniques are capable of effectively mitigating the majority of significant positioning errors. Wang et al. (2023) have demonstrated that the integration of an EKF with M-estimation theory can significantly enhance the ambiguity fixing ratio for RTK positioning in an urban vehicular context.

The common limitation of the aforementioned algorithms is that the effectiveness of these robust estimation theories is only guaranteed until the respective breakdown point is reached (see

Sec. 2.5). In the event that the number of measurement errors exceeds the number of available nominal observations, it becomes impossible to compute an optimal solution. Consequently, the following sections of this thesis present a method that ensures a near-optimal GNSS positioning solution in harsh propagation conditions, where the breakdown point is exceeded.

2.7 Performance Parameters

The performance of a navigation system is evaluated by several statistical parameters, with variations in their definitions based on the specific application and type of navigation system used. Typically, these parameters are not individually specified, but are correlated to each other. In European Comission (2003), the relationship of the typical performance parameters *accuracy*, *integrity*, *continuity* and *availability* are illustrated by depicting a pyramid, where accuracy serves as the basis (see Fig. 2.13). Integrity, continuity and availability are – in this ordering – solely a function of accuracy. The definitions of the performance parameters are given in the following subsections and are based on the standard textbooks Hofmann-Wellenhof et al. (2008), Farnworth (2017) and Pullen and Joerger (2021).

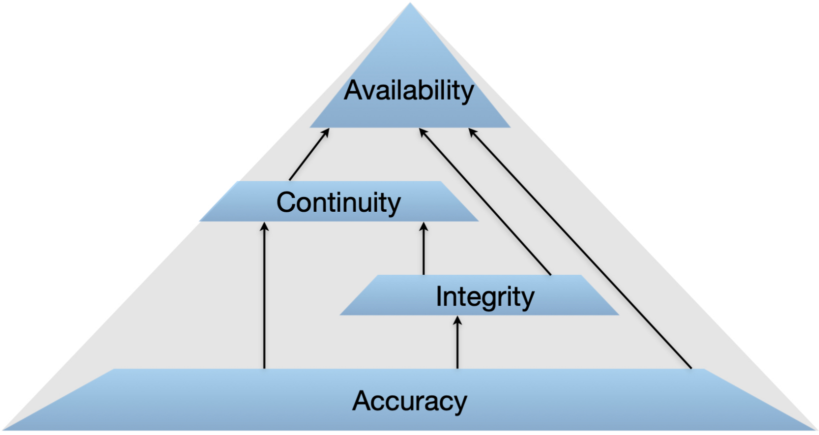

Figure 2.13: Hierarchy of GNSS performance parameters.

2.7.1 Accuracy

Accuracy refers to the systems ability to provide reliable and precise location information and is a quantitative measure of the error, that will be experienced by a user with a certain probability, between the estimated state (e.g., position and/or velocity) and the true value. In real-time applications, true state values are typically unknown, however, the accuracy of an operation can be evaluated under controlled conditions or in post-processing. In literature, it is further distinguished between the above described (absolute) accuracy and the repeatable accuracy – also called precision – which does not account for the true position but evaluates the scattering around a mean value. A typical mathematical measure of the accuracy is the Root Mean Square (RMS) which is defined as

$$\mathrm{RMS} = \sqrt{\frac{1}{n}\sum_{i=1}^{n} x_i^2}. \tag{2.83}$$

The scattering is typically described by the empirical Standard Deviation (STD)

$$\mathrm{STD} = \sqrt{\frac{1}{n-1}\sum_{i=1}^{n}(\bar{x}-x_i)^2}. \tag{2.84}$$

Both measures are computed from a finite number of n data points x_i with $i = \{1, 2, \dots, n\} \in \mathbb{N}$ and their corresponding mean value $\bar{x}$.

2.7.2 Integrity

Integrity is an important measure that determines the trustworthiness of a navigation system under a defined integrity risk. Integrity further describes the ability to provide timely warnings to a user when the navigation system is unavailable. Integrity risk is the probability of providing incorrect information without warning the user within a time period. In practice, it is the probability of a large error being undetected which – in safety-critical applications – could cause collision or accidents. Therefore, the integrity risk is required to be very low with a probability of typically less than 10^{-5} per operation. In order to evaluate the integrity of a particular application, the Alert Limit (AL), which is the boundary of unsafe errors, has to be defined based on the respective specifications. In addition, the Protection Level (PL) is computed by the user, which is defined as the error bound and typically represented as Vertical Protection Level (VPL) and Horizontal Protection Level (HPL). The integrity methods applied in GNSS are evolving, and several protection level computations have been defined (Zhu et al., 2018; Zabalegui et al., 2020). In this thesis, the method from ICAO (2006) is implemented, as it is a rather simple method suitable for comparing different positioning estimation strategies. The computation is straightforward when a zero-mean Gaussian fault-free error distribution is assumed and the equations are formulated as

$$\mathrm{VPL} = \kappa_{\mathrm{VPL}}\sigma_0\sqrt{q_{uu}}, \tag{2.85}$$

$$\mathrm{HPL} = \kappa_{\mathrm{HPL}}\sigma_0\sqrt{\frac{q_{nn}+q_{ee}}{2}+\sqrt{\left(\frac{q_{nn}-q_{ee}}{2}\right)^2+q_{ne}^2}} = \kappa_{\mathrm{HPL}}\sigma_0\sqrt{\lambda_{max}}, \tag{2.86}$$

where λ_{max} is the maximum eigenvalue of the covariance sub-matrix of horizontal positions, q_{nn}, q_{ee}, q_{uu} and q_{ne} are elements of the rotated covariance matrix of the estimated parameters in the local frame

$$\mathbf{Q}_x = \mathbf{R}\mathbf{Q}_X\mathbf{R}^T = \begin{bmatrix} q_{nn} & q_{ne} & q_{nu} \\ q_{en} & q_{ee} & q_{eu} \\ q_{nu} & q_{eu} & q_{uu} \end{bmatrix} \tag{2.87}$$

and $\mathbf{R}$ is the rotation matrix from the global to the local coordinate system. The a priori variance factor σ_0 and κ factors scale the PL, which is the position domain variance, to a level compatible with the integrity requirement of the particular application.

According to the International Civil Aviation Organization (ICAO) (ICAO, 2006) and Reid et al. (2019, 2023), the κ factors can be computed using the inverse complementary error function. Its relation with respect to the normal inverse cumulative distribution function is defined as

$$\mathrm{norminv}(1-p) = -\sqrt{2}\ \mathrm{erfcinv}\left(2\left(1-p\right)\right), \tag{2.88}$$

where p is the probability of failure. The κ factor for the horizontal case is correspondingly computed using the Rayleigh distribution. An overview of κ factor values for different probability of failures is given in Fig. 2.14 and significant values are summarized in Tab. 2.6.

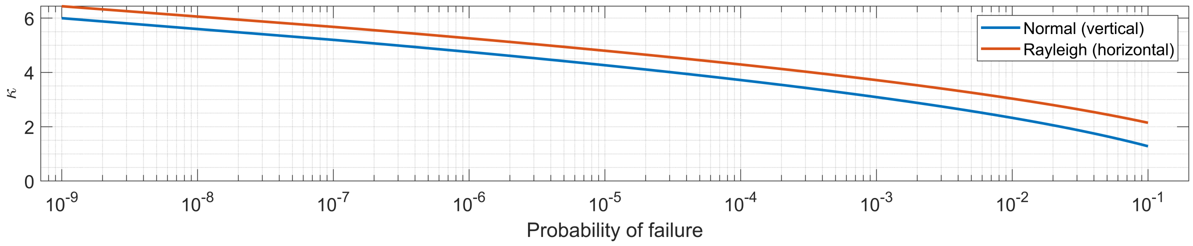

Figure 2.14: Values for the κ factor using the Rayleigh and normal distribution for the horizontal and vertical case with respect to different probability requirements.

Table 2.6: Overview of κ factors for different probabilities and the Rayleigh and normal distribution.

Probability / Distribution	10^{-3}	10^{-4}	10^{-5}	10^{-6}	10^{-7}	$0.5 \cdot 10^{-8}$
Rayleigh (horizontal)	3.72	4.29	4.80	5.26	5.68	6.18
Normal (vertical)	3.09	3.72	4.26	4.75	5.20	5.73

The relation between Position Error (PE), PL and AL is depicted in Fig. 2.15 with six different conditions depending on the magnitude of the respective parameters and whether the PE is bounded by the PL. The definition of the conditions is given in Tab. 2.7. The figure, where the PE is plotted versus the PL is commonly denoted as Stanford diagram (Toissant et al., 2006). In an optimal case, the PE is bounded by the PL and both values are below the AL chosen for the particular application, which means the system is in Nominal Operation (NO) mode. The system is unavailable if the protection levels are too conservative, hence, the condition PE $<$ PL holds true but the AL is exceeded. In this condition, safety can still be maintained if an alert is transmitted to the user indicating that the system is no longer safe to use within a specified Time to Alert (TTA). The most critical condition, which should be avoided in any case, is Hazardous Misleading Information (HMI), where the system thinks it is safe to use (PL $<$ AL) but in fact it is not (PE $>$ AL) and hence, the user is unable to be warned.

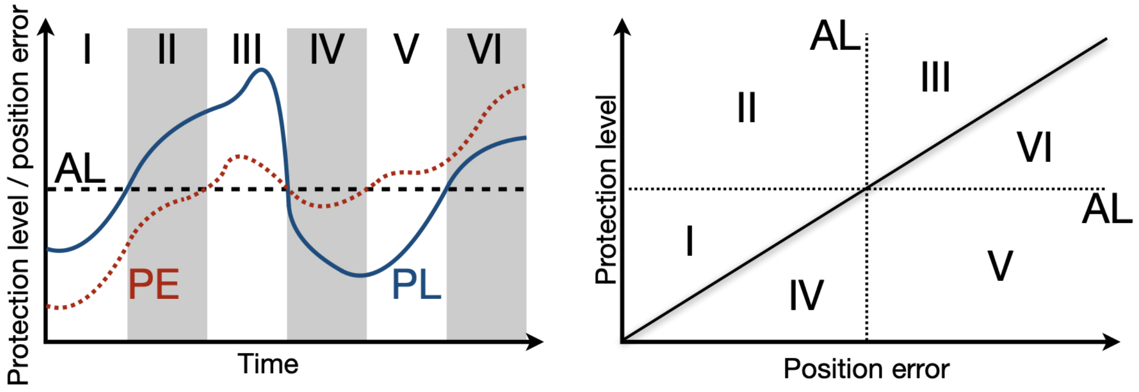

Figure 2.15: Relation between position error (PE), protection level (PL) and alert limit (AL). Adapted from Hofmann-Wellenhof et al. (2008).

2.7.3 Availability and Continuity

Availability serves as an indicator of the system's capability to provide functional service, i.e. required levels of accuracy, integrity and continuity are met within a specified coverage area. The availability itself can be measured by the percentage of time during which the system is available for the intended operation. A particular value of requirement in terms of availability

Table 2.7: Stanford diagram conditions.

I	PE < PL < AL	nominal operation
II	PE < AL < PL	system unavailable (too conservative)
III	AL < PE < PL	system unavailable
IV	PL < PE < AL	misleading information (too optimistic)
V	PL < AL < PE	hazardous misleading information
VI	AL < PL < PE	system unavailable and misleading information

needs to be selected for a specific operation depending on various factors described in ICAO (2006).

Assuming that the system is available at the beginning of an intended operation, continuity describes the ability of the system to maintain the functional service without nonscheduled interruptions. It is furthermore defined as the probability that the specified accuracy and integrity requirements are continuously ensured over the time interval of the intended operation. Typically, the probability of continuity is defined by the so-called continuity risk, which should be balanced with the integrity risk requirement.

2.7.4 Performance Specifications for Intelligent Transportation Systems

The definitions of the above described GNSS performance parameter are mainly based on aviation applications and defined by the ICAO (ICAO, 2006). Since GNSS-based navigation is becoming of increasing interest also in ITS, these performance parameters have to be adapted and new specifications for road transportation applications need to be defined. Currently, there are no standardized or generally-accepted specifications for ITS (Du et al., 2021). However, the European Cooperation in Science and Technology (COST) action Satellite Positioning Performance Assessment for Road Transport (SaPPART) was launched working towards standardized road scenarios. In an accepted European norm (EN 16803-1), the methodology and guidelines for the terminal performance assessment are provided. A quantitative overview of the performance requirements for road applications is given in Tab. 2.8 with impact scoring H (high), M (medium) and L (low) based on European GNSS Agency (2015) and Stern and Kos (2018).

In EN 16803-1, the performance metrics for accuracy and integrity are characterized by Cumulative Distribution Function (CDF) percentiles (50th, 75th and 95th) since the distribution of positioning errors – especially in challenging urban environments – suffer from heavy tails (Stern and Kos, 2018). That is why taking just one value, e.g. the mean RMS error, is not

Table 2.8: Quantitative evaluation of performance requirements for road applications.

Road applications	Accuracy	Availability	Integrity	Continuity
Autonomous driving	H	M	H	H
Advanced navigation	M/H	M	H	H
Fleet management	L/M	H	H	L/M
Road charging	L/M	H	H	L
Insurance telematics	L	M	H	L/M
eCall services	M	H	M	L
Road navigation	M	H	M	L
Vehicle tracking	L	M	M/H	L

robust enough. Since requirements are highly dependent on the respective application type, e.g. Advanced Driver Assistance Systems (ADAS), collision avoidance, and different levels of autonomous driving, detailed specifications for various ITS applications are mandatory (Zhu et al., 2018). The accuracy classification boundaries of different ITS applications – also standardized in EN 16803-1 (Stern and Kos, 2018) – are summarized in Tab. 2.9.

In Reid et al. (2019) and Reid et al. (2023), preliminary statements of localization requirements are derived – especially considering specifications for autonomously driving vehicles and different levels of autonomy. The three different levels of autonomy are defined as road determination, lane determination (if there are at least two lanes) and lane keeping, which requires the highest accuracy. Requirement specifications are derived based on the geometry dimensions of U.S. freeways and local roads and divided into lateral, longitudinal and vertical components. The latter are summarized in Tab. 2.10 for a given probability of failure of $10^{-6}/h$. U.S. local roads are assumed to have a minimum lane width of 3 m with a minimum curvature of 20 m or a minimum lane width of 3.3 m with a minimum curvature of 10 m. The derivation of the localization alert limits is based on a bounding box selection, which is a function of the road geometry, the vehicles dimensions and the desired level of autonomy. The bounding box geometry for the three levels of autonomy are shown in Fig. 2.16. Whereas

Table 2.9: Accuracy classification boundaries from the application perspective.

Application type	P = 50th percentile	P = 75th percentile	P = 95th percentile
In-lane	$P \leq 0.1$ m	$P \leq 0.15$ m	$P \leq 0.25$ m
Lane	$0.1 \text{ m} < P \leq 0.4$ m	$0.15 \text{ m} < P \leq 0.6$ m	$0.25 \text{ m} < P \leq 1.0$ m
Carriageway	$0.4 \text{ m} < P \leq 4.0$ m	$0.6 \text{ m} < P \leq 6.0$ m	$1.0 \text{ m} < P \leq 10.0$ m
Area	$4.0 \text{ m} < P \leq 40$ m	$6.0 \text{ m} < P \leq 60$ m	$10.0 \text{ m} < P \leq 100$ m
No specific	$P > 40$ m	$P > 60$ m	$P > 100$ m

Table 2.10: Combined localization and map error budget for U.S. local roads with probability of failure $10^{-6}/h$.

	Accuracy (95 %)			Alert limit		
	Lat. [m]	Long. [m]	Vert. [m]	Lat. [m]	Long. [m]	Vert. [m]
Road determination (two lanes)	1.09	1.24	0.56	2.73	3.10	1.40
Lane determination	0.50	1.26	0.56	1.26	3.15	1.40
Lane keeping	0.12	0.12	0.56	0.29	0.29	1.40

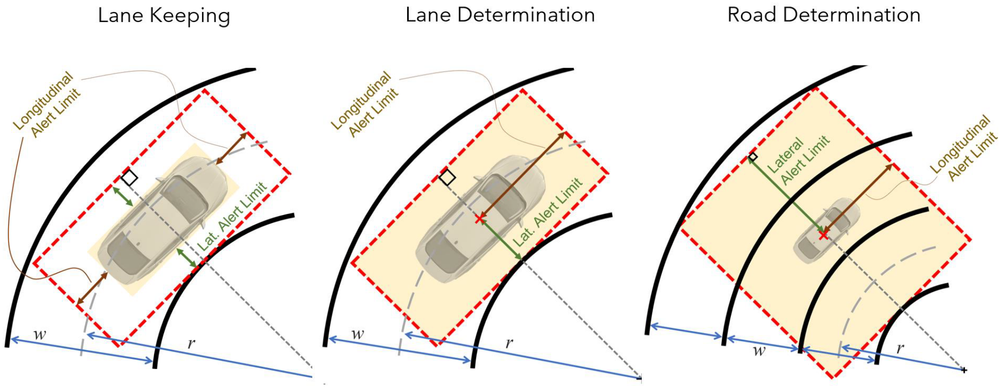

Figure 2.16: Comparison of bounding box geometry for different levels of autonomy: lane keeping, lane determination and road determination. Source: Reid et al. (2023).

other shapes have the characteristics of relaxing the alert limits (Feng et al., 2018; Kigotho and Rife, 2021), the bounding box has a more conservative nature. The location requirement specifications for U.S. local roads when further taking the vehicle dimension into account and using $10^{-8}/h$ as probability of failure are summarized in Tab. 2.11. The desired level of autonomy for these specifications is lane keeping. The differences in comparison to Tab. 2.8 can come from the difference in the derivation, the additional consideration of the vehicle dimension and the fact that Tab. 2.11 is representing the allowable bounds from the combined position, attitude and map errors of the collective system. However, the general order of magnitude is similar when taking into account that Tab. 2.8 describes the 2D horizontal accuracy classification boundaries.

Table 2.11: Localization requirements for U.S. local roads for different vehicle sizes and lane keeping application with probability of failure $10^{-8}/h$. The dimensions of the vehicle type can be found in Reid et al. (2019).

Vehicle type	Accuracy (95 %)			Alert limit		
	Lat. [m]	Long. [m]	Vert. [m]	Lat. [m]	Long. [m]	Vert. [m]
Mid-Size	0.15	0.15	0.48	0.44	0.44	1.40
Full-Size	0.13	0.13	0.48	0.38	0.38	1.40
Standard Pickup	0.12	0.12	0.48	0.34	0.34	1.40
Passenger Vehicle	0.10	0.10	0.48	0.29	0.29	1.40

3

An Extended Kalman Filter Framework for Urban Navigation

This chapter outlines the mathematical foundations of an EKF framework for estimating position and velocity using GNSS pseudorange and carrier phase measurements. It includes a detailed description of the functional and stochastic models, the corresponding Kalman filter equations for measurement and time updates, and the equations for state estimation. Additionally, the chapter describes integrated algorithms within the framework for outlier detection and the detection and exclusion of erroneous observations using 3D building models, alongside the entire computational procedure. The framework was independently developed, though it is based on state of the art methods. This algorithm serves as the basis for developing innovative methods in chapter 4 to improve accuracy and integrity, and for comparing the performance of the developed techniques in chapter 5.

3.1 State Estimation

A multi-GNSS, multi-frequency RTK positioning algorithm has been developed in an EKF to evaluate the positioning performance in terms of availability, accuracy, and integrity in urban environments. Although RTK positioning is real-time capable, the evaluation of collected raw-data will be conducted in post-processing. Using an EKF, the state vector $\mathbf{x}$ can be estimated with DD carrier phase, DD pseudorange, and DD Doppler measurements. Forming DD observation equations eliminates the receiver and satellite clock biases. For short distances between the rover and the reference station, atmospheric errors are assumed to be negligible. Thus, the DD observation equations (see Sec. 2.1.2) can be written as follows:

$$\Phi_{rb}^{ij} = \varrho_{rb}^{ij} + \lambda N_{rb}^{ij} + \epsilon_{rb,\Phi}^{ij}, \tag{3.1}$$

$$\rho_{rb}^{ij} = \varrho_{rb}^{ij} + \epsilon_{rb,\rho}^{ij}, \tag{3.2}$$

$$\dot{\rho}_{rb}^{ij} = \dot{\varrho}_{rb}^{ij} + \epsilon_{rb,\dot{\rho}}^{ij}, \tag{3.3}$$

consisting of the rover (r) and base station (b), rover (i) and reference satellite (j), the projection of the baseline vector onto the LOS ϱ_{rb}^{ij}, carrier phase wavelength (λ) and ambiguity (N_{rb}^{ij}) and the respective carrier phase ($\epsilon_{rb,\Phi}^{ij}$), pseudorange ($\epsilon_{rb,\rho}^{ij}$), and Doppler noise ($\epsilon_{rb,\dot{\rho}}^{ij}$). In order to obtain DD observations, the satellite-to-satellite SD computation is performed by selecting a reference satellite with maximum elevation angle in each epoch. The SD computation for different GNSS is independent, so no combination of measurements is formed between e.g., GPS and Galileo, even if they have the same carrier frequency.

The following equations and matrix definitions are based on a multi-GNSS, single-frequency solution for the sake of clarity. In order to extend the model to the multi-frequency solution, additional measurements per frequency are attached as sub-vectors to the observation vector and the covariance and measurement matrices are extended into block-diagonal structures using sub-matrices per frequency.

The state vector $\mathbf{x}$ consists of the rover coordinates and velocities represented in the 3D Cartesian coordinate system (ECEF) and the SD carrier phase float ambiguities of all GNSS:

$$\mathbf{x} = \left[x_r, y_r, z_r, v_{x_r}, v_{y_r}, v_{z_r}, \mathbf{N}_{rb}^G, \mathbf{N}_{rb}^R, \mathbf{N}_{rb}^E, \mathbf{N}_{rb}^C\right]^T , \tag{3.4}$$

where $\mathbf{N}_{rb}^G, \mathbf{N}_{rb}^R, \mathbf{N}_{rb}^E, \mathbf{N}_{rb}^C$ denote the SD float ambiguity vector of the respective GNSS. Assuming m available GPS satellites, the SD float ambiguity vector can be defined as

$$\mathbf{N}_{rb}^G = \left[N_{1,rb}^G, N_{2,rb}^G, \cdots, N_{m,rb}^G\right]^T . \tag{3.5}$$

The use of SD float ambiguities as state estimates instead of DD float ambiguities avoids the hand-over handling of reference satellites (Takasu and Yasuda, 2010).

Measurement Update of EKF

The measurement vector at time k consists of DD carrier phase, pseudorange, and Doppler observation vectors:

$$\mathbf{l}_k = \left[\boldsymbol{\Phi}_{rb}^G, \boldsymbol{\Phi}_{rb}^R, \boldsymbol{\Phi}_{rb}^E, \boldsymbol{\Phi}_{rb}^C, \boldsymbol{\rho}_{rb}^G, \boldsymbol{\rho}_{rb}^R, \boldsymbol{\rho}_{rb}^E, \boldsymbol{\rho}_{rb}^C, \dot{\boldsymbol{\rho}}_{rb}^G, \dot{\boldsymbol{\rho}}_{rb}^R, \dot{\boldsymbol{\rho}}_{rb}^E, \dot{\boldsymbol{\rho}}_{rb}^C\right]^T . \tag{3.6}$$

Assuming m available GPS satellites, the GPS observation vectors can be defined as

$$\boldsymbol{\Phi}_{rb}^G = \left[\Phi_{rb}^{i1}, \Phi_{rb}^{i2}, \ldots, \Phi_{rb}^{im}\right]^T , \tag{3.7}$$

$$\boldsymbol{\rho}_{rb}^G = \left[\rho_{rb}^{i1}, \rho_{rb}^{i2}, \ldots, \rho_{rb}^{im}\right]^T , \tag{3.8}$$

$$\dot{\boldsymbol{\rho}}_{rb}^G = \left[\dot{\rho}_{rb}^{i1}, \dot{\rho}_{rb}^{i2}, \ldots, \dot{\rho}_{rb}^{im}\right]^T . \tag{3.9}$$

The observation model, which maps the true state space into the observed space, is obtained by linearizing the mathematical relation between observations and parameters of the state vector around the latest state estimates:

$$\mathbf{H}_k = \begin{bmatrix} \mathbf{A}_k^G & 0 & \lambda^G \mathbf{D}_k^G & & & \\ \mathbf{A}_k^R & 0 & & \lambda^R \mathbf{D}_k^R & & \\ \mathbf{A}_k^E & 0 & & & \lambda^E \mathbf{D}_k^E & \\ \mathbf{A}_k^C & 0 & & & & \lambda^C \mathbf{D}_k^C \\ \mathbf{A}_k^G & 0 & 0 & & & \\ \mathbf{A}_k^R & 0 & & 0 & & \\ \mathbf{A}_k^E & 0 & & & 0 & \\ \mathbf{A}_k^C & 0 & & & & 0 \\ 0 & \mathbf{A}_k^G & 0 & & & \\ 0 & \mathbf{A}_k^R & & 0 & & \\ 0 & \mathbf{A}_k^E & & & 0 & \\ 0 & \mathbf{A}_k^C & & & & 0 \end{bmatrix} , \tag{3.10}$$

where $\mathbf{A}$ represents the geometry part and $\mathbf{D}$ the one of the SD ambiguities.
Assuming m available GPS satellites, the partial derivatives w.r.t. the rover position – which

is the difference of the LOS vectors from the rover position r at time k to the satellites 1 to m and reference satellite i – read

$$\mathbf{A}_k^G = \begin{bmatrix} \frac{x^1-x_r}{\rho_r^1} - \frac{x^i-x_r}{\rho_r^i} & \frac{y^1-y_r}{\rho_r^1} - \frac{y^i-y_r}{\rho_r^i} & \frac{z^1-z_r}{\rho_r^1} - \frac{z^i-z_r}{\rho_r^i} \\ \frac{x^2-x_r}{\rho_r^2} - \frac{x^i-x_r}{\rho_r^i} & \frac{y^2-y_r}{\rho_r^2} - \frac{y^i-y_r}{\rho_r^i} & \frac{z^2-z_r}{\rho_r^2} - \frac{z^i-z_r}{\rho_r^i} \\ \vdots & \vdots & \vdots \\ \frac{x^m-x_r}{\rho_r^m} - \frac{x^i-x_r}{\rho_r^i} & \frac{y^m-y_r}{\rho_r^m} - \frac{y^i-y_r}{\rho_r^i} & \frac{z^m-z_r}{\rho_r^m} - \frac{z^i-z_r}{\rho_r^i} \end{bmatrix}, \tag{3.11}$$

and the partial derivatives w.r.t. the SD float ambiguity consists of the respective wavelength of the used signal λ^G and the DD matrix $\mathbf{D}_k^G$ which transforms the SD model into the DD model at epoch k:

$$\mathbf{D}_k^G = \begin{bmatrix} 1 & & & -1 & & & \\ & 1 & & -1 & & & \\ & & \dots & \vdots & \dots & & \\ & & & -1 & & 1 & \\ & & & -1 & & & 1 \end{bmatrix}_{(m-1)\times m} \tag{3.12}$$

The column containing -1 indicates the column of the epoch-wise chosen reference satellite. This DD matrix is also used to transform the stochastic model of SD into the covariance matrix of DD measurements which includes the mathematical correlations between measurements of one GNSS:

$$\mathbf{Q}_{l_\Phi,k} = \begin{bmatrix} \mathbf{D}_k^G \mathbf{R}_\Phi^G \mathbf{D}_k^{G^T} & & & \\ & \mathbf{D}_k^R \mathbf{R}_\Phi^R \mathbf{D}_k^{R^T} & & \\ & & \mathbf{D}_k^E \mathbf{R}_\Phi^E \mathbf{D}_k^{E^T} & \\ & & & \mathbf{D}_k^C \mathbf{R}_\Phi^C \mathbf{D}_k^{C^T} \end{bmatrix} \tag{3.13}$$

$$\mathbf{Q}_{l_\rho,k} = \begin{bmatrix} \mathbf{D}_k^G \mathbf{R}_\rho^G \mathbf{D}_k^{G^T} & & & \\ & \mathbf{D}_k^R \mathbf{R}_\rho^R \mathbf{D}_k^{R^T} & & \\ & & \mathbf{D}_k^E \mathbf{R}_\rho^E \mathbf{D}_k^{E^T} & \\ & & & \mathbf{D}_k^C \mathbf{R}_\rho^C \mathbf{D}_k^{C^T} \end{bmatrix} \tag{3.14}$$

$$\mathbf{Q}_{l_{\dot\rho},k} = \begin{bmatrix} \mathbf{D}_k^G \mathbf{R}_{\dot\rho}^G \mathbf{D}_k^{G^T} & & & \\ & \mathbf{D}_k^R \mathbf{R}_{\dot\rho}^R \mathbf{D}_k^{R^T} & & \\ & & \mathbf{D}_k^E \mathbf{R}_{\dot\rho}^E \mathbf{D}_k^{E^T} & \\ & & & \mathbf{D}_k^C \mathbf{R}_{\dot\rho}^C \mathbf{D}_k^{C^T} \end{bmatrix} \tag{3.15}$$

$$\mathbf{Q}_{l,k} = \begin{bmatrix} \mathbf{Q}_{l_\Phi,k} & 0 & 0 \\ 0 & \mathbf{Q}_{l_\rho,k} & 0 \\ 0 & 0 & \mathbf{Q}_{l_{\dot\rho},k} \end{bmatrix} \tag{3.16}$$

The measurement noise matrices $\mathbf{R}_\Phi$, $\mathbf{R}_\rho$ and $\mathbf{R}_{\dot\rho}$ are diagonal matrices containing the weighted variances of the SD carrier phase, pseudorange and Doppler measurements of the different GNSS, respectively. Assuming m available GPS satellites, the GPS measurement noise matrices are expressed as

$$\mathbf{R}_\Phi^G = 2\sigma^2_{\Phi_0^G} \cdot \mathrm{diag}\left(w_1^{-1}, w_2^{-1}, \dots, w_m^{-1}\right), \tag{3.17}$$

$$\mathbf{R}_\rho^G = 2\sigma^2_{\rho_0^G} \cdot \mathrm{diag}\left(w_1^{-1}, w_2^{-1}, \dots, w_m^{-1}\right), \tag{3.18}$$

$$\mathbf{R}_{\dot\rho}^G = 2\sigma^2_{\dot\rho_0^G} \cdot \mathrm{diag}\left(w_1^{-1}, w_2^{-1}, \dots, w_m^{-1}\right), \tag{3.19}$$

where $\sigma^2_{\Phi^G_0}$, $\sigma^2_{\rho^G_0}$ and $\sigma^2_{\dot{\rho}^G_0}$ are the a priori variances of the GPS carrier phase, pseudorange and Doppler measurement noise and w_m is the respective weight of each satellite depending on the chosen weighting model.

Time Update of EKF

In the time update step of the EKF, the state estimates of the current epoch are propagated to the next epoch using the state transition matrix $\mathbf{F}_{k,k+1}$ using a constant velocity motion model and the process noise covariance matrix $\mathbf{Q}_{k,k+1}$:

$$\mathbf{F}_{k,k+1} = \begin{bmatrix} 1 & \Delta t & 0 \\ 0 & 1 & 0 \\ 0 & 0 & 1 \end{bmatrix}, \tag{3.20}$$

$$\mathbf{Q}_{k,k+1} = \begin{bmatrix} \operatorname{diag}\left(q_{\text{pos}}\Delta t + \frac{1}{3}\Delta t^3 q_{\text{vel}}\right) & \operatorname{diag}\left(\frac{1}{2}\Delta t^2 q_{\text{vel}}\right) & 0 \\ \operatorname{diag}\left(\frac{1}{2}\Delta t^2 q_{\text{vel}}\right) & \operatorname{diag}\left(q_{\text{vel}}\Delta t\right) & 0 \\ 0 & 0 & \operatorname{diag}\left(q_{\text{amb}}\Delta t\right) \end{bmatrix}, \tag{3.21}$$

where q_{pos} and q_{amb} are the spectral noise densities of the rover position, velocity and ambiguities and Δt is the time interval. The rover position and velocity is typically modelled as random walk process while the rover ambiguities are modelled as random constants.

EKF Formulation

The Kalman gain matrix, the estimated unknown state vector and its covariance matrix at time k reads

$$\mathbf{K}_k = \mathbf{Q}^-_{x,k}\mathbf{H}^T_k\left(\mathbf{H}_k\mathbf{Q}^-_{x,k}\mathbf{H}^T_k + \mathbf{Q}_{l,k}\right)^{-1}, \tag{3.22}$$

$$\mathbf{Q}^+_{x,k} = \left(\mathbf{I} - \mathbf{K}_k\mathbf{H}_k\right)\mathbf{Q}^-_{x,k}\left(\mathbf{I} - \mathbf{K}_k\mathbf{H}_k\right)^T + \mathbf{K}_k\mathbf{Q}_{l,k}\mathbf{K}^T_k, \tag{3.23}$$

$$\mathbf{x}^+_k = \mathbf{x}^-_k + \mathbf{K}_k\left(\mathbf{l}_k - \mathbf{H}_k \cdot \mathbf{x}^-_k\right). \tag{3.24}$$

Finally, the linear time update of the state vector and its covariance matrix is expressed as:

$$\mathbf{x}^-_{k+1} = \mathbf{F}_{k,k+1} \cdot \mathbf{x}^+_k, \tag{3.25}$$

$$\mathbf{Q}^-_{x,k+1} = \mathbf{F}_{k,k+1}\mathbf{Q}^+_{x,k}\mathbf{F}^T_{k,k+1} + \mathbf{Q}_{k,k+1}. \tag{3.26}$$

In Eq. 3.22 to Eq. 3.26, $(\cdot)^-$ and $(\cdot)^+$ indicate the specific vectors and matrices before and after the measurement update of the EKF, respectively.

3.2 Outlier Detection

The global detection and local identification technique (Teunissen, 1990) is implemented as a quality control of the filter solution. Therefore, the predicted residuals or innovations and their covariance matrix are computed:

$$\mathbf{d}_k = \mathbf{l}_k - \mathbf{H}_k\mathbf{x}^-_k, \qquad \mathbf{Q}_{d,k} = \mathbf{Q}_{l,k} + \mathbf{H}_k\mathbf{Q}^-_{x,k}\mathbf{H}^T_k. \tag{3.27}$$

The predicted residuals are assumed to be Gaussian distributed with zero mean and known covariance matrix forming the null hypothesis H_0 and alternative hypothesis H_a

$$H_0: \ \mathbf{d}_k \sim \mathcal{N}\left(\mathbf{0}, \mathbf{Q}_{d,k}\right), \qquad H_a: \ \mathbf{d}_k \sim \mathcal{N}\left(\nabla\mathbf{d}_k, \mathbf{Q}_{d,k}\right). \tag{3.28}$$

Based on the predicted residuals $\mathbf{d}_k$ and its covariance matrix $\mathbf{Q}_{d,k}$, it is tested whether the measurements are consistent with the system model. The test statistic T_k for detecting unspecified model errors in the null hypothesis H_0 with the degrees of freedom ζ reads

$$T_k = \frac{\mathbf{d}_k^T \mathbf{Q}_{d,k}^{-1} \mathbf{d}_k}{\zeta}. \tag{3.29}$$

The global detection is performed using the Fisher distribution $\mathcal{F}$ and a certain significance level α_G, The global test is failed if

$$T_k \geq \mathcal{F}_{\zeta,\infty,1-\alpha_G}. \tag{3.30}$$

If a local model error is present at time k, the global detection is followed by the identification of the most likely alternative hypothesis. The local slippage test statistic is

$$t_k = \frac{\mathbf{c}_k^T \mathbf{Q}_{d,k}^{-1} \mathbf{d}_k}{\sqrt{\mathbf{c}_k^T \mathbf{Q}_{d,k}^{-1} \mathbf{c}_k}} \tag{3.31}$$

where the test statistic t_k is computed ζ-times. The vector $\mathbf{c}_k$ has the form $[0,\ldots,0,1,0,\ldots,0]^T$ with the 1 corresponding to the suspect measurement. After computing the test statistic for each of the measurements, the likelihood of the most likely model error can be tested by comparing it with the critical value of the corresponding normal distribution $\mathcal{N}$. If

$$|t_k| \geq \mathcal{N}_{1-\alpha_L/2}, \tag{3.32}$$

then a significant error occurred and is successfully identified. The identified model error is removed from the measurement model and an updated filter solution is computed resulting in an updated predicted residual vector. This updated predicted residual vector is then used for the detection of possible remaining model errors and the procedure is repeated until all detected model errors are removed. The type I error probability of the local identification α_L and the probability of the global detection α_G are adjusted based on a fixed non-centrality parameter (Caspary, 2000).

3.3 3D-Mapping-Aided Fault Detection and Exclusion

The main error source for GNSS positioning in urban environment is the reception of reflected or blocked signals (see Fig. 3.1(a)). NLOS reception causes delays of up to several hundreds of meters, depending on the local environment (McGraw et al., 2021). Therefore, the exclusion of NLOS signals – the so-called 3D-Mapping-Aided Fault Detection and Exclusion (3DMA-FDE) – is a powerful method to mitigate large errors in urban GNSS positioning applications. The 3DMA-FDE approach is integrated into the developed RTK positioning algorithm based on epoch-wise ray tracing computation (see Fig. 3.1(b)) as described in Sec. 2.6.1. Required information are GNSS satellite positions, 3D building model data provided by the city of Hannover and the user location. In this thesis, the user location is available from pre-processed reference solutions leading to optimal ray tracing results. However, in real world scenarios, the user location input can be taken from either an a priori estimation or pre-defined routing information. By combining the available information, satellites are classified as LOS, multipath, NLOS and blocked. In this way, all NLOS and blocked satellites are identified and provided in a satellite exclusion list which is applied to the measurement processing step and consequently faulty satellites are excluded from the positioning solution.

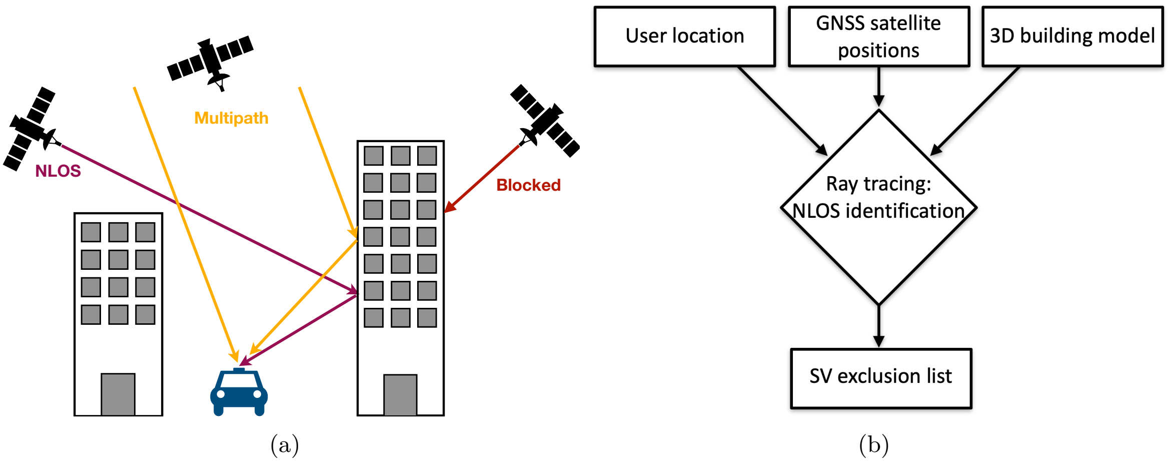

(a) (b)

Figure 3.1: Erroneous signal reception in urban areas (a) and its mitigation in positioning algorithms (b).

3.4 Computation Procedure

The implementation of the proposed approach is shown in Fig. 3.2 and will be explained in the following. Multi-GNSS carrier phase, pseudorange, and Doppler measurements from four systems (GPS, GLONASS, Galileo, BDS) and multiple frequencies serve as input data for the measurement processing.

Measurement Processing

In the measurement processing step, an elevation mask is applied, DD measurements are calculated based on raw carrier phase, pseudorange, and Doppler observations and epoch-wise selected reference satellites and the weight matrix is set up accordingly. The rising of new satellites and the setting or loss of satellites due to blockages is handled.

Pre-processing and Matrices Set-up

In this step, the SD covariance matrix and SD ambiguities are updated based on the measurement processing step and information from the previous epoch. The ambiguities of new satellites are initialized using the SD Code-Minus-Carrier (CMC) combination. For rising satellites, the corresponding diagonal element in the covariance matrix should be initialized with a user-defined large value so that the imprecise initialization has no impact on the other estimated parameters.

State Estimation

Having the DD measurements, the weight matrix, updated SD covariance matrix, SD ambiguity approximations and user-defined process noise and measurement noise parameters, the EKF framework produces state estimates of the coordinates and estimated SD float ambiguities. The SD float ambiguities and their covariance matrix are transformed into DD float ambiguities and DD covariance matrix, respectively.

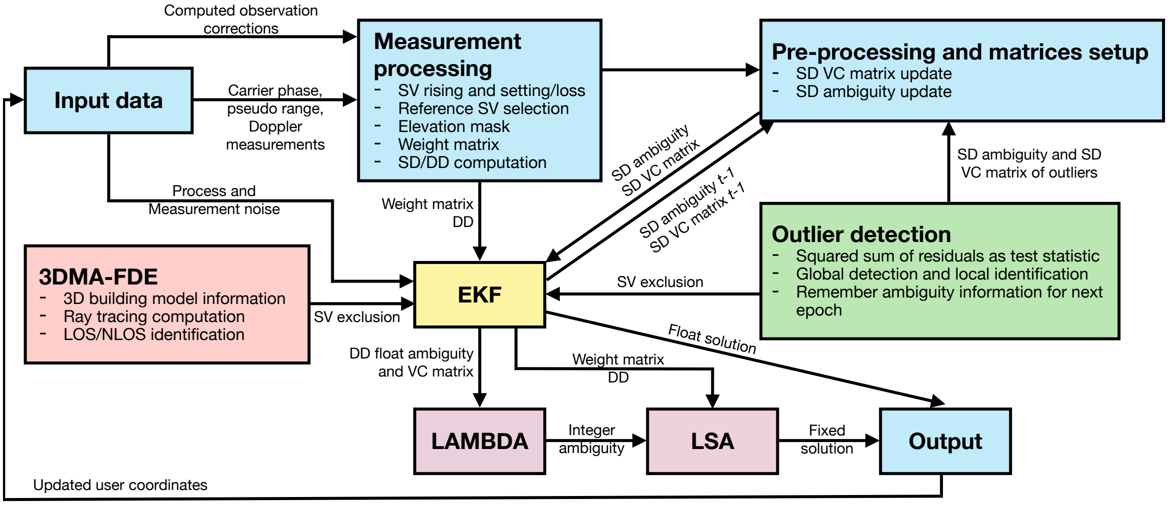
Computed observation corrections
Input data
Carrier phase, pseudo range, Doppler measurements
Measurement processing
- SV rising and setting/loss
- Reference SV selection
- Elevation mask
- Weight matrix
- SD/DD computation
Pre-processing and matrices setup
- SD VC matrix update
- SD ambiguity update
SD ambiguity SD VC matrix
SD ambiguity t-1 SD VC matrix t-1
SD ambiguity and SD VC matrix of outliers
Process and Measurement noise
Weight matrix DD
3DMA-FDE
- 3D building model information
- Ray tracing computation
- LOS/NLOS identification
SV exclusion
EKF
SV exclusion
Outlier detection
- Squared sum of residuals as test statistic
- Global detection and local identification
- Remember ambiguity information for next epoch
Float solution
DD float ambiguity and VC matrix
Weight matrix DD
LAMBDA
Integer ambiguity
LSA
Fixed solution
Output
Updated user coordinates

Figure 3.2: Flowchart of the developed EKF framework for GNSS RTK positioning.

Ambiguity Fixing

The DD float ambiguities and their covariance matrix serve as input parameters for the LAMBDA algorithm (Teunissen, 1995a). A common method to overcome the frequency-dependency of GLONASS signals is to keep GLONASS ambiguities as float values while fixing the ambiguities of all other systems (Ma et al., 2020). However, when using the same receiver types at both the rover and reference station, the inter-frequency bias remains constant (Wanninger, 2011). Although adding GLONASS data can deteriorate the ambiguity resolution performance in multi-GNSS solutions, the satellite geometry is strengthened and thus will improve the positioning performance (Brack et al., 2020). In this thesis, PAR is applied – which also can overcome the weakness of GLONASS ambiguity resolution (Teunissen, 2019) – in order to fix subsets of ambiguities if fixing the full set of ambiguities is not possible (Teunissen and Verhagen, 2009).

If the ambiguity fixing is successful, the rover position is updated by Eq. 2.43 or by performing a LSA using the vector of successfully fixed (or partially fixed and float) ambiguities. Consequently, the DD carrier phase observations are corrected by the estimated (integer) ambiguities $\breve{\mathbf{N}}$ resulting in the shortened observation vector $\Delta\breve{\mathbf{l}}$. Additionally, the number of parameters in the normal equation system is reduced to three, since only the three-dimensional rover position is estimated. In the following equations the time-dependent indices k are neglected for reasons of clarity:

$$\Delta\breve{\mathbf{l}} = \mathbf{l}_{\Phi} - \lambda\breve{\mathbf{N}} \tag{3.33}$$

$$\breve{\mathbf{x}} = \left(\mathbf{A}^T\mathbf{P}\mathbf{A}\right)^{-1}\mathbf{A}^T\mathbf{P}\Delta\breve{\mathbf{l}} \tag{3.34}$$

If the ambiguity fixing failed, only the float estimates of the filter solution are output.

4

GNSS Feature Map-Aided Robust EKF

This chapter describes the newly developed GNSS Feature Map-aided robust EKF approach, starting with the motivation why adapted robust estimation is necessary for urban navigation applications. Subsequently, the general principle of adapted robust estimation is described, including the methods GNSS Feature Map-Aided NLOS Exclusion (GNSS FMA-NE) and GNSS Feature Map-Aided Weighting (GNSS FMA-W). Furthermore, a newly developed, adapted loss function with its mathematical relationships is presented and its performance is compared with state-of-the-art loss functions. Another focus of this chapter is the GNSS Feature Map, its concept, the detailed description of the map generation, the map resolution, the similarity of GNSS ranging errors summarized in the map, and last but not least the provision of a complete GNSS Feature Map for automotive applications. The positioning strategies developed in this chapter are tested in Chap. 5 using real kinematic data and evaluated against state-of-the-art methods.

4.1 Motivation

Optimality of estimators is only guaranteed if the distribution of the measurements exactly fulfill the Gaussianity requirements with perfectly known covariance. In order to consider the varying uncertainty of GNSS measurements from different satellites, empirical weighting models are introduced in Sec. 2.1.3. Another method of mitigating gross errors is to make use of loss functions derived from robust statistics. However, the main drawback of these family of functions is the reduced efficiency for fractions of outliers close to 50 % and a failure of the estimator for fractions of outliers exceeding 50 %, because the robust estimator cannot distinguish between nominal and contaminated observations.

In dense urban environments, the availability of nominal distributed measurements is largely reduced due to high buildings in the vicinity of the antenna resulting in numerous multipath and NLOS signal receptions. An exemplary multi-GNSS satellite availability for a kinematic trajectory in a typical urban area in the city of Hannover is shown in Fig. 4.1. Using city model information and ray tracing, the respective satellites are classified as LOS, multipath (MP), NLOS and blocked (Blk), represented in each row of the figure. Depending on the local situation and the satellite geometry, the resulting LOS signal reception ratio is often close to or even below 50 %, which would cause the standard robust estimators to be inefficient or break down.

In order to further illustrate the need of an adapted robust estimator, the performance of state of the art robust estimators for SPP is compared to that of an optimal MLE using a simulation study. A real multi-GNSS satellite constellation (GPS, GLONASS, Galileo, BDS) is determined for a given location at a given time using final satellite orbit products provided

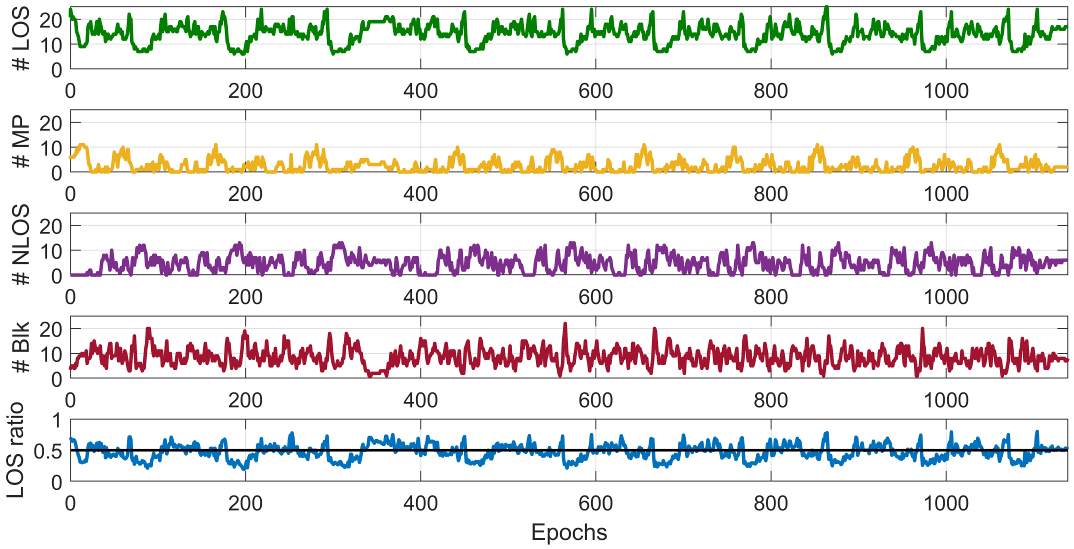

Figure 4.1: Multi-GNSS (GPS, GLONASS, Galileo, BDS) satellite availability for a kinematic trajectory in a typical urban area in the city of Hannover. The road width is ≈ 3 m surrounded by four-to-five storey buildings.

by the Center for Orbit Determination in Europe (CODE). The nominal observation errors are generated based on the normal distribution with zero mean and standard deviation $\sigma = 1$ m while the contaminated observations are uniformly distributed, i.e. the bias is randomly drawn from values between 20 m and 100 m. In total, 36 satellites are available in the multi-constellation case. All configuration parameters are summarized in Tab. 4.1. The multi-GNSS satellite constellation of the simulation configuration is shown in Fig. 4.2, where the left skyplot shows the observation errors for the 50 % contamination proportion case and the right skyplot represents the observation errors for the 70 % contamination proportion case. The observation errors are categorized into two classes: the nominal observations with magnitudes around 1 m and the contaminated observations with magnitudes larger than 20 m.

The loss functions of the MLE at the normal model (first column), Huber ($c_H = 1.345$, second column) and Geman-McClure ($c_G = 1$, third column) estimators for the SPP formulation projected in the North-East position domain using the simulated observation errors are depicted in Fig. 4.3.

The upper two rows represents the loss function as a surface and contour plot for a contamination proportion of 50 % and bottom two rows for a contamination proportion of 70 %, respectively. The global minimum is marked with a red cross and the ground truth is marked with a green diamond, respectively.

Table 4.1: Simulation configuration.

GPS time	2022/8/23 9:34:55
Location	Hannover, Germany
Cartesian coordinates	X: 3844924.5145 m, Y: 658244.2505 m, Z: 5029382.9620 m
Geodetic datum	ITRF2014, epoch 2023/235
Satellite orbits	Final CODE products
PDOP	0.74
Observation distribution	$l_{\text{in}} \sim \mathcal{N}(0,1)$, $l_{\text{out}} \sim \mathcal{U}(20,100)$
Contamination proportion	$n_{\text{out},1} = 50$ %, $n_{\text{out},2} = 70$ %

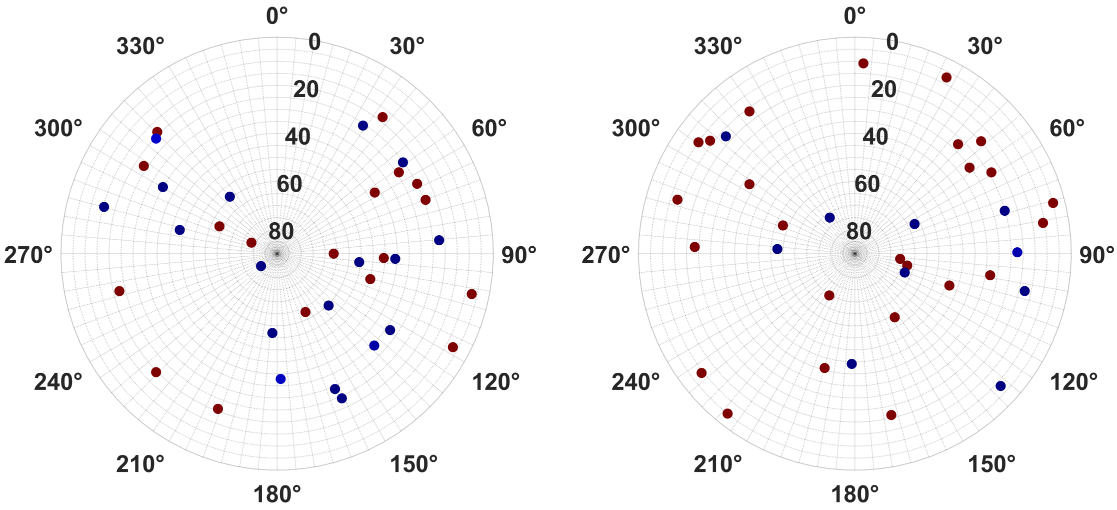

Figure 4.2: Multi-GNSS satellite constellation of the simulation configuration for 50 % (left) and 70 % (right) outliers. The measurement distribution is shown in blue (normal distribution) and red (uniform distribution).

As expected, the MLE and Huber estimators present a typical convex optimization with a single minimum and a guarantee for uniqueness and stability. However, the minimum is not characterized by a distinct peak, but rather by the shape of a flattened cone, especially for the 70 % contamination proportion case. The minimization of the loss function for the MLE results in a bias in the position domain for both simulated contamination proportions as already a single outlier could lead to a loss of the optimality characteristics. When applying the Huber estimator to the same observation errors, the minimization of the loss function leads to a position result close to zero for the 50 % contamination proportion case, while the breakdown point of 50 % is exceeded for the 70 % contamination proportion case and thus, the minimization leads to a bias in the position domain.

The results for the Geman-McClure estimator clearly represent the characteristics of non-convex optimization with a sharp peak at the global minimum but also an almost infinite number of possible solutions due to local minima. The higher the contamination proportion, the more important is the initialization of the non-convex solver, since the probability that the redescending solver could end up at a local minimum is increasing and thus, it would lead to a bias in the position domain. However, if the initial guess is close to the ground truth, the Geman-McClure estimator would still converge to a global minimum yielding a solution close to zero. This leads to the conclusion that a redescending type of robust estimator is very useful to mitigate the impact of outliers, especially when a large percentage of observations is contaminated.

4.2 Adapted Robust Estimation

A number of strategies are frequently used in current GNSS-based navigation solutions to mitigate gross errors due to faulty satellite signal receptions, including different (robust) weighting schemes (Sec. 2.1.3 and Sec. 2.5), 3DMA GNSS (Sec. 2.6.1) or outlier detection (Sec. 3.2). All these methods suffer from an overly conservative down-weighting of observations, lack of robustness for highly contaminated data, the need of additional 3D city model information or computationally intensive algorithms. To overcome these weaknesses, in this section two new strategies are defined which are utilizing prior information through the so-called *GNSS Feature Map* (Ruwisch and Schön, 2022a,b, 2023): i) GNSS FMA-NE uses map information

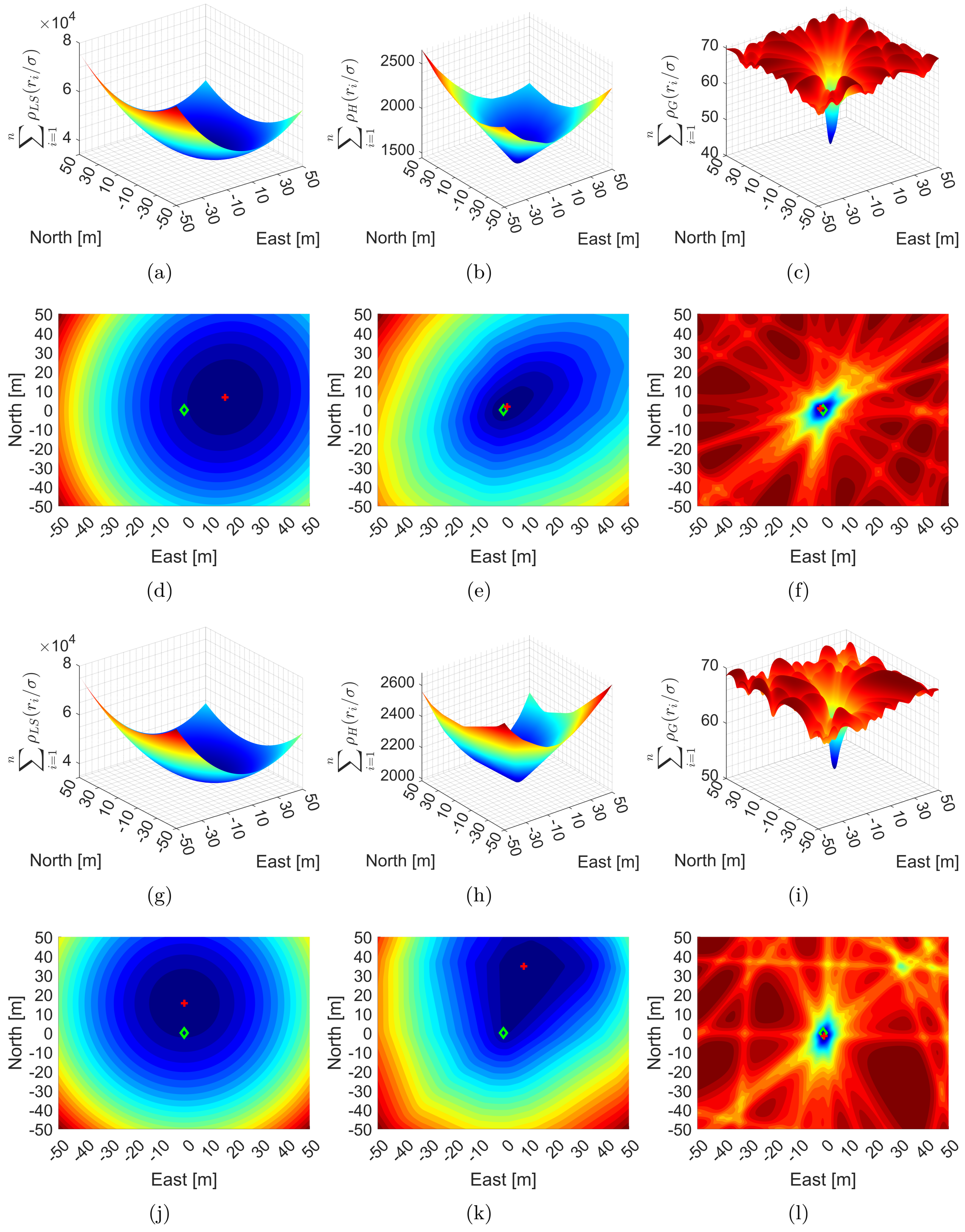

(a) (b) (c)

(d) (e) (f)

(g) (h) (i)

(j) (k) (l)

Figure 4.3: Loss functions of the MLE at the normal model (first column), Huber ($c_H = 1.345$, second column) and Geman-McClure ($c_G = 1$, third column) estimators for the SPP formulation using the simulated observation errors depicted in Fig. 4.2. Upper two rows represents the loss function as a surface and contour plot for a contamination proportion of 50 % and bottom two rows for a contamination proportion of 70 %, respectively. Thereby, the green diamond represents the ground truth at $[0, 0]$ m and the red cross depicts the respective minimum of the loss functions.

containing satellite visibility classification results and ii) GNSS FMA-W uses map information containing GNSS pseudorange residuals. The detailed process of the GNSS Feature Map generation is explained in Sec. 4.3.2.

In Fig. 4.4, the basic principle of utilizing GNSS Feature Map information for localization of autonomous vehicles is depicted. Vehicles driving through an urban trench are able to retrieve information from stored map data whenever the vehicle is located within a certain distance to the respective map point. The provided map information can be either satellite visibility classification information (left) or predicted pseudorange residual information (right), which are then processed by the user to enhance the vehicles localization accuracy.

The integration of the two proposed adaptive robust estimation strategies into the EKF framework for urban navigation is shown in Fig. 4.5, where the new and innovative part is highlighted compared to the EKF framework that has been described in Chap. 3. Definitions and implementation details of the algorithms are explained in the following subsections.

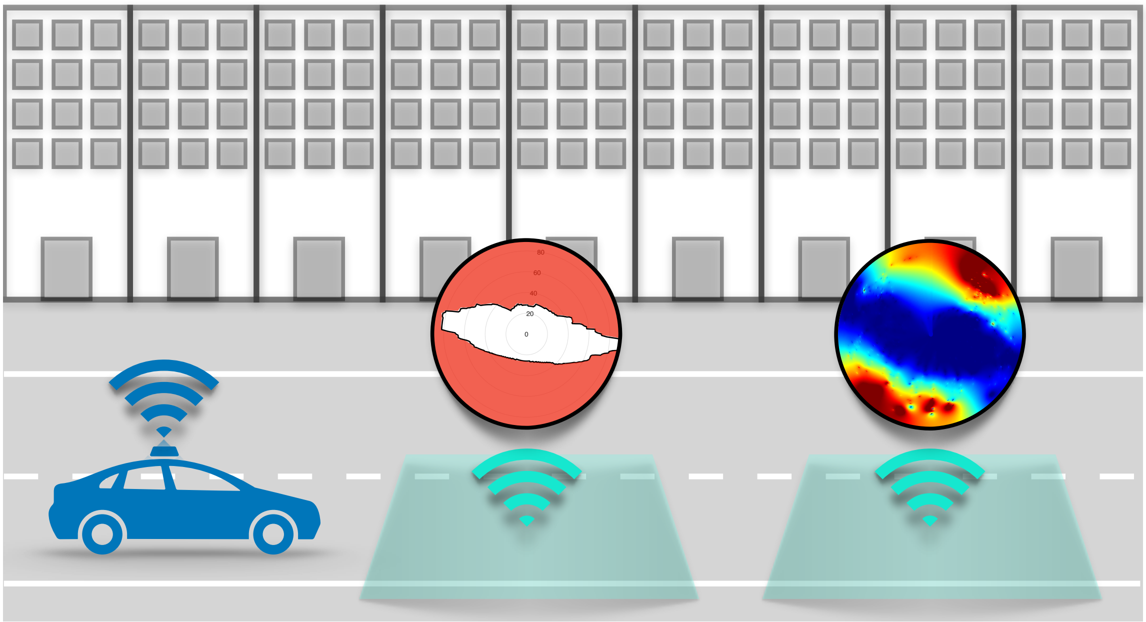

Figure 4.4: Conceptual application of GNSS Feature Maps for localization of autonomous vehicles.

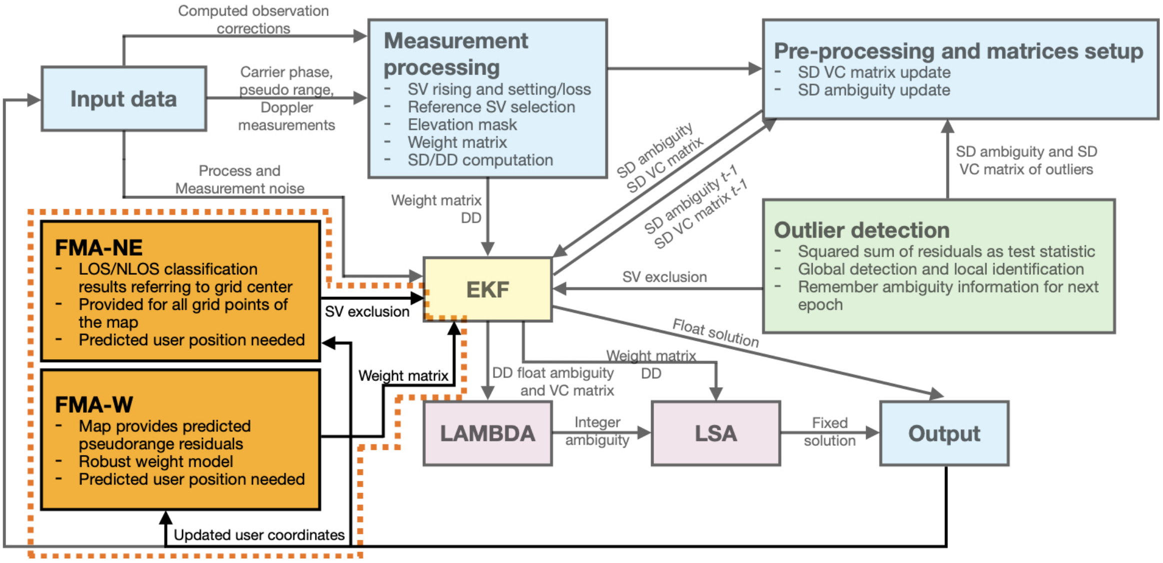
Computed observation corrections
Input data
Carrier phase, pseudo range, Doppler measurements
Process and Measurement noise
Measurement processing
- SV rising and setting/loss
- Reference SV selection
- Elevation mask
- Weight matrix
- SD/DD computation
Pre-processing and matrices setup
- SD VC matrix update
- SD ambiguity update
SD ambiguity SD VC matrix
SD ambiguity t-1 SD VC matrix t-1
SD ambiguity and SD VC matrix of outliers
Outlier detection
- Squared sum of residuals as test statistic
- Global detection and local identification
- Remember ambiguity information for next epoch
Weight matrix DD
EKF
SV exclusion
SV exclusion
FMA-NE
- LOS/NLOS classification results referring to grid center
- Provided for all grid points of the map
- Predicted user position needed
FMA-W
- Map provides predicted pseudorange residuals
- Robust weight model
- Predicted user position needed
Weight matrix
Float solution
Weight matrix DD
DD float ambiguity and VC matrix
LAMBDA
Integer ambiguity
LSA
Fixed solution
Output
Updated user coordinates

Figure 4.5: EKF framework integration of adapted robust estimation approaches (orange parts).

4.2.1 GNSS Feature Map-Aided NLOS Exclusion

The GNSS FMA-NE algorithm is an alternative to 3D city model-based ray tracing. Instead, it utilizes information from offline computed ray tracing results. Each grid of the map provides an obstruction mask for the center point of the box. As soon as the predicted vehicle position is located within one of these map grids, the provided obstruction mask is taken as an approximation of the vehicle's obstruction mask. If any of the received satellite signals are classified by the map as NLOS, the respective satellites are excluded from the estimation process. Conversely, if signals from potential LOS satellites are received, no action is required and all satellites in view are used in the estimation process.

The processing flow of the GNSS FMA-NE is displayed in Alg. 2. This approach ensures the rejection of NLOS satellites by leveraging 3D building model data and ray tracing computation results, thereby avoiding the necessity of epoch-wise ray tracing computations at the vehicle site.

Algorithm 2 GNSS Feature Map-Aided NLOS Exclusion

```
for every epoch do
    Calculate predicted user position
    Calculate satellite positions
    if Predicted position is inside any box polygon then
        Retrieve Feature Map classification information
        if any satellite is NLOS then
            Reject satellites from estimation
        else
            Use all satellites
        end if
    end if
    Update user position
end for
```

4.2.2 GNSS Feature Map-Aided Robust Weighting

Generated maps, which provide information on the spatial distribution of pseudorange residuals and thus, information on the potential received magnitude of ranging errors, can be used to modify existing robust weighting schemes. The general processing procedure is similar to the GNSS FMA-NE algorithm. The GNSS FMA-W is initiated subsequent to the computation of the predicted user position. Subsequently, the predicted user position is compared to the generated box polygons present on the map. If the aforementioned condition is found to be true, meaning that the predicted position is assigned to a map grid, the pseudorange residual information of the GNSS Feature Map is retrieved for the specific box in question. Then, the respective predicted residuals are normalized by the a priori pseudorange measurement noise σ_{ρ_0} as follows

$$\bar{\mathbf{v}}^{\mathrm{FM}} = \frac{\mathbf{v}^{\mathrm{FM}}}{\sigma_{\rho_0}}, \tag{4.1}$$

where $\mathbf{v}^{\mathrm{FM}}$ is the vector of predicted pseudorange residuals retrieved from map information, which is used for computing robust weights based on a defined robust loss function. Considering the minimization formulation in Eq. 2.67, it can be reformulated as minimization of the predicted pseudorange residuals

$$\hat{\mu}_{\mathrm{FM}} = \min_{\mu} \sum_{i=1}^{n} \rho \left(\frac{v_i^{\mathrm{FM}}}{\sigma_{\rho_0}} \right) \tag{4.2}$$

with $\rho(\cdot)$ denoting one of the robust loss functions and $i = 1, \ldots, n$ is the number of observations.

The algorithmic realization within an estimator is depicted in Alg. 3. Please note that no iteration of the estimation is required, since the obtained predicted residuals are taken as true values and thus, expected to solve the minimization in Eq. 4.2, which yields an efficient and costly inexpensive robust estimator.

Algorithm 3 GNSS Feature Map-Aided Weighting

```
for every epoch do
    Calculate predicted user position
    Calculate satellite positions
    if Predicted position is inside any box polygon then
        Retrieve Feature Map residual information $\mathbf{v}^{\mathrm{FM}}$
        Normalize $\mathbf{v}^{\mathrm{FM}}$ to $\bar{\mathbf{v}}^{\mathrm{FM}} = \frac{\mathbf{v}^{\mathrm{FM}}}{\sigma_{\rho_0}}$
        Adapt weights based on robust loss function $\rho(\cdot)$
    else
        Use conventional weighting
    end if
    Update user position
end for
```

4.2.3 The HG-estimator – An Adapted Robust Weight Model

In the preceding section, the Huber loss and Geman-McClure loss are assessed in terms of enhancing the robustness of GNSS based localization in the presence of contaminated data. The two methods of different weighting for large observation errors are based on the mathematical foundations described in Sec. 2.5. The review of the literature in Sec. 2.6.1 of urban GNSS positioning reveals that, when a sufficient number of healthy satellites are received, the exclusion of biased observations based on building models and ray tracing computations leads to a significant enhancement in the accuracy. Reformulating the NLOS exclusion strategy in terms of a weight model would entail maintaining the LOS satellites and assigning weights close to zero to the NLOS satellites (i.e., the observations with the larger residuals). Revisiting the aforementioned robust functions, it becomes evident that both the Huber loss and the Geman-McClure loss exhibit a significant limitation. The Huber function assigns weights of one for a range of smaller residuals (typically between -1.345 and +1.345), but only slightly dampens large residuals. In contrast, the Geman-McClure loss exhibits a pronounced dampening effect on increasing residuals, which aligns well with the NLOS exclusion strategy. However, the weights are already significantly reduced for residuals that are still relatively small.

Consequently, a new adapted robust weight model – the *HG-estimator* – is proposed, which incorporates the advantages of both robust functions and eliminates the drawbacks of both models. The new model demonstrates a high level of impact from observations with relatively small residuals, while strongly dampening the impact of observations with larger residuals. Thus, the combination of the Huber loss and the Geman-McClure loss yields a robust model that is comparable to a NLOS exclusion strategy. The corresponding equations for the loss function ($\rho(x)$), score function ($\psi(x)$) and weighting function ($w(x)$) are summarized in Tab. 4.2. A graphical representation is provided in Fig. 4.6. To illustrate the novel approach more effectively, the graphs presented in Fig. 2.7 have been included. It can be seen that for residuals between ±1.345 the HG function adheres to the Huber definition. Conversely, for residuals exceeding this value, the HG function aligns with the Geman-McClure loss, score and weighting function, respectively.

The discontinuity of the HG loss function gives rise to convergence problems and, under circumstances where the initial approximation values are not accurate, it is highly probable that the estimator will converge at the local minimum. In this study, the developed estimator is based on the assumption that feature map information is highly accurate and serves as a reliable initial estimate. This eliminates the need for iteration of the HG estimator, thereby ensuring that the disadvantages of discontinuity are negligible. As can be seen in Chap. 5, the HG loss improves the performance of carrier phase-based positioning compared to the existing robust functions.

In order to evaluate the applicability of the HG-estimator, the SPP performance is analyzed by depicting the loss function (see Fig. 4.7) for the same scenario as in the previous section, for the 70% contamination case. The global minimum of the loss function leads to a very small deviation from the ground truth, comparable to the outcome for the Geman-McClure loss function. Consequently, the HG-estimator is a robust estimator that effectively mitigates the impact of outliers at a high data contamination proportion. It is also evident that the redescending characteristic of the estimator results in the occurrence of numerous local minima of the loss function. That in turn requires accurate initial estimates in order for the algorithm to converge to the global minimum.

Table 4.2: Loss function $\rho(x)$, score function $\psi(x)$ and weighting function $w(x)$ of the proposed adapted robust HG-estimator. The parameters are set to $c_H = 1.345$ and $c_G = 1$.

Estimator	$\rho(x)$	$\psi(x)$	$w(x)$
HG $\begin{cases} \lvert x\rvert \le c_H \\ \lvert x\rvert > c_H \end{cases}$	$\begin{cases} \frac{x^2}{2} \\ \frac{2\frac{x^2}{c_G^2}}{\frac{x^2}{c_G^2}+4} \end{cases}$	$\begin{cases} x \\ \frac{16c_G^2 x}{(4c_G^2+x^2)^2} \end{cases}$	$\begin{cases} 1 \\ \frac{16c_G^2}{(4c_G^2+x^2)^2} \end{cases}$

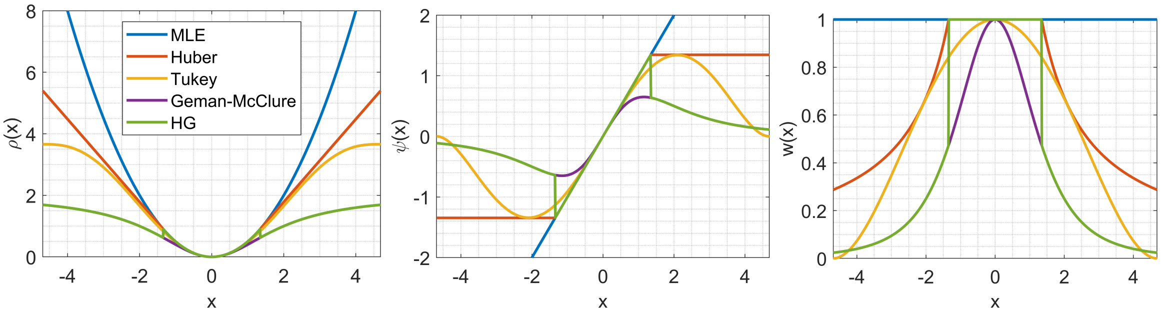

(a) (b) (c)

Figure 4.6: Loss function $\rho(x)$ (a), score function $\psi(x)$ (b), and weighting function $w(x)$ (c) of the proposed adapted robust HG-estimator. In addition, the MLE at the normal model and M-estimators based on the Huber's, Tukey's and Geman-McClure's family of functions are illustrated. The control parameters are set to $c_H = 1.345$, $c_T = 4.685$ for 95 % relative efficiency at the normal model and to $c_G = 1$.

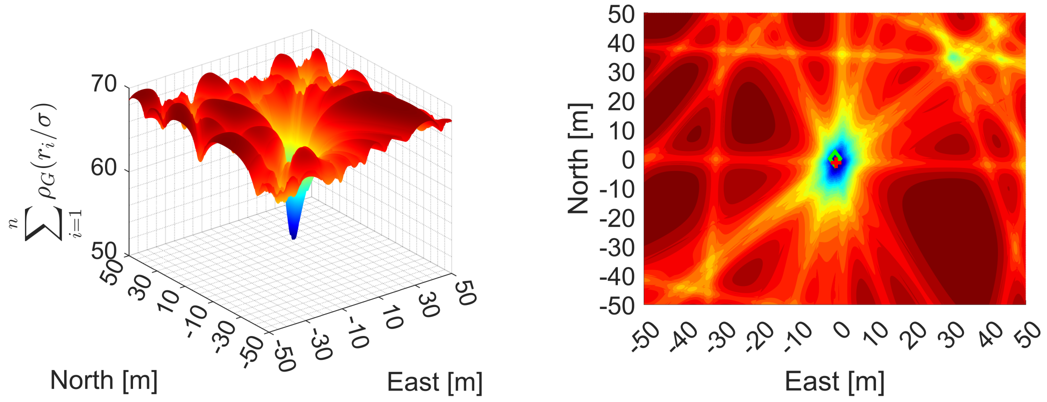

(a) (b)

Figure 4.7: Loss functions of the HG estimator for the SPP formulation using the simulated observation errors depicted in Fig. 4.2. (a) represents the loss function as a surface and (b) illustrates the loss function as a contour plot for a contamination proportion of 70 %, respectively. Thereby, the green diamond represents the ground truth at $[0, 0]$ m and the red cross depicts the minimum of the loss function.

4.2.4 Performance Simulation of Robust Estimators

The idea of GNSS FMA-W is to keep the satellite geometry while increasing the robustness of an estimator even in situations with sets of measurements containing more than 50 % outliers. A simulation study is conducted to compare the performance of pseudorange-based GNSS positioning using robust estimators to that of an optimal MLE. When performing multi-GNSS SPP, one independent clock offset per constellation has to be considered yielding in total seven parameters to be estimated. The basic simulation configuration of Sec. 4.1 is kept and thus, using four satellite systems, a total number of 36 satellites is available. The respective observations are simulated in a Monte-Carlo experimentation with 10^4 runs. Nominal observations follow a Gaussian distribution with zero mean and standard deviation $\sigma_{\text{in}} = 1$ m while outliers are simulated with varying standard deviations:

$$\mathbf{l} = \left[\mathbf{l}_{\text{in}}^T, \mathbf{l}_{\text{out}}^T\right], \ \mathbf{l}_{\text{in}} \sim \mathcal{N}(0, \sigma_{\text{in}}^2), \ \mathbf{l}_{\text{out}} \sim \mathcal{N}(0, \sigma_{\text{out}}^2). \tag{4.3}$$

Nominal observations and outlying observations are randomly assigned to the respective satellites during the Monte-Carlo simulation. The impact on the performance is studied for both the proportion of contaminated observations ϵ and the magnitude of biases σ_{out}, respectively. The parameters configuration for the Monte-Carlo simulation are summarized in Tab. 4.3. In addition to the MLE for the normal model, robust estimators with different loss functions are compared: (i) M-estimator based on Huber loss, (ii) M-estimator based on Tukey loss, (iii) M-estimator based on Geman-McClure loss, (iv) M-estimator based on HG loss. The performance of GNSS FMA-W is simulated by assuming the true range bias of the measurements to be known and thus, using the true range bias of the measurements for determining the respective weights of the robust estimators.

The resulting RMS errors of the different estimators for the 10^4 Monte-Carlo runs are visualized in Fig. 4.8. Each figure represents a percentage of outliers (30 %, 50 %, 70 % from

Table 4.3: Parameters configuration for the Monte-Carlo simulation.

Percentage of outliers	$\epsilon \in \{30, 50, 70\}$ %
Observation uncertainties	$\sigma_{\text{in}} = 1$ m, $\sigma_{\text{out}} \in \{1, 3, 6, 10, 30, 60, 100\}$ m
Robust parameters	$c_H = 1.345, \ c_T = 4.6851, \ c_G = 1$

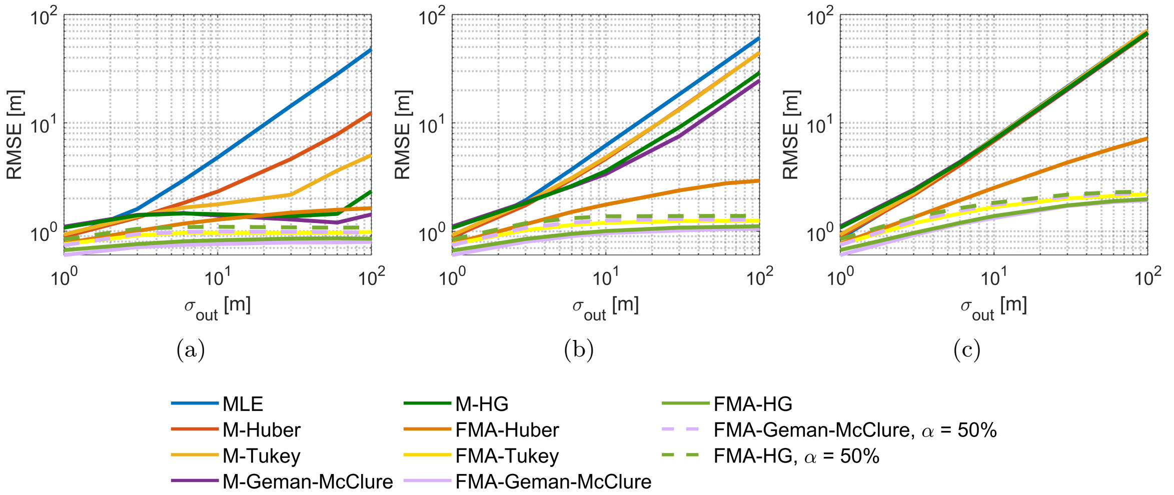

(a) (b) (c)

Figure 4.8: RMS errors of the 3D position obtained by different estimators for (a) 30 %, (b) 50 % and (c) 70 % contamination proportion.

left to right), respectively. Smaller contamination proportions are omitted, since it is proven that standard robust estimators are providing reliable results for data with a small amount of outliers. According to the rule of thumb in Langley et al. (2017), under nominal conditions, a three-dimensional position error of $\sigma_{\text{in}} \cdot \text{PDOP} \approx 0.74$ m is expected. Among the three cases, it is clear that the MLE suffers the most from a lack of robustness. The RMS errors are drastically influenced by the magnitude of outliers yielding to a failure of the estimator even for smaller standard deviations of the outlying measurements. The M-Huber, M-Tukey, M-Geman-McClure and M-HG estimators are improving the robustness of the solution for the case $\epsilon = 30$ % whereas the former showcases the best performance for the normal model ($\sigma_{\text{out}} = 1$ m) and latter two showcases the highest robustness due to its characteristics of the loss function. Even though the theoretical breakdown points of these estimators is 50 % and for the redescending type of estimators a global minimum would also exist for the case of $\epsilon = 70$ %, all four estimators already break down for the case of $\epsilon = 50$ % being characterized by a lack of robustness for highly contaminated data. On the other hand, when assuming the magnitude of the observation error to be known, the GNSS FMA-W based estimators provide the most accurate results. For the first two cases, the RMS errors barely increase despite the increasing magnitude of the biases. Even when only a small proportion of nominal observations is available ($\epsilon = 70$ %), reliable results can be computed. When comparing the GNSS FMA-W based estimators among each other, the more large outliers are damped by the respective weight function, the better the position performance and thus, FMA-Geman-McClure and FMA-HG show the best performance and FMA-Tukey performs better than FMA-Huber.

The two dotted lines in each figure represent the case when the true range bias of the respective measurement is not exactly known. When determining the weights using the Geman-McClure and HG loss function, respectively, the residuals are halved with respect to their true range bias, which simulates a $\alpha = 50$ % error in the predicted residuals. Since both specific loss functions are highly damping large residuals, the impact of the introduced uncertainty on the computed position is rather low. For all three evaluated measurement contamination proportions, the RMS error behaves similarly to the FM-Tukey estimator without introduced uncertainties. That means, even if 70 % of the available measurements are contaminated with a standard deviation of $\sigma_{\text{out}} = 100$ m, the resulting average RMS error is still below 2 m, yielding a very robust solution.

4.3 GNSS Feature Map

Characteristics of GNSS signals depend on both the antenna location and the satellite positions. In static multipath environments, a common method is to consider the ground-track repeatability of reflection-based errors to elaborate on algorithms that mitigate errors induced by the local environment (Braasch, 2017). Methods that have been developed for static scenarios are multipath stacking maps (Fuhrmann et al., 2014) and multipath hemispherical maps (Dong et al., 2015), which are both generated based on pseudorange or carrier phase residuals, or the multipath impact is mapped by using the C/N_0 value (Bilich and Larson, 2007).

In kinematic urban scenarios, signal propagation characteristics exhibit a complex spatiotemporal behavior, i.e., they are dependent upon the location of the moving user antenna, changing satellite positions, and surrounding buildings. In order to derive potential mitigation strategies for kinematic urban scenarios, a representation of these spatiotemporal dependencies is needed. To meet this research gap, the GNSS Feature Map (Ruwisch and Schön, 2022a) has been developed.

The proposed GNSS Feature Map is not limited to the representation of spatiotemporal dependencies, but, in addition, can also aid and thus enhance urban navigation (Ruwisch and Schön, 2022b, 2023). This is realized through the provision of a map that stores spatiotemporal-dependent features in a fully spatial-dependent tool. In terms of multi-sensor systems, one could think of storing any feature which is characterized by such dependencies and not limited to GNSS, e.g., based on fish-eye cameras providing visibility information or LiDAR sensor data, which provides building wall information. This thesis focuses on improving GNSS-based navigation in urban environments and thus, the storage and analysis of GNSS-related features is of utmost interest and is therefore addressed in the following sections.

4.3.1 Concept

The initial aim of the GNSS Feature Map has been to combine skyplots at each location of a moving user antenna into one common map to improve the understanding of spatiotemporal behaviours of GNSS signal propagation and to predict the signal characteristics when passing along a trajectory at any time. Environmental structures are highlighted by this type of map, e.g. by means of satellite ray classification, which allows the user to identify rapid changes of the geometry in addition to challenging reception properties of satellites which can deteriorate the positioning solution.

GNSS signal propagation-related features depend on both the varying user antenna location and satellite position. The GNSS Feature Map shows these dependencies in one common map. This map is two-dimensional, rectangular and constructed in the following way: At each along track position a skyplot is computed in the vehicle body frame and mapped onto one of the axes by appending each strip of constant azimuth below each other (see Fig. 4.9(a)). A $1^\circ \times 1^\circ$ grid resolution in azimuth and elevation, respectively, is proposed resulting in 360 azimuth bins containing 90 elevation bins each. The second axis (see Fig. 4.9(b)) represents the distance traveled by a vehicle. In the context of simulation data, features are generated intuitively at specific vehicle locations. Repeatedly driven trajectories, based on real measurements, are bounded longitudinally and laterally. However, these trajectories vary due to the inherent impossibility of reproducing an exact repeat of the trajectory. To account for these coordinate deviations, the user locations from the driven trajectory are perpendicularly projected onto a reference path. This reference path can be defined, e.g., from path planning or using available lane models. The perpendicularly projected coordinates result in the distance along track. The maximum orthogonal distances are contingent on the width of the streets.

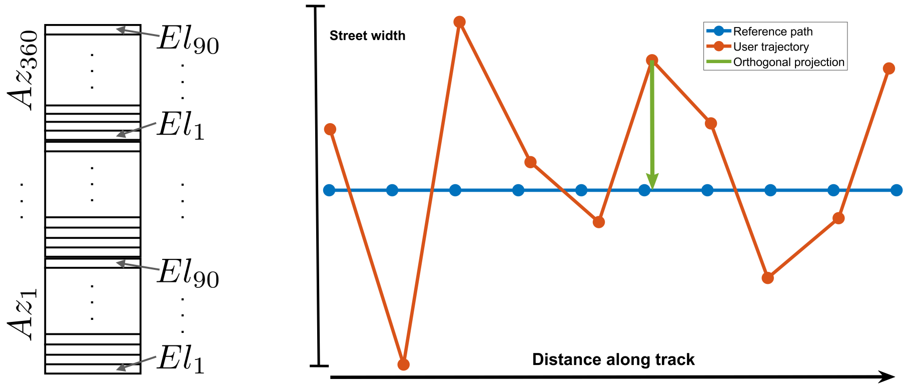

(a) (b)

Figure 4.9: GNSS Feature Map design. (a) Structure of the first axis where the upper antenna hemisphere is represented by a 360° × 90° grid. (b) Approach for representing the user antenna location on the second axis.

Exemplary GNSS Feature Maps are shown in Fig. 4.10. The x-axis represents the azimuth bins including elevation bins of the satellites and the y-axis represents the distance along track, e.g., from a moving vehicle. Features located in the direction of travel can be found parallel to the y-axis (constant azimuth and elevation, moving vehicle location). An azimuth angle of 0° corresponds to the driving direction considering a south-to-north oriented street. Features at a specific vehicle location can be found at lines parallel to the x-axis (constant vehicle location, changing satellite positions).

The exemplary GNSS Feature Maps are generated from kinematic GNSS data collected in the city of Hannover using both GPS L1 C/N_0 values and DD pseudorange residuals as features of interest. The black lines indicate respective sections of the trajectory each of them marking a approximately 90° turn in the heading angle of the vehicle. The heading of the vehicle is not taken into account in order to better detect dissimilarities due to the change of the environment. One GNSS-related characteristic is common for all four street segments, which is the north hole of northern hemisphere locations between azimuth angles of approximately -30° and 30°. However, some high-elevating satellites pass the zenith and thus have a strong variation in the azimuth which is also visible in the respective figures. Using the GNSS Feature Map, differences in the signal reception characteristics caused by the changing geometry or the street orientation is highlighted. The transitions between the specific street segments are sharp. The magnitude of both the C/N_0 values and DD residuals is subject to rapid variation for similar satellite positions, but this variation is accompanied by a changing geometry of the surrounding buildings. In this way, the signal propagation conditions in urban environments is represented in a comprehensive way. As previously discussed, a valuable GNSS Feature Map application is not only the visualization and path planning, but especially the aiding of urban navigation. The subsequent sections provide a comprehensive explanation of the generation of such a map that is designed to facilitate GNSS-based navigation in urban environments.

4.3.2 Map Generation

In this section, the location information extraction from Open Street Map (OSM) data is described, followed by the generation of simulated and real data GNSS Feature Maps based on OSM location information.

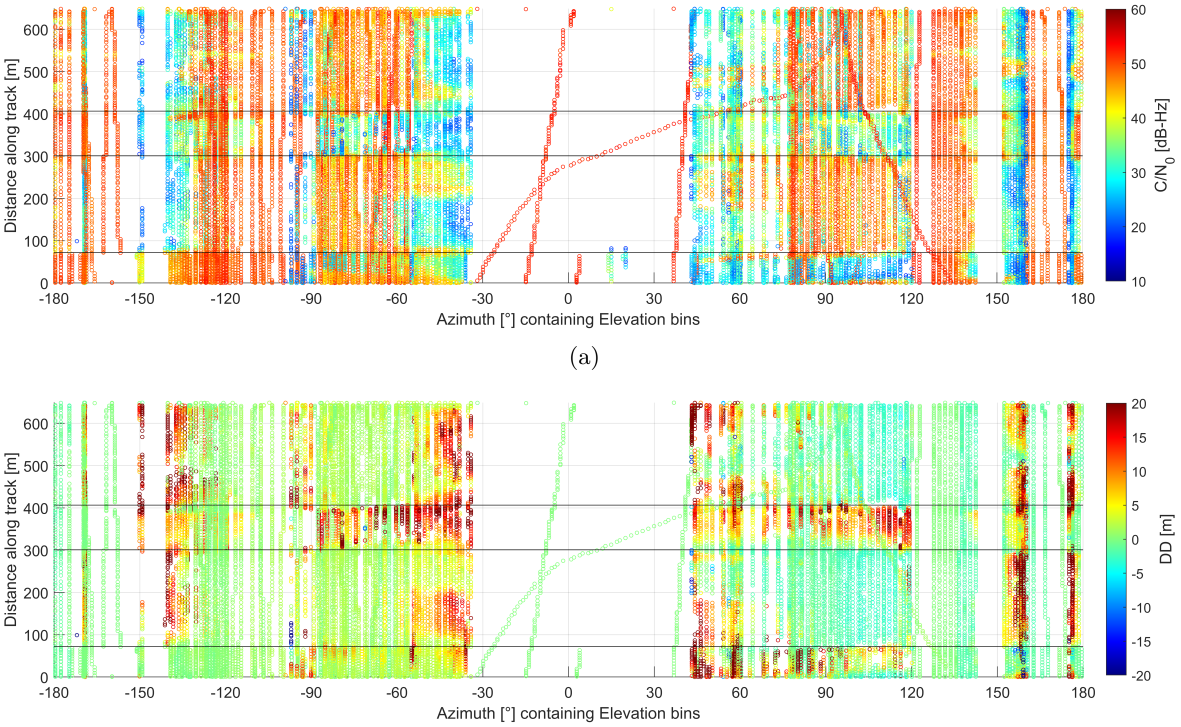

(a)

(b)

Figure 4.10: GNSS Feature Maps based on real data from a kinematic experiment in the city of Hannover. The black lines indicate respective sections of the trajectory each of them marking a approximately 90° turn in the heading angle of the vehicle. (a) shows the generated map using GPS L1 C/N$_0$ values as feature of interest while in (b) GPS L1 C/A code double difference residuals are depicted in a map.

Open Street Map

OSM is a free and open-source mapping project, licensed under the Open Data Commons Open Database License by the OSM Foundation (OpenStreetMap copyright, 2024). It allows users to create, edit, and use geographic data from around the world (Haklay and Weber, 2008), which has also attracted the attention of the scientific community, which makes use of the availability of the huge amounts of geographic data, e.g., for the autonomous robot navigation based on OSM data (Hentschel and Wagner, 2010).

OSM provides location information through XML files which can be extracted from the project's website (OpenStreetMap project homepage, 2024) and contain information about the various elements that make up a map, such as *nodes*, *ways*, and *relations*. The location information of streets can be found in the *way* elements, each of which represents a sequence of nodes that make up a line or shape on the map. Way nodes thereby are defining a line, which approximates the center of the road. For more details on the structure of OSM data, it is referred to the OSM map feature documentation (OpenStreetMap map features, 2024) or text books, e.g. Ramm et al. (2010).

An exemplary *way* element is depicted in Fig. 4.11. In this example the *way* element has an ID of 232160982 and is visible on the map. It contains a sequence of *nd* elements, each of which references a *node* element that defines a point in the street. The exemplary street contains 6 points. Another important information is the attribute with key *name* and value *Kniestraße* which defines the name of the street. By parsing all *way* elements in an OSM file, all available location information of specific streets can be extracted. These OSM location information is collected by volunteers, who contribute to the mapping project by performing systematic

```
<way id="232160982" visible="true" version="8" changeset="123881637"
timestamp="2022-07-21T08:30:40Z" user="oswa" uid="169839">
  <nd ref="1507724614"/>
  <nd ref="1378429609"/>
  <nd ref="1507724612"/>
  <nd ref="2794846555"/>
  <nd ref="2661137417"/>
  <nd ref="1507724593"/>
  <tag k="highway" v="residential"/>
  <tag k="maxspeed" v="30"/>
  <tag k="name" v="KniestraÃŸe"/>
  <tag k="parking:lane:both" v="parallel"/>
  <tag k="parking:lane:both:parallel" v="street_side"/>
  <tag k="sidewalk" v="both"/>
  <tag k="surface" v="paving_stones"/>
 </way>
```

Figure 4.11: Exemplary *way* element in an OSM file containing 6 nodes each referencing a *node* element that defines a point on the street.

ground surveys with handheld GPS receivers. Thereby, geographic coordinates, i.e. latitude and longitude, are provided referring to the World Geodetic System 84 (WGS84) ellipsoid and are specified in degrees with a precision of seven decimal places, which corresponds to a resolution of ± 1 cm. However, uncertainty information on the given data is not defined due to its nature of a collaborative project by volunteers. Typically, additional height information is not provided by maps, but can be complemented by digital terrain models.

An exemplary extracted OSM lane model in the city of Hannover is shown in Fig. 4.12(a). Different streets have different number of points forming the line which is dependent on the shape of the streets. Obviously, more points exist at street crossings where curves need to be modeled.

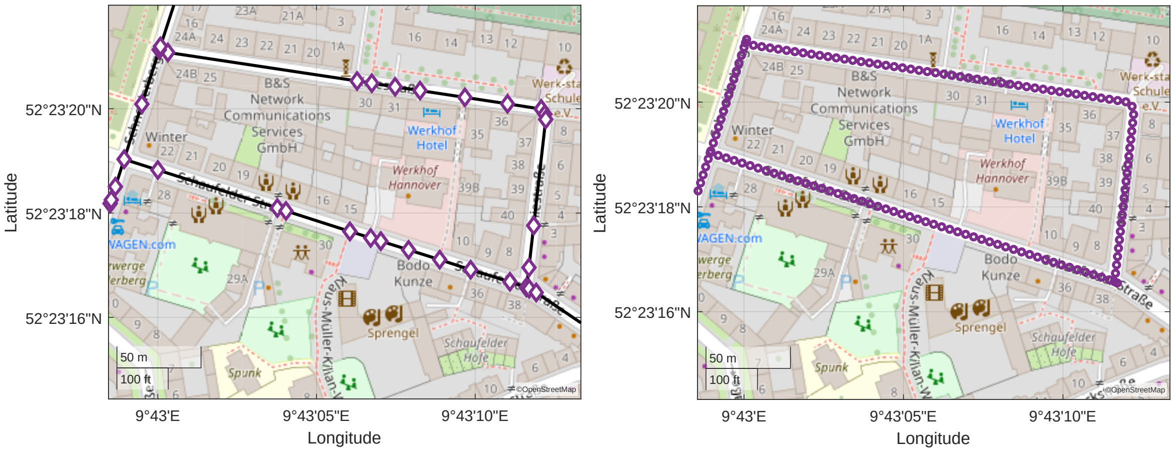
Latitude
52°23'20"N
52°23'18"N
52°23'16"N
9°43'E
9°43'05"E
9°43'10"E
Longitude
50 m
100 ft
B&S Network Communications Services GmbH
Werkhof Hotel
Werkhof Hannover
Winter
Bodo Kunze
Sprengel
Spunk
Schaufelder Höfe
©OpenStreetMap

(a) (b)

Figure 4.12: OSM lane model and its interpolation. (a) Exemplary extracted OSM lane model in the city of Hannover. The markers depict the lane model points which are connected to a lane. (b) OSM waypoints interpolated with a resolution of 5 m.

Satellite Visibility Classification Map

In order to apply the strategy of GNSS FMA-NE, satellite visibility classification results for selected locations are required for building such a map. Therefore, the OSM road coordinates are extracted for the streets of interest, a resolution of the distance between map points (details about this waypoint resolution are explained in the next section) is chosen and the OSM road coordinates are interpolated using this defined grid size. The resulting waypoints are shown in Fig. 4.12(b) with an exemplary resolution of 5 m. For each of the waypoints, ray tracing computation is performed for synthetic satellite positions, which cover the full sky in a 360° azimuth × 90° elevation grid with a resolution of 1°. This fine resolution allows for accurately determining the obstruction mask for each waypoint. The result is the classification whether a satellite is in LOS condition or blocked by a building for all possible satellite ray reception angles at these locations.

As illustrated in Fig. 4.13, the satellite visibility classification results for ten map waypoints along the trajectory are depicted in skyplots. Signals received from satellite positions inside the polygon, which represents the obstruction boundary, are labeled as LOS, while signals received from satellite positions below the obstruction boundary elevation angle are labeled as NLOS, indicating that they are blocked by a building. It is evident that the satellite visibility condition is subject to variation along the trajectory, particularly for waypoints that are in closer proximity to the street corner. The satellite ray classification conditions are related to the respective waypoint of the GNSS Feature Map. In this way, information on potential critical reception characteristics is provided by the GNSS Feature Map without the need of performing computational intensive ray tracing at the rover in real-time.

Pseudorange Residuals Map

Prior information on the observation's error magnitude, e.g., provided by the GNSS Feature Map containing pseudorange residuals, is integrated in GNSS FMA-W in order to improve and enhance the robustness of GNSS-based urban navigation. By utilizing such a pseudorange residuals map, the user becomes completely independent of city model information. Compared to the described satellite visibility classification map, this map is not generated by simulating waypoints and performing ray tracing, but a real GNSS measurement campaign is required to produce features based on GNSS pseudorange residuals. Therefore, multi-GNSS, multi-frequency training data is collected in a kinematic measurement campaign. Four antennas are mounted on the roof of the institute's test vehicle (see Fig. 4.14(a) and Fig. 4.14(b)). Three *Tallysman TW7972* patch antennas are each connected to a *Septentrio PolaRx5e* receiver. A geodetic antenna of type *NovAtel NOV850* is connected to a iMAR iNAT system (*RQT-4003*) which consists of a navigation-grade IMU (Inertial Measurement Unit) and a geodetic GNSS receiver. The institute's continuously operating reference station *EE01*, which is located at the Einstein-elevator tower close to the driven trajectory (< 1 km), serves as reference, where a Leica antenna (*LEIAR20 LEIM*) is connected to a *Septentrio PolaRx5TR* receiver. A precise reference trajectory is computed in post-processing in a tightly-coupled GNSS/IMU relative positioning solution using the commercial software TerraPOS (Kjørsvik et al., 2009).

In order to reliably derive a fully populated GNSS Feature Map (i.e. full sky coverage), the experiment is conducted during two days (Day of Year (DOY) 94 and 95, 2023) at different day times with a total driving time of ≈ 5.5 h periodically passing the same streets. In this way, data is collected during significant changes in the satellite constellations. The driven trajectory is shown in Fig. 4.14(c). Different routes in the city of Hannover were covered in order to generate maps for different local situations, i.e. different building height, streets

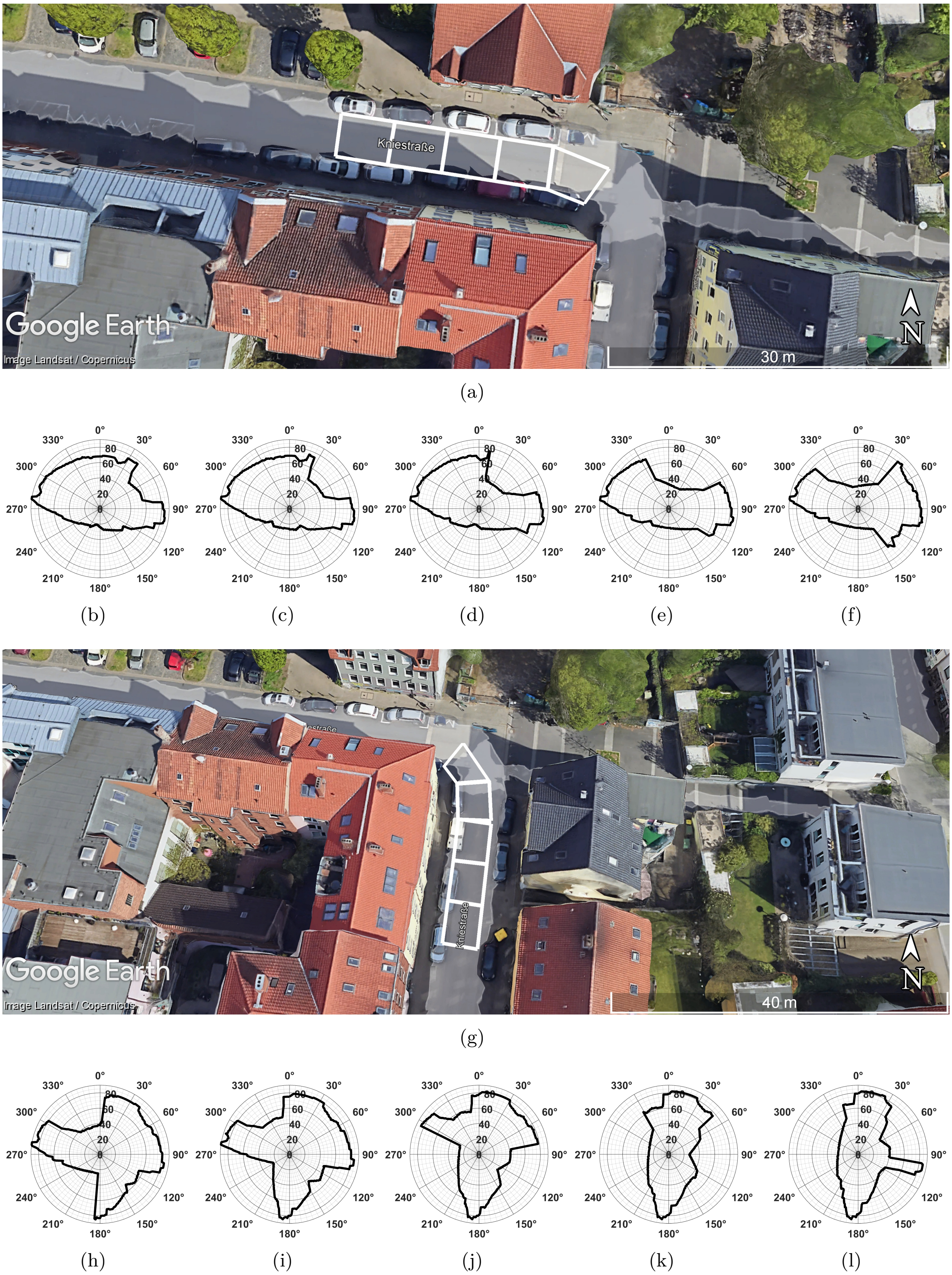
Kniestraße
Google Earth
Image Landsat / Copernicus
30 m
N
40 m
0°
30°
60°
90°
120°
150°
180°
210°
240°
270°
300°
330°
80
60
40
20
0

(a)

(b) (c) (d) (e) (f)

(g)

(h) (i) (j) (k) (l)

Figure 4.13: Skyplots for ten exemplary map waypoints of a satellite visibility classification map. (a) and (g) show the location of the boxes, (b)-(f) (left to right) and (h)-(l) (top to bottom) show the obstruction masks.

orientation and street width, and to be capable of testing the performance of the proposed algorithms in different environments and situations.

All necessary steps of the map generation work flow are depicted in Fig. 4.15. The first

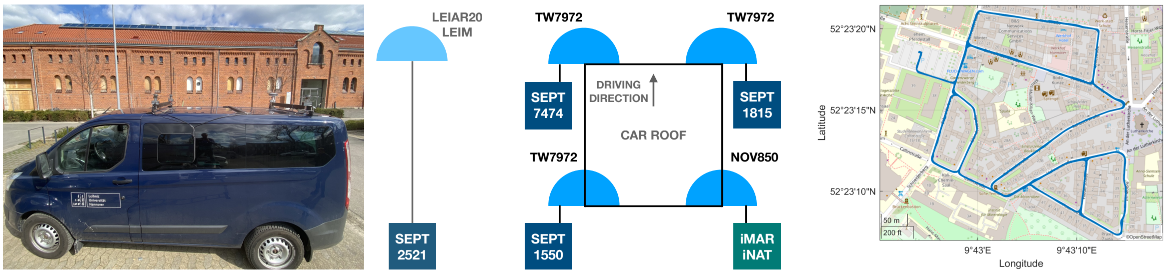

(a) (b) (c)

Figure 4.14: Training data experiment setup. (a) test vehicle with antenna mounts, (b) antenna and receiver connections (the distance between the lateral antennas is 103 cm and the distance between the longitudinal antennas is 195 cm), (c) driven trajectory in the city of Hannover.

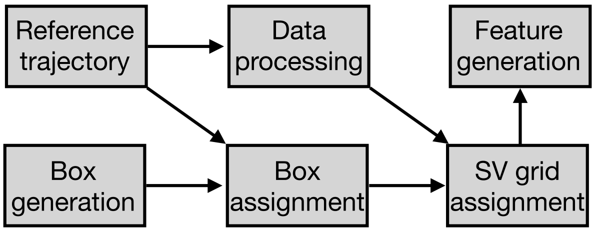

Figure 4.15: General concept of the data aggregation and GNSS Feature Map generation represented in a flow chart.

step in the direction of feature generation is to aggregate the huge amount of collected data. Therefore, box polygons need to be derived from the interpolated waypoints based on a user-defined width in longitudinal (driving direction) and lateral direction (cross street direction). The box sizes are set to dLongitudinal = 5 m and dLateral = 4 m. A detailed study on the waypoint resolution and how the box size is selected can be found in the next section (Section 4.3.3).

In Fig. 4.16, the generated boxes in conjunction with the reference trajectory data points are shown. Based on the coordinates obtained from the computed reference trajectory, all data points of the trajectory are assigned to a respective box polygon. Since the speed limit in the chosen area is 30 km/h, the measurement frequency is set to 10 Hz so that the distance between two measurement locations is smaller than the longitudinal box dimension and thus, data availability is increased. Due to the usage of three antennas and the repeatedly driven trajectory, each of the boxes contains many trajectory points leading to a large data pool for generating features. In parallel to the box assignment, the collected data is further processed to obtain pseudorange residuals from GNSS raw observations. Epoch-wise corrections are computed with respect to the reference trajectory and final satellite orbits provided by the CODE (Dach et al., 2024). The collected raw data is then rectified by applying these correction values, which include the geometry (Euclidean distance from satellite to the receiving antenna), relativistic effects, satellite clock errors and ionospheric and tropospheric effects by utilizing the Ionosphere Exchange Total Electron Content (IONEX TEC) map provided by the IGS and Vienna Mapping Functions 3 (VMF3) (Landskron and Böhm, 2018), respectively. Using these Observed-Minus-Computed (OMC) values, also known as pre-fit residuals, the DD pseudorange residuals are computed, as outlined in Ruwisch et al. (2020), by forming a short baseline to the reference station *EE01* and differencing with respect to a high-elevating LOS reference satellite.

In the next step, all computed DD pseudorange residuals of each box polygon are assigned to a 360° azimuth × 90° elevation grid, corresponding to a resolution of 1°, which is also

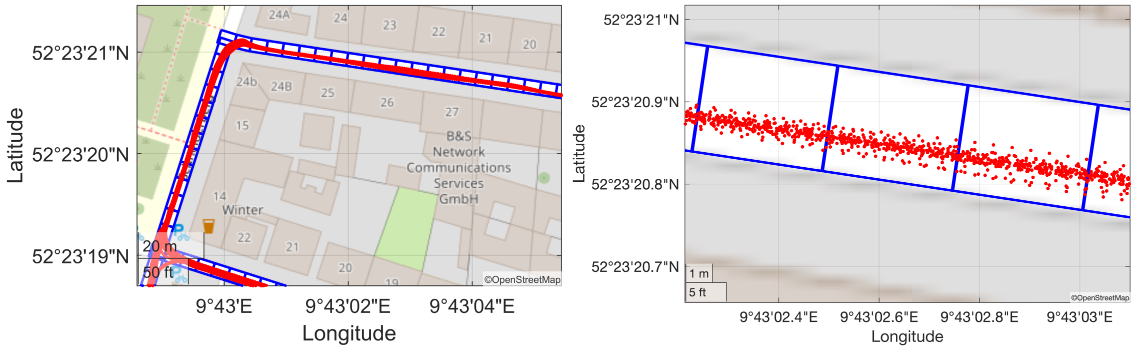

(a) (b)

Figure 4.16: GNSS Feature Map box polygon assignment. (a) trajectory sample with generated boxes in blue and trajectory points in red, (b) zoom-in for depicting the large data pool.

proposed for stacking residuals at static GNSS stations in Fuhrmann et al. (2014) and Dong et al. (2015). In this way, each of the satellite grids in a box contains several data points due to the multi-antenna setup and repetitions of driven trajectories. In order to provide one distinct value per satellite position and box polygon, the final pseudorange residuals feature is generated by calculating the mean values of each grid, respectively. In the end, the GNSS Feature Map consists of a skyplot for each of the box polygons containing pseudorange residual information with a resolution of 1°.

4.3.3 Waypoint Resolution

The density of the interpolated waypoints determines the resolution of the resulting map. The denser the interpolated points, the higher the resolution of the map. However, the complexity and computational costs also increase. The most significant variation in observed GNSS pseudorange errors arises when satellite visibility transitions from LOS to NLOS or vice versa. Therefore, it is important to study the changes in LOS and NLOS classification conditions and its transitions between waypoints with different distances to each other. The objective is to identify the similarities and differences caused by changes in the environmental situation in the longitudinal and lateral directions, as well as in height.

For this waypoint resolution study, three scenarios are simulated: i) points with a point distance of 20 cm each are simulated along the OSM road coordinates, ii) points with a point distance of 20 cm each are simulated perpendicular to the OSM line, iii) points are simulated by varying only the height component with a difference of 5 cm each. The location of the scenarios is depicted in Fig. 4.17, characterized by buildings on both sides of the street, which are 16 m to 18 m high, representing a typical urban trench in the city of Hannover. For each of these simulated points, ray tracing is performed for all satellite positions with a map resolution of 1° as described above, i.e. in a 360° azimuth × 90° elevation grid. In order to determine similarities and differences between signal propagation conditions of waypoints with different distances to each other, the LOS/NLOS classification results are compared. There are three possible outcomes: either the classification at the waypoints is the same, LOS satellite ray conditions turn into NLOS or NLOS satellite ray conditions transition to LOS.

Longitudinal Resolution

The results of the longitudinal waypoint resolution study are depicted in Fig. 4.18(a). In a perfect symmetric scenario, where the buildings have the same height and the distance of

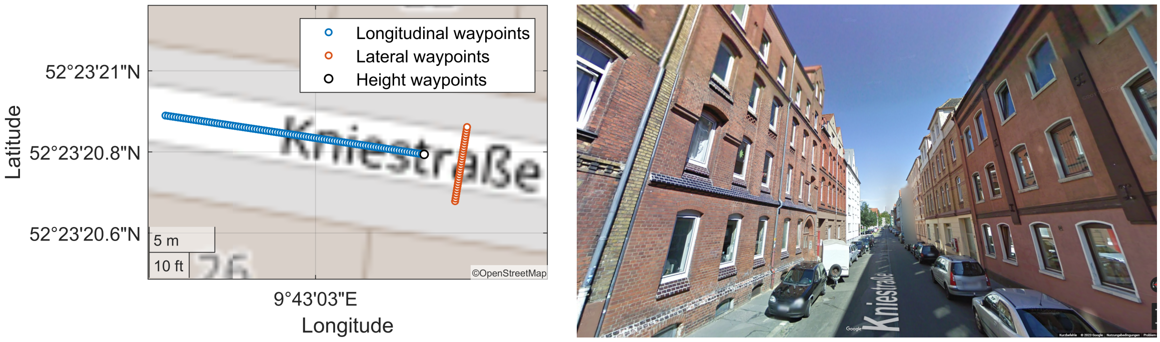

(a) (b)

Figure 4.17: Waypoint resolution simulation setup. (a) simulated waypoints displayed using OSM, (b) *GoogleStreetView* of the simulation environment.

the user to the surrounding buildings is not changing, no change in the satellite visibility would be expected. In a real-world scenario characterized by unequal heights of buildings and an absence of assurance regarding equivalent distances to those buildings, a change in the satellite visibility arises. As expected, the percentages of the same classifications decrease with increasing waypoint distance, as the local environment is more likely to vary. However, the similarities are substantial, with a percentage of up to 96 %, even for distances of up to 20 m. Consequently, there are only a limited number of satellite positions where the LOS-classified signals become NLOS or vice versa. Therefore, the more critical scenario is the classification of a true NLOS signal as an LOS signal, which would result in the decision to retain the satellite, e.g., in GNSS FMA-NE. For subsequent map generations, analyses, and applications, a longitudinal waypoint distance of 5 m is selected, which potentially leads to the same classification of > 96 % of the time.

As illustrated in Fig. 4.18(b), a visual aid is employed to ascertain the geometrical variations that give rise to the observed discrepancies. This figure demonstrates the shifting boundaries of the obstacles. The obstruction masks, which are computed for all simulated user locations, are presented in the skyplot and are color-coded according to their distance from the initial user location. The substantial similarity in the satellite classification outcomes is substantiated by the analogous structure of the obstruction masks. The minor discrepancies observed can be attributed to variations in the local building structures.

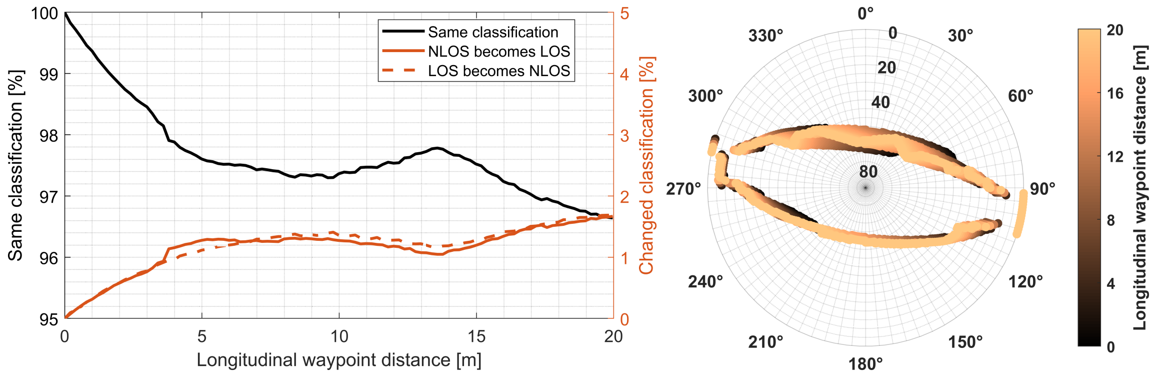

(a) (b)

Figure 4.18: Changes in ray classification conditions with longitudinally distant waypoints.

Lateral Resolution

The results of the analysis of the lateral waypoint resolution are shown in Fig. 4.19(a). As the user moves laterally in a street, the differences in the LOS/NLOS classification results are larger because the field of view varies more with slight changes in the user's location. This is confirmed by more deviations between the classification results of waypoints that have been laterally shifted. This variation is attributed to the change in the local environment, as the user moves closer to buildings on one side of the street while the buildings on the other side of the street are farther away from the simulated antenna location.The obstruction masks remain generally similar in shape, but they are shifted more as the distance between waypoints increases (see Fig. 4.19(b)). Consequently, the percentages of the same classifications decrease with increasing waypoint distance. When considering the potential user locations from curb to curb, the disparities reach up to 27 % for maximum distances of 5.7 m. However, given that the drive-able street width is less than 4 meters due to the presence of cars parked at the roadside, the number of instances falling into the same classification remains above 80 %. The uneven rise in LOS signals to NLOS and vice versa can be attributed to the imperfect real-world scenario, where buildings of varying heights result in changing visibility as one moves laterally along the street.

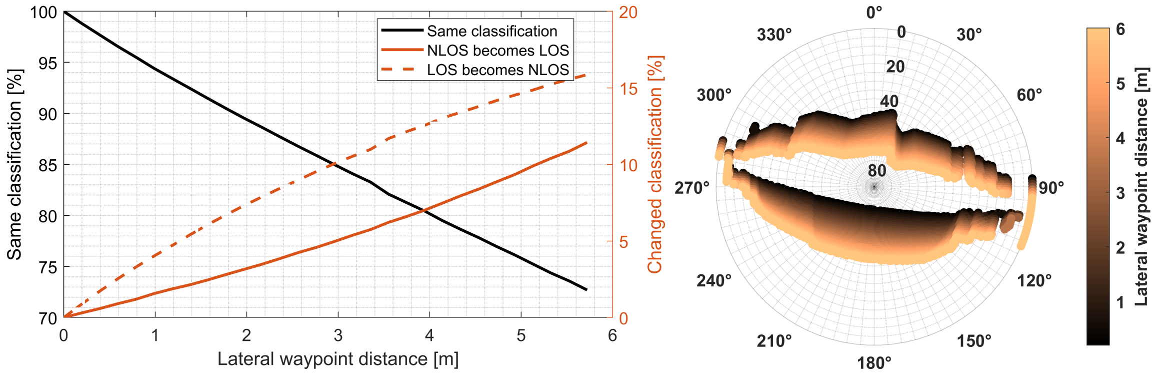

(a) (b)

Figure 4.19: Changes in ray classification conditions with laterally distant waypoints.

Height Resolution

The resolution of the map's height necessitates evaluation to ascertain whether cars with varying dimensions, such as sports vehicles or camper vans, can utilize the same map or if separate maps for different vehicle heights are required. Even in a perfectly symmetric reflection surface scenario, the visibility would vary when the height of the reception point is different. This study should determine the magnitude of the change in the LOS/NLOS classification of satellite signals. To this end, the findings of the classification analysis presented in Fig. 4.20(a) are supplemented with graphical representations depicting the varied dimensions of different vehicle types. The one extreme is the *Lamborghini Aventador* with only 1.13 m height above ground (Lamborghini Webpage, 2023). Many medium cars have dimensions around 1.50 m height above ground exemplary shown by a *Volkswagen Golf Variant* (Automobile Dimensions, 2023). The other extreme is a *Volkswagen Grand California* which is a van supplemented with a camper high roof leading to a total height above ground of 2.97 m (Automobile Dimensions, 2023).

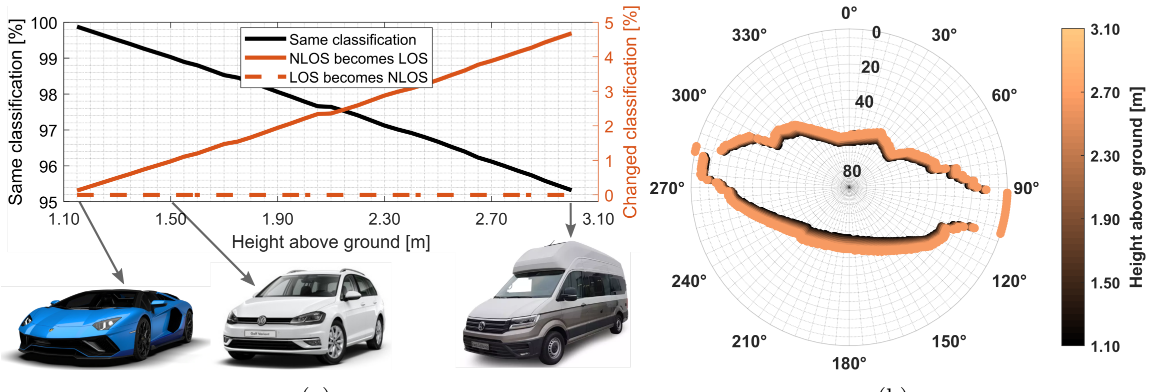

(a) (b)

Figure 4.20: Changes in ray classification conditions with varying height of the waypoints.

Since the field of view increases as the height of the vehicle is increasing, it is evident that the number of LOS satellite rays transitioning to NLOS condition is zero. Conversely, a subset NLOS satellite rays transition to LOS condition as the height of the vehicle is increasing, which is illustrated in Fig. 4.20(b). The obstruction mask for the sports vehicle defines the inner data points, while the mask for the camper van forms the outer frame in the skyplot. However, the number of changed classification conditions is marginal (less than 5 %) when comparing the sports vehicle with the camper van. The findings suggest that the incorporation of an additional map layer for vehicles exhibiting substantial variations in height is not necessary, given the minimal alterations in satellite ray classification conditions. Furthermore, when considering the three-dimensional scenario, the uncertainty is predicted to be predominantly influenced by the lateral resolution.

4.3.4 On the Similarity of GNSS Ranging Errors

For the validity of the GNSS Feature Map, it is necessary to ensure that observations received in a common box at the same satellite positions have similar error characteristics. The measurement campaign described in Sec. 4.3.2 provides several ways to test the error characteristics: i) Spatially distributed antennas on the roof of the test vehicle simultaneously collecting GNSS data provide information on the stochastic distribution of errors with respect to the changing antenna location. ii) Multi-GNSS data is available, providing information on the potential combination of different systems in a common map.

Antenna Combination

The DD code residuals computed for the front left and front right antennas (see Fig. 4.14(b)) are compared with respect to their error distribution. Each signal of the left and right antenna is analyzed individually for the entire training data, resulting in about one million residuals per signal. To compare the error distributions, Gaussian Mixture Model (GMM) with one, two, three, and four components are fitted to the extracted residuals of each signal.

The resulting fitted GMM curves together with the histogram of the respective data are shown in Fig. 4.21. The left column shows the results of the left antenna, the middle column shows the results of the right antenna, and the right column shows the results of the epoch-by-epoch residual differences between the two antennas. It is clearly visible that the undifferenced residuals of all signals show a non-normal distributed behaviour, because the environmentally caused ranging errors lead to positive ranging biases. Therefore, the single-component GMM

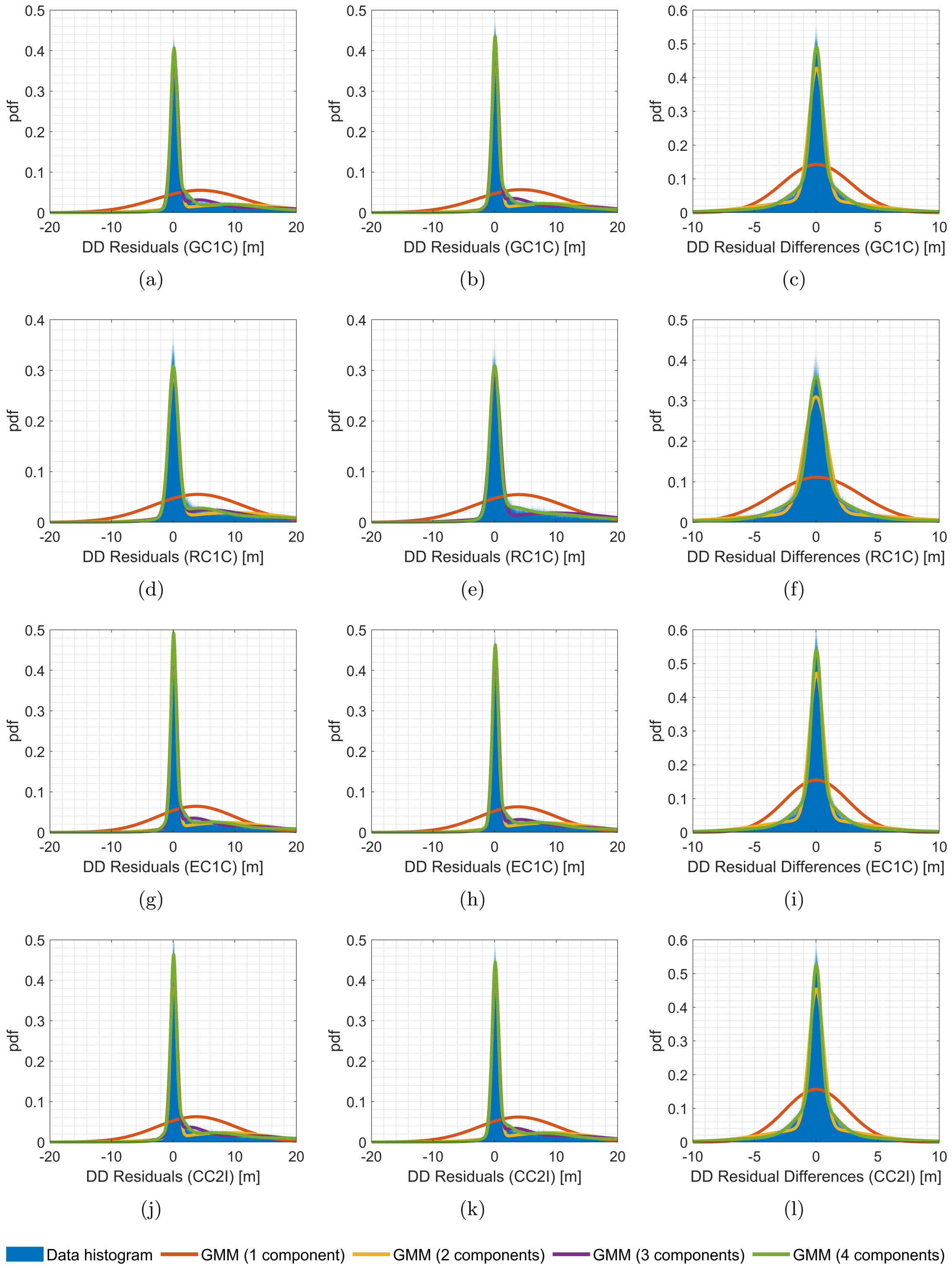

(a) (b) (c) (d) (e) (f) (g) (h) (i) (j) (k) (l)

Figure 4.21: Fitted GMM curves in conjunction with the histogram of the respective data. The left column shows the results of the left antenna, center column shows the results of the right antenna and the right column shows the results of the residual differences between these antennas. In each row, a different GNSS is evaluated.

does not fit to the residual data at all. Since different types of error sources (multipath, NLOS, diffraction) have different characteristics in terms of magnitude and noise, the best fitting GMM is the one with four components. For the residuals of the left and right antennas, the green curves smoothly follow the histogram data. The characteristics of the four-component

GMM estimation, i.e., the proportion, mean, and standard deviation, are shown in Tab. 4.4. The error distribution between the two antennas of the signals *GC1C*, *RC1C*, *EC1C* and *CC2I* is very similar, which is expressed by the proportions of the four components differing by a maximum of 6 %. Besides the GLONASS signal, the other signals also show a strong agreement in the mean values and standard deviations of the respective components. The component with the highest fraction always has a mean close to zero with a standard deviation around 0.2 m. The second largest component has a mean shift of about 7 m and a large standard deviation of more than 20 m. The third component still has a large influence (proportion values around 15 %). There is a small mean shift of less than 1 m and the standard deviation is around 2 m. The component with the least influence has a large mean of about 20 m and a standard deviation of 15 m to 25 m. Summing up the different components results in a GMM that represents the error distribution of the residuals.

To further check the agreement of the residual distributions, the differences between the residuals of the left and right antennas are analyzed. In the figures in the right column of Fig. 4.21 it can be seen that the positive tail of the histograms is eliminated by calculating the differences of the residuals. The residual differences have a zero mean, but the slope is too steep and the tails are too long to fit a normal distribution. Therefore, a GMM is still the best fit to the actual distribution of the residuals. Since there is almost no difference between a GMM with three or four components, the characteristics of the three component estimation are shown in Tab. 4.5. Again, all signals show similar proportions of the three components. The mean values of all components are close to zero after differencing, indicating the removal of any biases. The GMM is composed of a very low noise component (about 0.2 m), a moderate noise component (2 m to 3 m), and the least influential component has the highest noise (20 m to 30 m), representing the long tails. This is true for the signals *GC1C*, *EC1C* and *CC2I*, while the noise is approximately doubled for the signal *RC1C*.

Table 4.4: GMM parameters (mixing proportion, mean value μ and standard deviation σ) for the four component estimation.

		Left antenna			Right antenna		
Signal	Component	Proportion	μ [m]	σ [m]	Proportion	μ [m]	σ [m]
GC1C	1	0.43	0.07	0.20	0.48	0.13	0.26
	2	0.31	7.48	31.05	0.32	8.22	36.34
	3	0.17	0.82	1.81	0.14	1.32	1.83
	4	0.08	21.39	24.78	0.06	23.99	24.30
RC1C	1	0.56	0.01	0.57	0.54	0.002	0.57
	2	0.20	11.97	76.35	0.20	13.94	95.30
	3	0.20	3.79	13.38	0.16	2.04	6.48
	4	0.04	18.76	66.99	0.10	8.51	14.69
EC1C	1	0.45	0.06	0.17	0.49	0.11	0.22
	2	0.30	6.38	21.80	0.31	6.93	25.99
	3	0.17	0.59	1.50	0.13	0.92	1.51
	4	0.09	18.95	16.81	0.07	20.26	17.24
CC2I	1	0.44	0.06	0.19	0.50	0.09	0.23
	2	0.29	6.67	24.65	0.29	7.60	26.96
	3	0.18	0.62	1.80	0.14	1.15	2.31
	4	0.09	19.17	17.04	0.07	20.79	16.98

Table 4.5: GMM parameters (mixing proportion, mean value μ and standard deviation σ) for the components 1 to 3 of the four component estimation using DD residual differences between right and left antenna.

Signal	Component	Proportion	μ [m]	σ [m]
GC1C	1	0.43	0.03	0.19
	2	0.36	0.04	2.99
	3	0.21	0.10	31.24
RC1C	1	0.48	-0.003	0.43
	2	0.37	0.04	6.18
	3	0.15	0.45	67.99
EC1C	1	0.43	0.03	0.16
	2	0.35	0.02	2.45
	3	0.22	0.004	26.37
CC2I	1	0.40	0.02	0.15
	2	0.36	0.01	2.18
	3	0.24	0.06	23.75

GNSS Signal Combination

The above analyses demonstrate that observations from spatially distributed antennas can be aggregated and also provide insight into the characteristics of signals from different GNSS. While direct comparison of observation errors is not possible due to the transmission of measurements from different satellites, an evaluation of the overall distribution of observation errors can be made. Examining the estimated GMM parameters presented in Table 4.4, it was observed that the values of the four components for the different signals (*GC1C*, *RC1C*, *EC1C* and *CC2I*) are largely consistent, regardless of whether the observations were received on the left or right antenna. This means that the ranging errors received are similar, so the data can be used together to generate the map. Similarities are achieved in the respective proportions, with a large part of the first component having an approximate zero mean and a standard deviation below 1 m. Except for the GLONASS signal, the proportions of all components differ only between 1 % and 2 % and the means vary in a range below 2 m. Although the standard deviations of the *RC1C* signal differ from those of the other signals, the mean values remain consistent, with a maximum difference of less than 5 m. As shown, a basic understanding of the observation error is sufficient to mitigate the influence of erroneous satellites on position estimation (see Sec. 4.2.2). Consequently, the incorporation of GLONASS observations during the aggregation step of map generation remains advantageous. The following section provides a more comprehensive analysis, with illustrative examples, of the need to integrate all four systems in map generation.

4.3.5 Fully Populated Map Provision

To guarantee the consistent and reliable functionality of the map in subsequent applications, it is essential to ensure that it is fully completed, i.e. containing information for all elevation-azimuth combinations. This includes the provision of information on possible observation errors from all available satellites at a given location. As the foundation of the map generation in this thesis is the training data experiment (see Sec. 4.3.2), the number of observations in this training data set is finite. Consequently, it is necessary to ascertain whether the number of available measurements is sufficient for the generation of a reliable and fully populated map.

The most straightforward method of providing maps would be to generate a map for each signal, as this would ensure the lowest possible level of uncertainty in the data aggregation, given that only data from a single system and frequency are combined. To evaluate this possibility, two boxes from the map were selected for analysis in terms of GPS L1 measurement availability. Figure 4.22(a) and Figure 4.22(b) give an overview of the respective locations while Fig. 4.22(c) to Fig. 4.22(d) show the skyplots of the aggregated data from the aforementioned experiment and the interpolation results for the first location and Fig. 4.22(e) to Fig. 4.22(f) correspond to the second location. The interpolation, i.e. an eight-neighbor aver-

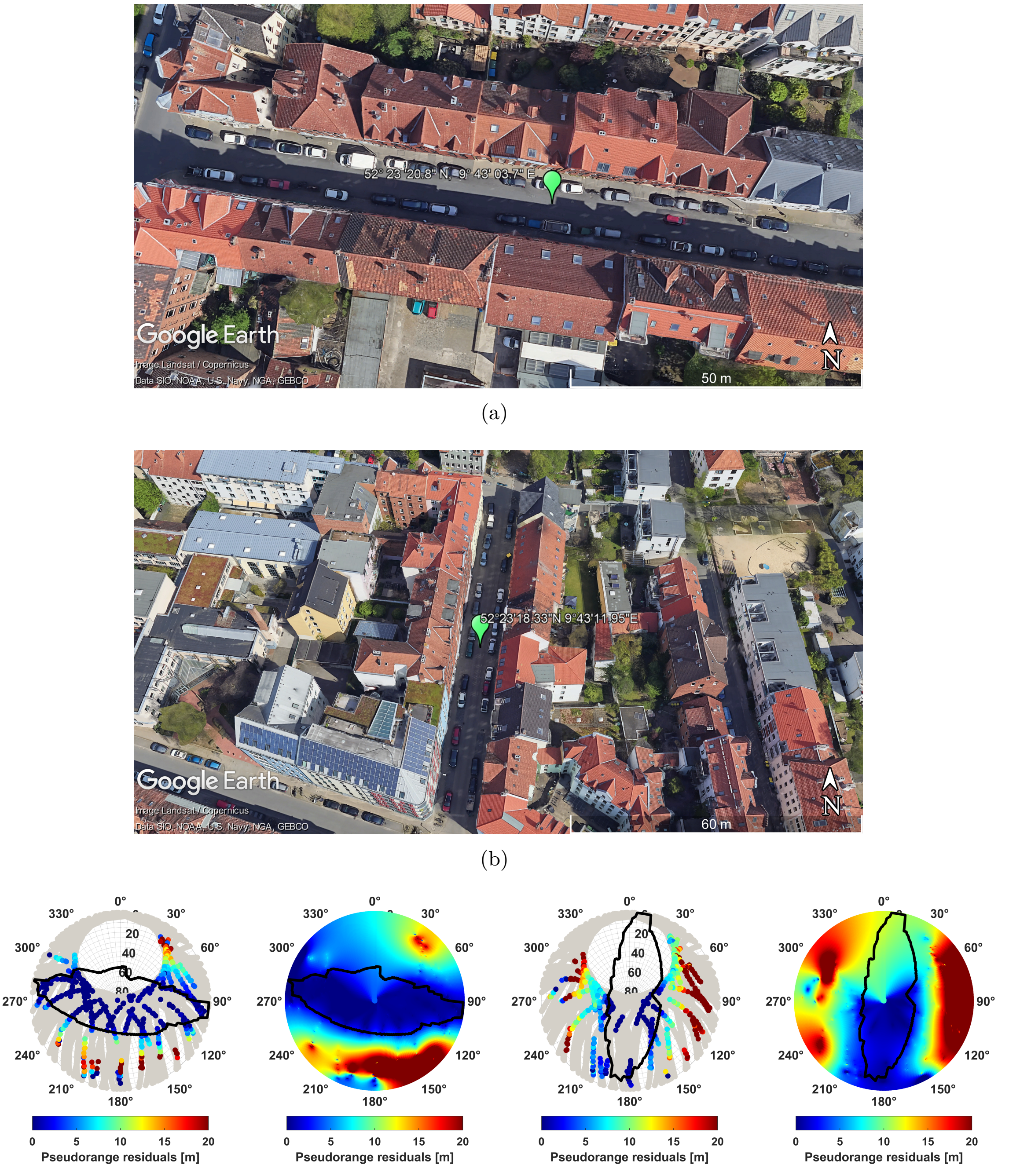

(a)

(b)

(c) (d) (e) (f)

Figure 4.22: GPS L1 pseudorange error map for two exemplary locations. (a) and (b) provide an overview of the respective locations with the green markers representing the center points of the boxes, (c) - (f) depict the skyplots of the aggregated data and interpolation results, respectively.

age interpolation, is necessary to ensure that features for all observed satellites are available in the later application. This specific interpolation method was selected because the behavior of multipath errors is not necessarily linear. Therefore, changes in all directions are considered by applying the eight-neighbor average interpolation. As illustrated by the figures, the data is interpolated through the north hole, a practice that yields no usable information, but also does not impact subsequent data. The data points are color-coded according to the mean pseudorange measurement error in each satellite bin. In addition, the theoretically available GPS satellite positions, computed for the center point of the box using IGS final orbit information, are shown in gray. An obstruction mask computed by ray tracing, is utilized to complete the figures. Given the impracticality of having hundreds of stationary stations transmitting GNSS measurements for data aggregation, and given that the data basis is a kinematic experiment, the map is always a generalization of the true situation. It is therefore to be expected that not each of the satellite bins is covered. However, the areas with gray satellite arcs and no map information are extensive for both locations. The interpolation guarantees full sky coverage of the generated maps, even in areas where training data availability was previously lacking. However, the larger the areas with no information, the higher the probability of providing incorrect information. To illustrate, in the region between 240 and 260 degrees of azimuth (see Fig. 4.22(c)), the aggregated data exhibits a significant gap in that area, and it is uncertain if the interpolation accurately represents the actual measurement error situation. A comparable case can be observed in Fig. 4.22(e) between 240 and 270 degrees of azimuth, where large measurement errors are expected due to the interpolation process, although the supporting data is lacking in that area.

In order to fulfill the reliability criterion of the map provision, it is necessary to evaluate an alternative method of providing maps. In the previous section, the similarity of GNSS pseudorange observation errors of different systems using the same frequency was derived. Consequently, another method of providing maps would be to generate a map using GPS, GLONASS, Galileo and BDS L1 measurements for data aggregation. The same locations were used for the evaluation, and the resulting skyplots of the aggregated data and the interpolation results are presented in Fig. 4.23. In comparison to the GPS L1 map generation, the skyplots show three times as many satellite bins covered. In particular, the regions situated beyond the obstruction border exhibit higher density,reducing the uncertainty associated with the interpolation process. The interpolation result provides a more detailed representation of pseudorange measurement error changes than the generalized pattern observed in Fig. 4.22. Additionally, notable discrepancies in magnitude are apparent. The aforementioned lack of data in Fig. 4.22(e) between 240 and 270 degrees of azimuth results in interpolated measurement errors of approximately 10 to 20 m. However, incorporating additional observations from other GNSS sources yields interpolated measurement errors of less than 3 m in that specific region.

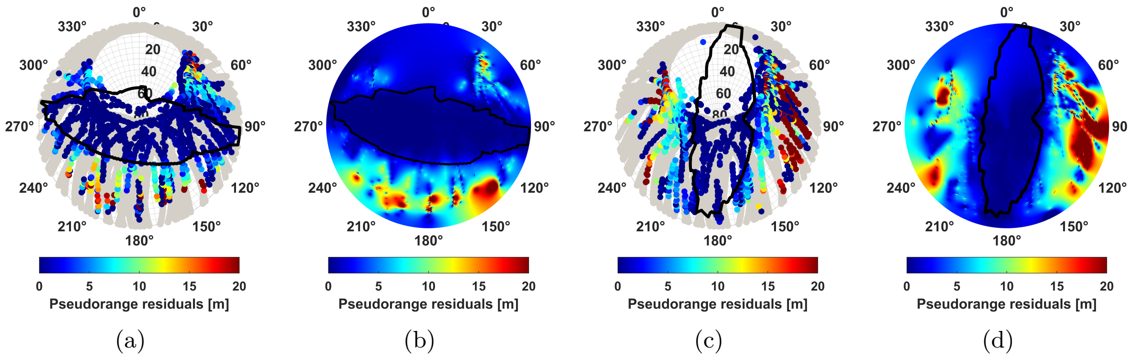

(a) (b) (c) (d)

Figure 4.23: Multi-GNSS L1 pseudorange error map for two exemplary locations.

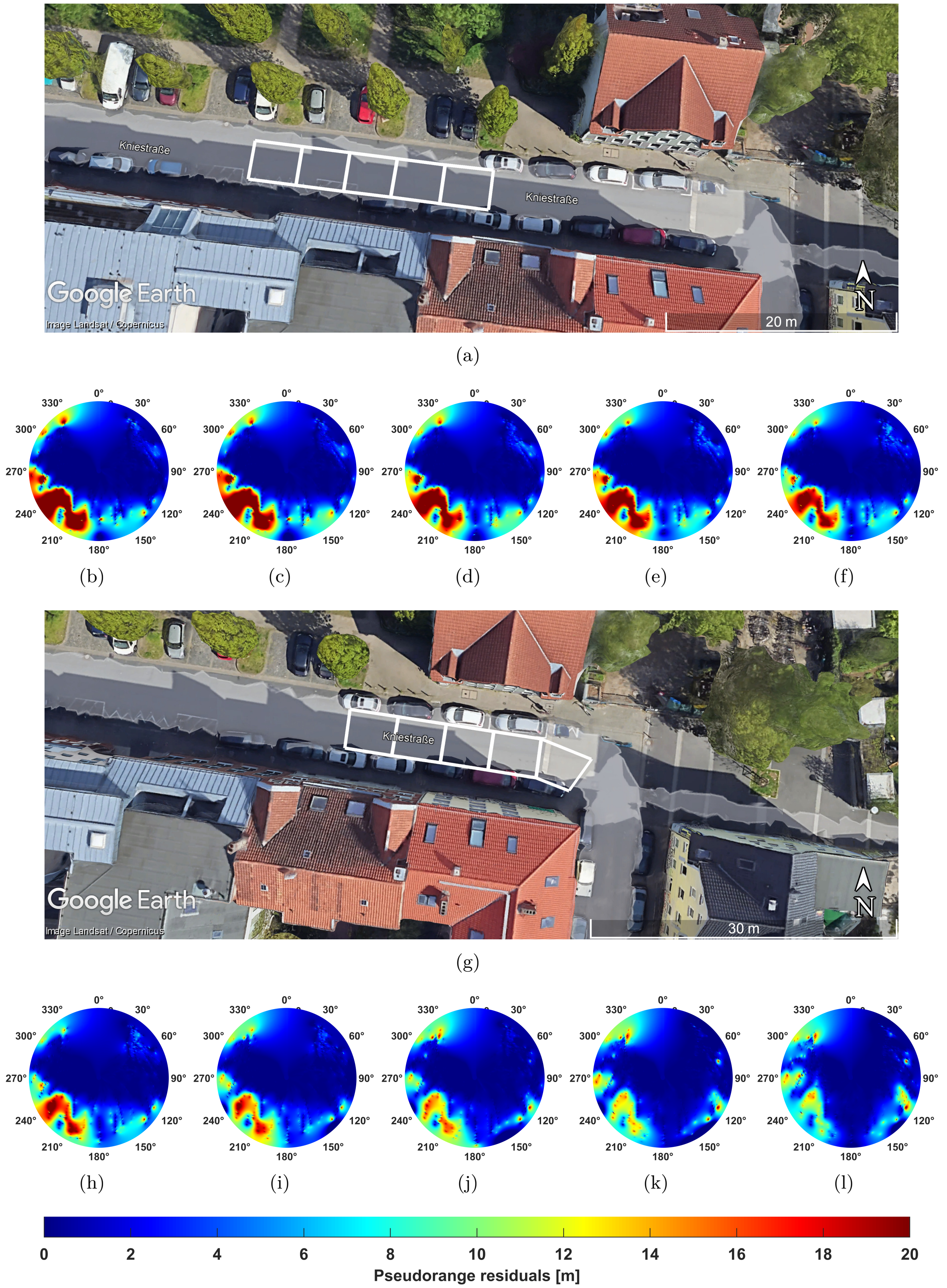
(a)

(b) (c) (d) (e) (f)

(g)

(h) (i) (j) (k) (l)

Figure 4.24: Skyplots for ten exemplary map waypoints of a pseudorange residuals map generated by aggregating multi-GNSS L1 pseudorange data. First and third row show the location of the boxes, second and fourth row show the resulting skyplots containing interpolated pseudorange residual information.

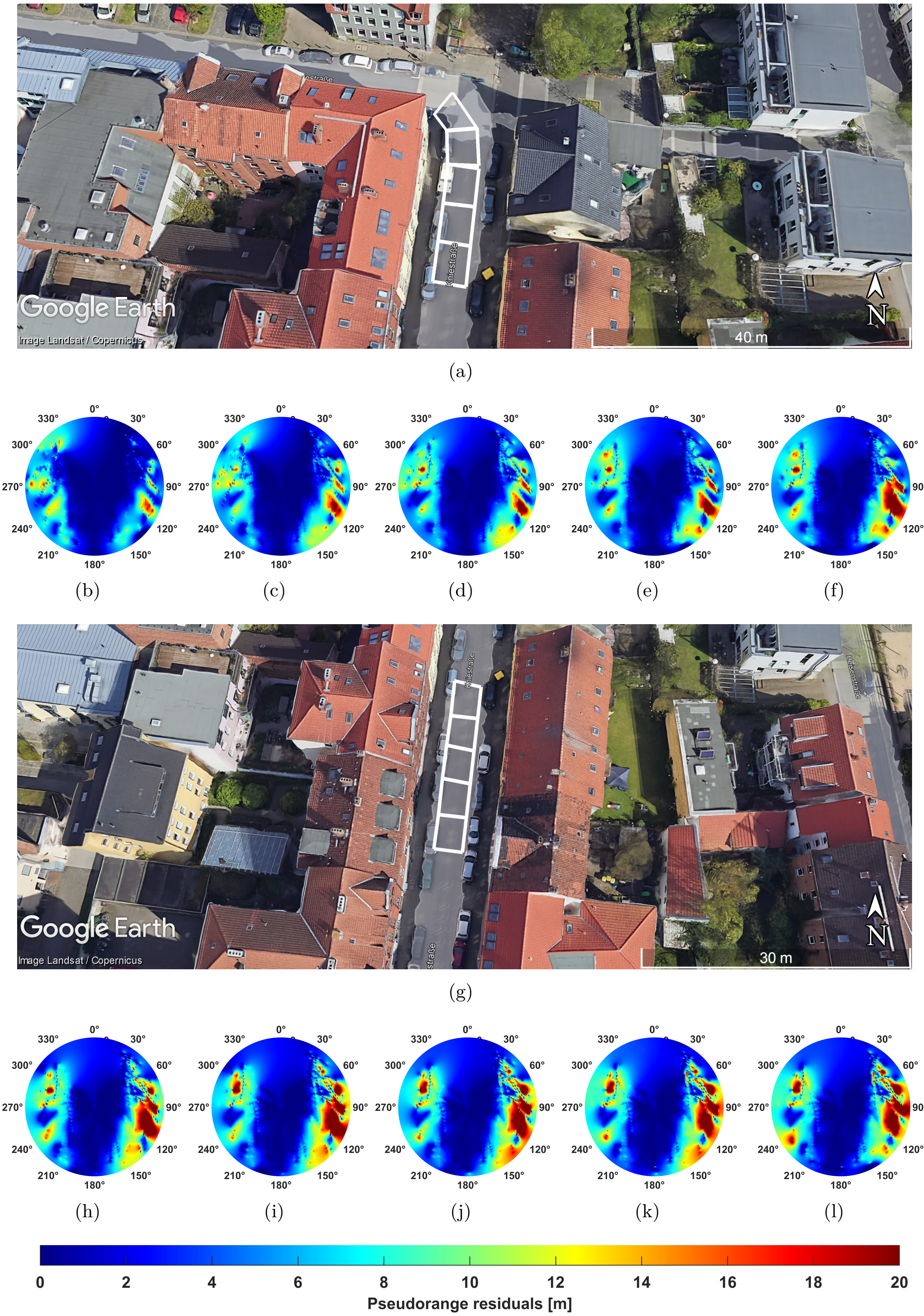

(a)

(b) (c) (d) (e) (f)

(g)

(h) (i) (j) (k) (l)

Figure 4.25: Skyplots for ten exemplary map waypoints of a pseudorange residuals map generated by aggregating multi-GNSS L1 pseudorange data. First and third row show the location of the boxes, second and fourth row show the resulting skyplots containing interpolated pseudorange residual information.

It can be concluded that the incorporation of multiple systems into a single map increases the availability of measurement error, thereby reducing the uncertainty associated with interpolation. Furthermore, the map is less generalized and provides more detailed information on the error distribution, particularly in areas beyond the obstruction border. For utilization in the following sections, a map is generated based on the available L1-band frequencies (Receiver Indeptendent Exchange Format (RINEX) observation codes: GPS *GC1C*, GLONASS *RC1C*, Galileo *EC1C*, BDS *CC2I*). The final product is a GNSS Feature Map consisting of pseudorange residuals for all satellite positions at all boxes along the selected trajectory. Exemplary map sections of that trajectory are depicted in Fig. 4.24 and Fig. 4.25.

5

Application Examples and Case Studies

This chapter is dedicated to the practical evaluation of the proposed methods. The core of the analyses are several vehicle test drives, where the impact of the proposed observation exclusion and weighting strategies is investigated with respect to the performance parameters introduced in Sec. 2.7 and with respect to GNSS receiver internal solutions. These kinematic case studies are further distinguished by their environmental situation, which encompasses two distinct scenarios: moderate signal reception conditions in a *medium urban trench* and harsh signal reception conditions in a *deep urban trench*. Note that parts of these application examples are based on the author's contributions Ruwisch and Schön (2022b), Ruwisch and Schön (2023) and Ruwisch and Schön (2025).

5.1 Kalman Filter Settings

The Kalman filter is a mathematical algorithm that is employed for the estimation of the state of a dynamic system from a series of measurements that are susceptible to noise and other forms of inaccuracy (see Sec. 2.2). It is of significant importance to ensure that the Kalman

Table 5.1: GNSS RTK EKF Settings.

Satellite Orbit/Clock	Final CODE MGEX Products (Montenbruck et al., 2013)
Observation Data	Multi-GNSS Multi-Frequency
Elevation Cutoff	10°
Standard weight model	C/N$_0$-dependent (see Eq. 2.23)
Ambiguity Resolution	Partial Ambiguity Resolution using LAMBDA (Teunissen, 1995a)
Probability of false alert	$1 \cdot 10^{-2}$
Probability of missed detection	$1 \cdot 10^{-3}$
σ_{Φ_0}	0.005 m
σ_{ρ_0}	0.5 m
$\sigma_{\dot{\rho}_0}$	$0.1\ \frac{\text{m}}{\text{s}}$
σ_{pos}	10 m
σ_{vel}	$10\ \frac{\text{m}}{\text{s}}$
σ_{amb}	10 cycles
q_{pos}	$100\ \text{m}^2/\text{s}$
q_{vel}	$100\ \frac{\text{m}^2}{\text{s}}/\text{s}$
q_{amb}	$10^{-4}\ \text{cycles}^2/\text{s}$

filter is correctly configured, as this has a considerable impact on its overall performance and the precision of the estimation. These settings encompass the selection of process and measurement noise covariance, initial state estimates, and the state transition model. The process noise covariance matrix represents the uncertainty inherent to the model's dynamics, whereas the measurement noise covariance reflects the uncertainty inherent to the sensor measurements. Accurate tuning of these matrices is of vital importance, as overly optimistic settings may result in filter divergence, whereas overly conservative settings may result in a failure to respond adequately to changes in the system state. The correct configuration of these settings determines the Kalman filter's ability to provide optimal state estimates, influencing the accuracy and reliability of the navigation solution.

In the context of applying the proposed Kalman filter to automotive experiments, where the environment is subject to rapid change and the dynamics of the vehicle are neither constant nor known in advance, it is evident that a single set of parameters cannot yield optimal results for a range of data sets. The objective of this thesis is to evaluate the relative performance of the proposed algorithms in comparison to established navigation solutions. Therefore, the focus is not on achieving the optimal tuning of Kalman filter parameters, but rather on utilizing the same set of parameters for all approaches. The set of parameters employed to generate the results presented in the following sections is illustrated in Tab. 5.1.

5.2 Automotive Experiment in Medium Urban Trench

5.2.1 Setup

In order to evaluate the performance of the proposed approaches for urban GNSS navigation, a kinematic experiment was carried out in a residential area in the city of Hannover, Germany, on DOY 235 in 2023 (23rd August 2023). The test drive was planned and conducted within the framework of the KOMET project (Ruwisch et al., 2024).

The ground truth of the trajectory together with the institute's reference station *EE01* is depicted in Fig. 5.1(a). The trajectory starts and ends with a static phase on a parking space with only few obstructions and in between, the rectangular shaped part was repeatedly driven (ten times). The kinematic part of the route passes through a residential area in the city of Hannover, where the streets are about 5 m wide and the surrounding houses are about 20 m high. A typical situation of this trajectory is shown in Fig. 5.1(b), where additionally the projected grids of the generated map are displayed with white boxes.

The measurement configuration depicted in Fig. 5.1(c) consisted of one *Septentrio PolaRx5e* receiver connected to a *Tallysman TW7972* patch antenna mounted on the roof of the test vehicle. The receiver collected raw multi-GNSS data at a sampling rate of 1 Hz. The used observation data, given in the RINEX notation, is depicted in Tab. 5.2. In addition, a high quality inertial navigation system (*iMAR iNAT-RQT-4003*) was connected to a *NavXperience NAX3G+C* antenna collecting multi-GNSS data at a sampling rate of 1 Hz and IMU data at a sampling rate of 400 Hz. To this end, the ground truth of the trajectories is computed by combining the GNSS carrier phase and Doppler observations with the IMU data in a tightly coupled relative positioning that was computed in post-processing using the commercial software *TerraPOS* (Kjørsvik et al., 2009).

In post-processing, the data is further evaluated with regards to the multi-GNSS satellite visibility condition by investigating ray tracing classification results. All observed satellite signals are classified as LOS, MP, NLOS and blocked. The number of available satellites per ray condition is illustrated in Fig. 5.1(d) (upper row), together with the percentage of LOS

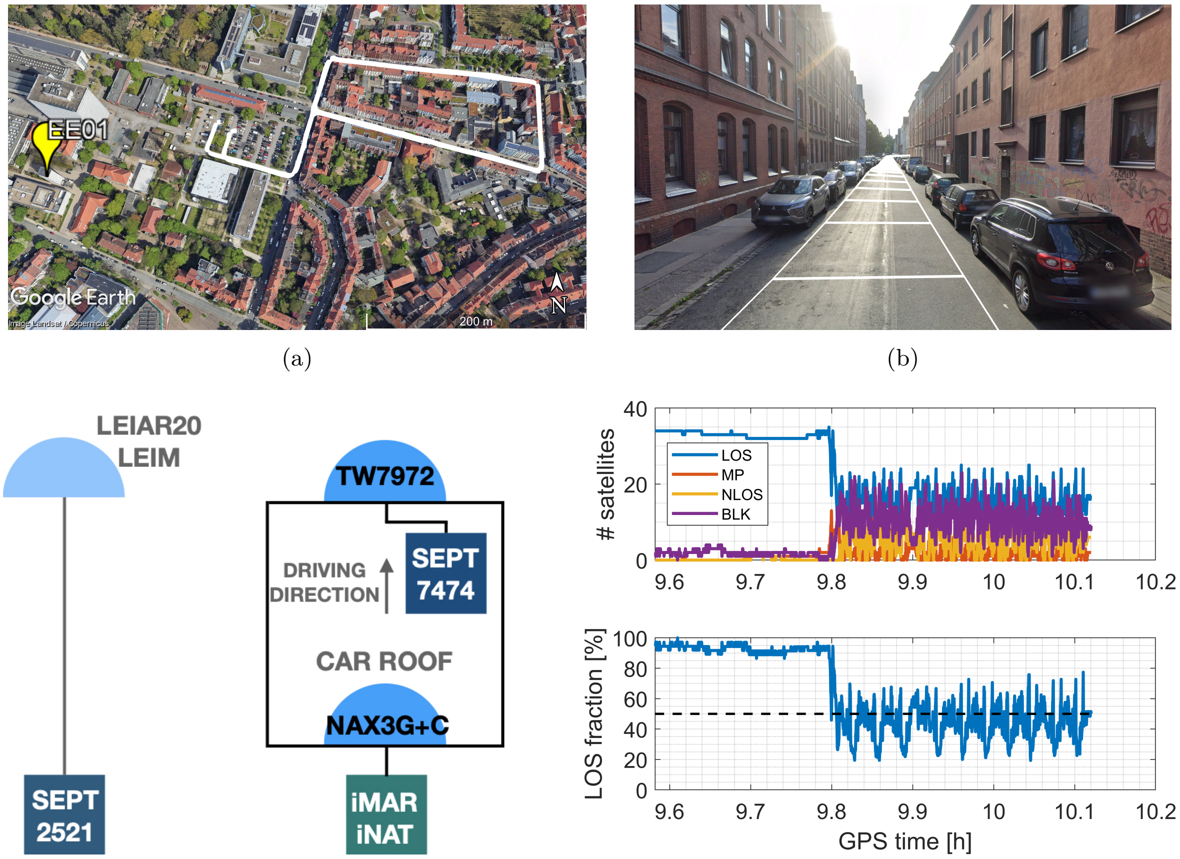

(a) (b)

(c) (d)

Figure 5.1: Kinematic experiment setup of the automotive experiment in medium urban trench. (a) ground truth of the ten times repeatedly driven trajectory, (b) typical environmental situation with map grids depicted as white polygons, (c) measurement configuration, (d) multi-GNSS satellite visibility information based on ray tracing results.

Table 5.2: Observation data recorded by the *Septentrio PolaRx5e* receiver, given in RINEX notation.

Observation Data	*GL1C, GL2L, GL2W, GL5Q, RL1C, RL1P, RL2C, RL2P, EL1C, EL5Q, EL7Q, EL8Q, CL1P, CL5P, CL2I, CL6I, CL7I*

satellites (bottom row). The data set is classified as a *medium urban trench*, given that in a majority of the trajectory, the LOS satellite availability is below 50 % (minimum 20 % LOS satellites), yet there is a recovery in availability between these parts, reaching up to 70 %. This provides a foundation for evaluating the performance of existing state-of-the-art GNSS RTK algorithms and for assessing the effectiveness of our proposed approaches.

5.2.2 Accuracy Performance

At first, the position solution of the GNSS RTK EKF with respect to the reference trajectory is shown in Fig. 5.2. Two approaches from existing literature, i.e., C/N$_0$ weighting and 3DMA NLOS exclusion (3DMA-NE) are compared with the developed GNSS Feature Map-aided approaches, i.e., GNSS FMA-NE, GNSS FMA-W using Huber loss function, GNSS FMA-W using Geman-McClure loss function, and GNSS FMA-W using HG loss function.

The horizontal and vertical PE with respect to the ground truth are illustrated in Fig. 5.2 versus time and as a cumulative distribution. Thereby, the static phases at the parking space have been excluded from the analyses, as for this non-dynamic, nearly open-sky scenario, all methods provide deviations of a few centimeters, which can be considered typical for an RTK solution. During the drive through the medium urban trench, the horizontal deviations varied between centimeters and decimeters. However, notable discrepancies between the various estimation methods are evident. Both NLOS exclusion strategies (3DMA-NE and GNSS FMA-NE) transition from an RTK fix solution to a DGNSS solution at 9.83 h and 9.86 h, respectively, due to the absence of LOS carrier phase availability. This results in a maximum horizontal

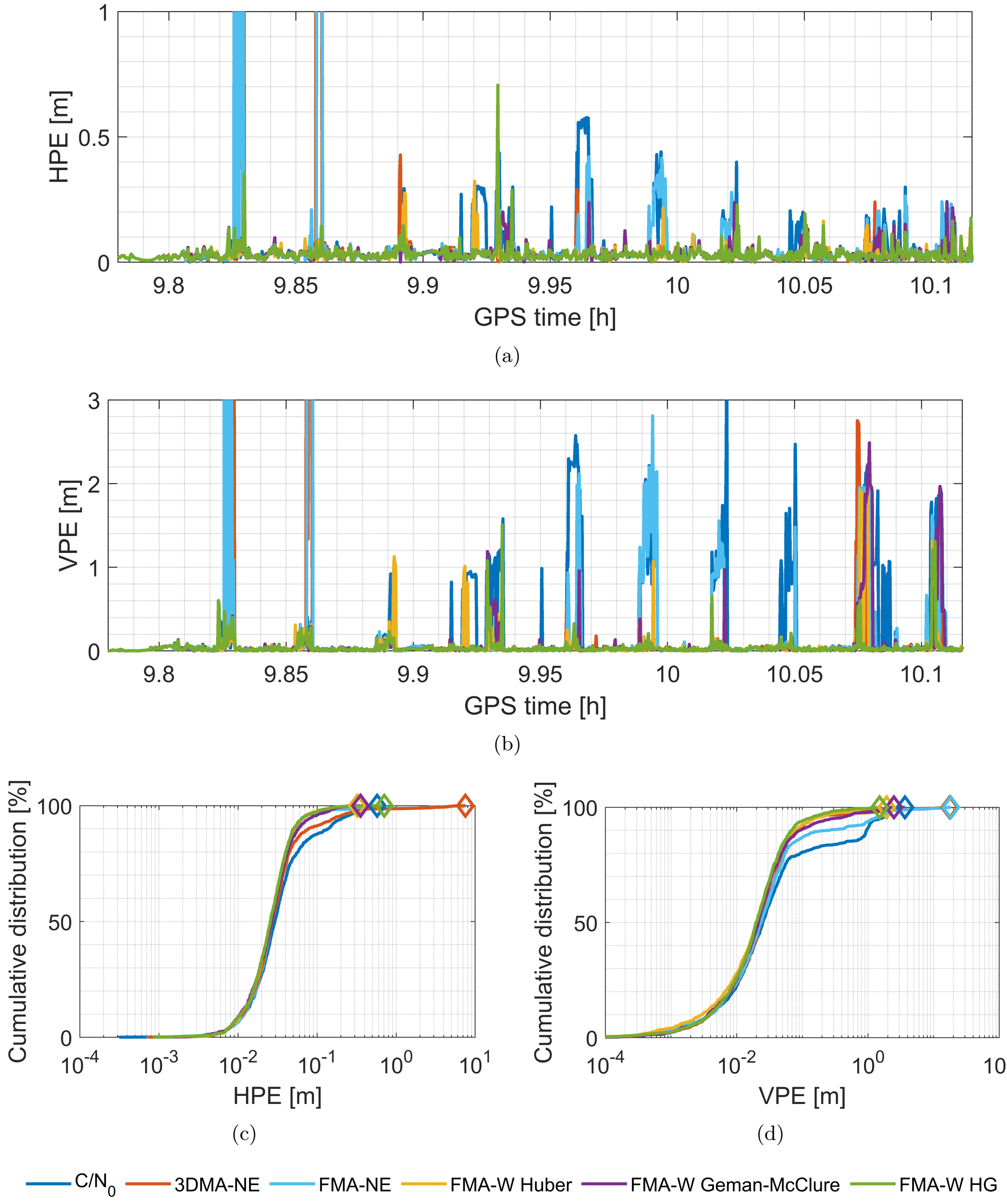

(a)

(b)

(c)

(d)

Figure 5.2: Horizontal and vertical position errors of the different approaches versus time ((a) and (b)) and as cumulative frequency diagrams ((c) and (d)). Note the different axis limits for horizontal and vertical errors.

PE of approximately 8 m. All the remaining strategies are capable of maintaining centimeter-to-decimeter accuracy throughout the entire trajectory, even in scenarios with only 20 % LOS observation availability. The GNSS FMA-W methods demonstrate a comparable performance, exhibiting a notable reduction in horizontal PE at epochs where the C/N_0 weighting solution reaches deviations that exceed 40 cm. The similarity is further emphasized by the cumulative distribution, in which the yellow, purple and green graphs are superimposed. They follow the 3DMA-NE graph at small deviations but show a steeper slope as soon as the deviations increase, indicating a reduction in larger errors.

The relative performance of the aforementioned approaches is similar when investigating the vertical PE. However, since the vertical component is less precisely determinable, the magnitude of the error is increased to the meter-level in challenging situations. In particular, the NLOS exclusion strategies and the C/N_0 weighting approach demonstrate repeatable meter-level deviations from the ground truth. Conversely, all GNSS FMA-W approaches are capable of mitigating larger errors while still providing solutions within the centimeter to decimeter range.

Table 5.3 provides an overview of the characteristic values of the different approaches for horizontal and vertical position accuracy. As expected, the proposed GNSS FMA-NE method shows comparable performance to the 3DMA-NE method, given that the similar principle of excluding faulty satellites is employed. Furthermore, the similarity in performance of the three GNSS FMA-W approaches is evidenced by the minor differences in position errors observed for specific percentiles. In consideration of the performance specifications for automotive applications outlined in Section 2.7.4, Tab. 2.10, it can be seen that the C/N_0 weighting and the GNSS FMA-NE methods are unable to meet the lane keeping application requirements for 95 % accuracy in both the horizontal and vertical directions. On the other hand, 3DMA-NE, GNSS FMA-W Huber, GNSS FMA-W Geman McClure and GNSS FMA-W HG methods provide a 95 % accuracy of the horizontal and vertical component, which meets the specified lane keeping requirement. A comparison of the overall RMS reveals that the GNSS FMA-W methods enhance accuracy in comparison to C/N_0 weighting. The utilization of map information and the Huber, Geman-McClure and HG loss functions has resulted in an improvement of the RMS of the horizontal PE by 58 %, 54 % and 54 %, respectively, and an improvement of the

Table 5.3: Horizontal and vertical position accuracy of the different approaches given in percentiles.

	Horizontal position accuracy [m]					
	50 %	75 %	95 %	99 %	RMS	Ratio [%]
C/N_0	0.029	0.046	0.222	0.536	0.101	-
3DMA-NE	0.027	0.039	0.067	2.295	0.466	-362
GNSS FMA-NE	0.027	0.041	0.172	2.080	0.482	-379
GNSS FMA-W Huber	0.026	0.037	0.069	0.146	0.043	58
GNSS FMA-W Geman-McClure	0.027	0.038	0.086	0.176	0.047	54
GNSS FMA-W HG	0.026	0.037	0.068	0.146	0.046	54
	Vertical position accuracy [m]					
	50 %	75 %	95 %	99 %	RMS	Ratio [%]
C/N_0	0.025	0.055	1.519	2.229	0.557	-
3DMA-NE	0.023	0.043	0.148	2.751	1.068	-92
GNSS FMA-NE	0.024	0.047	1.214	3.994	1.276	-129
GNSS FMA-W Huber	0.020	0.039	0.155	1.126	0.209	62
GNSS FMA-W Geman-McClure	0.021	0.041	0.290	1.829	0.272	51
GNSS FMA-W HG	0.020	0.037	0.120	0.533	0.116	79

RMS of the vertical PE by 62 %, 51 % and 79 %, respectively. Conversely, the 3DMA-NE and GNSS FMA-NE methods have an adverse impact on the overall result due to the transition from an RTK fix solution to a DGNSS solution at specific epochs.

5.2.3 Attainable Integrity

The integrity of the different position solutions is evaluated by Stanford diagrams for the horizontal and vertical components, respectively. The corresponding protection levels of the solutions were computed using Eq. 2.85 and Eq. 2.86 based on a probability of failure of 10^{-8}. The corresponding alert limits are HAL $= \sqrt{0.44^2 + 0.44^2} = 0.622$ [m] and VPL $= 1.40$ [m] (see Tab. 2.11), although values for German roads have recently been defined (Kulemann and Schön, 2025; Schön et al., 2025).

The resulting Stanford diagrams are illustrated in Fig. 5.3 for the horizontal component and in Fig. 5.4 for the vertical component. Again, the static phases at the parking space have been excluded from the analyses, as for this non-dynamic, nearly open-sky scenario, all methods provide an accuracy better than the alert limits and the position errors are well bounded. Therefore, the presented integrity evaluation is an accurate reflection of the actual situation and have not been embellished by the static part of the experiment. The attainable integrity is assessed on the basis of a probability of failure of 10^{-8}. In this regard, the test data (1211 epochs) provide a good estimate of integrity. However, more test data must be evaluated in order to assess the defined probability of failure.

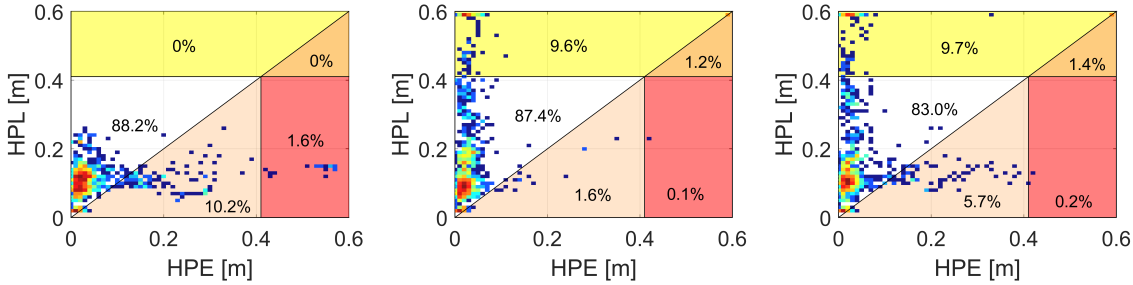

(a) C/N$_0$ (b) 3DMA-NE (c) GNSS FMA-NE

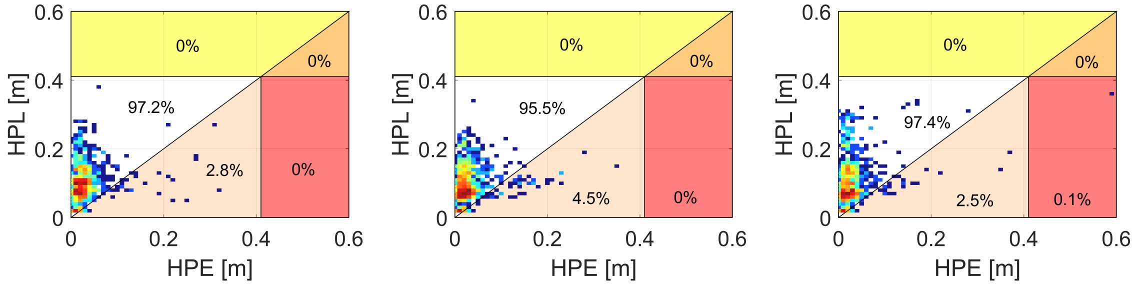

(d) GNSS FMA-W Huber (e) GNSS FMA-W GMC (f) GNSS FMA-W HG

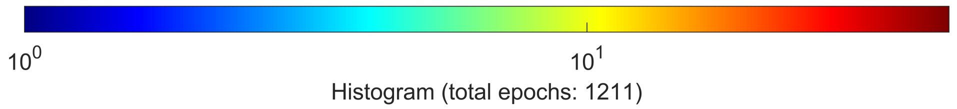

Figure 5.3: Integrity evaluation of the horizontal component for the different methods.

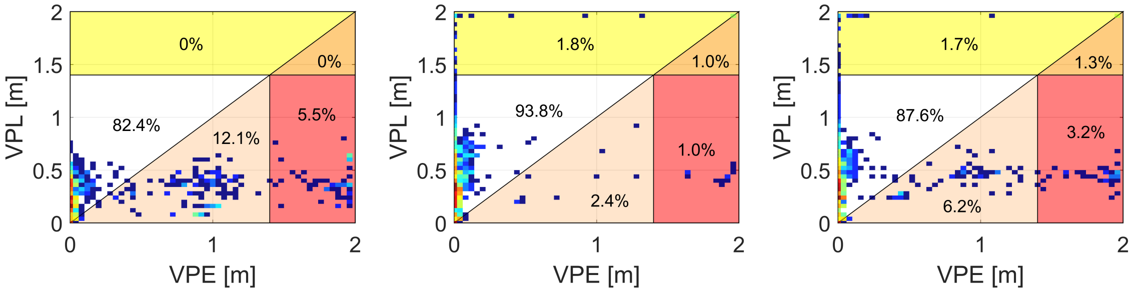

(a) C/N$_0$ (b) 3DMA-NE (c) GNSS FMA-NE

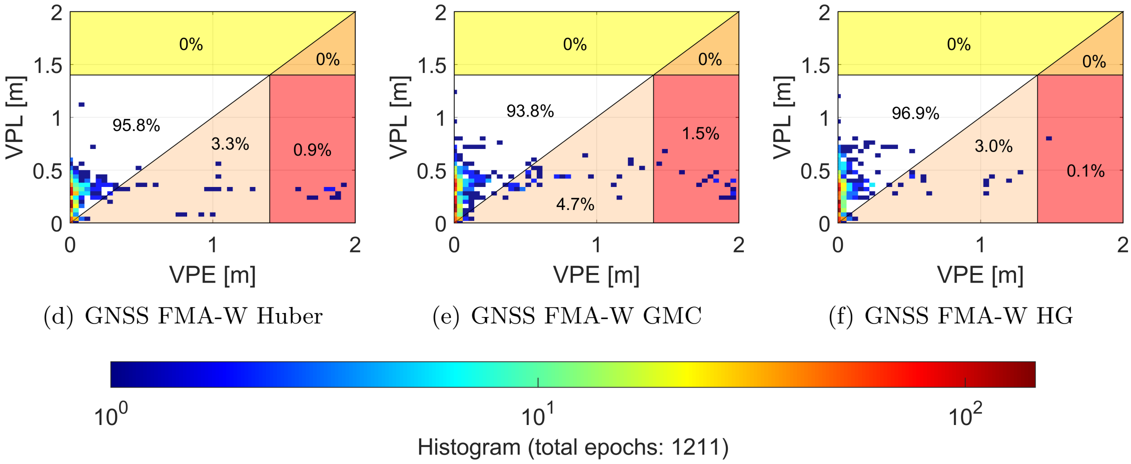

(d) GNSS FMA-W Huber (e) GNSS FMA-W GMC (f) GNSS FMA-W HG

Figure 5.4: Integrity evaluation of the vertical component for the different methods.

Horizontal Component

In 88.2 % of cases, the system operates in nominal mode when using the C/N$_0$ weighting method. Nevertheless, 10.2 % of the epochs are misleading information, as the protection level is smaller than the position error, thereby bounding the error inadequately. Additionally, a small number of hazardous misleading information epochs (1.6 %) are present, representing the most critical condition. When applying 3DMA-NE, these instances are reduced to a single epoch (0.1 %), although this reduction comes at the cost of an increase in the number of system unavailability instances and a slight decrease in the proportion of nominal operation epochs, which account for 87.2 % of the total. The result for GNSS FMA-NE is similar to 3DMA-NE, with the difference that a few data points moved from nominal operation mode to misleading information condition. All three feature map-aided robust estimation methods improve the overall integrity of the system, with only slight differences in the proportion of nominal operation epochs. Among the GNSS FMA-W Huber, GNSS FMA-W Geman-McClure and GNSS FMA-W HG methods, the latter demonstrates the most extensive improvement (97.4 %) in nominal operations, while there are no instances where the system is unavailable. On only 2.5 % of instances is misleading information present, and just one epoch yields hazardous misleading information.

Vertical Component

In comparison to horizontal PE, vertical PE is of a greater magnitude, given that the vertical component is less precisely determinable using the GNSS sensor. Conversely, the vertical alert limit for automotive applications is less stringent, resulting in overall proportions of Stanford diagram conditions that are comparable. A comparison of the six estimation methods reveals that the C/N$_0$ weighting exhibits the lowest number of nominal operations (82.4 %), followed by the GNSS FMA-NE approach (87.6 %). Due to the less stringent alert limit, the number of system unavailability for the 3DMA-NE method is decreased, resulting in the same proportion of nominal operations as for the GNSS FMA-W Geman-McClure method. The largest nominal operation proportions are achieved by the GNSS FMA-W Huber (95.8 %) and GNSS FMA-W HG (96.9 %) methods. Consequently, the proposed GNSS FMA-W HG method shows the best overall integrity, having only a few (3.0 %) misleading information instances and only one hazardous misleading information epoch.

5.2.4 Ambiguity Resolution

Using GNSS RTK positioning technology, the ambiguity resolution is an important measure that helps to understand the occurrence of position error magnitudes as well as the correct observation uncertainty assignment. Figure 5.5 illustrates the 3D position error of the float (yellow) and fixed (green) solution along with the ambiguity success rate (gray) for C/N$_0$ weighting, 3DMA-NE, GNSS FMA-NE, GNSS FMA-W Huber, GNSS FMA-W Geman-McClure and GNSS FMA-W HG method. It is evident that the more robust the estimation method, the smaller the error of the float solution will be. Consequently, there is a greater probability of achieving an accurate fixed solution, as superior float estimates typically result in more precise fixed estimates. As illustrated by the time series, the 3D position error of the fixed solution frequently reaches deviations in the meter-level at instances where the float solution already shows deviations in the meter range. This phenomenon is particularly evident when employing the C/N$_0$ weighting method. In numerous epochs, the fixed solution is demonstrably inferior to the float solution, which is indicative of an erroneous fixed set of ambiguities despite the ambiguity success rate being 100 %.

In contrast, all three feature map-aided robust estimation methods yield a more precise float solution, with only a small number of data points in the fixed solution exhibiting significant deviations. It is noteworthy that the ambiguity success rate exhibits a significant drop, particularly for the GNSS FMA-W German-McClure and GNSS FMA-W HG methods, which are

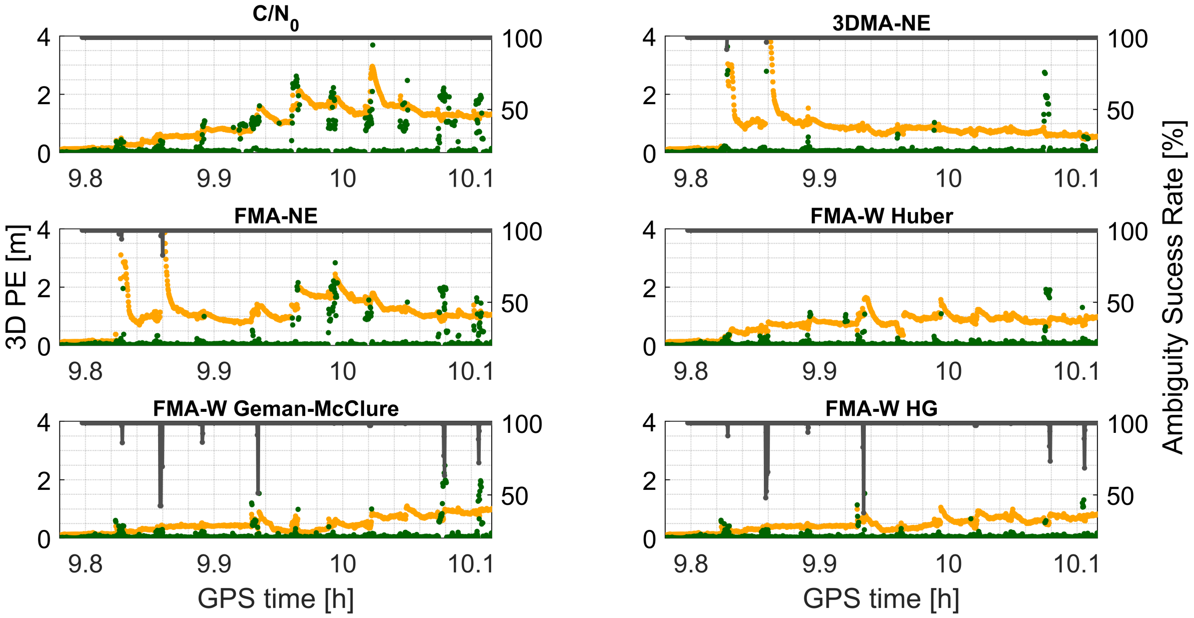

Figure 5.5: 3D position error of the float (yellow) and fixed (green) solution along with the ambiguity success rate (gray) for C/N$_0$ weighting, 3DMA-NE, GNSS FMA-NE, GNSS FMA-W Huber, GNSS FMA-W Geman-McClure and GNSS FMA-W HG.

known to be highly damping larger observation errors. However, these drops are not directly linked to large observation errors; rather, the opposite is true. Despite a decline in the ambiguity success rate, the position error remains low. The drop in success rate can be attributed to erroneous observations, which are correctly identified with considerable uncertainties. This results in a larger ambiguity search space, ultimately leading to a reduction in the success rate. During the same epochs, the C/N_0 weighting method exhibits a 100 % ambiguity success rate, yet the position error increases. This phenomenon can be attributed to the low uncertainty associated with erroneous observations, which subsequently impairs the ambiguity resolution and results in a false fix.

In order to substantiate these theses, Figure 5.6 illustrates the percentage of fixed ambiguities versus time, as cumulative distribution, and as the relation between the percentage of fixed ambiguities with the 3D position error. Figure 5.6(a) and Figure 5.6(b) illustrate the impact of the applied weight model on the number of fixed ambiguities. In the case of C/N_0 weighting, a minimum of 70 % of the ambiguities were fixed per epoch. The percentage of fixed ambiguities per epoch is inversely proportional to the effectiveness of the weight model in dampening larger observation errors. This is because erroneous observations with large uncertainties are no longer able to contribute to the fixed set of ambiguities. Consequently, the GNSS FMA-W Geman-McClure and HG methods exhibit a lower fixed ambiguity proportion than the GNSS FMA-W Huber and C/N_0 weighting methods. Figure 5.6(c) links the fixed ambiguity rate with the corresponding 3D position error. The aforementioned methods, particularly the

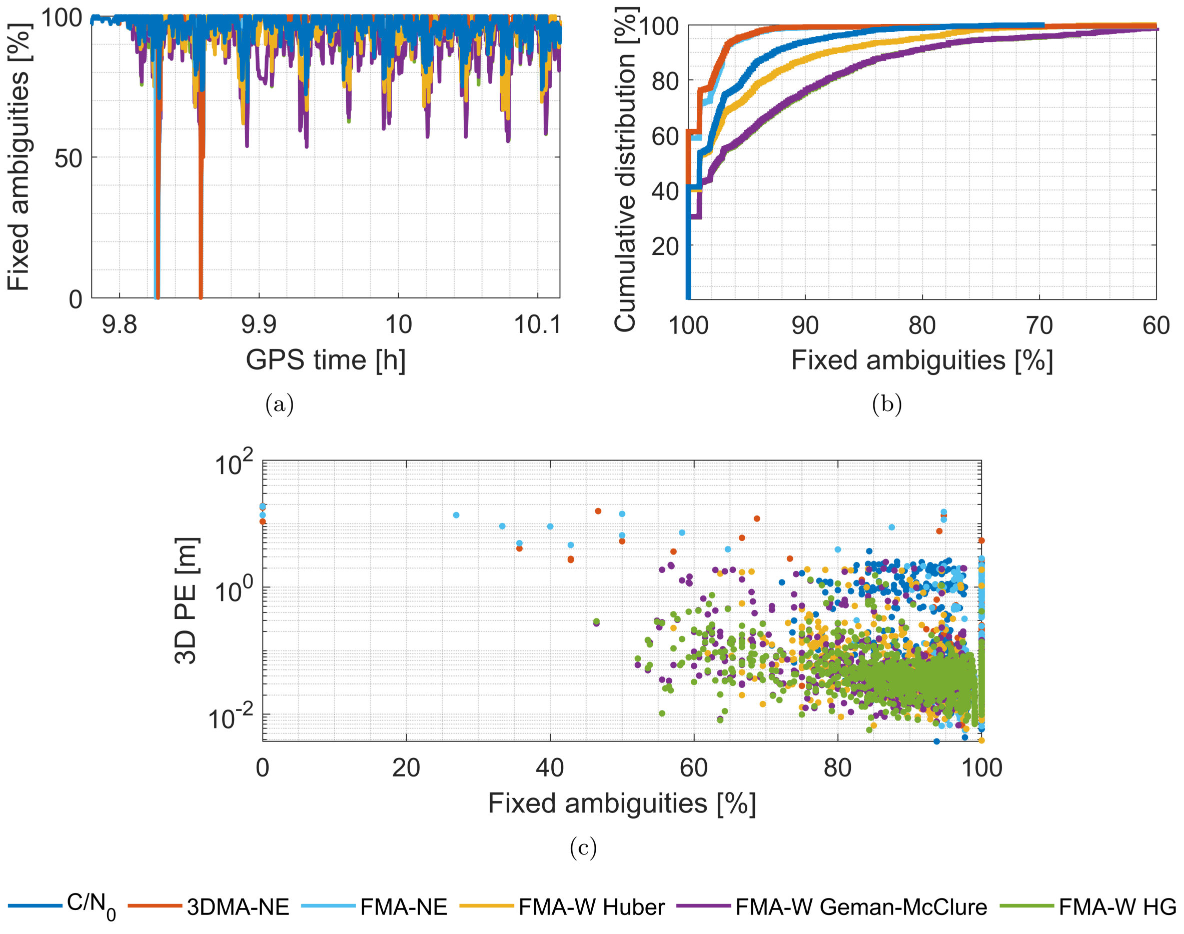

(a)

(b)

(c)

Figure 5.6: Percentage of fixed ambiguities versus time (a), as cumulative distribution (b), and versus the 3D position error (c) for C/N_0 weighting, 3DMA-NE, GNSS FMA-NE, GNSS FMA-W Huber, GNSS FMA-W Geman-McClure and GNSS FMA-W HG.

C/N_0 weighting method, can be successfully identified and located with ease when falsely fixed ambiguities are present. In the case of the C/N_0 weighting method, a cluster of data points is observed at a location where the 3D position error is approximately 1 m, while the fixed ambiguities exceed 80 %. This kind of cluster is not observed for the feature map-aided robust estimation methods. Instead, a very clear pattern is observed: if the proportion of fixed ambiguities is high, the 3D position error is low, and larger position errors are observed when the proportion of fixed ambiguities is low, indicating a low number of qualitatively good observations.

Overall, the combination of feature map information and robust loss functions into a GNSS FMA-W method has been demonstrated to improve the ambiguity resolution. While the percentage of ambiguities fixed in a single epoch may be lower, the overall number of correctly fixed ambiguities is higher. Furthermore, the robust GNSS FMA-W estimation methods have been shown to reduce the number of erroneous ambiguity fixes, which in turn mitigates the occurrence of larger position errors.

5.3 Automotive Experiment in Deep Urban Trench

5.3.1 Setup

Another kinematic experiment was carried out in a similar residential area in the city of Hannover, Germany, on DOY 44 in 2024 (13th February 2024). The ground truth of the trajectory together with the institute's reference station *EE01* is depicted in Fig. 5.7(a). The trajectory starts and ends with a static phase on a parking space with only few obstructions and in between, the triangular shaped part was repeatedly driven (eight times). The kinematic part of the route passes through a residential area in the city of Hannover, where the streets are about 5 m wide and the surrounding houses are about 22 m high. A typical situation of this trajectory is shown in Fig. 5.7(b), where the projected grids of the generated map are displayed with white boxes. The measurement configuration depicted in Fig. 5.7(d) consisted of one *Septentrio PolaRx5e* receiver, one *Septentrio mosaicX5* receiver and one *u-blox F9P (L1/L5)* receiver. Each of the receivers were connected via an active GNSS signal splitter (i.e., all receivers recording virtually the same observations) to a *Tallysman TW7972* patch antenna mounted on the roof of the test vehicle. The receivers were set to collect raw multi-GNSS data at a sampling rate of 1 Hz and to compute an internal RTK positioning solution based on the SAPOS® Satellite Positioning Service of the Official German Surveying and Mapping (2024), which provides GNSS correction data in the standardized RTCM format in real time via NTRIP. The used observation data, given in the RINEX notation, is depicted in Tab. 5.4. In addition, a high quality inertial navigation system (*iMAR iNAT-RQT-4003*) was connected to the same antenna collecting multi-GNSS data at a sampling rate of 1 Hz and IMU data at a sampling rate of 400 Hz. In the same way as in the previous experiment, the ground truth of the trajectory is computed by combining the GNSS carrier phase and Doppler observations with the IMU data in a tightly coupled relative positioning that was computed in post-processing using the commercial software *TerraPOS* (Kjørsvik et al., 2009).

Figure 5.7(f) indicates that this data set is classified as a *deep urban trench.* This categorization is based on the received GNSS satellite signals classified by ray tracing, which reveals that in some cases, the number of blocked signals received is even greater than that of received LOS signals. This is also reflected in the percentage availability of LOS signals, which is below 50 % for almost the entire kinematic phase (13.43 h to 13.65 h). In some cases, data from less than 15 % of LOS satellites are available in one epoch. In contrast to the previous data set, the maximum percentage of LOS satellite availability in this period is only about 50 %. These reception characteristics present significant challenges for any positioning algorithm, which is why this deep urban trench data set is an ideal test case for evaluating the effectiveness of the presented approaches under extremely challenging conditions on the one hand and for identifying their limitations on the other.

Please note that, unless otherwise stated, all subsequent results are processed using the recorded raw observations from the *Septentrio PolaRx5e* receiver. The results obtained from the other two receivers' data will be evaluated in Sec. 5.3.5.

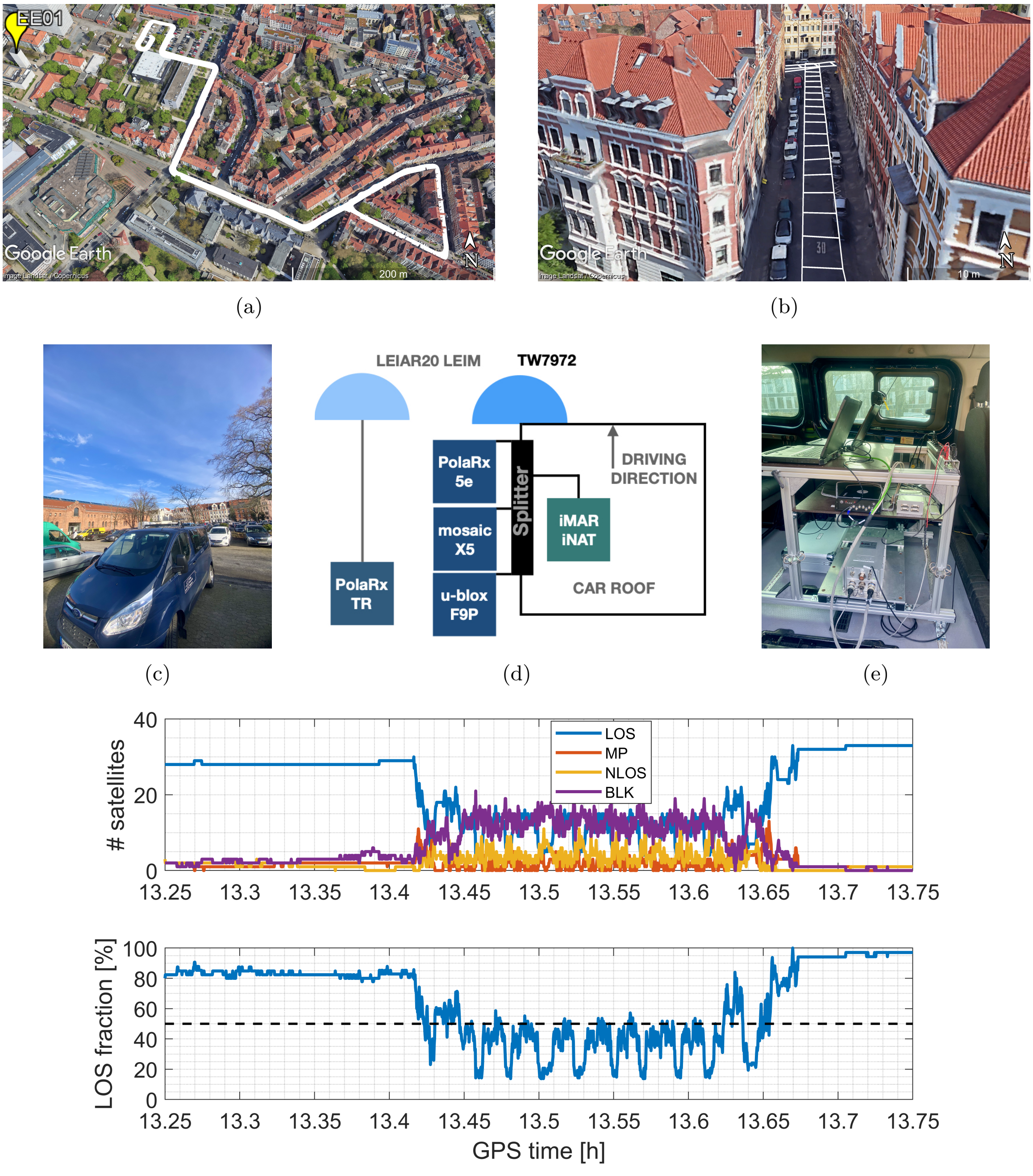

(a) (b)

(c) (d) (e)

(f)

Figure 5.7: Kinematic experiment setup of the automotive experiment in a deep urban trench. (a) ground truth of the eight times repeatedly driven trajectory, (b) typical environmental situation with map grids depicted as white polygons, (c), test vehicle, (d) measurement configuration, (e) equipment installed inside the test vehicle, (f) multi-GNSS satellite visibility information based on ray tracing results.

Table 5.4: Observation data recorded by the three receivers, given in RINEX notation.

Septentrio PolaRx5e	*GL1C, GL2L, GL2W, GL5Q, RL1C, RL1P, RL2C, RL2P, EL1C, EL5Q, EL7Q, EL8Q, CL1P, CL5P, CL2I, CL6I, CL7I*
Septentrio mosaicX5	*GL1C, GL2L, GL2W, RL1C, RL2C, EL1C, EL5Q, EL7Q, CL2I, CL6I, CL7I*
u-blox F9P (L1/L5)	*GL1C, GL5Q, RL1C, EL1C, EL5Q, CL5P, CL2I*

5.3.2 Accuracy Performance

At first, the accuracy of the position solution computed by the GNSS RTK EKF with different error mitigation strategies is evaluated. The GNSS FMA-NE method was not employed for the deep urban trench data set, as it did not yield any enhancements in accuracy, integrity and ambiguity resolution measures when compared to 3DMA-NE. Therefore, C/N$_0$ weighting and 3DMA-NE will be evaluated in comparison with the developed GNSS FMA-W approaches, specifically the GNSS FMA-W utilizing the Huber, Geman-McClure and HG loss functions. The analysis is divided into four sections, (i) presentation of general measures, (ii) evaluation by the measurement contamination proportion, (iii) location-dependency of errors, and (iv) a residual analysis. Again, the static phases at the parking space have been excluded from all further analyses, as for this non-dynamic, nearly open-sky scenario, all methods provide deviations of a few centimeters, which can be considered typical for an RTK solution. Consequently, the results are an accurate reflection of the actual situation and have not been embellished by the static part of the experiment.

General Measures

Figure 5.8 illustrates the horizontal and vertical PE with respect to the time, as well as a cumulative distribution diagram. Please note that the y-axis of the time series figures has been truncated for improved visual clarity. For the sake of completeness, the maximum errors, indicated by the respective diamond marker, can be ascertained from the cumulative distribution diagram. Considering both time series, it is obvious that the solution using C/N$_0$ weighting exhibits a degraded performance, particularly between 13.46 h and 13.57 h. During this time period, the centimeter-level deviations from the start of the trajectory could not be maintained, resulting in horizontal PE of 1 m to 4 m and vertical PE of up to 16 m.

The 3DMA-NE solution indicates that the availability of LOS carrier phase measurements was not consistently present, leading to numerous DGNSS epochs due to NLOS satellite exclusion. In these epochs, the horizontal PE increases to 10 m and the vertical PE reaches values of up to 37 m. However, when more than four LOS carrier phase measurements are tracked, the estimation strategy rapidly provides a solution with centimeter deviations.

The GNSS FMA-W Huber method has been providing very robust results for the medium urban trench data set. However, its improvement with respect to C/N$_0$ weighting under very harsh signal reception conditions is comparatively limited. Both, the horizontal and vertical PE time series show similar deviations, despite the incorporation of supplementary feature map information in the estimation process. The limitation is likely due to the fact that erroneous observations are not sufficiently attenuated by the Huber loss function during the estimation process.

The GNSS FMA-W Geman-McClure method provides stable results in between the repeated most challenging part of the trajectory. A similar performance is achieved through the utilization of the GNSS FMA-W HG method. Following the abrupt rise of position deviations

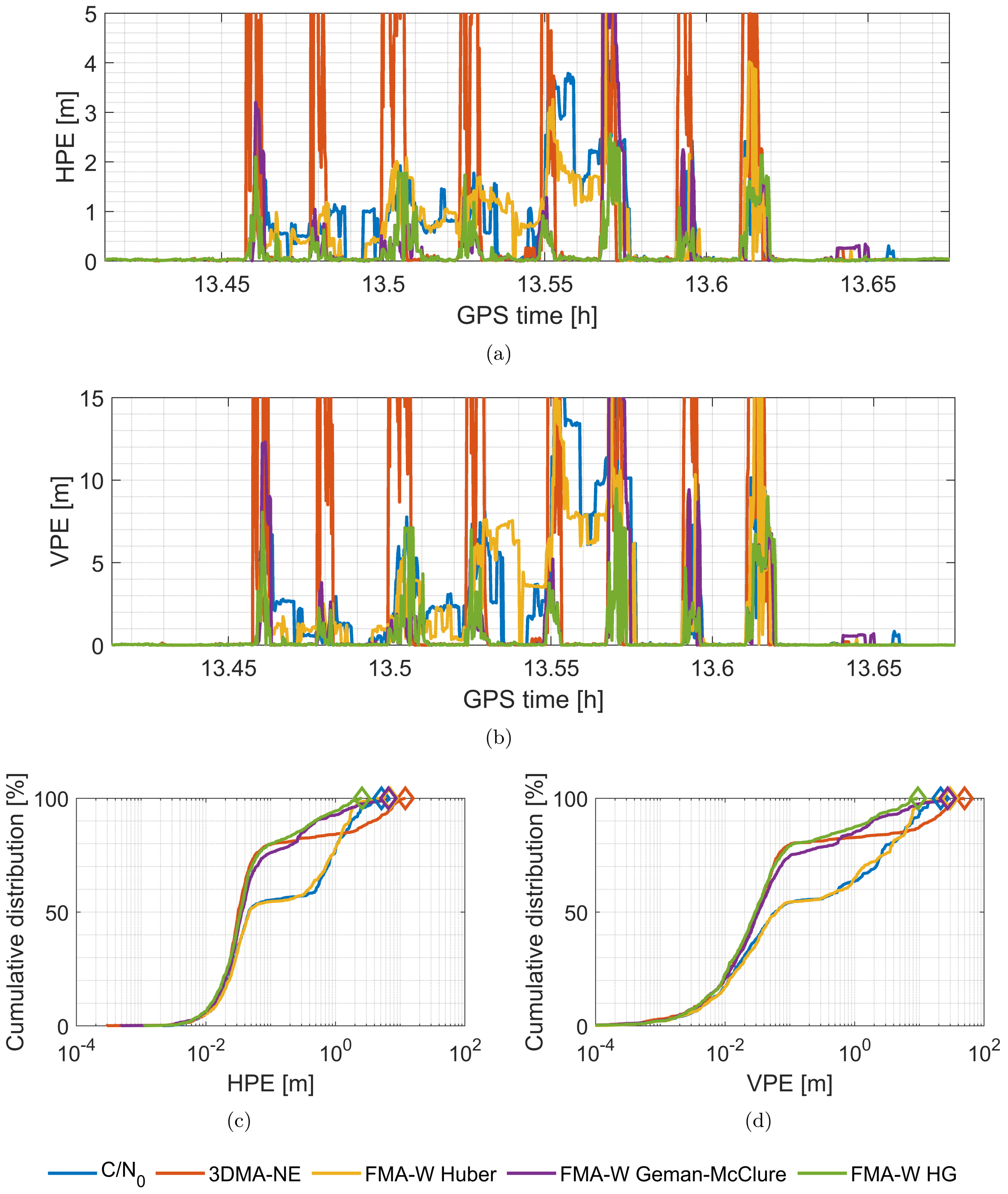

(a)

(b)

(c)

(d)

Figure 5.8: Horizontal and vertical position errors of the different approaches versus time ((a) and (b)) and as cumulative distribution diagram ((c) and (d)). Note the different axis limits.

at instances where the 3DMA-NE method transitioned from RTK fix mode to DGNSS mode, both estimation strategies demonstrate the capacity to rapidly attain deviations within a centimeter range. A comparative analysis of the two methods reveals that the HG loss function is more effective in reducing gross errors and provides more stable results in less challenging scenarios.

The cumulative distribution diagrams underline the aforementioned findings of the performance with respect to the position accuracy. The illustrated graphs of the different approaches are superimposed upon one another for small horizontal and vertical position errors. As the position errors increase, the curves for $\mathrm{C/N_0}$ weighting and GNSS FMA-W Huber are characterized by a relatively shallow slope, which results in the worst overall performance. The curves of the 3DMA-NE and GNSS FMA-W HG methods are well aligned until a horizontal PE of 15 cm and a vertical PE of 25 cm, which is reached at a proportion of 80 % of the values. As position errors continue to increase, the curve of the 3DMA-NE approach becomes increasingly shallow, resulting in the highest maximum error of all methods. In contrast, the curve of the GNSS FMA-W HG method remains relatively steep, demonstrating the best performance with respect to horizontal and vertical PE among all approaches.

The characteristic values presented in Tab. 5.5 further substantiate the preceding results of the horizontal and vertical position accuracy. For the 50 % and 75 % values of the horizontal and vertical position accuracy, the 3DMA-NE and GNSS FMA-W HG method yield comparable results. For higher percentiles, the GNSS FMA-W HG estimation strategy performs the best among all methods. In consideration of the performance specifications for automotive applications outlined in Section 2.7.4, Tab. 2.10, it can be seen that all approaches are unable to meet the lane keeping application requirements for 95 % accuracy in both the horizontal and vertical directions due to the harsh signal propagation conditions in the deep urban trench situation.

In order to evaluate the lane determination capability, the horizontal PE is further distinguished as longitudinal and lateral PE, which are illustrated as a cumulative distribution diagram in Fig. 5.9. The diamond markers represent the respective 95 % value of the different estimation strategies, while the black dashed line marks the lane determination accuracy requirement with respect to the same percentile. It is evident that the GNSS FMA-W HG approach is the only one capable of providing satisfactory accuracy values in order to meet the specified lane determination requirements in both the longitudinal and lateral directions. The horizontal position accuracy (95 %) is 0.91 m in longitudinal direction and 0.28 m in lateral direction.

A comparison of the overall RMS reveals that all three GNSS FMA-W methods improve the accuracy in comparison to $\mathrm{C/N_0}$ weighting. The combination of map information with the Huber, Geman-McClure and HG loss functions has resulted in an improvement of the RMS of the horizontal PE by 17 %, 17 % and 60 %, respectively, and an improvement of the RMS of the vertical PE by 11 %, 17 % and 64 %, respectively. Conversely, the 3DMA-NE method

Table 5.5: Horizontal and vertical position accuracy of the different approaches given in percentiles.

	Horizontal position accuracy [m]					
	50 %	75 %	95 %	99 %	RMS	Ratio [%]
$\mathrm{C/N_0}$	0.046	0.889	2.450	3.924	1.091	-
3DMA-NE	0.032	0.057	7.132	9.835	2.400	-120
GNSS FMA-W Huber	0.047	0.878	1.811	3.261	0.907	17
GNSS FMA-W Geman-McClure	0.036	0.085	1.544	5.468	0.901	17
GNSS FMA-W HG	0.034	0.063	1.170	2.130	0.432	60
	Vertical position accuracy [m]					
	50 %	75 %	95 %	99 %	RMS	Ratio [%]
$\mathrm{C/N_0}$	0.060	2.613	11.039	16.070	4.409	-
3DMA-NE	0.030	0.067	25.101	36.883	8.938	-103
GNSS FMA-W Huber	0.063	2.773	8.052	15.260	3.922	11
GNSS FMA-W Geman-McClure	0.033	0.104	6.584	22.143	3.644	17
GNSS FMA-W HG	0.029	0.074	4.461	7.115	1.593	64

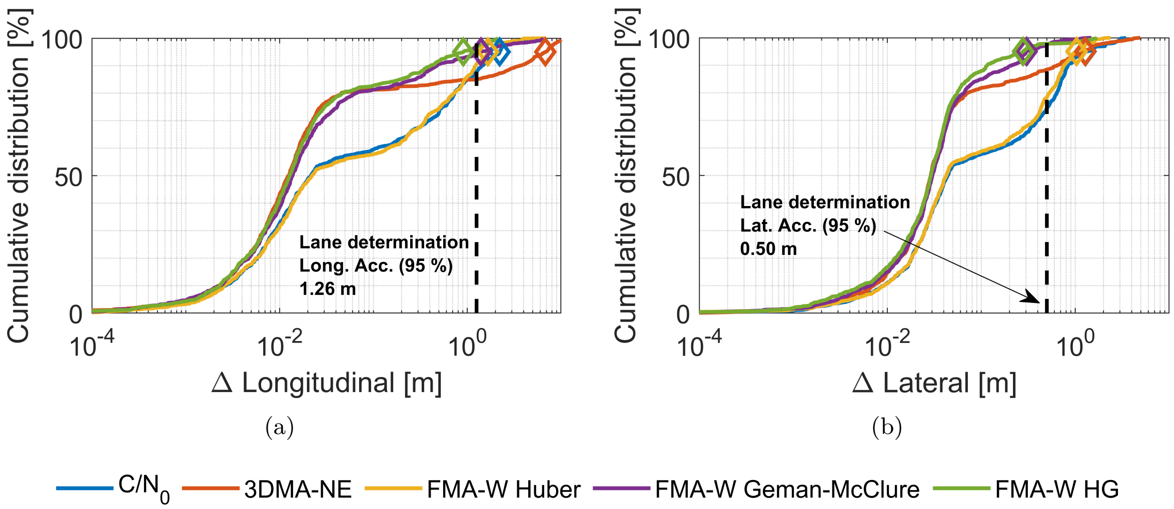

(a) (b)

Figure 5.9: Longitudinal and lateral position errors of the different approaches as cumulative distribution diagram. The black dashed line depicts the 95 % accuracy requirement for lane determination applications according to Tab. 2.10.

has an adverse impact on the overall result due to the transition from an RTK fix solution to a DGNSS solution at specific epochs.

Evaluation by Measurement Contamination Proportion

Given the expectation that the introduced estimators will behave differently under varying measurement contamination proportions, the performance with respect to the LOS ratio is illustrated in Fig. 5.10. The LOS ratio is determined using ray tracing computation at the ground truth positions. As expected, the largest position errors are observed at the lowest LOS ratios (indicated by the red ellipses). This is due to the low number of nominal observations in comparison to number of faulty satellites in NLOS conditions. Thereby, the GNSS FMA-W HG method is the most effective in reducing the overall magnitude of errors.

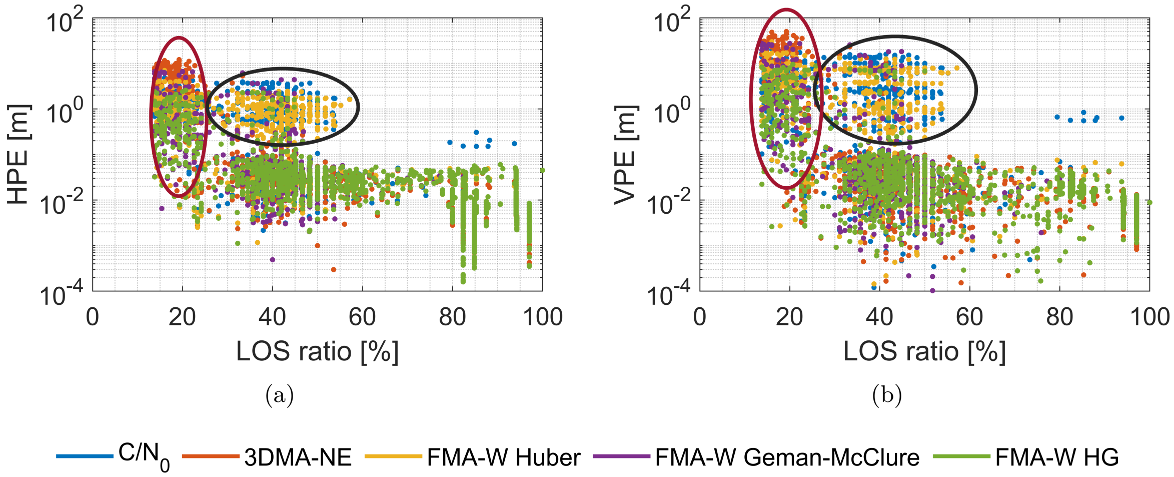

(a) (b)

Figure 5.10: Horizontal (a) and vertical (b) position error with respect to the LOS ratio obtained from ray tracing computation. The red and black ellipses depict areas of special interest.

The second remarkable characteristic of this type of figure, indicated by the black ellipses, is observed for LOS ratios between 25 % and 60 %. At these instances, the C/N$_0$ weighting and the GNSS FMA-W Huber method exhibit significant position deviations. In contrast, the combination of map information with a more robust loss function (i.e., Geman-McClure and HG) results in the disappearance of such a cluster of data points. Instead, the magnitude of position errors remains at the same level as for higher LOS ratios, which depicts a significant improvement.

Location-dependency of Errors

As a result of the aforementioned analyses, a pattern of repeatable position errors was identified. This section therefore addresses the investigation of the location-dependency of these errors. The design of the driven trajectory, i.e. a small triangular section that is passed repeatedly in a counterclockwise direction, allows for an evaluation of whether conclusions can be drawn with respect to the location. Figure. 5.11(a) depicts the LOS ratio at the ground truth in a geographical plot, thereby recalling the prevailing reception conditions of the trajectory. The north-south oriented section of the triangular shaped trajectory is the most challenging one with LOS ratios of approximately 15 %. The remaining two streets, which complement the triangle, show similar reception characteristics with LOS ratios of approximately 40 % to 50 %.

Figure 5.11(b) to 5.11(f) illustrate the horizontal PE at the estimated positions in a geographical plot for C/N$_0$ weighting, 3DMA-NE, GNSS FMA-W Huber, GNSS FMA-W Geman-McClure (GMC) and GNSS FMA-W HG, respectively. The majority of the larger position errors are consistently identified at the north-south oriented section of the trajectory, where the LOS ratio is relatively low. It is notable that the 3DMA-NE method exhibits a greater degree of scatter in the estimated positions within the section displaying the largest position errors. During the drive through the remaining two streets, where a sufficient number of LOS carrier phases are available, the position error rapidly decreases to a very low level. The C/N$_0$ weighting and GNSS FMA-W Huber methods also demonstrates the largest errors in the north-south oriented section. However, in many following epochs, the estimators were unable to recover from the gross errors, resulting in the deviations remaining large. The GNSS FMA-W Geman-McClure and GNSS FMA-W HG methods exhibit comparable location-dependent characteristics. The largest errors are observed in the north-south oriented section of the trajectory, yet both estimators were capable to recover, providing low position errors in the two remaining streets. A comprehensive comparison of both estimators reveals that the GNSS FMA-W HG method demonstrates superior performance in mitigating errors exceeding 2 m.

Residual Analysis

In order to gain a deeper insight into the underlying principles of the GNSS FMA-W methods and their ability to yield accurate and robust position solutions, an in-depth analysis of the residuals is conducted. Therefore, the DD pre-fit residuals are computed using the OMC values, which are based on the ground truth of the trajectory and indicate the true ranging error of the observed pseudorange observations. Figure 5.12 depicts a comparison of DD pre-fit residuals and GNSS Feature Map residuals for typical individual satellites. The time series for a single satellite for each L1 signal from the four GNSS together with the corresponding received signal strength is shown in Fig. 5.12(a) to 5.12(d), while Fig. 5.12(e) shows an overview of the residuals by summarizing all satellites and all signals in one histogram, and Fig. 5.12(f) illustrates the result when subtracting the pre-fit residuals from the feature map residuals. Please note that the beginning and end of the time series correspond to locations where no

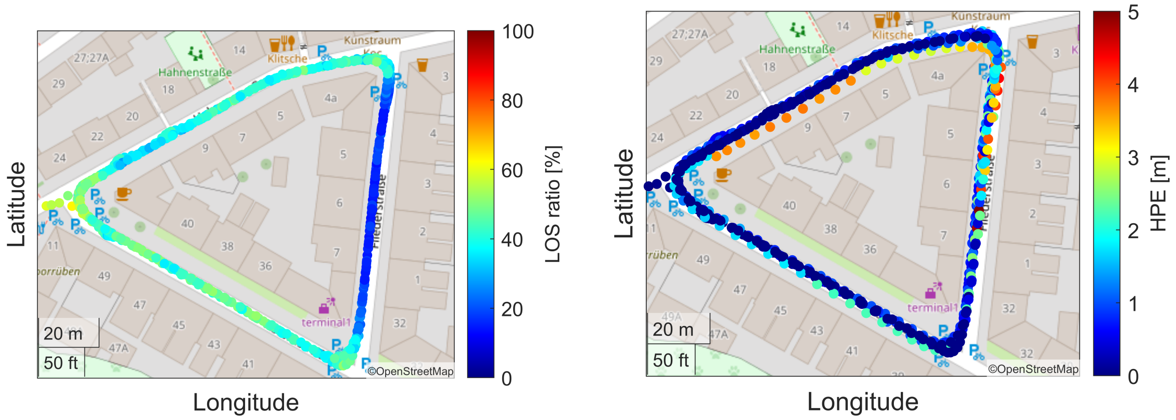
Latitude
Longitude
LOS ratio [%]
100
80
60
40
20
0
20 m
50 ft
©OpenStreetMap
Latitude
Longitude
HPE [m]
5
4
3
2
1
0
20 m
50 ft
©OpenStreetMap

(a) LOS ratio (b) C/N$_0$

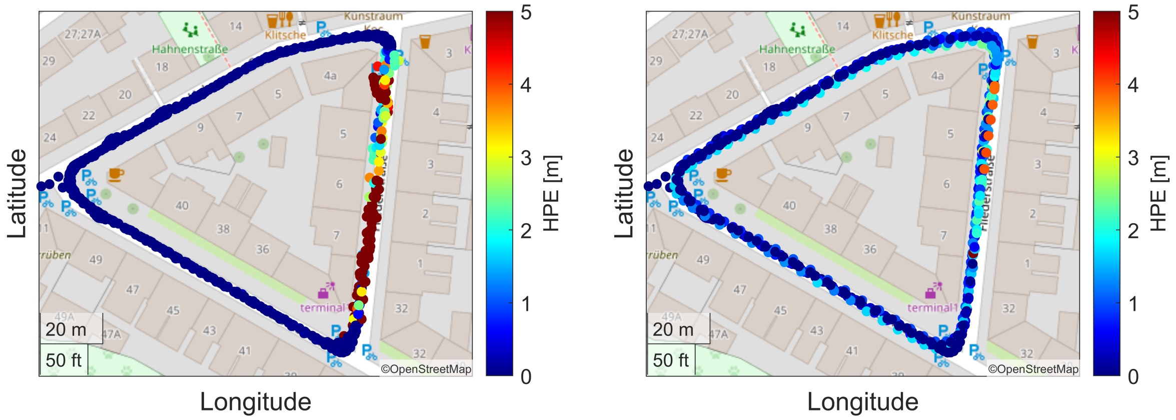
Latitude
Longitude
HPE [m]
5
4
3
2
1
0
20 m
50 ft
©OpenStreetMap
Latitude
Longitude
HPE [m]
5
4
3
2
1
0
20 m
50 ft
©OpenStreetMap

(c) 3DMA-NE (d) GNSS FMA-W Huber

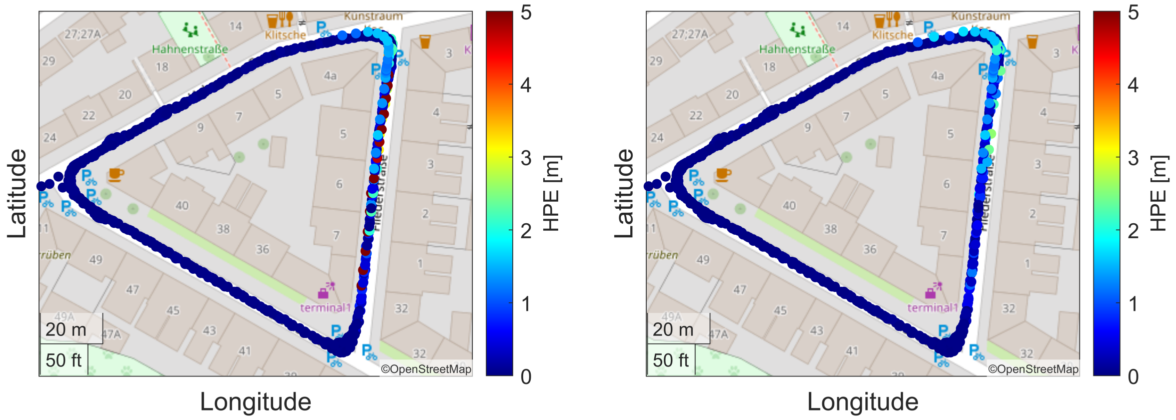
Latitude
Longitude
HPE [m]
5
4
3
2
1
0
20 m
50 ft
©OpenStreetMap
Latitude
Longitude
HPE [m]
5
4
3
2
1
0
20 m
50 ft
©OpenStreetMap

(e) GNSS FMA-W GMC (f) GNSS FMA-W HG

Figure 5.11: Analysis of the location-dependency of errors. (a) shows the color-coded LOS ratio at the ground truth, and (b) to (f) shows the color-coded horizontal PE at the estimated positions for C/N$_0$ weighting, 3DMA-NE, GNSS FMA-W Huber, GNSS FMA-W Geman-McClure (GMC) and GNSS FMA-W HG, respectively. The driving direction is counterclockwise.

feature map data is available. The feature map residuals provide a fairly accurate description of the actual received ranging error. In situations where the DD pre-fit residuals are relatively small, the obtained feature map residual is likewise small and vice versa, thereby providing an approximate estimation of the observations' variance. In detail, the feature map residuals are larger than the DD pre-fit residuals in the majority of the cases. This results in a more conservative variance model, which safely mitigates faulty observations. As illustrated in

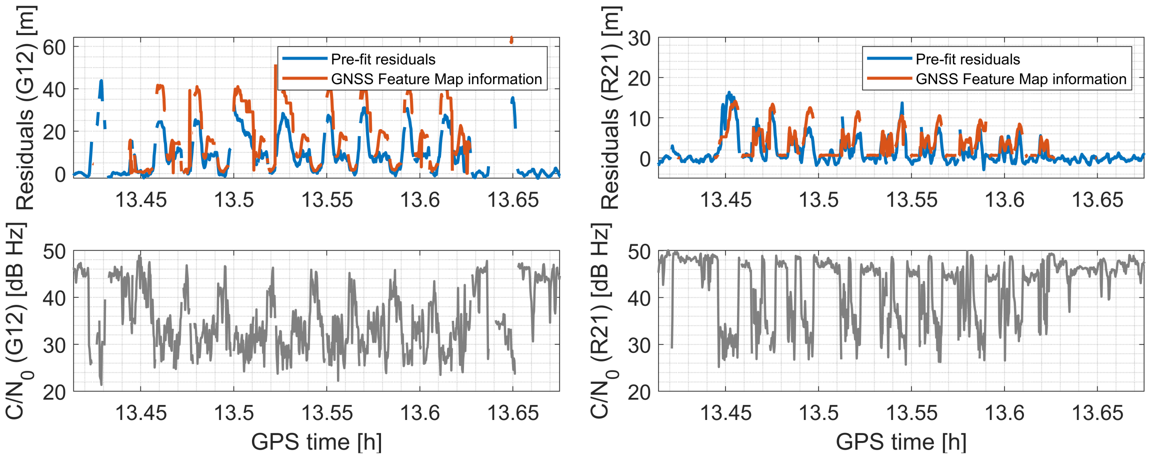

(a) GC1C (b) RC1C

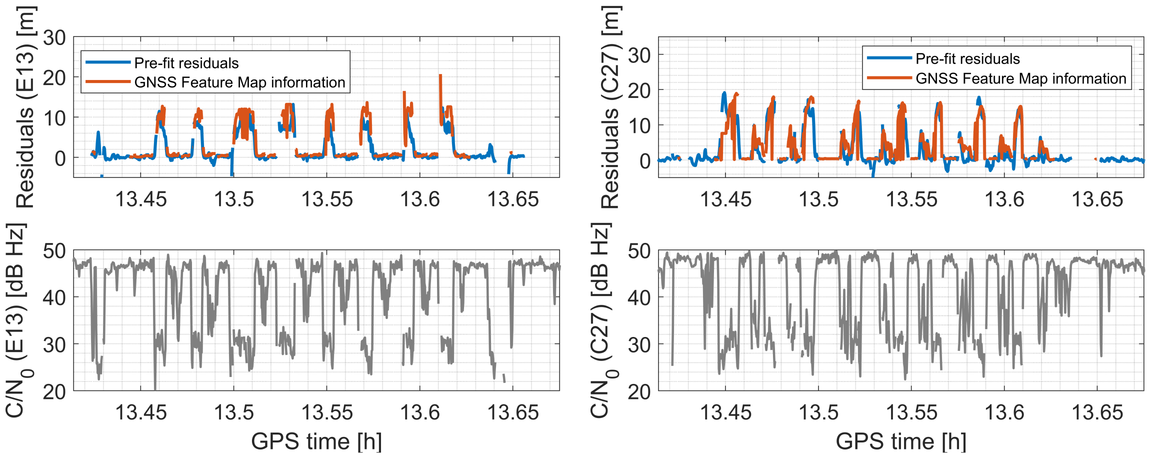

(c) EC1C (d) CC1P

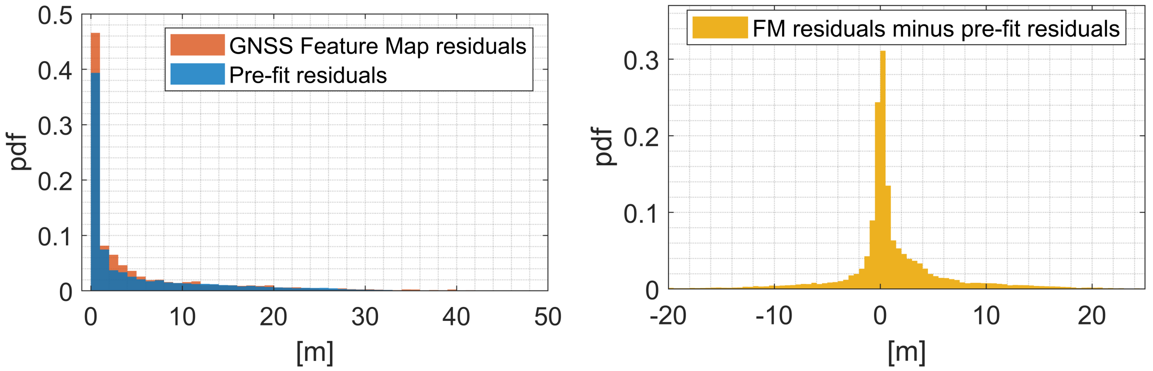

(e) (f)

Figure 5.12: Comparison of DD pre-fit residuals and GNSS Feature Map residuals. (a) to (d) show the time series for a single satellite for each L1 signal from the four GNSS, and (e) to (f) show an overview of all satellites and all signals in a histogram.

the histograms, there are instances where the actual observation error exceeds the obtained feature map residual (indicated by negative values in Fig. 5.12(f)). As demonstrated by the simulation in Sec. 4.2.2, the robust loss functions effectively mitigate these outliers, ensuring that the overall performance remains within an acceptable range. Conversely, the C/N$_0$ weighting may be overly optimistic in situations where large ranging errors of up to 30 m are encountered. That is attributable to the received C/N$_0$ value at these epochs, representing a relatively high value (> 30 dB Hz) in comparison to the maximum of approximately 50 dB Hz. This information substantiates the findings of the preceding sections, which indicate that the incorporation of feature map data leads to a reduction in gross errors and an enhancement in the stability of the solution.

5.3.3 Attainable Integrity

The integrity of the different position solutions is evaluated by Stanford diagrams for the horizontal and vertical components, respectively. The corresponding protection levels of the solutions were computed using Eq. 2.85 and Eq. 2.86 based on a probability of failure of 10^{-8}. In the analyses of the accuracy for the deep urban trench data, it has been shown that the requirements for lane keeping applications are not met. However, to investigate how far the provided solutions are from these requirements, the integrity will be evaluated based on the corresponding alert limits $\text{HAL} = \sqrt{0.44^2 + 0.44^2} = 0.622$ [m] and $\text{VPL} = 1.40$ [m] (see Tab. 2.11), although values for German roads have recently been defined (Kulemann and Schön, 2025; Schön et al., 2025). The resulting Stanford diagrams are illustrated in Fig. 5.13 for the horizontal component and in Fig. 5.14 for the vertical component. Please note that data points that exceed the axis limits of the position error or protection level, are displayed at the respective border of the figure. Again, the static phases at the parking space have been excluded from the analyses, as for this non-dynamic, nearly open-sky scenario, all methods provide an accuracy better than the alert limits and the position errors are well bounded. The attainable integrity is assessed on the basis of a probability of failure of 10^{-8}. In this regard, the test data (942 epochs) provide a good estimate of integrity. However, more test data must be evaluated in order to assess the defined probability of failure.

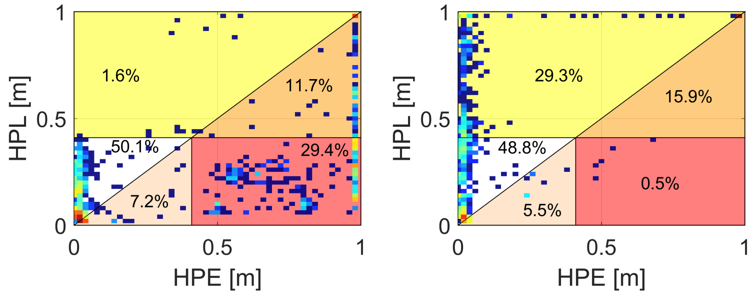

(a) C/N$_0$ (b) 3DMA-NE

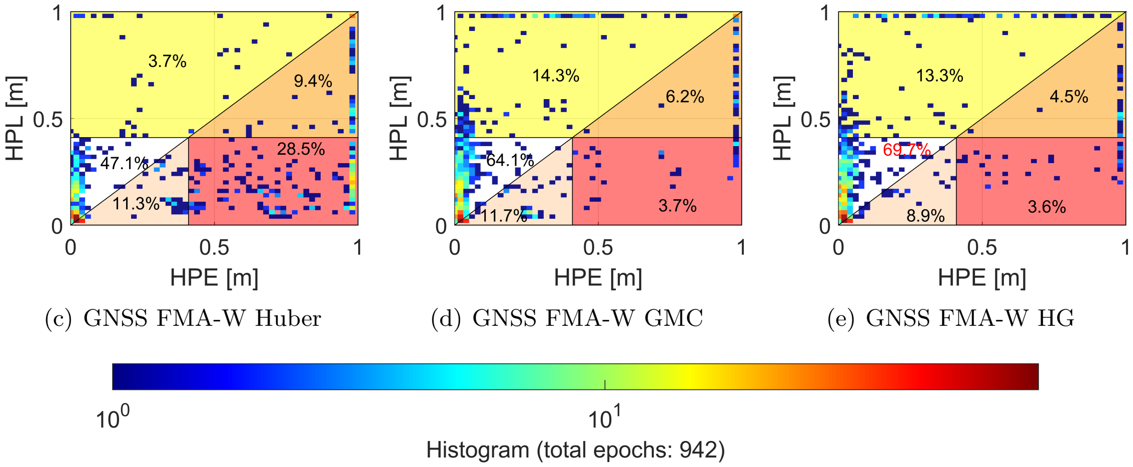

(c) GNSS FMA-W Huber (d) GNSS FMA-W GMC (e) GNSS FMA-W HG

Figure 5.13: Integrity evaluation of the horizontal component for the different methods.

Horizontal Component

In 50.1 % of the cases, the system operates in nominal mode when using the C/N$_0$ weighting method. However, a large number of hazardous misleading information epochs (29.4 %) are present, representing the most critical condition. Additionally, 10.2 % of the epochs are misleading information, as the protection level is smaller than the position error, thereby bounding the error inadequately. When applying 3DMA-NE, the most critical instances of hazardous misleading information are reduced to 0.5 %, although this reduction comes at the cost of an increase in the number of system unavailability instances (29.3 %) and a slight decrease in the proportion of nominal operation epochs, which account for 48.8 % of the total. This indicates that, despite the method's capacity to accurately overbound the position errors, the increased protection level values result in the system no longer operating within the nominal mode with the given specifications. As already stated before, the GNSS FMA-W Huber method does not enhance the solution. In terms of integrity measures, the characteristic values are comparable to that of the C/N$_0$ weighting solution, yielding a large number of hazardous misleading information instances (28.5 %). The GNSS FMA-W Geman-McClure and GNSS FMA-W HG approaches improve the overall integrity of the system, demonstrating an extensive improvement in nominal operations (64.1 % and 69.7 %). Thereby, the combination of map information with the HG loss function results in the best performance compared to the Geman-McClure loss function, showing less system unavailability, misleading information and hazardous misleading information epochs.

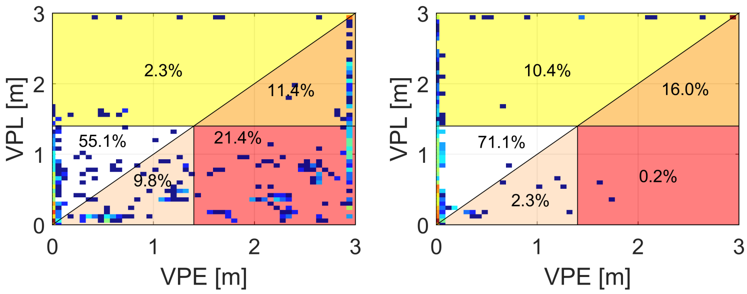

(a) C/N$_0$ (b) 3DMA-NE

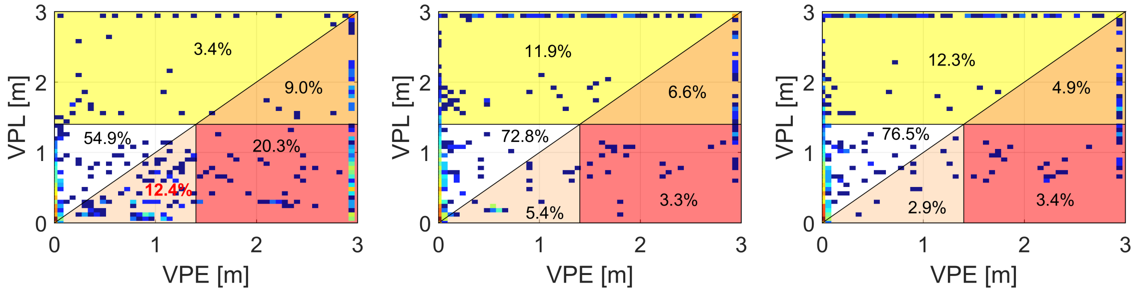

(c) GNSS FMA-W Huber (d) GNSS FMA-W GMC (e) GNSS FMA-W HG

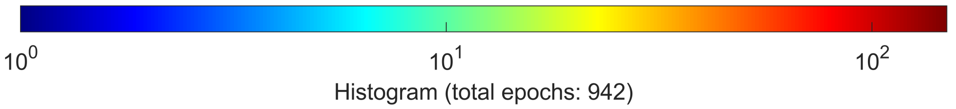

Figure 5.14: Integrity evaluation of the vertical component for the different methods.

Vertical Component

In comparison to horizontal PE, vertical PE is of a greater magnitude, given that the vertical component is less precisely determinable using the GNSS sensor. Conversely, the vertical alert limit for automotive applications is less stringent, resulting in overall proportions of Stanford diagram conditions that are comparable. A comparison of the five estimation methods reveals that the GNSS FMA-W Huber approach exhibits the lowest number of nominal operations (54.9 %) together with the C/N_0 weighting (55.1 %). Due to the less stringent alert limit, the number of system unavailability for the 3DMA-NE method is decreased to 10.4 %, resulting in a similar number of nominal operations (71.1 %) as for the GNSS FMA-W Geman-McClure method (72.8 %). The proportion of hazardous misleading information is 0.2 %, which is the lowest among the five methods. However, the largest nominal operation proportions are achieved by the GNSS FMA-W HG (76.5 %) method. Consequently, the proposed GNSS FMA-W HG method shows the best overall integrity, having only a few (2.9 %) misleading information instances and only a few hazardous misleading information epochs (3.4 %).

5.3.4 Ambiguity Resolution

Using GNSS RTK positioning technology, the ambiguity resolution is an important measure that helps to understand the occurrence of position error magnitudes as well as the correct observation uncertainty assignment. Figure 5.15 illustrates the 3D position error of the float (yellow) and fixed (green) solution along with the ambiguity success rate (gray) for C/N_0 weighting, 3DMA-NE, GNSS FMA-W Huber, GNSS FMA-W Geman-McClure and GNSS FMA-W HG method. It is evident that the more robust the estimation method, the smaller the error of the float solution will be. Consequently, there is a greater probability of achieving an accurate fixed solution, as superior float estimates typically result in more precise fixed estimates. The findings of the deep urban trench trajectory are analogous to those of the medium urban trench data set. By investigating the time series for the C/N_0 weighting and GNSS FMA-W Huber methods, the 3D position error of the fixed solution frequently reaches

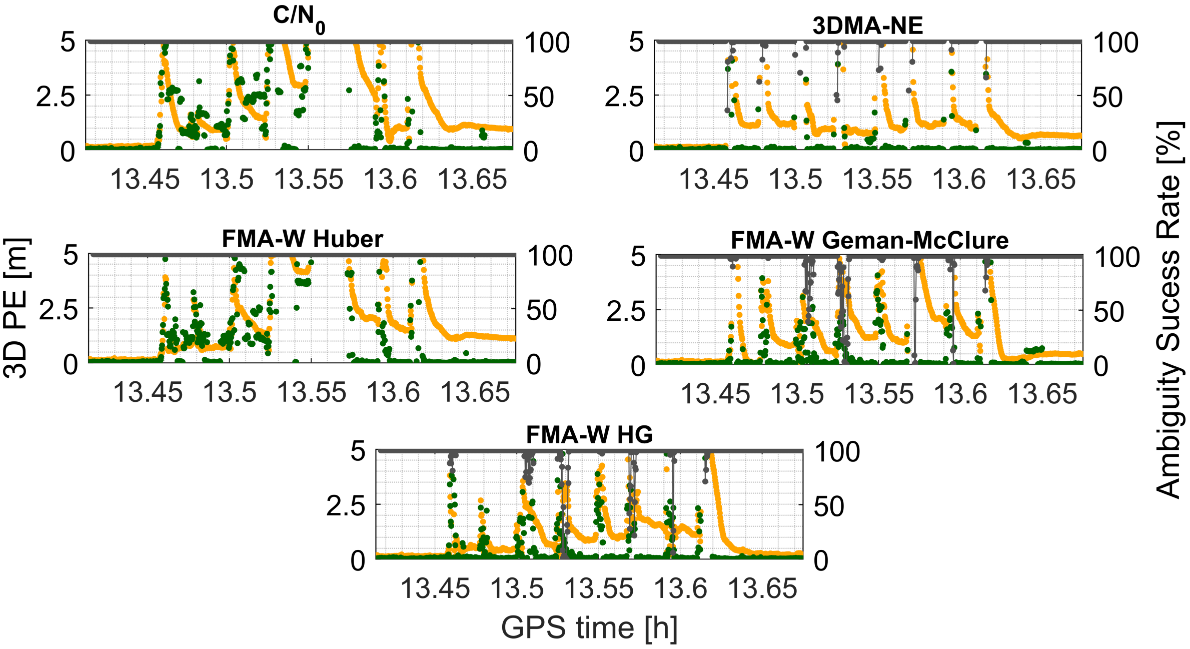

Figure 5.15: 3D position error of the float (yellow) and fixed (green) solution along with the ambiguity success rate (gray) for the different methods.

deviations in the meter-level and even exceeds the 5 m axis limit of the figure. Although the float solution show relatively large deviations, the fixed solution is, in numerous epochs, demonstrably inferior to the float solution. This is indicative of an erroneous fixed set of ambiguities despite the ambiguity success rate being 100 %.

In contrast, the GNSS FMA-W Geman-McClure and GNSS FMA-W HG method yield a more precise float solution, with only a small number of data points in the fixed solution exhibiting significant deviations and exceeding the float deviation. It is noteworthy that the ambiguity success rate exhibits a significant drop at specific time instances where the C/N$_0$ weighting and GNSS FMA-W Huber approaches are unable to provide an accurate solution despite the ambiguity success rate being 100 % and the 3DMA-NE transitions to a DGNSS solution. However, these drops are not directly linked to large observation errors; rather, the opposite is true. Despite a decline in the ambiguity success rate, the position error remains comparably lower. The drop in success rate can be attributed to erroneous observations, which are correctly identified with considerable uncertainties. This results in a larger ambiguity search space, ultimately leading to a reduction in the success rate and thereby drastically reducing the number of falsely fixed ambiguities.

In order to substantiate these hypotheses, Figure 5.16 illustrates the percentage of fixed ambiguities versus time as well as the connection between the percentage of fixed ambiguities with the 3D position error. Figures 5.16(a) and 5.16(b) illustrate the impact of the applied

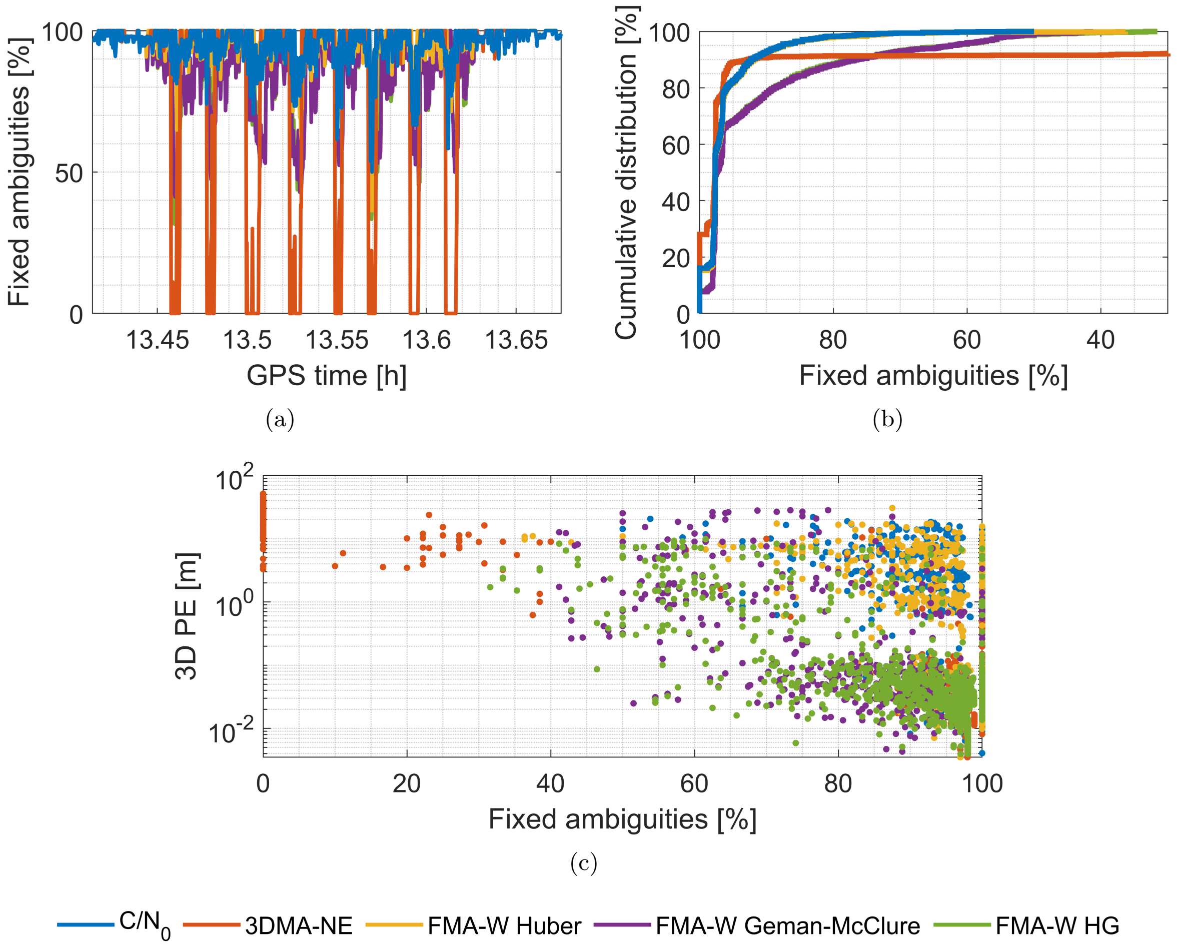

(a) (b)

(c)

Figure 5.16: Percentage of fixed ambiguities versus time (a), as cumulative distribution (b), and versus the 3D position error (c) for C/N$_0$ weighting, 3DMA-NE, GNSS FMA-W Huber, GNSS FMA-W Geman-McClure and GNSS FMA-W HG.

estimation strategy on the number of fixed ambiguities. In the case of C/N$_0$ weighting, a minimum of 50 % of the ambiguities were fixed per epoch. The percentage of fixed ambiguities per epoch is inversely proportional to the effectiveness of the weight model in dampening larger observation errors. This is because erroneous observations with large uncertainties are no longer able to contribute to the fixed set of ambiguities. It can be seen that the GNSS FMA-W Geman-McClure and GNSS FMA-W HG methods result in a lower fixed ambiguity rate than the GNSS FMA-W Huber and C/N$_0$ weighting methods. The former methods exhibit a fixed ambiguity rate of approximately 30 % at a few challenging epochs.

Figure 5.16(c) links the fixed ambiguity rate with the corresponding 3D position error. The aforementioned methods, particularly the C/N$_0$ weighting and the GNSS FMA-W Huber method, can be successfully identified and located with ease when falsely fixed ambiguities are present. In the case of these two methods, a cluster of data points is observed at a location where the 3D position error is approximately 3 m to 20 m, while the number of fixed ambiguities exceeds 80 %. This kind of cluster is not observed in the case of the more robust GNSS FMA-W methods, specifically those utilizing the Geman-McClure and HG loss functions. Instead, a very clear pattern is observed: if the proportion of fixed ambiguities is high ($>$ 80 %), the 3D position error is low, and larger position errors are observed when the proportion of fixed ambiguities is lower, indicating a low number of qualitatively good observations.

Overall, the combination of feature map information and robust loss functions into a GNSS FMA-W method has been demonstrated to enhance the ambiguity resolution. While the percentage of ambiguities fixed in a single epoch may be lower, the overall number of correctly fixed ambiguities is higher. Furthermore, the robust GNSS FMA-W Geman-McClure and GNSS FMA-W HG estimation methods have been shown to reduce the number of erroneous ambiguity fixes, which in turn mitigates the occurrence of larger position errors.

5.3.5 Evaluation of Hardware-dependency

As the GNSS Feature Maps containing pseudorange residuals are generated using a *Septentrio PolaRx5e* receiver, the objective of this section is to evaluate the applicability of the map to other hardware. The results obtained from the *Septentrio mosaicX5* receiver and the *u-blox F9P (L1/L5)* receiver will therefore be subjected to analysis. As the receivers are of a different grade and recorded a different number of observation types (see Tab. 5.4), direct comparison of their solutions is not possible. As illustrated in Fig. 5.17, the number of available observations is greater for the *Septentrio PolaRx5e* receiver than for the *Septentrio mosaicX5* receiver and

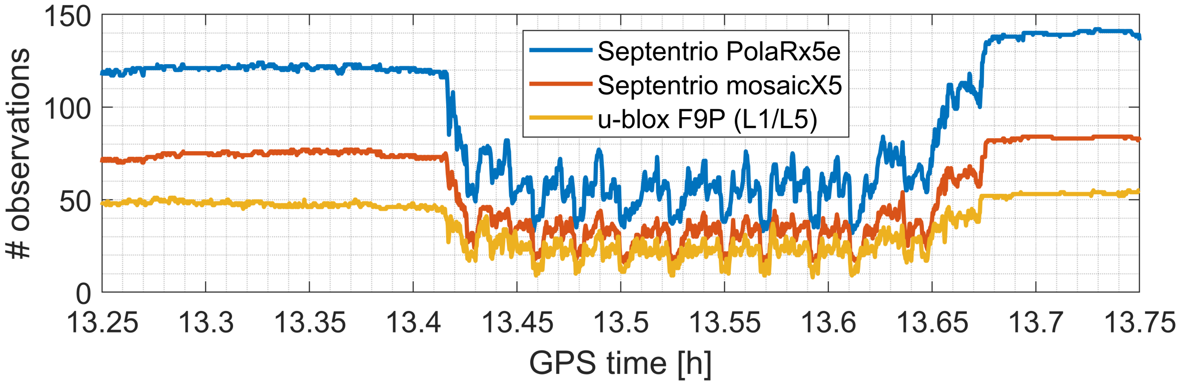

Figure 5.17: Number of carrier phase observations available for the *Septentrio PolaRx5e*, *Septentrio mosaicX5* and *u-blox F9P (L1/L5)* receivers.

the *u-blox F9P (L1/L5)* receiver. Instead, the objective is to assess the potential of the GNSS FMA-W approaches to enhance existing estimation strategies, specifically the C/N$_0$ weighting and 3DMA-NE. This section will focus on a comparison between the existing methods, C/N$_0$ weighting and 3DMA-NE, and the GNSS FMA-W HG method, which demonstrated the most promising results in the previous section. For purposes of completeness, the results of the GNSS FMA-W Huber and GNSS FMA-W Geman-McClure methods will also be included.

Septentrio mosaicX5 Receiver

Figure 5.18 illustrates the horizontal and vertical PE with respect to the time, as well as a cumulative distribution diagram. Please note that the y-axis of the time series figures has been truncated for improved visual clarity. For the sake of completeness, the maximum errors, indicated by the respective diamond marker, can be ascertained from the cumulative distribution diagram. In general, the overall behavior of the *Septentrio mosaicX5* receivers' position errors is quite similar to those of the *Septentrio PolaRx5e* receiver, exhibiting repetitive larger position errors that can be attributed to the most challenging segment of the trajectory. In consideration of the different estimation strategies, it is evident that the GNSS FMA-W HG method improves both the horizontal and vertical PE in comparison to C/N$_0$ weighting and 3DMA-NE. In particular, between 13.48 h and 13.55 h, the larger position errors are mitigated, and instead, deviations in the centimeter to decimeter range are achieved.

In the cumulative distribution diagrams, the green curve of the GNSS FMA-W HG method is well aligned with the red curve of the 3DMA-NE method at small position errors. As the position errors increase, the slope of the green curve becomes the steepest. However, the maximum error that is above 6 m horizontally and above 18 m vertically for all methods, could not be reduced. Tab. 5.6 provides an overview of the characteristic values for the horizontal and vertical position accuracy, which further substantiates the preceding results. For the 50th and 75th percentiles, the corresponding position accuracy is comparable to that of the 3DMA-NE method. The greatest improvement by the GNSS FMA-W HG method is achieved until the 95th percentile, where the estimation strategy performs the best among all other methods. A comparison of the overall RMS reveals that the robust GNSS FMA-W exhibits a

Table 5.6: Septentrio mosaicX5 receiver: Horizontal and vertical position accuracy of the different approaches given in percentiles.

	Horizontal position accuracy [m]					
	50 %	75 %	95 %	99 %	RMS	Ratio [%]
C/N$_0$	0.037	0.472	2.872	3.818	1.024	-
3DMA-NE	0.033	0.059	6.932	9.545	2.424	-137
GNSS FMA-W Huber	0.034	0.078	3.156	4.924	1.246	-22
GNSS FMA-W Geman-McClure	0.038	0.263	2.995	4.614	1.119	-9
GNSS FMA-W HG	0.035	0.066	1.334	6.911	1.280	-25
	Vertical position accuracy [m]					
	50 %	75 %	95 %	99 %	RMS	Ratio [%]
C/N$_0$	0.031	1.772	7.123	13.629	3.140	-
3DMA-NE	0.024	0.054	25.338	37.108	9.154	-192
GNSS FMA-W Huber	0.026	0.088	11.131	15.802	4.049	-29
GNSS FMA-W Geman-McClure	0.029	0.763	7.098	13.317	3.015	4
GNSS FMA-W HG	0.026	0.060	4.227	19.328	3.536	-13

slight decrease in performance, which is attributed to a few larger position errors that have a deteriorating effect on the overall RMS.

Similar to the preceding section, an in-depth analysis of the residuals is conducted by comparing the DD pre-fit residuals, which are based on the ground truth of the trajectory and indicate the true ranging error of the observed pseudorange observations, with the obtained information from the GNSS Feature Map. Figure 5.19 illustrates the comparison of DD pre-fit residuals and GNSS Feature Map residuals. The time series for a single satellite for each L1 signal from the four GNSS together with the corresponding received signal strength is shown in Fig. 5.19(a) to 5.19(d). Please note that the beginning and end of the time series correspond to locations where no feature map data is available.

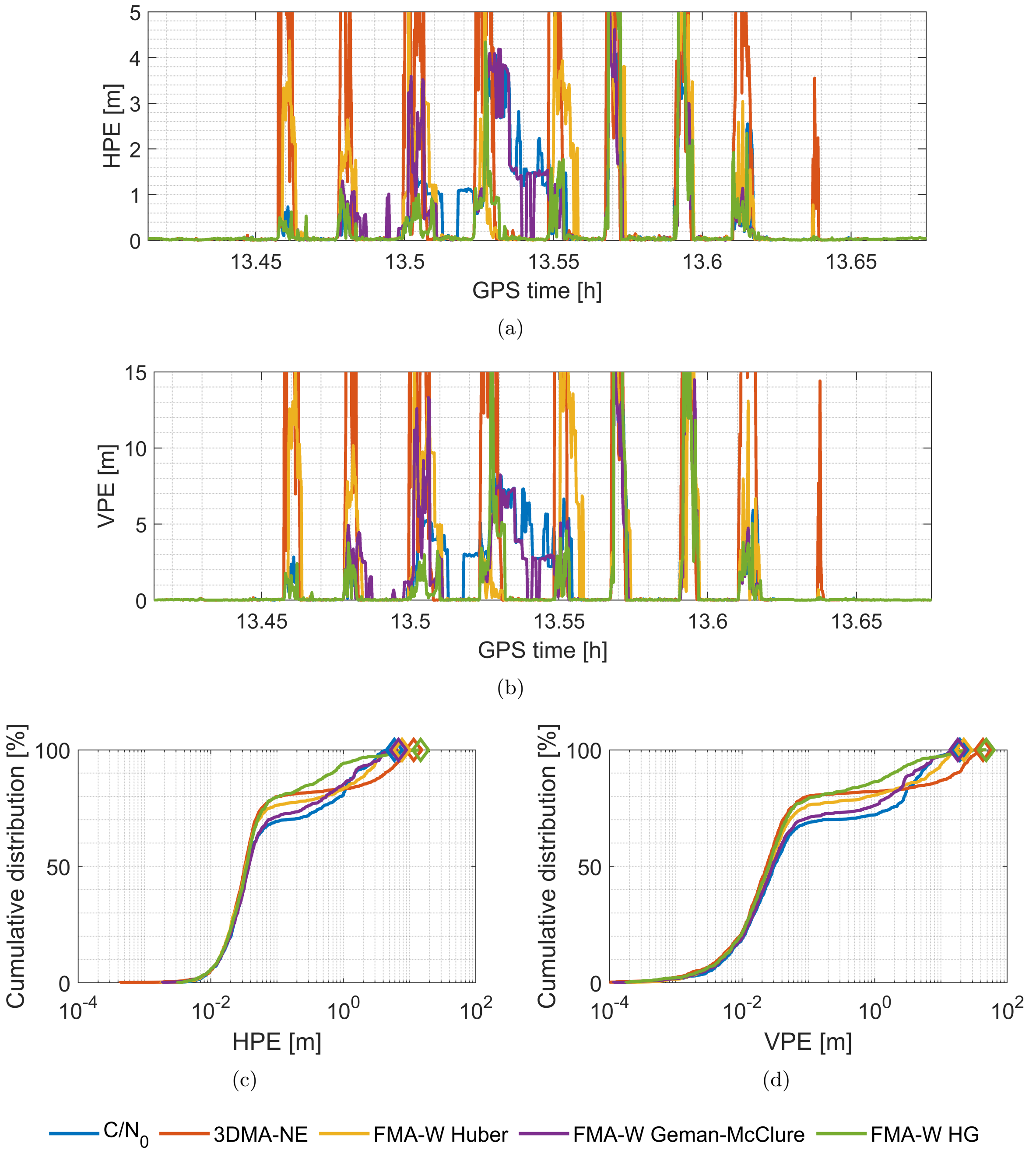

(a)

(b)

(c)

(d)

Figure 5.18: Septentrio mosaicX5 receiver: Horizontal and vertical position errors of the different approaches versus time ((a) and (b)) and as cumulative distribution diagram ((c) and (d)). Note the different axis limits.

The feature map residuals provide a fairly accurate description of the actual received ranging error, although the utilized hardware is different. In situations where the DD pre-fit residuals are relatively small, the obtained feature map residual is likewise small and vice versa, thereby providing an approximate estimation of the observations' variance. In detail, the feature map residuals of the GPS L1 signal are larger than the DD pre-fit residuals in the majority of the cases. This results in a more conservative variance model, which safely mitigates faulty observations. With regard to the other three GNSS, the feature map residuals do not exceed the true ranging error, yet the overall magnitude is within the same range.

As the robust loss functions are able to effectively mitigate outliers when a rough estimation of the received error is available, the overall performance remains within an acceptable range. Conversely, the C/N_0 weighting may be overly optimistic in situations where large ranging errors of up to 30 m are encountered. That is attributable to the received C/N_0 value at these epochs, representing a relatively high value (> 30 dB Hz) in comparison to the maximum of approximately 50 dB Hz. This information substantiates the findings of the preceding sections, which indicate that the incorporation of feature map data leads to a reduction in gross errors and an improvement in the position solution in the majority of the situations.

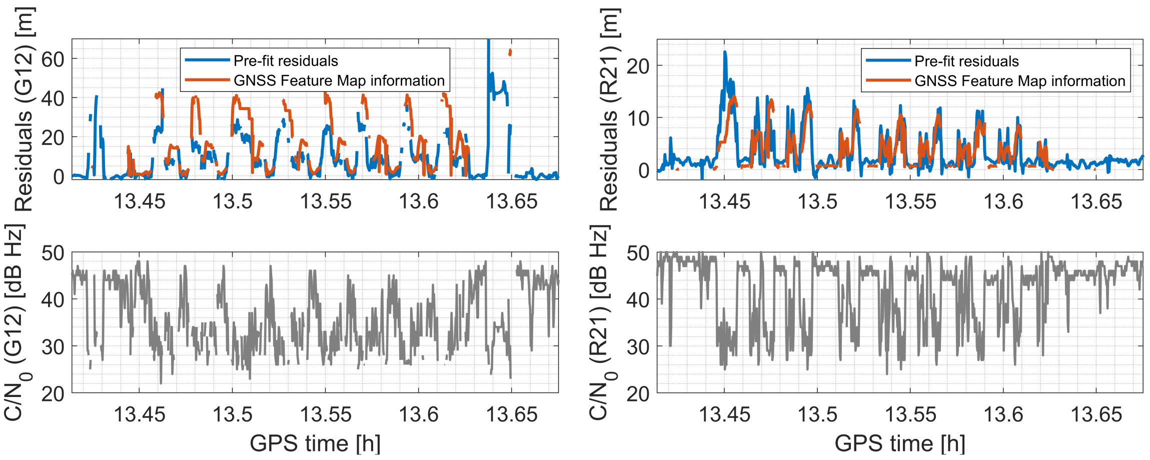

(a) GC1C (b) RC1C

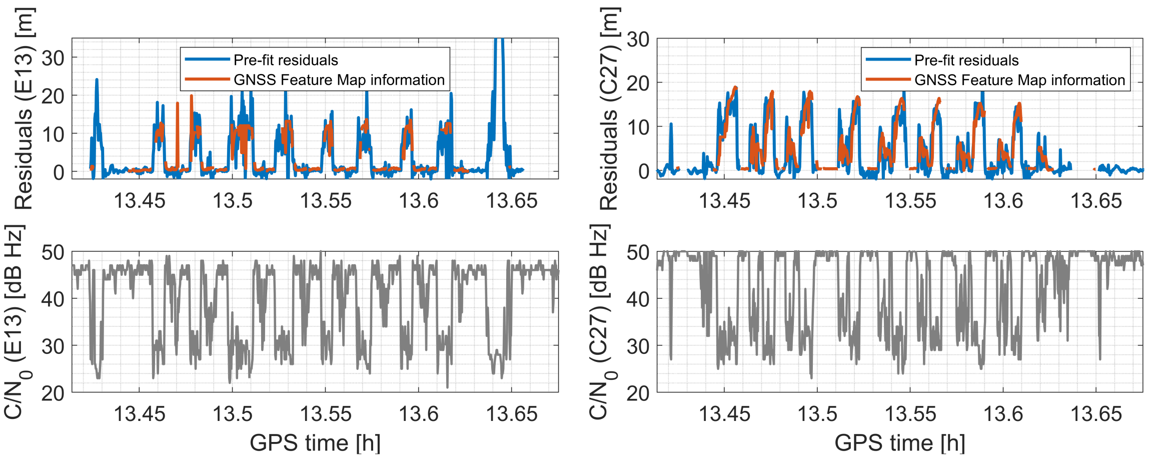

(c) EC1C (d) CC2I

Figure 5.19: Septentrio mosaicX5 receiver: Comparison of DD pre-fit residuals and GNSS Feature Map residuals. (a) to (d) show the time series for a single satellite for each L1 signal from the four GNSS.

u-blox F9P (L1/L5) Receiver

The most significant variation in performance is anticipated for the *u-blox F9P (L1/L5)* receiver, as this receiver type can be classified as a high-sensitivity consumer-grade receiver, distinguished by elevated observation noise levels (Ruwisch et al., 2020; Kersten and Paffenholz, 2020). Furthermore, it has a limited number of channels, consequently limiting the available observation types from 17 (*Septentrio PolaRx5e* receiver) and 11 (*Septentrio mosaicX5* receiver) to a reduced set of 7 carrier frequencies. This limitation is further expressed by the total number of observations per epoch, as depicted in Fig. 5.17.

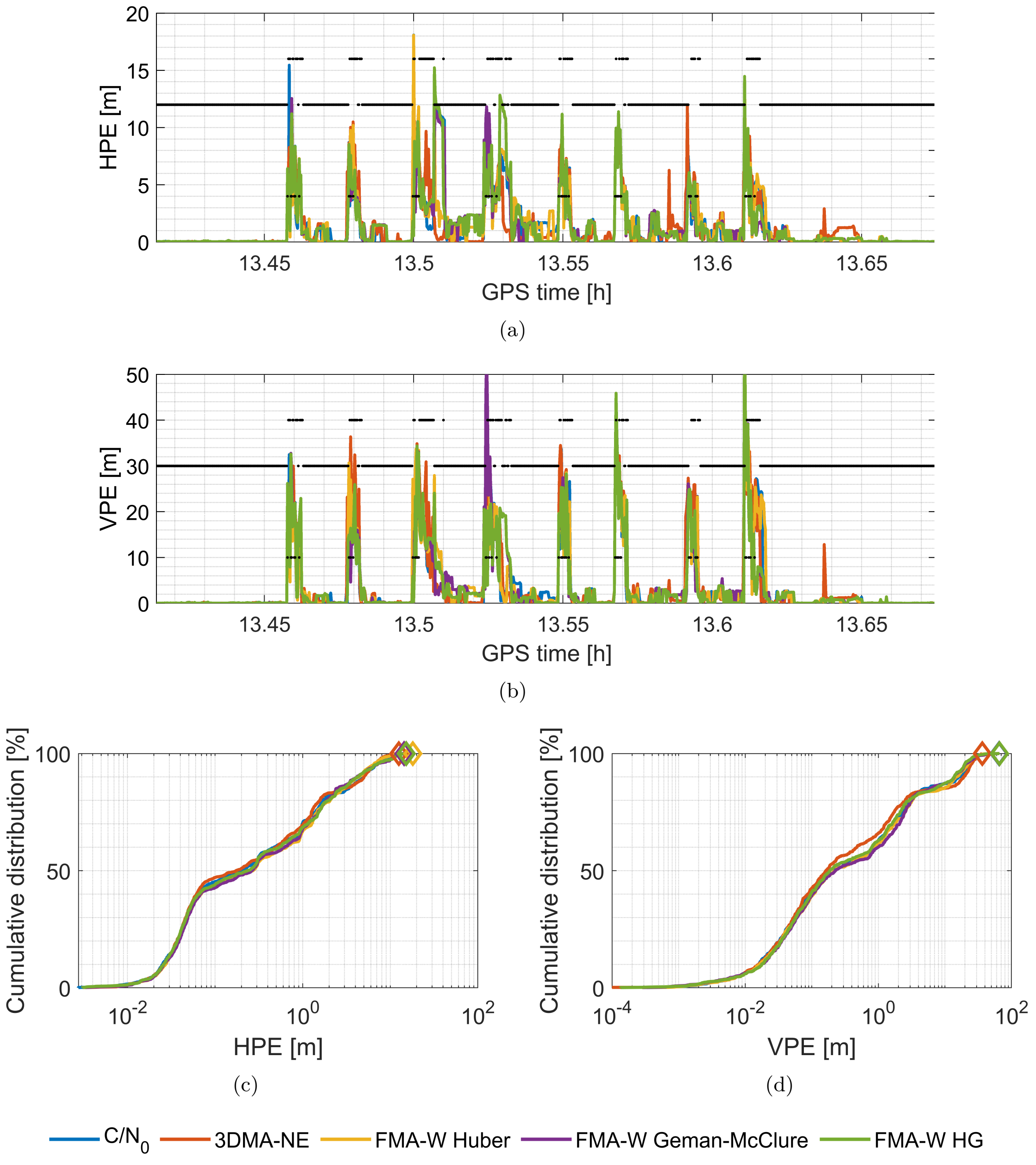

(a)

(b)

(c)

(d)

Figure 5.20: u-blox F9P (L1/L5) receiver: Horizontal and vertical position errors of the different approaches versus time ((a) and (b)) including the position mode (DGNSS: 2, RTK fix: 4, RTK float: 5) and as cumulative distribution diagram ((c) and (d)). Note the different axis limits.

Figure 5.20 illustrates the horizontal and vertical PE along with the corresponding position mode (DGNSS: 2, RTK fix: 4, RTK float: 5), exemplary included for the GNSS FMA-W HG method, with respect to the time, as well as a cumulative distribution diagram. Please note that the y-axis of the time series figures has been truncated for improved visual clarity. The results demonstrate a distinct difference compared to the characteristics of the other receivers. Due to the limited number of available observations, the position mode frequently transitions to DGNSS mode, resulting in horizontal and vertical position deviations of over 10 m and 30 m, respectively. The reduced availability of nominal observations leads to a longer time until the solution converges from RTK float to RTK fix. Thereby, it is not guaranteed that the solution is in the centimeter to decimeter range when the solution is in RTK fix mode, which is attributable to wrong ambiguity fixing. The aforementioned characteristics are observed in all five estimation strategies. Irrespective of the exclusion of NLOS satellites from the estimation process or the down-weighting of potential faulty satellites by the combination of feature map information with robust loss functions, the resulting position deviations are comparable. This behavior is clearly observed in the cumulative frequency diagrams, where all five curves are superimposed on each other.

To further illustrate the similarity of the horizontal and vertical position accuracy among the different estimation strategies, the RMS errors are depicted in Tab. 5.7. The horizontal PE varies between approximately 2.5 m and 2.8 m, whereas the vertical position error varies between approximately 7.7 m and 9 m among the different approaches. These variations are considered to be negligible when viewed in comparison to the overall magnitude of the respective RMS error.

To evaluate the applicability of the proposed GNSS FMA-W methods with different hardware, residuals are analyzed by comparing GNSS Feature Map residuals to DD pre-fit residuals derived from the ground truth, reflecting true ranging errors. The comparison is depicted in Figure 5.21, featuring time series data for a single satellite across each L1 signal of the four GNSS, along with corresponding signal strength. Note that the time series begins and ends where no feature map data is available. Despite differing hardware, feature map residuals offer a reliable estimate of the actual ranging error, closely matching DD pre-fit residuals for smaller errors and aligning variances for larger errors accordingly. Conversely, significant ranging errors can lead to overly optimistic C/N_0 weightings due to relatively high C/N_0 ($>$ 30 dB Hz) compared to a maximum of about 50 dB Hz. For *u-blox F9P (L1/L5)* receiver data, the use of feature map data does not markedly reduce gross errors or enhance solution stability; however, the predicted and actual errors remain consistent, supporting the method's applicability.

The aforementioned analysis revealed that the robust feature map-aided variance model not being aligned with the actual observation errors, could be excluded as the cause of the estimation providing less accurate results compared to the other receivers. The potential reasons for this discrepancy are more likely attributable to the overall low observation availability

Table 5.7: u-blox F9P (L1/L5) receiver: RMS of the horizontal and vertical position error for the different approaches.

	RMS of horizontal PE [m]	RMS of vertical PE [m]
C/N_0	2.827	8.502
3DMA-NE	2.525	8.991
GNSS FMA-W Huber	2.564	8.356
GNSS FMA-W Geman-McClure	2.782	8.245
GNSS FMA-W HG	2.802	7.744

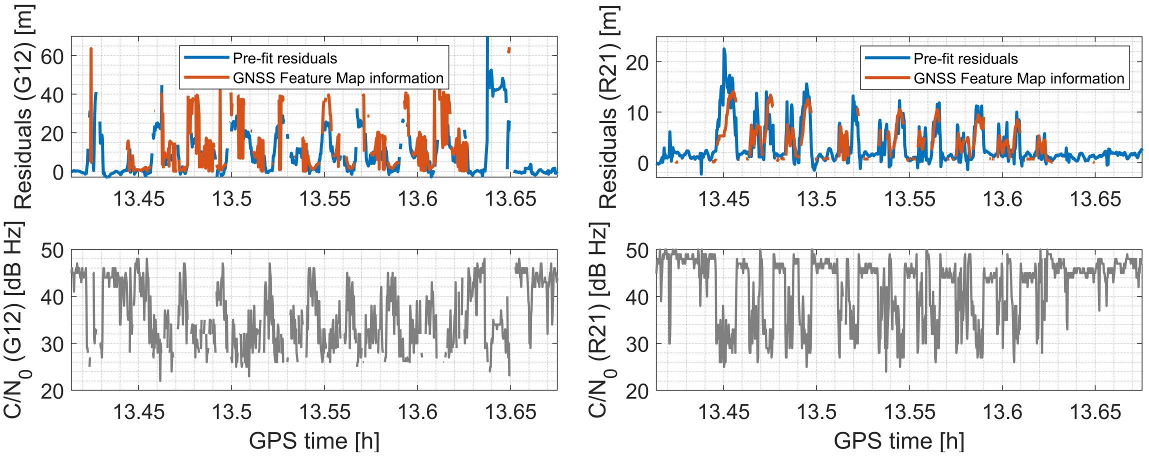

(a) GC1C (b) RC1C

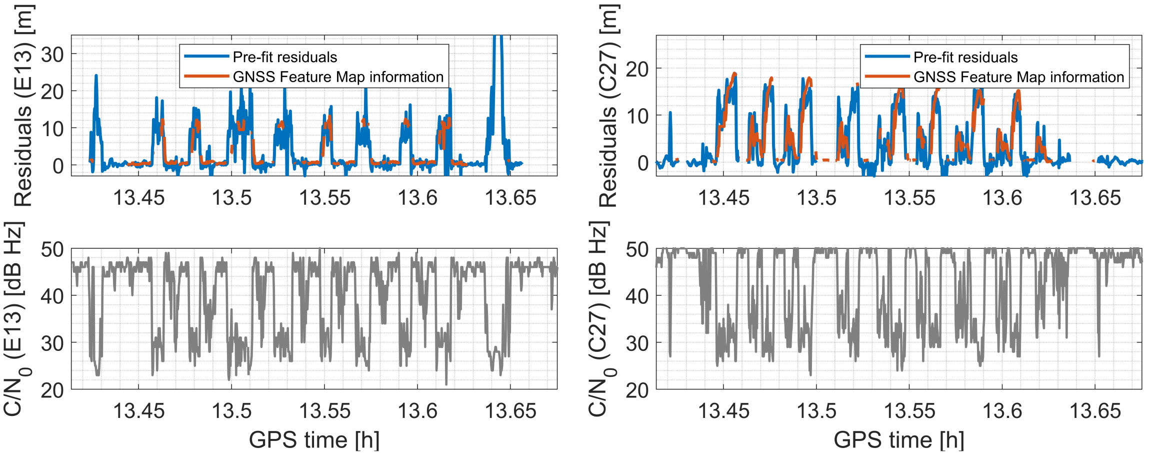

(c) EC1C (d) CC2I

Figure 5.21: u-blox F9P (L1/L5) receiver: Comparison of DD pre-fit residuals and GNSS Feature Map residuals. (a) to (d) show the time series for a single satellite for each L1 signal from the four GNSS.

and comparable poor observation quality. It has previously been demonstrated that due to the limited number of observation types, the carrier phase availability is reduced and consequently, the solution more frequently transitions to DGNSS mode. As illustrated in Tab. 5.8, the *u-blox F9P (L1/L5)* receiver exhibits 4.7 % DGNSS epochs, while the proportion is 0.2 % for the *Septentrio mosaicX5* receiver and 0 % for the *Septentrio PolaRx5e* receiver. Table 5.8 further depicts the number of observations in addition to the number of carrier phase interruptions, which is another indicator of the observation quality. It is important to note that an interruption includes all cases where the gap between two data points is less than 10 seconds. As expected, the number of available observations is the lowest for the *u-blox F9P (L1/L5)* receiver compared to the other receivers. In consideration of the observation quality, the *u-*

Table 5.8: Proportion of DGNSS modes, number of carrier phase observations, and number of carrier phase interruptions (data gap below 10 epochs) for the different receiver types. Please note that the number of carrier phase frequencies varies for the different receivers.

	Septentrio PolaRx5e	Septentrio mosaicX5	u-blox F9P
Proportion of DGNSS epochs	0 %	0.2 %	4.7 %
Number of observations	59,220	33,938	23,439
Number of interruptions	1,253	893	2,048

blox F9P (L1/L5) receiver demonstrates the highest number of signal interruptions, yielding the highest interruption-to-observation proportion (approximately 9 % compared to approximately 2 % for the *Septentrio PolaRx5e* and *Septentrio mosaicX5* receivers). Therefore, it is concluded that the primary factors hindering the efficiency of the GNSS FMA-W methods in enhancing the positioning solutions are the low observation availability and the poor observation quality.

5.3.6 Comparison with Receiver-internal RTK Solution

This section presents a comprehensive comparison of the receivers' internal RTK performance with the results obtained from the preceding sections. For the sake of clarity, only the 3DMA-NE and GNSS FMA-W HG methods are subjected to analysis. It is evident that a direct comparison between the solutions is not feasible, given that the receiver provides a real-time position, whereas the other solutions are computed in post-processing, thereby eliminating latency errors. Nevertheless, the comparison provides an overview of the potential of the different approaches.

Septentrio PolaRx5e Receiver

Figure 5.22 illustrates the 3D position error as a function of time, as a cumulative distribution, and color-coded by the respective solution type for the *Septentrio PolaRx5e* receiver. It should be noted that the y-axes are scaled differently. In this instance, Fig. 5.22(b) and Fig. 5.22(c) include the static phases at the parking space with nearly open-sky conditions. It can be observed that the receiver-internal RTK solution and the two post-processed solutions yield comparable results, with an accuracy of a few centimeters, for the static parking space periods. Consequently, all methods are in RTK fix mode.

Upon entering the deep urban trench, the receiver-internal solution transitions from RTK fix to RTK float and subsequently to pseudorange-based DGNSS and SPP modes. Consequently, the 3D PE increases to approximately 5 m to 20 m until the vehicle was moving back to the parking lot at approximately 13.65 h. This behavior is similarly reflected in the cumulative distribution diagram, which depicts two distinctly separate clusters of deviations. One cluster is below 10 cm, while the other is above 2.5 m, with only a few values in between. In contrast, as stated in the preceding sections, the 3DMA-NE and GNSS FMA-W HG methods provide a substantial number of RTK fix epochs even in deep urban trench situations. The GNSS FMA-W HG method is capable of effectively mitigating larger position errors due to a continuous carrier phase-based solution. In contrast, the 3DMA-NE method transitions to DGNSS mode in between, resulting in a 3D PE of up to 50 m.

Septentrio mosaicX5 Receiver

The 3D position error as a function of time, as cumulative distribution and color-coded by the respective solution type obtained from *Septentrio mosaicX5* receiver data is depicted in Fig. 5.23. It should be noted that the y-axes are scaled differently. In this instance, Fig. 5.23(b) and Fig. 5.23(c) include the static phases at the parking space with nearly open-sky conditions. During the static phases, the receiver-internal RTK solution and the two post-processed solutions yield comparable results with an accuracy of a few centimeters. The position mode of the receiver-internal solution alternates between RTK fix and pseudorange-based DGNSS, despite the fact that it provides centimeter-level deviations. Upon entering the deep urban trench, the receiver-internal solution exhibited an increased scattering of the

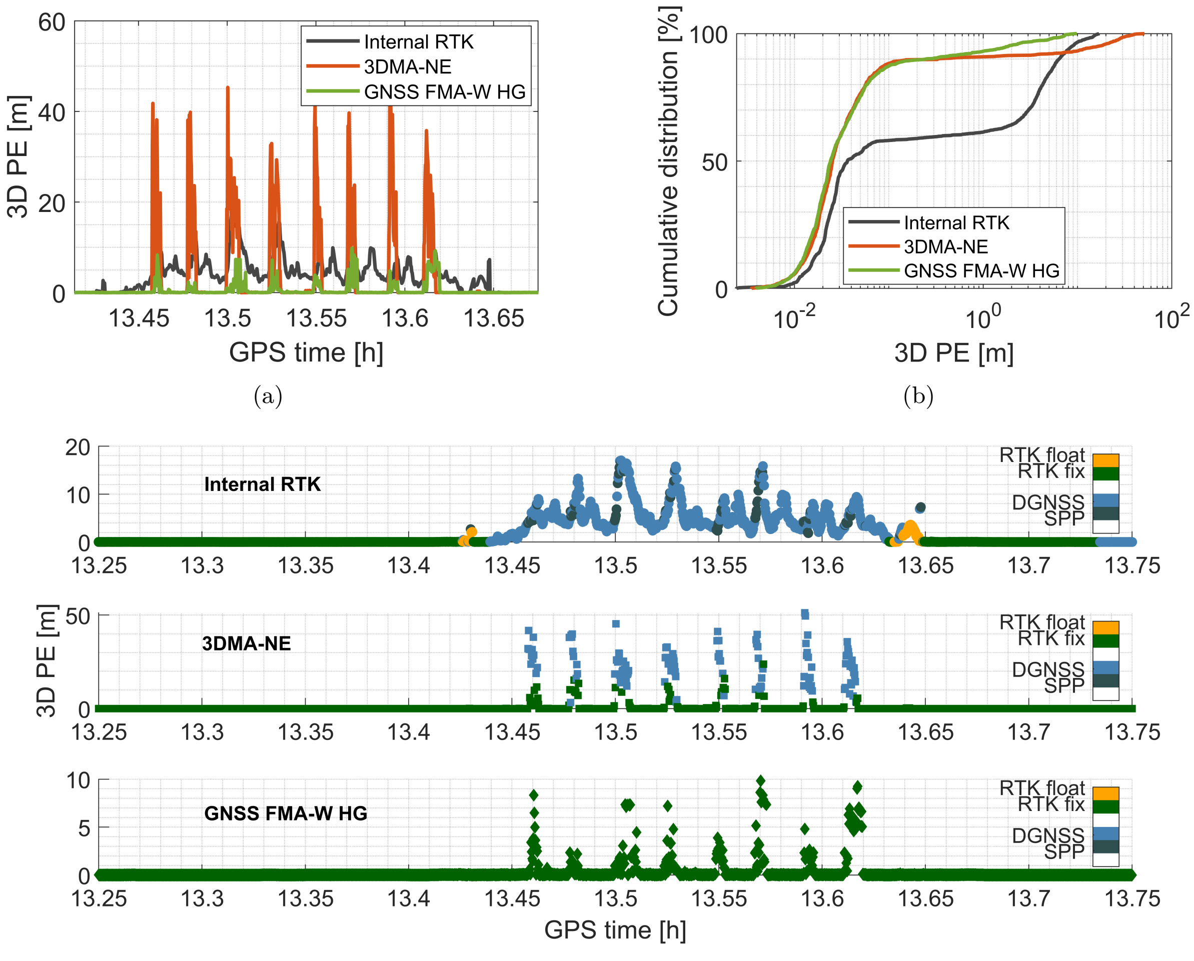

(a)

(b)

(c)

Figure 5.22: Septentrio PolaRx5e receiver: Positioning accuracy of the 3DMA-NE and GNSS FMA-W HG methods compared to the receiver-internal RTK solution. (a) shows the 3D PE over time, (b) shows the cumulative distribution of the 3D PE, and (c) shows the 3D PE over time color-coded by the solution type.

3D PE, yielding deviations of up to 10 m during DGNSS mode. However, the receiver is able to recover and transition back to RTK float and RTK fix mode, respectively, thereby providing centimeter-level deviations. This behavior is similarly reflected in the cumulative distribution diagram, which depicts a substantial number of values below 10 cm. These values can be assigned to the RTK fix epochs, which are primarily associated with the static phase. Afterwards, the curve show a relatively shallow slope, indicating the scattering in the range of decimeters to several meters. In contrast, as stated in the preceding sections, the 3DMA-NE and GNSS FMA-W HG methods provide a substantial number of RTK fix epochs even in deep urban trench situations. Despite two short time periods, where the position mode transitions to DGNSS, the GNSS FMA-W HG method is capable of effectively mitigating larger position errors due to a continuous carrier phase-based solution. In contrast, the 3DMA-NE method frequently transitions to DGNSS mode in between, resulting in a 3D PE frequently increasing to 50 m.

u-blox F9P (L1/L5) Receiver

Figure 5.24 illustrates the 3D position error as a function of time, as a cumulative distribution, and color-coded by the respective solution type for the *u-blox F9P (L1/L5)* receiver. It should

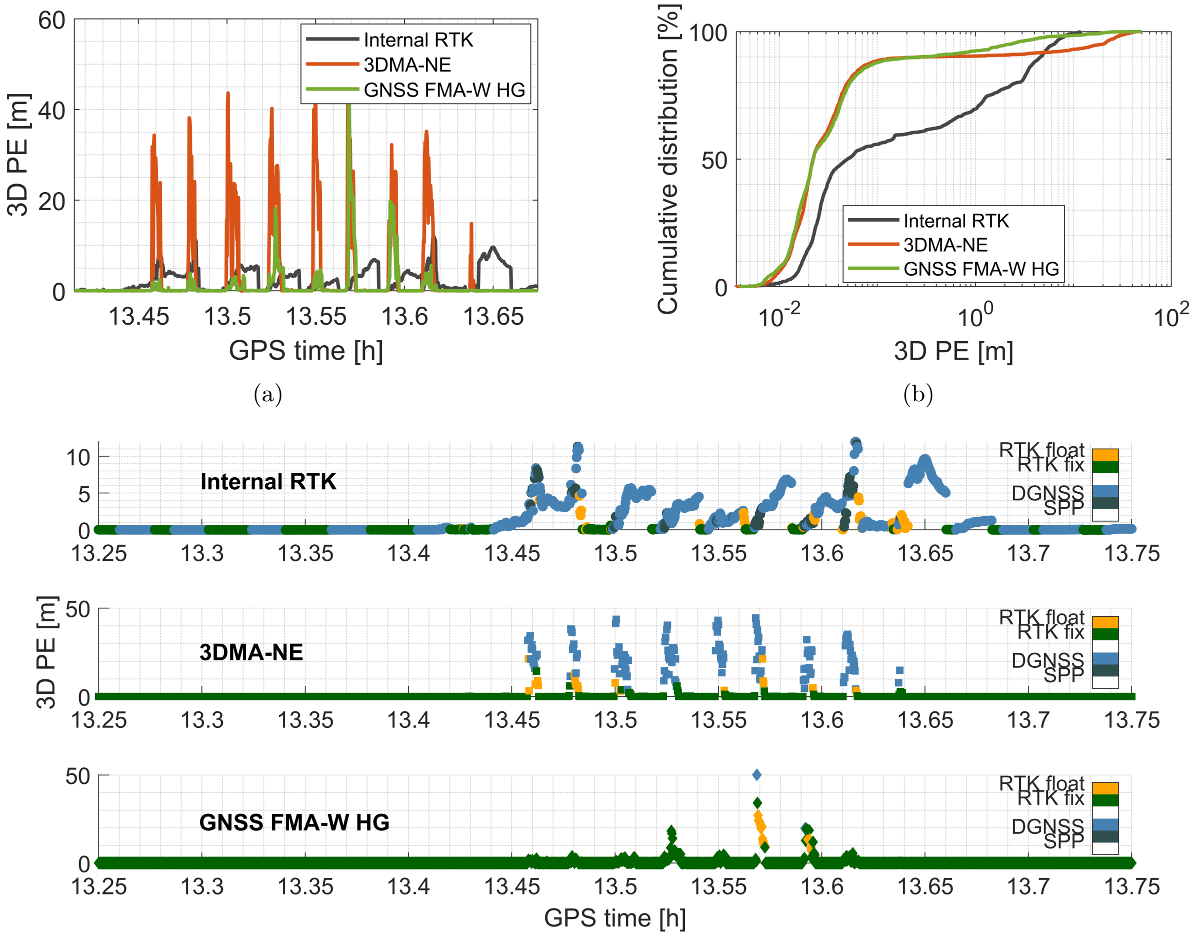

(a)

(b)

(c)

Figure 5.23: Septentrio mosaicX5 receiver: Positioning accuracy of the 3DMA-NE and GNSS FMA-W HG methods compared to the receiver-internal RTK solution. (a) shows the 3D PE over time, (b) shows the cumulative distribution of the 3D PE, and (c) shows the 3D PE over time color-coded by the solution type.

be noted that the y-axes are scaled differently. In this instance, Fig. 5.24(b) and Fig. 5.24(c) include the static phases at the parking space with nearly open-sky conditions. As a consequence of the transition from RTK fix to pseudorange-based DGNSS position mode at approximately 13.42 h and 13.62 h, the number of centimeter-level deviations is reduced for the receiver-internal solution. This is indicated by a relatively shallow slope in the cumulative distribution, whereas the slope for the two post-processed methods is rather steep. However, upon entering the deep urban trench, the *u-blox F9P (L1/L5)* receiver provides a way more stable solution. Only a small number of epochs are classified as DGNSS, with the 3D PE still being below 2 m. The position mode alternates primarily between an RTK fix and RTK float, yielding deviations that are in the centimeter to decimeter range and occasionally reaching up to 2 m. In contrast, the 3DMA-NE and GNSS FMA-W HG methods yield results that are comparable to one another, yet neither is able to match the performance of the receiver-internal solution. Both methods frequently transition to DGNSS mode and subsequently are unable to rapidly recover from the significant deviations. Although the RTK fix solution is provided, the resulting deviations are in the meter-level, indicating a significant number of erroneous ambiguity fixes, as stated in the preceding section. The *u-blox F9P (L1/L5)* receivers' internal RTK solution performance is enhanced due to a more advanced motion model in the filter implementation, which effectively mitigates larger position errors during the pseudorange-based position modes. This facilitates the receivers' capability to recover from these epochs.

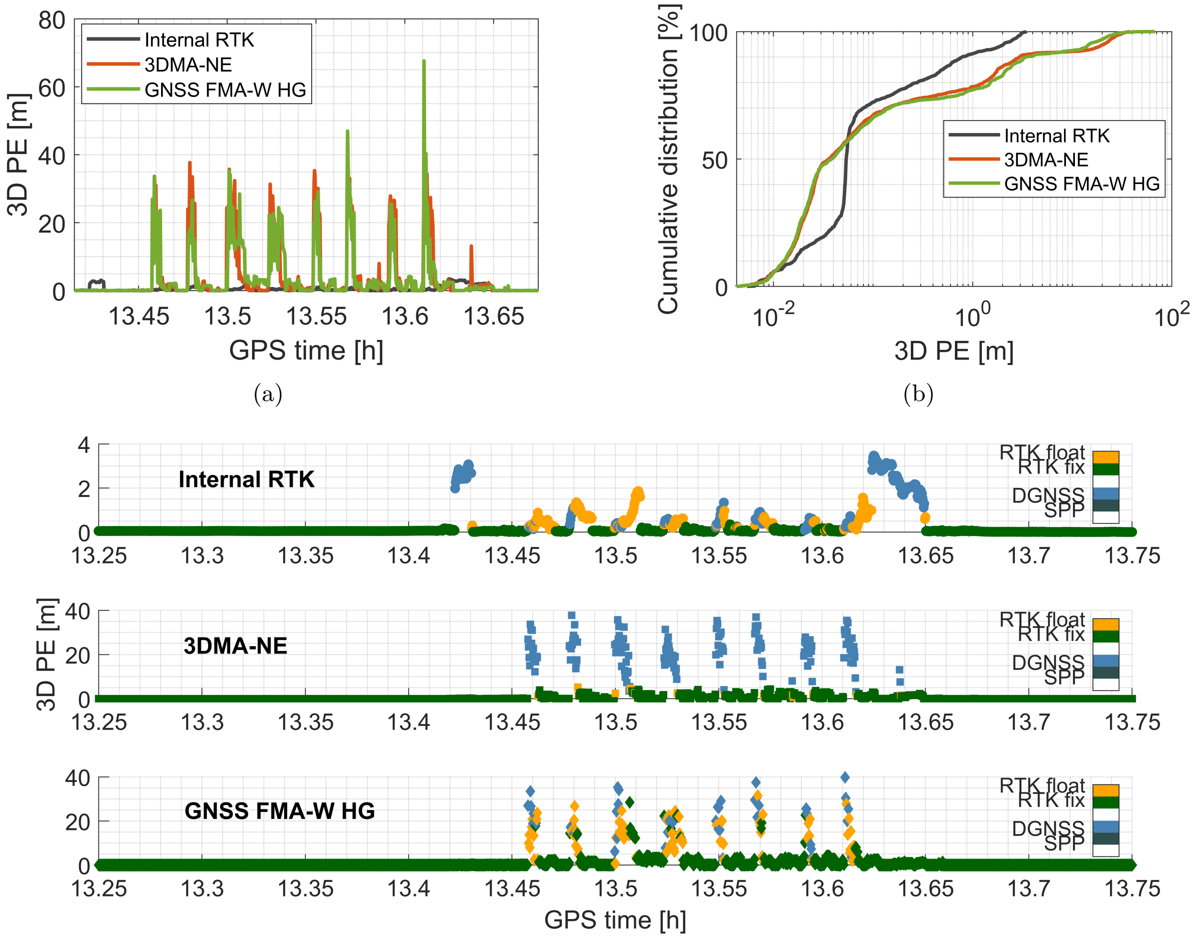

(a)

(b)

(c)

Figure 5.24: u-blox F9P (L1/L5) receiver: Positioning accuracy of the 3DMA-NE (red) and GNSS FMA-W HG (green) methods compared to the receiver-internal RTK solution (gray). (a) shows the 3D PE over time, (b) shows the cumulative distribution of the 3D PE, and (c) shows the 3D PE over time color-coded by the solution type.

6

Conclusions

6.1 Summary

Many ITS applications, such as autonomous driving, rely on an accurate localization from the GNSS sensor as the only source of absolute positioning information. The main error source for vehicle localization in urban environments is the reception of signals that are reflected on the surfaces of buildings, resulting in significant errors in the vehicle position estimation. The primary objective of this thesis is to leverage the ground-track repeatability of reflection-based GNSS errors in a GNSS Feature Map and its application to urban vehicle navigation. The scope of this thesis is subdivided into four main parts, that is (i) the theoretical derivation of the need for an adaption of existing robust estimation strategies for urban GNSS navigation, (ii) the definition of two innovative position estimation strategies, i.e., GNSS FMA-NE and GNSS FMA-W, and the performance simulation of the latter method compared to existing robust estimators, (iii) the generation of GNSS Feature Maps, and (iv) the practical validation of the proposed GNSS Feature Map-aided robust EKF. The most important investigations and findings are summarized in the following.

Conventional robust estimators are able to provide nearly optimal results in the presence of multiple outliers upon a particular breakdown point. As the proportion of contaminated observations reaches 50 %, nominal and contaminated observations cannot be separated. This, in turn, leads to a biased estimation. The signal reception environment of a vehicle moving through urban trenches presents significant challenges, as the field of view for receiving LOS signals is limited by the surrounding buildings. Typical signal reception characteristics have been illustrated for an exemplary trajectory in a residential area with four-to-five-story buildings on both sides of the road, demonstrating that the LOS ratio frequently drops below 50 %. That in turn demonstrates the need for the adaptation of existing robust estimation techniques.

Existing strategies (e.g., the utilization of different (robust) weighting models, 3DMA GNSS, data snooping) are susceptible to several limitations, i.e., an overly conservative down-weighting of observations, lack of robustness for highly contaminated data, the need of additional 3D city model information or computationally intensive algorithms. To overcome these weaknesses, two innovative strategies have been proposed for improving GNSS-based navigation in urban trenches. These strategies make use of additional information made available through the GNSS Feature Map. The GNSS FMA-NE method employs map information containing satellite visibility classification results, while the GNSS FMA-W method utilizes map information containing pseudorange residuals. Both adapted estimation strategies have been incorporated into the GNSS RTK EKF framework. The performance of the proposed GNSS FMA-W method, employing various robust loss functions for computing the observation weights, is theoretically evaluated through a Monte-Carlo simulation. Thereby, the HG-estimator, an adapted robust estimator, is introduced. The HG-estimator incorporates the presented advantages and mitigates the particular drawback of the Huber and Geman-McClure loss functions. The simulation results of the multi-GNSS SPP demonstrate that when the ranging errors of the received GNSS signals are known prior to and utilized for the observation weights computation, the use of robust loss functions yields localization results close to the ground truth. The 3D position error is approximately 2 m even though 70 % of the observations have a standard deviation of 100 m.

As the GNSS Feature Map constitutes a fundamental part of the developed estimation strategies, its generation has been described in detail. This detailed description initially starts with the conceptualization of extending the existing multipath mitigation strategies for single, static stations (i.e., utilizing the ground-track repeatability of ranging errors) with the objective of generating a map tailored for automotive applications. The generation of the map is comprised of a series of steps, with the OSM coordinate information serving as the foundation of the map. The generation of boxes is based on OSM road information, with alignment in a regular grid. These boxes are containing either satellite visibility information from offline ray tracing computations or pseudorange residual information obtained from a real-data measurement campaign. The resolution of the waypoints (i.e., the center point of the boxes) have been analyzed by a detailed simulation study, revealing that the number of transitions in the LOS/NLOS classification of satellite signals is only marginal when moving the users' location longitudinally and laterally in an urban trench. The maps' required height resolution, as demonstrated by heights above ground for the most extreme vehicle dimensions, leads to the conclusion that incorporating additional map layers for different vehicle types is not necessary. To generate maps containing pseudorange residual information, the data of a measurement campaign must be aggregated in the respective boxes of the map. Therefore, the similarity of GNSS ranging errors have been investigated with respect to a lateral shift of an GNSS antenna on the roof of a vehicle and with respect to signals from different systems. The GMMs have been computed from the pseudorange residuals of the two antennas, and the GMM with four components exhibited the strongest alignment with the observed ranging error distribution. The overall distribution consists of four components, which account for the varying magnitude of the different types of error sources, including multipath, NLOS, and diffraction. The main findings of these analyses are that, for both the lateral antenna shift and the analysis of signals from different systems, the characteristic values of the GMM component estimation are comparable and within the range for the expected pseudorange measurement noise.

As the foundation of the map generation in this thesis is a training data experiment, the number of observations in this training data set is finite. Consequently, the number of available measurements have been evaluated with regard to the possibility of generating a reliable and fully populated map. Despite the fact that the generation of one map for each signal would ensure the lowest possible level of uncertainty in the data aggregation, the utilized pseudorange residuals map in this thesis utilizes the L1 measurements of all available GNSS (GPS, GLONASS, Galileo, BDS). This is due to the available data density in each of the boxes. To guarantee the consistent and reliable functionality of the map in subsequent applications, it is essential to ensure that it is fully completed, i.e., containing information for all elevation-azimuth combinations. The reliability of interpolation of the GPS L1-only map is found to be unsatisfactory due to the substantial size of areas lacking available information, resulting in a highly generalized interpolation pattern. Conversely, when utilizing data from the four GNSS, the regions situated beyond the obstruction border particularly exhibit a higher degree of density, thereby reducing the uncertainty associated with the interpolation process. The interpolation result provides a more detailed representation of pseudorange measurement errors.

The practical evaluation and validation of the proposed models have been carried out by two kinematic automotive experiments in different urban environments, classified as *medium urban trench* and *deep urban trench*. The ground truth of both trajectories has been computed in post-processing by combining GNSS carrier phase and Doppler observations with raw measurements from a high quality INS in a tightly coupled relative positioning with respect to the institute's reference station. The proposed GNSS Feature Map-aided methods have been integrated into the GNSS RTK EKF framework using multi-GNSS multi-frequency observations. The benefits of the adapted robust estimation have been quantified in terms of the impact on the accuracy and integrity of the coordinate estimates, and on the ambiguity resolution, respectively.

The *medium urban trench* trajectory is characterized by predetermined measurement contamination proportions between 30 % and 80 %. Due to the relatively moderate signal reception conditions, all methods provide coordinate estimates deviating from the ground truth in the centimeter to decimeter range. In consideration of the performance specifications for automotive applications it was found that the 3DMA-NE, GNSS FMA-W Huber, GNSS FMA-W Geman-McClure, and GNSS FMA-W HG methods provide a 95 % accuracy of the horizontal and vertical component, which meets the specified lane keeping requirement. Among all methods, the adapted robust HG-estimator yields the most accurate results, resulting in an improvement of the overall RMS error compared to the C/N_0 weighting by 54 % horizontally and 79 % vertically. Consequently, the integrity is further improved due to the reduced position error and better observation uncertainty assignment, yielding the largest number of nominal operation epochs and the lowest number of hazardous misleading instances. As indicated by the ambiguity resolution analyses, the reasons for the aforementioned findings can be understood as follows: while the percentage of fixed ambiguities is the lowest for the GNSS FMA-W approaches, the position error remains low as well due to the mitigation of false fixes, which would lead to larger position errors.

The *deep urban trench* trajectory presents a particularly challenging scenario, as the predetermined measurement contamination proportion for this data fluctuates within the range of 50 % to 85 %, which is a contamination level where all conventional estimators are expected to break down. Due to the limited number of available LOS carrier phase measurements, the 3DMA-NE method frequently provides DGNSS solutions, resulting in position deviations at the meter level. Among all estimation strategies, the GNSS FMA-W HG method provides the most accurate solution, reducing the overall RMS error compared to the C/N_0 weighting by 60 % horizontally and 64 % vertically. The adapted robust estimation thereby primarily mitigates gross errors in the most challenging situations. For the deep urban trench trajectory, lane keeping accuracy requirements have not been achieved. However, the GNSS FMA-W HG method is the only one capable of providing satisfactory accuracy values in order to meet the specified lane determination requirements in both the longitudinal and lateral directions. It was found that the combination of map information with a more robust loss function (i.e., Geman-McClure and HG) significantly reduces the position error for LOS ratios between 25 % and 60 %. This enhancement is achieved by the utilization of a map that contains pseudorange residual information, which corresponds to the observed ranging errors, thereby leading to a reliable approximation of the observations' uncertainty. Consequently, the integrity of the system is improved by increasing the number of nominal operations and reducing the number of hazardous misleading information, similar to the medium urban trench trajectory. Furthermore, the ambiguity resolution has been enhanced, as evidenced by the observation that a significant proportion of fixed ambiguities result in accurate coordinate estimates when more robust loss functions are employed, and larger errors are observed at low fixing proportions. In contrast, C/N_0 weighting and the less robust GNSS FMA-W Huber methods do not necessarily exhibit accurate position solutions at high ambiguity fixing proportions.

The hardware dependency of the proposed methods has been investigated by evaluating the performance of the adapted robust estimation with data from different GNSS receivers. The performance comparison indicates that the pseudorange residual information, obtained from the maps, still provides a fairly accurate description of the actual received ranging error, even though the map was generated by a different grade of receiver. The observed discrepancy in performance is attributable to variations in measurement availability across different receivers, which is primarily influenced by the tracking capability of the receivers. It has been determined that the presence of more GNSS signals serves to reduce the likelihood of the solution transitioning to DGNSS mode. Beyond the reduced number of available observations, the second limiting factor identified is the observation quality. The presence of a substantial number of interruptions has been demonstrated to negatively impact the position solution.

Lastly, the achieved performance of the 3DMA-NE and GNSS FMA-W HG methods has been compared to the respective receiver-internal RTK solutions. The internal solutions of the *Septentrio PolaRx5e* and *Septentrio mosaicX5* receivers exhibit deviations in the centimeter range for the static parts of the trajectory. Upon entering the deep urban trench, the receiver-internal solution transitions from RTK fix to RTK float and subsequently to pseudorange-based DGNSS and SPP modes. Consequently, for the majority of the trajectory, both receivers provide a position accuracy at the meter level. In contrast, the 3DMA-NE and GNSS FMA-W HG methods are capable of providing centimeter-to-decimeter level deviations in the deep urban trench. Thereby, the utilization of the GNSS FMA-W HG method results in the best overall performance due to a continuous carrier phase-based solution. The *u-blox F9P (L1/L5)* receivers' internal RTK solution performance is enhanced due to a more advanced motion model in the filter implementation, which effectively mitigates larger position errors during the pseudorange-based position modes. This facilitates the receivers' capability to recover from these epochs. Therefore, the proposed methods are not able to achieve the performance of the receiver-internal solution.

In conclusion, the generation of the GNSS Feature Map has been introduced and its generalization of GNSS signal propagation-related features has been investigated. The combination of map information with robust estimation strategies, both existing and newly defined, has been theoretically and practically evaluated in various experiments including simulated observation data and true kinematic experiments. The findings of these studies demonstrate that the proposed methodology significantly improves the accuracy and integrity of the navigation system compared to existing strategies. This ensures increased availability of automotive GNSS-based navigation applications, such as lane keeping and lane determination, for vehicles navigating through urban trenches.

6.2 Outlook

Despite the evident advances in GNSS navigation in urban trenches that have been demonstrated by combining GNSS Feature Map information with robust estimation strategies, there are still multiple open questions that emerged during the course of the presented investigations. These open questions give room for further research, some of which will be addressed in the following.

The analyses in this thesis have been carried out in post-processing, despite the fact that the RTK algorithm was originally designed for real-time applications. In order for the presented methodology to be integrated into automotive applications, it must be real-time capable, a feature that has yet to be tested and must be investigated in the future. Therefore, the GNSS FMA-W must be implemented into a GNSS receiver. However, this is virtually impossible for a conventional user since there is no straightforward way to access the firmware of a typical commercial receiver. The implementation necessitates even more advanced low-level programming skills. A potential way of still being able to test the real-time capability would be the utilization of a Software-defined Radio (SDR), which is more flexible in terms of different or new signal processing algorithms.

This thesis presents the generation of GNSS Feature Maps for a selected area in the city of Hannover. The size of the grid has been studied based on exemplary situations in that area, yielding fixed characteristic values of the generated map. In order to apply these maps in practice, they must to be valid for larger areas covering entire cities with varying road characteristics and environmental conditions. Therefore, two possible topics or research questions, respectively, come to mind. First, can the grid size of the map be optimized when the environmental situation changes and/or can environmental context detection techniques (Groves et al., 2013) help for a dynamic grid size computation? The second possible research direction is on the maps' coordinate basis. It is obvious that the performance depends on the accuracy of the available lane/road model. In situations with more than one lane, OSM might not be best choice as typically only one coordinate per street is available. Therefore, the generation and/or investigation of a more accurate lane model is of particular interest.

Another important topic is that of feature computation, which is the content that the map provides to the user. Due to the relatively slow movement of the GNSS satellites, it is challenging to collect a high density of training data using a single vehicle. However, the hardware independence affords the opportunity to leverage crowd-sourced data for the purpose of map generation. The vast majority of modern automobiles are equipped with GNSS sensors, thereby enabling the collection of a substantial volume of data, provided that data security and privacy concerns are addressed. This abundance of data has the potential to further ensure the continuous updating of maps. A primary research direction should involve the assessment of whether post-processed GNSS-only ground truth solutions are adequate for feature computation. The generalization of the map demonstrates significant potential for leveraging these data. Another promising avenue for the collection of training data that is less time-consuming is the utilization of Low Earth Orbit (LEO) satellite data, as the orbital repeat time is much shorter. This would result in larger areas being covered in less time. However, the initial step should involve the investigation of the ranging errors received from LEO satellites, as the efficiency of this approach hinges on the ability to compare these errors with those of GNSS ranging.

In this thesis, the provision of pseudorange residual information is solely used for an improved observation uncertainty assignment. Existing 3DMA GNSS methods are separated into NLOS exclusion and observation rectification strategies. One potential research direction could be the development of a more advanced observation exclusion strategy based on the magnitude of the expected ranging error or, the utilization of the provided information for correcting the observed NLOS observations. However, the implementation of an observation rectification strategy within carrier phase-based positioning necessitates a detailed investigation of the carrier phase NLOS error.

So far, the enhancement of GNSS navigation has been presented based on a rather simple Kalman filter algorithm with no specific parameter tuning and a simple process noise model, as the focus has been on the pure relative improvement among the different methods. To further enhance the accuracy of the navigation solution, one option could be the tuning of filter parameters, e.g., different variances per frequency and GNSS, potentially achieved by variance component estimation. Alternatively, the implementation of a more advanced and powerful estimation technique, such as particle filters or factor graph optimization, has the potential to further improve the overall performance.

Bibliography

Abramovich, Y. I. and Turcaj, P. (1999). Impulsive Noise Mitigation in Spatial and Temporal Domains for Surface-Wave Over-the-Horizon Radar. Technical Report, DTIC Document, Cooperative Research Centre for Sensor Signal and Information Processing.

Akram, M., Liu, P., Wang, Y., and Qian, J. (2018). GNSS positioning accuracy enhancement based on robust statistical MM estimation theory for ground vehicles in challenging environments. *Applied Sciences*, 8(6):876.

Automobile Dimensions (2023). https://de.automobiledimension.com/abmessungen-autos-volkswagen.html.

Baasch, K.-N., Icking, L., Ruwisch, F., and Schön, S. (2023). Coordinate Frames and Transformations in GNSS Ray-Tracing for Autonomous Driving in Urban Areas. *Remote Sensing*, 15(1):180.

Barron, J. T. (2019). A general and adaptive robust loss function. In: *2019 IEEE/CVF Conference on Computer Vision and Pattern Recognition (CVPR)*. IEEE.

Betaille, D., Peyret, F., Ortiz, M., Miquel, S., and Fontenay, L. (2013). A New Modeling Based on Urban Trenches to Improve GNSS Positioning Quality of Service in Cities. *IEEE Intelligent Transportation Systems Magazine*, 5(3):59–70.

Betz, J. W. (2021). Fundamentals of Satellite-Based Navigation and Timing. In: Morton, Y. J., van Diggelen, F., Spilker Jr., J. J., and Parkinson, B. W. (Ed.), *Position, Navigation, and Timing Technologies in the 21st Century: Integrated Satellite Navigation, Sensor Systems, and Civil Applications*, pp. 43–64. John Wiley & Sons, Inc., Hoboken, New Jersey.

Bilich, A. and Larson, K. M. (2007). Mapping the GPS multipath environment using the signal-to-noise ratio (SNR). *Radio Science*, 42(6).

Bisnath, S. (2021). Relative Positioning and Real-Time Kinematic (RTK). In: Morton, Y. J., van Diggelen, F., Spilker Jr., J. J., and Parkinson, B. W. (Ed.), *Position, Navigation, and Timing Technologies in the 21st Century: Integrated Satellite Navigation, Sensor Systems, and Civil Applications*, pp. 481–502. John Wiley & Sons, Inc., Hoboken, New Jersey.

Blankenship, T. K., Kriztman, D. M., and Rappaport, T. S. (1997). Measurements and simulation of radio frequency impulsive noise in hospitals and clinics. In: *1997 IEEE 47th Vehicular Technology Conference. Technology in Motion*, VETEC-97. IEEE.

Blewitt, G. (1989). Carrier phase ambiguity resolution for the Global Positioning System applied to geodetic baselines up to 2000 km. *Journal of Geophysical Research: Solid Earth*, 94(B8):10187–10203.

Braasch, M. S. (2017). Multipath. In: Teunissen, P. J. G. and Montenbruck, O. (Ed.), *Springer Handbook of Global Navigation Satellite Systems*, pp. 443–468. Springer International Publishing.

Brack, A., Männel, B., and Schuh, H. (2020). GLONASS FDMA data for RTK positioning: a five-system analysis. *GPS Solutions*, 25(9).

Bradbury, J., Ziebart, M., Cross, P. A., Boulton, P., and Read, A. (2007). Code multipath modelling in the urban environment using large virtual reality city models: Determining the local environment. *Journal of Navigation*, 60:95 – 105.

Brown, R. and Hwang, P. (2012). *Introduction to random signals and applied Kalman filtering with Matlab exercises*. Wiley, 4th edition.

Brown, R. G. (1992). A Baseline GPS RAIM Scheme and a Note on the Equivalence of Three RAIM Methods. *Navigation*, 39(3):301–316.

Brunner, F. K., Hartinger, H., and Troyer, L. (1999). GPS signal diffraction modelling: the stochastic SIGMA-Δ model. *Journal of Geodesy*, 73(5):259–267.

Business Location Center (2022). Berlin 3D - Download Portal.
URL: https://www.businesslocationcenter.de/en/economic-atlas/download-portal/. Accessed: 25.02.2022.

Butsch, F. and Kipka, A. (2004). Die Bedeutung des Signal-zu-Rauschleistungsverhältnisses und verwandter Parameter für die Messgenauigkeit bei GPS. *Allgemeine Vermessungsnachrichten (AVN)*, 2(111):46–55.

Caspary, W. F. (2000). *Concepts of Network And Deformation Analysis.* School of Geomatic Engineering, The University of New South Wales, Australia, 3rd corrected edition.

Chen, D. and Lachapelle, G. (1995). A Comparison of the FASF and Least-Squares Search Algorithms for on-the-Fly Ambiguity Resolution. *Navigation*, 42(2):371–390.

Crespillo, O. G., Andreetti, A., and Grosch, A. (2020). Design and Evaluation of Robust M-estimators for GNSS Positioning in Urban Environments. In: *Proceedings of the 2020 International Technical Meeting of The Institute of Navigation*, pp. 750–762.

Crespillo, O. G., Medina, D., Skaloud, J., and Meurer, M. (2018). Tightly coupled GNSS/INS integration based on robust M-estimators. In: *2018 IEEE/ION Position, Location and Navigation Symposium (PLANS)*, pp. 1554–1561. IEEE.

Crespillo, O. G., Ruiz-Sicilia, J. C., Kliman, A., and Marais, J. (2023). Robust design of a machine learning-based GNSS NLOS detector with multi-frequency features. *Frontiers in Robotics and AI*, 10:1171255.

Dach, R., Lutz, S., Walser, P., and Fridez, P. (2015). Initial Phase Ambiguities and Ambiguity Resolution. In: *Bernese GNSS Software Version 5.2*, pp. 191–208. University of Bern, Bern Open Publishing.

Dach, R., Schär, S., Arnold, D., Brockmann, E., Kalarus, M. S., Lasser, M., Stebler, P., and Jäggi, A. (2024). CODE final product series for the IGS. Published by Astronomical Institute, University of Bern.

De Jonge, P. J. and Tiberius, C. C. J. M. (1996). The LAMBDA method for integer ambiguity estimation: implementation aspects. *Delft Geodetic Computing Centre, LGR series No.12, Delft University of Technology.*

Department of Information Technology and Telecommunications (DoITT) (2022). NYC 3-D Building Model. URL: https://www1.nyc.gov/site/doitt/initiatives/3d-building.page. Accessed: 25.02.2022.

Ding, Y., Feriol, F., Watanabe, Y., Asseman, P., Pages, G., and Vivet, D. (2023). Adaptive Robust-Statistics GNSS Navigation Based on Environmental Context Detection. In: *Proceedings of the 2023 International Technical Meeting of The Institute of Navigation.* Institute of Navigation.

Dong, D. and Bock, Y. (1989). Global Positioning System Network analysis with phase ambiguity resolution applied to crustal deformation studies in California. *Journal of Geophysical Research: Solid Earth*, 94(B4):3949–3966.

Dong, D., Wang, M., Chen, W., Zeng, Z., Song, L., Zhang, Q., Cai, M., Cheng, Y., and Lv, J. (2015). Mitigation of multipath effect in GNSS short baseline positioning by the multipath hemispherical map. *Journal of Geodesy*, 90(3):255–262.

Du, Y., Wang, J., Rizos, C., and El-Mowafy, A. (2021). Vulnerabilities and integrity of precise point positioning for intelligent transport systems: overview and analysis. *Satellite Navigation*, 2(1).

Du, Z., Chai, H., Xiao, G., Wang, M., Yin, X., and Chong, Y. (2020). A method for undifferenced and uncombined PPP ambiguity resolution based on IF FCB. *Advances in Space Research*, 66(12):2888–2899.

El-Mowafy, A., Xu, B., and Hsu, L.-T. (2020). Integrity monitoring using multi-GNSS pseudorange observations in the urban environment combining ARAIM and 3D city models. *Journal of Spatial Science*, 67(1):91–110.

Elallid, B. B., Benamar, N., Hafid, A. S., Rachidi, T., and Mrani, N. (2022). A Comprehensive Survey on the Application of Deep and Reinforcement Learning Approaches in Autonomous Driving. *Journal of King Saud University - Computer and Information Sciences*, 34(9):7366–7390.

Elsayed, H., El-Mowafy, A., and Wang, K. (2023). A new method for fault identification in real-time integrity monitoring of autonomous vehicles positioning using PPP-RTK. *GPS Solutions*, 28(32).

El-Mowafy, A. (2020). Fault detection and integrity monitoring of GNSS positioning in intelligent transport systems. *IET Intelligent Transport Systems*, 14(3):164–171.

Etter, P. C. (2003). *Underwater Acoustic Modelling and Simulation.* CRC Press.

Euler, H.-J. and Goad, C. C. (1991). On optimal filtering of GPS dual frequency observations without using orbit information. *Bulletin Géodésique*, 65(2):130–143.

Euler, H.-J. and Landau, H. (1992). Fast GPS ambiguity resolution on-the-fly for real-time application. In: *Proceedings of the 6th International Geodetic Symposium on Satellite Positioning, Columbus, OH*, pp. 650–659.

European Comission (2003). World wide radionavigation system - evaluation of the Galileo performance against maritime GNSS requirements. *Submitted to the International Maritime Organization, Subcommittee on Safety of Navigation, NAV 49/14*.

European GNSS Agency (2015). Report on the Performance and Level of Integrity for Safety and Liability Critical Multi-Applications. Technical Report, European GNSS Agency.

European GNSS Agency (2020). GNSS User Technology Report. Technical Report Issue 3, European GNSS Agency.

EUSPA (2024). EUSPA EO and GNSS: Market Report. Technical Report Issue 2, European Union for the Space Programme.

Falco, G., Pini, M., and Marucco, G. (2017). Loose and Tight GNSS/INS Integrations: Comparison of Performance Assessed in Real Urban Scenarios. *Sensors*, 17(2):255.

Farnworth, R. (2017). Aviation Applications. In: Teunissen, P. J. G. and Montenbruck, O. (Ed.), *Springer Handbook of Global Navigation Satellite Systems*, pp. 877–903. Springer International Publishing.

Farrell, J. A. (2008). Optimal State Estimation. In: *Aided Navigation: GPS with High Rate Sensors*, pp. 169–216. The McGraw-Hill Companies.

Feng, Y., Wang, C., and Karl, C. (2018). Determination of required positioning integrity parameters for design of vehicle safety applications. In: *Proceedings of the 2018 International Technical Meeting of The Institute of Navigation*, pp. 129–141.

Fernàndez-Plazaola, U., Martín-Guerrero, T. M., Entrambasaguas-Munoz, J. T., and Martín-Neira, M. (2004). The Null method applied to GNSS three-carrier phase ambiguity resolution. *Journal of Geodesy*, 78(1–2):96–102.

França, R. P., Borges Monteiro, A. C., Arthur, R., and Iano, Y. (2021). An overview of deep learning in big data, image, and signal processing in the modern digital age. In: Piuri, V., Raj, S., Genovese, A., and Srivastava, R. (Ed.), *Trends in Deep Learning Methodologies*, pp. 63–87. Academic Press.

Frei, E. and Beutler, G. (1990). Rapid static positioning based on the fast ambiguity resolution approach FARA: theory and first results. *Manuscripta Geodaetica*, 76:351–361.

Fuhrmann, T., Luo, X., Knöpfler, A., and Mayer, M. (2014). Generating statistically robust multipath stacking maps using congruent cells. *GPS Solutions*, 19(1):83–92.

Gaglione, S., Innac, A., Carbone, S. P., Troisi, S., and Angrisano, A. (2017). Robust estimation methods applied to GPS in harsh environments. In: *2017 European Navigation Conference (ENC)*. IEEE.

Gelb, A. (1974). *Applied optimal estimation*. M.I.T. Press, Cambridge, Mass.

Geman, S. and McClure, D. E. (1985). Bayesian image analysis: An application to single photon emission tomography. In: *Proceedings of the American Statistical Association*, pp. 12–18.

Godha, S. and Cannon, M. E. (2007). GPS/MEMS INS integrated system for navigation in urban areas. *GPS Solutions*, 11(3):193–203.

Gröger, G., Kolbe, T. H., Nagel, C., and Häfele, K.-H. (2012). *OGC City Geography Markup Language (CityGML) Enconding Standard*. Open Geospatial Consortium, 2.0.0 edition.

Groves, P. D. (2011). Shadow Matching: A New GNSS Positioning Technique for Urban Canyons. *Journal of Navigation*, 64(3):417–430.

Groves, P. D. (2013a). Multipath vs. NLOS signals: How Does Non-Line-of-Sight Reception Differ From Multipath Interference? *Inside GNSS*, 63:40–44.

Groves, P. D. (2013b). *Principles of GNSS, inertial, and multisensor integrated navigation systems*. Artech House, 2nd edition.

Groves, P. D. and Jiang, Z. (2013). Height Aiding, C/N0 Weighting and Consistency Checking for GNSS NLOS and Multipath Mitigation in Urban Areas. *Journal of Navigation*, 66(5):653–669.

Groves, P. D., Martin, H., Voutsis, K., Walter, D., and Wang, L. (2013). Context Detection, Categorization and Connectivity for Advanced Adaptive Integrated Navigation. In: *Proceedings of the 26th International Technical Meeting of the Satellite Division of The Institute of Navigation (ION GNSS+ 2013)*, pp. 1039–1056.

Groves, P. D., Wang, L., Adjrad, M., and Ellul, C. (2015). GNSS Shadow Matching: The Challenges Ahead. In: *Proceedings of the 28th International Technical Meeting of the Satellite Division of The Institute of Navigation (ION GNSS+ 2015)*, pp. 2421–2443.

Haklay, M. and Weber, P. (2008). OpenStreetMap: User-Generated Street Maps. *IEEE Pervasive Computing*, 7(4):12–18.

Hampel, F. R. (1971). A general qualitative definition of robustness. *The Annals of Mathematical Statistics*, 42(6):1887–1896.

Harris, R. A. (1997). Direct resolution of carrier-phase ambiguity by bridging the wavelength gap. *ESA Publication TST/60 107/RAH/Word*.

Hartinger, H. and Brunner, F. K. (1999). Variances of GPS Phase Observations: The SIGMA-ϵ Model. *GPS Solutions*, 2(4):35–43.

Hatch, R. (1991). Instantaneous Ambiguity Resolution. In: Schwarz, K.-P. and Lachapelle, G. (Ed.), *Kinematic Systems in Geodesy, Surveying, and Remote Sensing. International Association of Geodesy Symposia*, vol. 107, pp. 299–308. Springer, New York.

Hatch, R., Jung, J., Enge, P., and Pervan, B. (2000). Civilian GPS: The Benefits of Three Frequencies. *GPS Solutions*, 3(4):1–9.

Hauschild, A. (2017a). Basic Observation Equations. In: Teunissen, P. J. G.; Montenbruck, O. (Ed.), *Springer Handbook of Global Navigation Satellite Systems*, pp. 561–582. Springer International Publishing.

Hauschild, A. (2017b). Combinations of Observations. In: Teunissen, P. J. G. Montenbruck, O. (Ed.), *Springer Handbook of Global Navigation Satellite Systems*, pp. 583–604. Springer International Publishing.

Hentschel, M. and Wagner, B. (2010). Autonomous robot navigation based on OpenStreetMap geodata. In: *13th International IEEE Conference on Intelligent Transportation Systems*. IEEE.

Hofmann-Wellenhof, B., Lichtenegger, H., and Wasle, E. (2008). *GNSS - Global Navigation Satellite Systems. GPS, GLONASS, Galileo and more.* Springer, Wien, NewYork.

Hsu, L.-T. (2017a). Analysis and modeling GPS NLOS effect in highly urbanized area. *GPS Solutions*, 22(7).

Hsu, L.-T. (2017b). GNSS multipath detection using a machine learning approach. In: *2017 IEEE 20th International Conference on Intelligent Transportation Systems (ITSC)*, pp. 1–6. IEEE.

Hsu, L.-T., Gu, Y., and Kamijo, S. (2015). NLOS Correction/Exclusion for GNSS Measurement Using RAIM and City Building Models. *Sensors*, 15(7):17329–17349.

Hsu, L.-T., Gu, Y., and Kamijo, S. (2016). Sensor integration of 3D map aided GNSS and smartphone PDR in urban canyon with dense foliage. In: *2016 IEEE/ION Position, Location and Navigation Symposium (PLANS)*, pp. 85–90. IEEE.

Hsu, L.-T., Tokura, H., Kubo, N., Gu, Y., and Kamijo, S. (2017). Multiple faulty GNSS measurement exclusion based on consistency check in urban canyons. *IEEE Sensors Journal*, 17(6):1909–1917.

Huber, P. J. (1964). Robust estimation of a location parameter. *The Annals of Mathematical Statistics*, 35(1):73–101.

Huber, P. J. and Ronchetti, E. M. (2009). *Robust Statistics.* Wiley, 2nd edition.

ICAO (2006). *Convention on International Civil Aviation. Annex 10: Aeronautical Telecommunications. Volume I: Radio Navigation Aids.* International Civil Aviation Organization, 6th edition.

Icking, L., Kersten, T., and Schön, S. (2020). Evaluating the Urban Trench Model For Improved GNSS Positioning in Urban Areas. In: *2020 IEEE/ION Position, Location and Navigation Symposium (PLANS)*, pp. 631–638. IEEE.

Icking, L., Zhang, G., Hsu, L.-T., and Schön, S. (2022). Quantification of GNSS NLOS Spatial Correlation – A Case Study in Hong Kong's Urban Canyon. In: *Proceedings of the 2022 International Technical Meeting of The Institute of Navigation*, pp. 712–722, Long Beach, California.

Isaacs, J. T., Irish, A. T., Quitin, F., Madhow, U., and Hespanha, J. P. (2014). Bayesian localization and mapping using GNSS SNR measurements. In: *2014 IEEE/ION Position, Location and Navigation Symposium - PLANS 2014*. IEEE.

Iwase, T., Suzuki, N., and Watanabe, Y. (2012). Estimation and exclusion of multipath range error for robust positioning. *GPS Solutions*, 17(1):53–62.

Jin, S. G. and Park, P. H. (2005). A new precision improvement in zenith tropospheric delay estimation by GPS. *Current Science*, 89(6):997–1000.

Joosten, P. and Tiberius, C. (2002). LAMBDA: FAQs. *GPS Solutions*, 6(1-2):109–114.

Jung, J., Enge, P., and Pervan, B. (2000). Optimization of Cascade Integer Resolution with Three Civil GPS Frequencies. In: *Proceedings of the 13th International Technical Meeting of the Satellite Division of The Institute of Navigation (ION GPS 2000)*, pp. 2191–2200.

Kalman, R. E. (1960). A new approach to linear filtering and prediction problems. *Journal of Basic Engineering*, 82(1):35–45.

Kersten, T. and Paffenholz, J.-A. (2020). Feasibility of consumer grade GNSS receivers for the integration in multi-sensor-systems. *Sensors*, 20(9):2463.

Kigotho, O. N. and Rife, J. H. (2021). Comparison of Rectangular and Elliptical Alert Limits for Lane-Keeping Applications. In: *Proceedings of the 34th International Technical Meeting of the Satellite Division of The Institute of Navigation (ION GNSS+ 2021)*, pp. 93–104.

Kim, D. and Langley, R. B. (1999). An Optimized Least-Squares Technique for Improving Ambiguity Resolution and Computational Efficiency. In: *Proceedings of the 12th International Technical Meeting of the Satellite Division of The Institute of Navigation (ION GPS 1999)*, pp. 1579–1588.

Kim, D. and Langley, R. B. (2000). GPS Ambiguity Resolution and Validation: Methodologies, Trends and Issues. In: *Proceedings of 7th GNSS Workshop, Seoul, Korea.*

Kim, D. and Langley, R. B. (2001). Quality control techniques and issues in GPS applications: Stochastic modelling and reliability testing. In: *Proceedings of the 8th GNSS Workshop, 2001 International Symposium on GPS/GNSS*, pp. 76–85.

Kim, K. and Shevlyakov, G. (2008). Why Gaussianity? *IEEE Signal Processing Magazine*, 25(2):102–113.

Kjørsvik, N. S., Øvstedal, O., and Gjevestad, J. G. O. (2009). Kinematic Precise Point Positioning During Marginal Satellite Availability. In: Sideris, M. G. (Ed.), *Observing our Changing Earth. International Association of Geodesy Symposia*, vol. 133, pp. 691–699. Springer, Berlin, Heidelberg.

Knight, N. L. and Wang, J. (2009). A comparison of outlier detection procedures and robust estimation methods in GPS positioning. *Journal of Navigation*, 62(4):699–709.

Kouba, J. and Héroux, P. (2001). Precise Point Positioning Using IGS Orbit and Clock Products. *GPS Solutions*, 5(2):12–28.

Kulemann, D. and Schön, S. (2025). Contributions to Velocity Integrity for Autonomous Navigation in Urban Environments. In: *2025 IEEE/ION Position, Location and Navigation Symposium (PLANS)*, pp. 1455–1466. IEEE.

Lamborghini Webpage (2023). https://www.lamborghini.com/de-en/modelle/aventador.

Land Information Centre (LIC), Survey and Mapping Office (SMO), Lands Department (2021). Information Sheet on 3D Spatial Data. The Government of the Hong Kong Special Administrative Region.

Landeshauptstadt Hannover, FB Planen und Stadtentwicklung, Bereich Geoinformation (2017). *Produktinformation Digitales 3D-Stadtmodell.* Landeshauptstadt Hannover, Rudolf-Hillebrecht-Platz 1, 30159 Hannover, 3rd edition.

Landskron, D. and Böhm, J. (2018). VMF3/GPT3: refined discrete and empirical troposphere mapping functions. *Journal of Geodesy*, 92(4):349–360.

Langley, R. B., Teunissen, P. J. G., and Montenbruck, O. (2017). Introduction to GNSS. In: P. J. G. Teunissen and Montenbruck, O. (Ed.), *Springer Handbook of Global Navigation Satellite Systems*, pp. 3–23. Springer International Publishing.

Larson, K. M., Small, E. E., Gutmann, E., Bilich, A., Axelrad, P., and Braun, J. (2007). Using GPS multipath to measure soil moisture fluctuations: initial results. *GPS Solutions*, 12(3):173–177.

Lau, L. and Cross, P. (2007). Development and testing of a new ray-tracing approach to GNSS carrier-phase multipath modelling. *Journal of Geodesy*, 81(11):713–732.

Lawrence, D. G. (2009). A new method for partial ambiguity resolution. In: *Proceedings of the 2009 International Technical Meeting of The Institute of Navigation*, pp. 652–663, Anaheim, CA.

Li, B., Feng, Y., and Shen, Y. (2010). Three carrier ambiguity resolution: distance-independent performance demonstrated using semi-generated triple frequency GPS signals. *GPS Solutions*, 14(2):177–184.

Li, B., Lou, L., and Shen, Y. (2016). GNSS elevation-dependent stochastic modeling and its impacts on the statistic testing. *Journal of Surveying Engineering*, 142(2):04015012.

Li, H., Medina, D., Vilà-Valls, J., and Closas, P. (2019). Robust Kalman Filter for RTK Positioning under Signal-Degraded Scenarios. In: *Proceedings of the 32nd International Technical Meeting of the Satellite Division of The Institute of Navigation (ION GNSS+ 2019)*, pp. 3717–3729.

Li, X., Li, X., Huang, J., Shen, Z., Wang, B., Yuan, Y., and Zhang, K. (2021). Improving PPP–RTK in urban environment by tightly coupled integration of GNSS and INS. *Journal of Geodesy*, 95(132).

Liso Nicolas, M., Smyrnaios, M., Schön, S., and Kurner, T. (2012). Investigation of diffraction effects in GNSS using ray tracing channel modelling: Preliminary results. In: *2012 6th European Conference on Antennas and Propagation (EUCAP)*, pp. 3154–3158. IEEE.

Luo, X., Mayer, M., and Heck, B. (2009). Improving the Stochastic Model of GNSS Observations by Means of SNR-based Weighting. In: Sideris, M. G. (Ed.), *Observing our Changing Earth. International Association of Geodesy Symposia*, vol. 133, pp. 725–734. Springer, Berlin, Heidelberg.

Lyu, Z. and Gao, Y. (2023). An efficient pixel shader-based ray-tracing method for correcting GNSS non-line-of-sight error with large-scale surfaces. *GPS Solutions*, 27(4).

Ma, H., Zhao, Q., Verhagen, S., Psychas, D., and Liu, X. (2020). Assessing the Performance of Multi-GNSS PPP-RTK in the Local Area. *Remote Sensing*, 12(20):3343.

Maqsood, M., Gao, S., and Montenbruck, O. (2017). Antennas. In: Teunissen, P. J. G.; Montenbruck, O. (Ed.), *Springer Handbook of Global Navigation Satellite Systems*, pp. 505–534. Springer International Publishing.

Maronna, R., Bustos, O., and Yohai, V. (1979). Bias- and Efficiency-Robustness of General M-Estimators for Regression with Random Carriers. In: Gasser, T. and Rosenblatt, M. (Ed.), *Smoothing Techniques for Curve Estimation: Proceedings of a Workshop held in Heidelberg*, pp. 91–116. Springer Berlin, Heidelberg.

Martin-Neira, M., Toledo, M., and Pelaez, A. (1995). The null space method for GPS integer ambiguity resolution. In: *Proceedings of DSNS'95, Bergen, Norway*, vol. 31.

McGraw, G. A., Groves, P. D., and Ashman, B. W. (2021). Robust Positioning in the Presence of Multipath and NLOS GNSS Signals. In: Morton, Y. J., van Diggelen, F., Spilker Jr., J. J., and Parkinson, B. W. (Ed.), *Position, Navigation, and Timing Technologies in the 21st Century: Integrated Satellite Navigation, Sensor Systems, and Civil Applications*, pp. 551–589. John Wiley & Sons, Inc., Hoboken, New Jersey.

Medina, D., Li, H., Vila-Valls, J., and Closas, P. (2019). On Robust Statistics for GNSS Single Point Positioning. In: *2019 IEEE Intelligent Transportation Systems Conference (ITSC)*, pp. 3281–3287. IEEE.

Medina, D., Li, H., Vilà-Valls, J., and Closas, P. (2021). Robust Filtering Techniques for RTK Positioning in Harsh Propagation Environments. *Sensors*, 21(4):1250.

Medina, D. A. (2021). *Robust GNSS Carrier Phase-based Position and Attitude Estimation.* Diss., Universidad Carlos III. de Madrid.

Medina, D. A., Romanovas, M., Herrera-Pinzon, I., and Ziebold, R. (2016). Robust position and velocity estimation methods in integrated navigation systems for inland water applications. In: *2016 IEEE/ION Position, Location and Navigation Symposium (PLANS)*, pp. 491–501. IEEE.

Middleton, D. (1999). Non-Gaussian noise models in signal processing for telecommunications: new methods an results for class A and class B noise models. *IEEE Transactions on Information Theory*, 45(4):1129–1149.

Miura, S., Hsu, L.-T., Chen, F., and Kamijo, S. (2015). Gps error correction with pseudorange evaluation using three-dimensional maps. *IEEE Transactions on Intelligent Transportation Systems*, 16(6):3104–3115.

Möller, T. and Trumbore, B. (2005). Fast, Minimum Storage Ray/Triangle Intersection. In: *ACM SIGGRAPH 2005 Courses*, SIGGRAPH '05, New York, NY, USA. ACM.

Montenbruck, O., Steigenberger, P., Khachikyan, R., Weber, G., Langley, R. B. und Mervart, L., and Hugentobler, U. (2014). IGS-MGEX: Preparing the Ground for Multi-Constellation GNSS Science. *Inside GNSS*, 9(1):42–49.

Montenbruck, O., Steigenberger, P., Khachikyan, R., Weber, G., Langley, R., Mervat, L., and Hugentobler, U. (2013). IGS-MGEX: Preparing the Ground for Multi-Constellation GNSS Science. In: *4th International Colloquium on Scientific and Fundamental Aspects of the Galileo System, Dezember 4-6, Prague,.*

Nagai, K., Spenko, M., Henderson, R., and Pervan, B. (2024). Fault-Free Integrity of Urban Driverless Vehicle Navigation with Multi-Sensor Integration: A Case Study in Downtown Chicago. *NAVIGATION: Journal of the Institute of Navigation*, 71(1).

Obst, M., Bauer, S., and Wanielik, G. (2012). Urban multipath detection and mitigation with dynamic 3D maps for reliable land vehicle localization. In: *Proceedings of the 2012 IEEE/ION Position, Location and Navigation Symposium*, pp. 685–691. IEEE.

O'Connor, M., Kersten, T., Skupin, C., Ruwisch, F., Ren, L., Wübbena, T., and Schön, S. (2024). Low-latency GNSS multipath simulation and building wall detection in urban environments. *SIMULATION*, 100(1):71 – 89.

O'Connor, M., Ruwisch, F., Kersten, T., Skupin, C., Ren, L., Wübbena, T., and Schön, S. (2021). Low-latency GNSS multipath simulator for real-time applications in autonomous driving. In: *2021 IEEE/ACM 25th International Symposium on Distributed Simulation and Real Time Applications (DS-RT)*, pp. 1–9. IEEE.

Odijk, D. (2017). Positioning Model. In: P. J. G. Teunissen and Montenbruck, O. (Ed.), *Springer Handbook of Global Navigation Satellite Systems*, pp. 605–638. Springer International Publishing.

Official German Surveying and Mapping (2024). SAPOS® - Precise Positioning in Location and Height. Technical Report, Agency for Geoinformation and State Survey of Lower Saxony (LGLN).

OpenStreetMap copyright (2024). https://www.openstreetmap.org/copyright/en.

OpenStreetMap map features (2024). https://wiki.openstreetmap.org/wiki/Mapfeatures.

OpenStreetMap project homepage (2024). https://www.openstreetmap.org/.

Orabi, M., Khalife, J., Abdallah, A. A., Kassas, Z. M., and Saab, S. S. (2020). A Machine Learning Approach for GPS Code Phase Estimation in Multipath Environments. In: *2020 IEEE/ION Position, Location and Navigation Symposium (PLANS)*, pp. 1224–1229. IEEE.

Ozeki, T. and Kubo, N. (2022). GNSS NLOS Signal Classification Based on Machine Learning and Pseudorange Residual Check. *Frontiers in Robotics and AI*, 9:868608.

Parkins, A. (2011). Increasing GNSS RTK availability with a new single-epoch batch partial ambiguity resolution algorithm. *GPS Solutions*, 15(4):391–402.

Pervan, B. S., Pullen, S. P., and Christie, J. R. (1998). A Multiple Hypothesis Approach to Satellite Navigation Integrity. *Navigation*, 45(1):61–71.

Peyraud, S., Bétaille, D., Renault, S., Ortiz, M., Mougel, F., Meizel, D., and Peyret, F. (2013). About Non-Line-Of-Sight Satellite Detection and Exclusion in a 3D Map-Aided Localization Algorithm. *Sensors*, 13(1):829–847.

Pozo-Pérez, J. A., Medina, D., Herrera-Pinzón, I. D., Heßelbarth, A., and Ziebold, R. (2017). Robust outlier mitigation in multi-constellation GNSS-based positioning for waterborne applications. In: *Proceedings of the 2017 International Technical Meeting of The Institute of Navigation*, pp. 1330–1343.

Pullen, S. and Joerger, M. (2021). GNSS Integrity and Receiver Autonomous Integrity Monitoring (RAIM). In: Morton, Y. J., van Diggelen, F., Spilker Jr., J. J., and Parkinson, B. W. (Ed.), *Position, Navigation, and Timing Technologies in the 21st Century: Integrated Satellite Navigation, Sensor Systems, and Civil Applications*, pp. 591–617. John Wiley & Sons, Inc., Hoboken, New Jersey.

Ramm, F., Topf, J., and Chilton, S. (2010). *OpenStreetMap: Using and Enhancing the Free Map of the World.* Uit Cambridge Limited.

Realini, E. and Reguzzoni, M. (2013). goGPS: open source software for enhancing the accuracy of low-cost receivers by single-frequency relative kinematic positioning. *Measurement Science and Technology*, 24(11):115010.

Reid, T. G. R., Houts, S. E., Cammarata, R., Mills, G., Agarwal, S., Vora, A., and Pandey, G. (2019). Localization Requirements for Autonomous Vehicles. *SAE International Journal of Connected and Automated Vehicles*, 2(3):173–190.

Reid, T. G. R., Neish, A., and Manning, B. (2023). Localization & Mapping Requirements for Level 2+ Autonomous Vehicles. In: *Proceedings of the 2023 International Technical Meeting of The Institute of Navigation*, pp. 107–123.

Rost, C. and Wanninger, L. (2009). Carrier phase multipath mitigation based on GNSS signal quality measurements. *Journal of Applied Geodesy*, 3(2):81–87.

Rothacher, M. and Beutler, G. (1998). The role of GPS in the study of global change. *Physics and Chemistry of the Earth*, 23(9–10):1029–1040.

Rousseeuw, P. J. (1984). Least median of squares regression. *Journal of the American Statistical Association*, 79(388):871–880.

Ruwisch, F., Jain, A., and Schön, S. (2020). Characterisation of GNSS Carrier Phase Data on a Moving Zero-Baseline in Urban and Aerial Navigation. *Sensors*, 20(14):4046.

Ruwisch, F., Kersten, T., and Schön, S. (2024). Schlussbericht des Instituts für Erdmessung der Leibniz Universität Hannover zum Verbundvorhaben Korrektur von GNSS-Mehrwegeffekten für die zuverlässige Eigenlokalisierung von hochautomatisierten Fahrzeugen in innerstädtischen Bereichen (KOMET). Technical Report, Institut für Erdmessung, Leibniz Universität Hannover.

Ruwisch, F. and Schön, S. (2022a). GNSS Feature Map: Representation of Signal Propagation-related Features in Urban Trenches. In: *The International Technical Meeting of The Institute of Navigation*, pp. 701–711.

Ruwisch, F. and Schön, S. (2022b). Performance Assessment of GNSS RTK Positioning in Urban Environments: Outlier Detection versus 3DMA-FDE. In: *Proceedings of the 35th International Technical Meeting of the Satellite Division of The Institute of Navigation (ION GNSS+ 2022)*, pp. 2649–2663.

Ruwisch, F. and Schön, S. (2023). GNSS Feature Map Aided RTK Positioning in Urban Trenches. In: *2023 IEEE 26th International Conference on Intelligent Transportation Systems (ITSC): iLoc - High-integrity Localization for Automated Vehicles*, pp. 5798–5804. IEEE.

Ruwisch, F. and Schön, S. (2025). Feature Map Aided Robust High Precision GNSS Positioning in Harsh Urban Environments. *IEEE Transactions on Intelligent Transportation Systems*, pp. 1–13.

Schaper, A., Ruwisch, F., and Schön, S. (2022). Diffraction Modeling for Improved 3DMA GNSS Urban Navigation. In: *Proceedings of the 35th International Technical Meeting of the Satellite Division of The Institute of Navigation (ION GNSS+ 2022)*, pp. 1902–1916.

Schön, S., Baasch, K.-N., KarimiDoona, A., Kulemann, D., Ruwisch, F., Schaper, A., and Su, J. (2025). Advancements in Enhancing GNSS RTK Positioning Accuracy and Integrity for Automated Driving. In: *2025 IEEE Intelligent Vehicles Symposium (IV)*, pp. 460–467. IEEE.

Schön, S. and Brunner, F. K. (2008). A proposal for modelling physical correlations of GPS phase observations. *Journal of Geodesy*, 82(10):601–612.

Simon, D. (2006a). *Optimal State Estimation: Kalman, H_∞, and Nonlinear Approaches.* John Wiley & Sons, Inc.

Simon, D. (2006b). The discrete-time Kalman filter. In: *Optimal State Estimation: Kalman, H_∞, and Nonlinear Approaches*, pp. 123–148. John Wiley & Sons, Inc.

Smyrnaios, M. (2016). *Carrier-phase Multipath in Satellite-based Positioning.* phdthesis, Leibniz University Hanover.

Smyrnaios, M., Schon, S., Nicolas, M. L., and Kurner, T. (2012). Ray-tracing approach versus double difference, multipath characterization in a multiple ray scenario. In: *2012 6th ESA Workshop on Satellite Navigation Technologies (Navitec 2012) & European Workshop on GNSS Signals and Signal Processing*, pp. 1–8. IEEE.

Stern, A. and Kos, A. (2018). Positioning Performance Assessment of Geodetic, Automotive, and Smartphone GNSS Receivers in Standardized Road Scenarios. *IEEE Access*, 6:41410–41428.

Strandjord, K. L., Axelrad, P., and Mohiuddin, S. (2020). Improved urban navigation with shadow matching and specular matching. *NAVIGATION*, 67(3):547–566.

Sun, R., Hsu, L.-T., Xue, D., Zhang, G., and Ochieng, W. Y. (2019). GPS Signal Reception Classification Using Adaptive Neuro-Fuzzy Inference System. *Journal of Navigation*, 72(3):685–701.

Sun, R., Wang, G., Zhang, W., Hsu, L.-T., and Ochieng, W. Y. (2020). A gradient boosting decision tree based GPS signal reception classification algorithm. *Applied Soft Computing*, 86:105942.

Suzuki, T. and Kubo, N. (2012). GNSS Positioning with Multipath Simulation using 3D Surface Model in Urban Canyon. In: *Proceedings of the 25th International Technical Meeting of the Satellite Division of The Institute of Navigation (ION GNSS+ 2012)*, pp. 438–447.

Suzuki, T. and Kubo, N. (2013). Correcting GNSS Multipath Errors Using a 3D Surface Model and Particle Filter. In: *Proceedings of the 26th International Technical Meeting of the Satellite Division of The Institute of Navigation (ION GNSS+ 2013)*, pp. 1583–1595.

Suzuki, T., Nakano, Y., and Amano, Y. (2017). NLOS Multipath Detection by Using Machine Learning in Urban Environments. In: *Proceedings of the 30th International Technical Meeting of The Satellite Division of the Institute of Navigation (ION GNSS+ 2017)*, GNSS 2017, pp. 3958–3967.

Takasu, T. and Yasuda, A. (2010). Kalman-Filter-Based Integer Ambiguity Resolution Strategy for Long-Baseline RTK with Ionosphere and Troposphere Estimation. In: *Proceedings of the 23rd International Technical Meeting of the Satellite Division of The Institute of Navigation (ION GNSS+ 2010)*, pp. 161–171.

Teunissen, P. J. G. (1990). An Integrity and Quality Control Procedure for use in Multi Sensor Integration. In: *Proceedings of the 3rd International Technical Meeting of the Satellite Division of the Institute of Navigation (ION GPS 1990)*, pp. 513–522.

Teunissen, P. J. G. (1993). Least-squares estimation of the integer GPS ambiguities. *Invited Lecture. Section IV Theory and Methodology, IAG General Meeting, Beijing, China.*

Teunissen, P. J. G. (1995a). The least-squares ambiguity decorrelation adjustment: a method for fast GPS integer ambiguity estimation. *Journal of Geodesy*, 70(1-2):65–82.

Teunissen, P. J. G. (1995b). The invertible GPS ambiguity transformations. *Manuscripta Geodaetica*, 20:489–497.

Teunissen, P. J. G. (1999). An optimality property of the integer least-squares estimator. *Journal of Geodesy*, 73:587–593.

Teunissen, P. J. G. (2000). The success rate and precision of GPS ambiguities. *Journal of Geodesy*, 74:321–326.

Teunissen, P. J. G. (2003). Theory of integer equivariant estimation with application to GNSS. *Journal of Geodesy*, 77:402–410.

Teunissen, P. J. G. (2019). A new GLONASS FDMA model. *GPS Solutions*, 23(100).

Teunissen, P. J. G. (2021). GNSS Precise Point Positioning. In: Morton, Y. J., van Diggelen, F., Spilker Jr., J. J., and Parkinson, B. W. (Ed.), *Position, Navigation, and Timing Technologies in the 21st Century: Integrated Satellite Navigation, Sensor Systems, and Civil Applications*, pp. 503–528. John Wiley & Sons, Inc., Hoboken, New Jersey.

Teunissen, P. J. G., Joosten, P., and Tiberius, C. C. J. M. (1999). Geometry-free Ambiguity Success Rates in Case of Partial Fixing. In: *Proceedings of the 1999 National Technical Meeting of The Institute of Navigation*, pp. 201–207.

Teunissen, P. J. G. and Montenbruck, O. (Ed.) (2017). *Springer Handbook of Global Navigation Satellite Systems.* Springer International Publishing.

Teunissen, P. J. G. and Verhagen, S. (2009). GNSS Carrier Phase Ambiguity Resolution: Challenges and Open Problems. In: Sideris, M. G. (Ed.), *Observing our Changing Earth. International Association of Geodesy Symposia*, vol. 133, pp. 133–145. Springer, Berlin, Heidelberg.

Tiberius, C. and Kenselaar, F. (2000). Estimation of the Stochastic Model for GPS Code and Phase Observables. *Survey Review*, 35(277):441–454.

Toissant, M., Samson, J., Toran, F., Ventura-Traveset, J., Sanz, J., Hernandez-Pajares, M., and Juan, J. M. (2006). The Stanford - ESA Integrity Diagram: Focusing on SBAS Integrity. In: *Proceedings of the 19th International Technical Meeting of the Satellite Division of The Institute of Navigation (ION GNSS+ 2006)*, pp. 894–905.

Tukey, J. W. (1960). A survey of sampling from contaminated distributions. In: Olkin, I., Ghurye, S. G., Hoeffding, W., Madow, W. G., and Mann, H. B. (Ed.), *Contributions to Probability and Statistics: Essays in Honor of Harold Hotelling*, pp. 448–485. Stanford University Press.

van den Brink, L., Stoter, J. E., and Zlatanova, S. (2013). Establishing a national 3D standard compliant to CityGML: good practice of a national 3D SDI. *International Journal of Geographical Information Science*, pp. 92–113.

van Diggelen, F. (2021). End Game for Urban GNSS: Google's Use of 3D Building Models. *Inside GNSS*, 16(2):42–49.

Verhagen, S. (2004). Integer ambiguity validation: an open problem? *GPS Solutions*, 8(1):36–43.

Verhagen, S. (2005). *The GNSS integer ambiguities : estimation and validation.* phdthesis, Delft University of Technology.

Vollath, U., Birnbach, S., Landau, H., Fraile-Ordoñez, J. M., and Martín-Neira, M. (1998). Analysis of Three-Carrier Ambiguity Resolution (TCAR) Technique for Precise Relative Positioning in GNSS-2. In: *Proceedings of the 11th International Technical Meeting of the Satellite Division of The Institute of Navigation (ION GPS 1998)*, pp. 417–426.

Walter, T. and Enge, P. (1995). Weighted RAIM for Precision Approach. In: *Proceedings of the 8th International Technical Meeting of the Satellite Division of The Institute of Navigation (ION GPS 1995)*, pp. 1995–2004.

Wang, J., Satirapod, C., and Rizos, C. (2002). Stochastic assessment of GPS carrier phase measurements for precise static relative positioning. *Journal of Geodesy*, 76(2):95–104.

Wang, L., Groves, P. D., and Ziebart, M. K. (2012). GNSS Shadow Matching: Improving Urban Positioning Accuracy Using a 3D City Model with Optimized Visibility Prediction Scoring. In: *Proceedings of the 25th International Technical Meeting of the Satellite Division of The Institute of Navigation (ION GNSS+ 2012)*, pp. 423–437.

Wang, L., Groves, P. D., and Ziebart, M. K. (2015). Smartphone Shadow Matching for Better Cross-street GNSS Positioning in Urban Environments. *Journal of Navigation*, 68(3):411–433.

Wang, R., Becker, D., and Hobiger, T. (2023). Stochastic modeling with robust Kalman filter for real-time kinematic GPS single-frequency positioning. *GPS Solutions*, 27(3).

Wanninger, L. (2011). Carrier-phase inter-frequency biases of GLONASS receivers. *Journal of Geodesy*, 86(2):139–148.

Wanninger, L., Thiemig, M., and Frevert, V. (2021). Multi-frequency quadrifilar helix antennas for cm-accurate GNSS positioning. *Journal of Applied Geodesy*, 16(1):25–35.

Weiss, J. P., Axelrad, P., and Anderson, S. (2007). A GNSS Code Multipath Model for Semi-Urban, Aircraft, and Ship Environments. *Navigation*, 54(4):293–307.

Wen, W. (2020). 3D LiDAR Aided GNSS and Its Tightly Coupled Integration with INS Via Factor Graph Optimization. In: *Proceedings of the 33rd International Technical Meeting of the Satellite Division of The Institute of Navigation (ION GNSS+ 2020)*, pp. 1649–1672.

Wen, W. and Hsu, L.-T. (2021). 3D LiDAR Aided GNSS Real-time Kinematic Positioning. In: *Proceedings of the 34th International Technical Meeting of the Satellite Division of The Institute of Navigation (ION GNSS+ 2021)*, pp. 2212–2220.

Wendel, J. (2022). GNSS Pseudorange Fault Detection and Exclusion with Multiple Outliers. In: *Proceedings of the 35th International Technical Meeting of the Satellite Division of The Institute of Navigation (ION GNSS+ 2022)*, pp. 1481–1495.

Wieser, A. and Brunner, F. K. (2000). An extended weight model for GPS phase observations. *Earth, Planets and Space*, 52(10):777–782.

Wieser, A. and Brunner, F. K. (2002). Short Static GPS Sessions: Robust Estimation Results. *GPS Solutions*, 5(3):70–79.

Williams, A., Barrus, S., Morley, R. K., and Shirley, P. (2005). An Efficient and Robust Ray-box Intersection Algorithm. In: *ACM SIGGRAPH 2005 Courses*, SIGGRAPH '05, New York, NY, USA. ACM.

Won, J.-H. and Pany, T. (2017). Signal Processing. In: Teunissen, P. J. G.; Montenbruck, O. (Ed.), *Springer Handbook of Global Navigation Satellite Systems*, pp. 401–442. Springer International Publishing.

Wübbena, G., Schmitz, M., and Bagge, A. (2005). PPP-RTK: Precise Point Positioning Using State-Space Representation in RTK Networks. In: *Proceedings of the 18th International Technical Meeting of the Satellite Division of The Institute of Navigation (ION GNSS 2005)*, pp. 25840–2594.

Xin, S., Geng, J., Zhang, G., Ng, H.-F., Guo, J., and Hsu, L.-T. (2022). 3D-mapping-aided PPP-RTK aiming at deep urban canyons. *Journal of Geodesy*, 96:78.

Yang, L., Li, Y., Wu, Y., and Rizos, C. (2013). An enhanced MEMS-INS/GNSS integrated system with fault detection and exclusion capability for land vehicle navigation in urban areas. *GPS Solutions*, 18(4):593–603.

Yohai, V. J. (1987). High Breakdown-Point and High Efficiency Robust Estimates for Regression. *The Annals of Statistics*, 15(2).

Yozevitch, R. and Moshe, B. b. (2015). A Robust Shadow Matching Algorithm for GNSS Positioning: Particle Filter for Shadow Matching. *Navigation*, 62(2):95–109.

Yozevitch, R., Moshe, B. B., and Weissman, A. (2016). A Robust GNSS LOS/NLOS Signal Classifier. *NAVIGATION*, 63(4):429–442.

Zabalegui, P., De Miguel, G., Perez, A., Mendizabal, J., Goya, J., and Adin, I. (2020). A Review of the Evolution of the Integrity Methods Applied in GNSS. *IEEE Access*, 8:45813–45824.

Zhang, G., Hai, D., Ng, H.-F., and Hsu, L.-T. (2023). Extending 3DMA GNSS with Diffraction Features in Urban Areas: Feasibility Analysis and Preliminary Results. In: *Proceedings of the 36th International Technical Meeting of the Satellite Division of The Institute of Navigation (ION GNSS+ 2023)*, pp. 2884–2896.

Zhang, G. and Hsu, L. (2021). Performance assessment of GNSS diffraction models in urban areas. *NAVIGATION*, 68(2):369–389.

Zhu, N. (2018). *GNSS Propagation Channel Modeling in Constrained Environments: Contribution to the Improvement of the Geolocation Service Quality.* phdthesis, Institut Français des Sciences et Technologies des Transports, del'Aménagement et des RéseauxUniversité de Lille.

Zhu, N., Marais, J., Betaille, D., and Berbineau, M. (2018). GNSS Position Integrity in Urban Environments: A Review of Literature. *IEEE Transactions on Intelligent Transportation Systems*, 19(9):2762–2778.

Zimmermann, F., Schmitz, B., Klingbeil, L., and Kuhlmann, H. (2019). GPS Multipath Analysis Using Fresnel Zones. *Sensors*, 19(1):25.

Zoubir, A. M., Koivunen, V., Chakhchoukh, Y., and Muma, M. (2012). Robust Estimation in Signal Processing: A Tutorial-Style Treatment of Fundamental Concepts. *IEEE Signal Processing Magazine*, 29(4):61–80.

Zumberge, J. F., Heflin, M. B., Jefferson, D. C., Watkins, M. M., and Webb, F. H. (1997). Precise Point Positioning for the efficient and robust analysis of GPS data from large networks. *Journal of Geophysical Research*, 102(B3):5005–5017.

Acknowledgements

This thesis was developed during my time at the Institut für Erdmessung (IfE) at Leibniz Universität Hannover. Throughout this journey, many individuals have significantly contributed to my work. Their support, insights, and encouragement have been invaluable, and I am truly grateful to everyone who played a part, directly or indirectly, in this project.

First of all, I would like to express my deepest gratitude to my main supervisor, Prof. Dr.-Ing. Steffen Schön, for his invaluable guidance, support, and encouragement throughout my PhD journey. Without his efforts to attract funding for a project on the topic of multipath correction and mitigation in the context of urban GNSS navigation, this thesis would not have been possible. Furthermore, his expertise and insights have been instrumental in the successful completion of this thesis. I am also grateful for his accessibility and the time he dedicated to engaging in intensive discussions. He consistently introduced new ideas whenever they were needed while also granting me the freedom to develop my own, which greatly enriched my learning experience.

I am also profoundly thankful to my co-supervisors, Associate Prof. Dr. Li-Ta Hsu and apl. Prof. Dr.-Ing. Claus Brenner, for taking the time to review my work and providing constructive feedback, which have significantly shaped the quality of the thesis. Moreover, I am grateful to Associate Prof. Dr. Li-Ta Hsu for the numerous discussions we had at conferences, on-site in Hong Kong, and during his visits to Hannover. These interactions greatly enriched my understanding and perspective.

A heartfelt thanks to all my colleagues at the IfE for the great camaraderie and the daily discussions we shared. Your support and knowledge have been invaluable to both my academic work and personal growth. Sometimes our talks were in-depth and serious, yet I've found that some of the best ideas and solutions came from joking around during coffee breaks.

A major part of this work was carried out within the framework of a project named „Korrektur von GNSS-Mehrwegeffekten für die zuverlässige Eigenlokalisierung von hochautomatisierten Fahrzeugen in innerstädtischen Bereichen (KOMET)“ and funded by the Federal Ministry for Economic Affairs and Climate Action (BMWK). I extend my sincere thanks to the responsible people at BMWK, as well as to my colleagues from project partners Bosch and Geo++ for the excellent collaboration and insights.

Last but not least, I am deeply grateful to my family for their unwavering mental and financial support from the very start of my academic journey. Special thanks to Lucy for inspiring me to start, persevere, and ultimately see this journey through to the end. Thanks for being a part of countless work-related discussions, always backing me and for your understanding of the many long working hours. Your support has been a cornerstone of my achievements.

Thank you all for making this journey possible.

Curriculum Vitæ

Personal Information

Name: Fabian Ruwisch
Date of Birth: December 29, 1993
Place of Birth: Bielefeld, Germany

Course of Education

09/2004 - 07/2013	High school
10/2013 - 11/2019	Study of Geodesy and Geoinformatics at Leibniz Universität Hannover (LUH): *Bachelor of Science* (2016), *Master of Science* (2019)

Work Experience

07/2013 - 09/2013	*Intern* at publicly appointed surveyor in Oerlinghausen and Cadastre office in Bielefeld
02/2015 - 03/2015, 08/2015 - 09/2015	*Student Worker* at publicly appointed surveyor in Oerlinghausen
10/2015 - 10/2019	*Research Assistant* at Institut für Erdmessung, LUH and Geodätisches Institut, LUH
06/2018 - 10/2018	*Intern* at VMT (Shanghai) Technical Measurement Co., Ltd. in Shanghai, China
since 11/2019	*Research Assistant* at Institut für Erdmessung, LUH

List of Publications

Peer-review

1. **Ruwisch, F.** and Schön, S. (2025). Feature Map Aided Robust High Precision GNSS Positioning in Harsh Urban Environments. *IEEE Transactions on Intelligent Transportation Systems, pp. 1-13.*
2. O'Connor, M., Kersten, T., Skupin, C., **Ruwisch, F.**, Ren, L., Wübbena, T., and Schön, S. (2024). Low-latency GNSS multipath simulation and building wall detection in urban environments. *SIMULATION*, 100(1):71 – 89
3. **Ruwisch, F.** and Schön, S. (2023). GNSS Feature Map Aided RTK Positioning in Urban Trenches. In: *2023 IEEE 26th International Conference on Intelligent Transportation Systems (ITSC): iLoc - High-integrity Localization for Automated Vehicles*, pp. 5798–5804, Bilbao, Spain. IEEE
4. Baasch, K.-N., Icking, L., **Ruwisch, F.**, and Schön, S. (2023). Coordinate Frames and Transformations in GNSS Ray-Tracing for Autonomous Driving in Urban Areas. *Remote Sensing*, 15(1):180
5. **Ruwisch, F.** and Schön, S. (2022). Performance Assessment of GNSS RTK Positioning in Urban Environments: Outlier Detection versus 3DMA-FDE. In: *Proceedings of the 35rd International Technical Meeting of the Satellite Division of The Institute of Navigation (ION GNSS+ 2022)*, pp. 2649–2663, Denver, Colorado.
6. Schaper, A., **Ruwisch, F.**, and Schön, S. (2022). Diffraction Modeling for Improved 3DMA GNSS Urban Navigation. In: *Proceedings of the 35rd International Technical Meeting of the Satellite Division of The Institute of Navigation (ION GNSS+ 2022)*, pp. 1902–1916, Denver, Colorado.
7. Schön, S., Baasch, K.-N., Icking, L., Karimidoona, A., Lin, Q., **Ruwisch, F.**, Schaper, A., and Su, J. (2022). Towards integrity for GNSS-based urban navigation – challenges and lessons learned. In: *2022 IEEE Intelligent Vehicles Symposium (IV)*, pp. 1774-1781, Aachen, Germany. IEEE
8. **Ruwisch, F.** and Schön, S. (2022). GNSS Feature Map: Representation of Signal Propagation-related Features in Urban Trenches. In: *The International Technical Meeting of The Institute of Navigation*, pp. 701–711, Long Beach, California.
9. Icking, L., **Ruwisch, F.**, Schön, S. (2022). Multipath Characterization Using Ray-Tracing in Urban Trenches. In: Freymueller, J. T., Sánchez, L. (eds), *Geodesy for a Sustainable Earth. International Association of Geodesy Symposia*, vol 154. Springer.
10. O'Connor, M., **Ruwisch, F.**, Kersten, T., Skupin, C., Ren, L., Wübbena, T., and Schön, S. (2021). Low-latency GNSS multipath simulator for real-time applications in autonomous driving. In: *2021 IEEE/ACM 25th International Symposium on Distributed Simulation and Real Time Applications (DS-RT)*, pp. 1–9, Valencia, Spain. IEEE
11. Icking, L., **Ruwisch, F.**, and Schön, S. (2020). Doppler as a quality indicator for GNSS-based urban navigation - an evaluation with different receivers and clocks. In: *2020 European Navigation Conference (ENC)*, pp. 1-11, Dresden, Germany. IEEE
12. **Ruwisch, F.**, Jain, A., and Schön, S. (2020). Characterisation of GNSS Carrier Phase Data on a Moving Zero-Baseline in Urban and Aerial Navigation. *Sensors*, 20(14):4046

Non Peer-review

1. **Ruwisch, F.**, Ren, L., Skupin, C., Kersten, T., O'Connor, M., Schön, S., and Wübbena, T. (2022). Intelligent database architecture for high-integrity urban navigation. Poster Presentation at *33rd IEEE Intelligent Vehicles Symposium*, Aachen, Germany.

2. Karimidoona, A., Icking, L., **Ruwisch, F.**, and Schön, S. (2022). On the Prediction of Network RTK Integrity Performance in Urban Environments. In: *10th ESA Workshop on Satellite Navigation Technologies and European Workshop on GNSS Signals and Signal Processing (NAVITEC)*, Noordwijk, Netherlands.

3. **Ruwisch, F.**, Ren, L., Skupin, C., Kersten, T., O'Connor, M., Schön, S., and Wübbena, T. (2021). Analysis of the Carrier Phase Multipath Error in the Context of Correction Maps for Urban Navigation. Poster Presentation at *2021 European Navigation Conference (ENC)*, Edinburgh, United Kingdom.

Wissenschaftliche Arbeiten der Fachrichtung Geodäsie und Geoinformatik der Leibniz Universität Hannover

(Eine vollständige Liste der Wiss. Arb. ist beim Geodätischen Institut, Nienburger Str. 1, 30167 Hannover erhältlich.)

Nr. 388	HARTMANN, Jens:	Hochgenaue 3D-Erfassung von Großstrukturen durch kinematisches terrestrisches Laserscanning (Diss. 2023)
Nr. 389	ZHUGE, Xia:	Characterizing slope instability kinematics by integrating multi-sensor satellite remote sensing observations (Diss. 2023)
Nr. 390	DOROZYNSKI, Mareike Marianne:	Image Classification and Retrieval in the Context of Silk Heritage using Deep Learning (Diss. 2023)
Nr. 391	KNABE, Annike:	New Concepts for Gravity Field Recovery using Satellites (Diss. 2023)
Nr. 392	KALIA, Andre:	Landslide activity detection based on nationwide Sentinel-1 PSI datasets (Diss. 2023)
Nr. 393	BROCKMEYER, Marco:	Modellierung von Bodenbewegungen anhand heterogener Messverfahren am Beispiel der niedersächsischen Landesfläche (Diss. 2023)
Nr. 394	ZHANG, Mingyue:	Characteristics and Benefits of Differential Lunar Laser Ranging (Diss. 2023)
Nr. 395	DENNIG, Dirk:	Entwicklung eines kinematischen Profilvermessungssystems am Beispiel Kranbahnvermessung (Diss. 2024)
Nr. 396	FUEST, Stefan:	Nudging travelers to societally favorable routes by means of cartographic symbolization (Diss. 2024)
Nr. 397	MOFTIZADEH, Rozhin:	Advanced Particle Filtering for Vehicle Navigation based on Collaborative Information (Diss. 2024)
Nr. 398	VASSILEVA, Magdalena Stefanova:	Satellite Radar Interferometry for Geohazards: from ground deformation to processes understanding (Diss. 2024)
Nr. 399	MALINOVSKAYA, Anna:	Statistical Process Monitoring of Networks (Diss. 2024)
Nr. 400	BANNERT, Jörn:	Der Einfluss von Straßenverkehrslärm und Umgehungsstraßen auf Grundstückswerte in Ortslagen - Bestimmung mittels Expertenbefragung nach der Delphi-Methode (Diss. 2024)
Nr. 401	AXMANN: Jeldrik:	Maximum consensus localization using LiDAR (Diss. 2024)
Nr. 402	TENNSTEDT, Benjamin:	Concept and Evaluation of a Hybridization Scheme for Atom Interferometers and Inertial Measurement Units (Diss. 2024)
Nr. 403	HAKE, Frederic:	Schadenserkennung an Bauwerken mittels maschinellem Lernens (Diss. 2025)
Nr. 404	KARIMIDOONA, Ali:	On Integrity Prediction for Network-RTK Positioning in Urban Environments (Diss. 2025)
Nr. 405	ORTEGA, Mabel:	Domain Adaptation for Deforestation Detection in Remote Sensing: Addressing Class Imbalance and Performance Estimation (Diss. 2025)
Nr. 406	KUPRIYANOV, Alexey:	Investigation of Optical Accelerometry and Novel Satellite Formations for Future Gravimetry Missions (Diss. 2025)
Nr. 407	BREVA, Yannick:	On the Observation Quality of Robot-based GNSS Antenna Calibration for Determining Codephase Corrections (Diss. 2025)
Nr. 408	GUO, Zelong:	Co- and Post-seismic Slip Models Inferred from InSAR Geodesy (Diss. 2025)
Nr. 409:	YUAN, Yunshuang:	Collective Perception: A Fully-Sparse Deep Learning Framework for Multi-Agent Data Fusion (Diss. 2025)
Nr. 410	SU, Jingyao:	Towards interval-based autonomous integrity monitoring: Error bounding and uncertainty propagation (Diss. 2025)
Nr. 411	VINCENT, Asha:	Clock Networks for Geodetic Applications (Diss. 2025)
Nr. 412	KAMALASANAN, Vinu:	Control of Walking Behavior in Shared Spaces using Augmented Reality (Diss. 2025)
Nr. 413	TRUSHEIM, Philipp:	Kooperative Positionierung mittels Bündelausgleichung mit dynamischen Objekten (Diss. 2025)
Nr. 414	KRÖGER, Johannes:	Estimation and Validation of multi-GNSS multi-Frequency Phase Center Corrections (Diss. 2025)
Nr. 415	RUWISCH, Fabian:	GNSS Feature Maps – Robust Lane-level Accurate GNSS Navigation in Urban Trenches (Diss. 2025)